



# THÈSE

En vue de l'obtention du

## DOCTORAT DE L'UNIVERSITÉ DE TOULOUSE

Délivré par **l'Institut Supérieur de l'Aéronautique et de l'Espace**  
Spécialité : Génie mécanique

---

Présentée et soutenue par **Pierre SELVA**  
le 29 septembre 2009

**Modélisation du système vestibulaire et modèles non-linéaires  
de perception de l'orientation spatiale**

**Modeling of the vestibular system and nonlinear models  
for human spatial orientation perception**

---

### JURY

M. Ali Zolghadri, président  
M. Daniel Brun-Picard, rapporteur  
M. Yves Gourinat, directeur de thèse  
M. Jean-François de Lauzun, co-directeur de thèse  
M. Joseph Morlier  
M. Laurence Retman Young, rapporteur

---

École doctorale : **Aéronautique-Astronautique**

Unité de recherche : **Équipe d'accueil ISAE DMSM**

Directeur de thèse : **M. Yves Gourinat**

Co-directeur de thèse : **M. Jean-François de Lauzun**

**[This page intentionally left blank]**

# ACKNOWLEDGMENTS

I am deeply indebted to my thesis advisors Prof. Yves Gourinat and ENT specialist Jean-François Delauzun as they always believed in my abilities and provided whatever advice and resources necessary to accomplish my goals. I learned a lot from our discussions, and your advices were always wise and most useful.

I am most grateful to Dr. Charles Oman for giving the opportunity to work at the Man Vehicle Lab at MIT and who made significant contributions to the success of this investigation. Thank you for providing many invaluable hours meeting to discuss aspects of my research and working revisions of my various publications.

Tremendous thanks to Associate Prof. Joseph Morlier for guidance and support throughout the last three years. The willingness to answer questions and help with challenges of all sorts was greatly appreciated.

My thesis committee, Professor Laurence R. Young and Professor Daniel Brun Picard, deserve special thanks.

For funding my stay in the US I am grateful to François Prieur. I would not have lived this great experience without your support. I also thank ISAE and MIT for giving me the chance to study in the US.

To my roommates Annie Park, Jennifer Burger, Kimberley Clark and Yui Kumnerdpun: thank you guys for all the fun and the time we spent together. Thank you Annie for your generosity and friendship and for always caring for me, MAMA!! Thank you Jen for being an awesome roommate, for your support, and for improving my English! Kim, you are an amazing person, thank you for the energy and craziness you brought to the house. Thank you Yui for all the chicken salads and Ronny burgers we split together, and, above all, thank you for all the fun and laugh shared. My thoughts as well to Christopher O’Keeffe and Christine Newsham, thank you for your generosity and for all the fun and the time we spent together, you guys are awesome. Many thanks to all the other people I met in Cambridge. I really had a great time with all of you guys, you all participated in making my stay in the US an unforgettable story.

Thank you to Liz Zotos for always being so pleasant and helpful with administrative issues.

A lot of people have contributed their time, ideas, feedback and support over the last three years. Thank you, Michael Newman, Dr. Howard Stone, Dr. Grégoire Casalis, Dr. Dan Merfeld, Faisal Kamali, Guilhem Michon, Mathieu Bizeul, Amir Shahdin, Damien Guillon, Boris Cherman, Issam Tawk, Javier Toral Vazquez, Elias Abi Adallah, and all the other labmates and friends who have given me wonderful advice, inspiration and friendship over the years.

I would like to acknowledge everyone who provided technical support, especially for the zero G flight. Big thanks to Guy Mirabel, Xavier Foulquier, Marc Chartrou, Joel Xuereb, Thierry Duigou, Marc Chevalier, and Philippe Fargeout.

To all my friends from Bagnères de Bigorre and Toulouse who have supported and helped me along the way, and who have given me inspiration and friendship over the years. There are far too many people to list, but I think you all know who you are.

To my family, your love and support made this possible. You always believed in me and it gave me the strength to succeed. Mom, Dad, Françoise, Josette, and Michel, thank you so much.

Last but not least, thank you to “mon coeur”, Mélanie: you have always been with me from the start and I could never have gone so far without you. When you hold my hands, nothing is out of reach, not even my dreams.

# Table of contents

<b>ACKNOWLEDGMENTS .....</b>	<b>3</b>
<b>List of figures .....</b>	<b>7</b>
<b>List of tables .....</b>	<b>9</b>
<b>General introduction.....</b>	<b>10</b>
Contributions of this work.....	11
Objectives of the thesis .....	13
Thesis organization .....	15
<b>Chapter I: Background.....</b>	<b>16</b>
1.1. Vestibular physiology .....	16
1.1.1. The semicircular canals .....	17
1.1.2. Otolith organs .....	20
1.2. Mathematical modeling .....	21
1.2.1. Semicircular canals .....	21
1.2.2. Otolith organs .....	25
1.3. History of spatial orientation.....	28
1.4. State estimation of dynamic state-space models .....	32
1.4.1. Introduction .....	32
1.4.1.1. Probabilistic inference .....	33
1.4.1.2. Gaussian approximate methods.....	33
1.4.2. Linear state space estimation.....	34
1.4.2.1. Kalman filtering .....	35
1.4.3. Nonlinear state-space estimation.....	37
1.4.3.1. Nonlinear transformation of random variables .....	38
1.4.3.2. The extended Kalman filter.....	42
1.4.3.3. The unscented Kalman filter .....	44
<b>Chapter II: Finite element modeling.....</b>	<b>50</b>
2.1. Modeling of the cupula .....	50
2.1.1. Background .....	50
2.1.3. Analytical model using thin and thick bending membrane theory.....	54
2.1.4. Finite-element models .....	55
2.1.4.1. Computation of the Young's modulus .....	55
2.1.4.2. Comparison with other estimates .....	57
2.1.4.3. Analysis of different cupula shapes .....	58
2.1.4.5. Mechanical influence of cupula channels .....	61
2.1.5. Biologically similar material.....	62
2.2. Fluid structural interaction model .....	64
2.2.1. Introduction .....	64
2.2.2. Fluid-structure interaction .....	64
2.2.3. Arbitrary Lagrangian Eulerian methodology .....	65
2.2.4. 2D model .....	67
2.2.4.1. Geometry of the 2D model.....	67
2.2.4.2. Governing equations .....	68



2.2.4.3. Boundary conditions .....	70
2.2.4.4. Moving mesh.....	72
2.2.4.5. Simulations.....	73
2.2.5. Three-dimensional model of a single canal.....	79
2.2.6. 3D model of the entire set of canals.....	81

**Chapter III: Virtual reality model..... 84**

3.1. Virtual reality model .....	84
3.1.1. Introduction .....	84
3.1.2. Formulation of the kinematic problem.....	85
3.1.2.1. Rotation of reference frames .....	87
3.1.2.2. Orientation of the SCC coordinate system.....	87
3.1.2.3. Expression of the angular velocity vectors .....	88
3.1.2.4. Expression of the angular acceleration vector.....	89
3.1.2.5. Expression of the linear acceleration vectors.....	90
3.1.3. Programming and implementation .....	94
3.1.3.1. Graphical user interface .....	94
3.1.3.2. Simulink model .....	95
3.1.3.4. Virtual reality model .....	98
3.1.3.5. Simulation and visualization .....	99
3.1.3.6. Conclusion.....	101

**Chapter IV: Models for human spatial orientation..... 102**

4.1. Introduction .....	102
4.1. Relationships between Observer and Kalman filter models for human dynamics spatial orientation.....	104
4.1.2. Observer and KF model comparison: yaw rotation in darkness .....	104
4.1.2.1. Merfeld 1-D Observer model .....	104
4.1.2.2. Borah 1-D Kalman filter model .....	105
4.1.2.3. Ecologic basis for 1-D Kalman filter model parameters.....	107
4.1.3. Observer and KF 3-D model for somatogravic illusion in darkness.....	109
4.1.3.1. Three-dimensional Merfeld Observer model for large tilts .....	110
4.1.3.2. Three-dimensional Borah steady state Kalman filter for small tilts.....	111
4.2. Nonlinear models for human spatial orientation based on the hybrid extended and unscented Kalman filter .....	117
4.2.1. Coordinate system .....	117
4.2.2. Modeling of the sensors .....	118
4.2.3. Description of the model.....	119
4.2.3.1. Real world model .....	120
4.2.3.2. Internal model of the CNS .....	121
4.2.4. Estimation process.....	122
4.2.4.1 State vector update .....	122
4.2.4.2. Measurement equations: outputs of the real world model .....	127
4.2.5. Implementation consideration .....	128
4.2.6. Simulation results.....	129
4.2.6.1. Parameters .....	129
4.2.6.2. Constant velocity rotation about an earth vertical axis .....	130
4.2.6.3. Forward linear acceleration in darkness.....	133
4.2.6.4. Vestibular “Coriolis” Cross-coupling .....	134
4.2.6.5. Pseudo-Coriolis illusion .....	136

4.2.7 Sensitivity study .....	138
4.2.7.1. Yaw angular velocity in darkness .....	138
4.2.7.2. Forward linear acceleration in darkness .....	139
4.2.7.3. Vestibular Coriolis illusion .....	142
<b>Chapter 5. Scale model of the semicircular canals .....</b>	<b>143</b>
5.1. Similitude study.....	143
5.2. Choice of materials.....	147
5.3. Results .....	148
<b>Chapter 6. Conclusion and future works .....</b>	<b>150</b>
6.1. Overall conclusion.....	150
6.2. Perspectives .....	154
<b>References .....</b>	<b>156</b>
<b>Appendix 1: .....</b>	<b>163</b>
<b>Numerical model for the resolution of the fluid flow within a single canal</b> <b>.....</b>	<b>163</b>
<b>Appendix 2: Quaternions and spatial rotation.....</b>	<b>171</b>
<b>Appendix 3: Example of Simulink model used to generate sensors output</b> <b>for motion paradigms in darkness.....</b>	<b>172</b>
<b>Appendix 4: EKF and UKF models: Matlab code .....</b>	<b>173</b>

# List of figures

**Figure 1.1.** Visualization of the inner ear.

**Figure 1.2.** Orientation of the semicircular canals.

**Figure 1.3.** Cross-section of the ampulla and functioning of the hair cells.

**Figure 1.4.** Detection of an angular acceleration of the SCC through inertia of the endolymph fluid relative to the canal motion.

**Figure 1.5.** Physiology of the utricular macula.

**Figure 1.6.** Mechanism of the otolith organs, showing their sensitivity to linear acceleration and head tilt.

**Figure 1.7.** Mechanical model of a semicircular canal.

**Figure 1.8.** Curve of typical cupula displacement and Bode diagram of the transfer function between head angular velocity and cupula displacement.

**Figure 1.9.** Schematic diagram of the functioning of the Otolith organs.

**Figure 1.10.** Borah et al. multisensory model using steady state Kalman filter to represent neural central processing.

**Figure 1.11.** Outline of the three-dimensional model of Merfeld.

**Figure 1.12.** Principle of human spatial orientation estimation model.

**Figure 1.13.** Demonstration of the accuracy of the unscented transformation for mean and covariance propagation.

**Figure 2.1.** Three-dimensional model of the cupula.

**Figure 2.2.** Transversal displacement  $w(r)$  provided by the thin and thick analytical membrane models, and the finite element circular plate model.

**Figure 2.3.** Top view of the skate cupula which is thicker on the sides and thin in the center.

**Figure 2.4.** CAD models of the cupula considering different shapes.

**Figure 2.5.** Transversal displacement of the human cupula provided by a finite element simulation in response to a static pressure of 0.05 Pa.

**Figure 2.6.** Analysis of the shear strain above the crista.

**Figure 2.7.** Modeling of a section of cupula material having vertical empty tubes

**Figure 2.8.** Results provided by the finite-element model of a section of cupula material having vertical empty tubes.

**Figure 2.9.** Representative frequency sweeps of  $G'$  and  $G''$  for collagen hydrogels at each polymerization temperature.

**Figure 2.10.** Comparison Lagrangian and Eulerian descriptions. 2D example of a beam that undergoes a pressure  $P$ .

**Figure 2.11.** Comparison Lagrangian, Eulerian, and ALE descriptions

**Figure 2.12.** Dimensions of the human lateral semicircular canal and reconstruction of a 2D model under Comsol Multiphysics.

**Figure 2.13.** Concept of fluid-structure interaction (FSI).

**Figure 2.14.** Smoothed Heaviside function  $flc2hs(t-t_0, \Delta t)$  with a continuous second derivative

**Figure 2.15.** Visualization of the subdomains that have different conditions for mesh displacement.

**Figure 2.16.** Rotational motion applied to the semicircular canal.

**Figure 2.17.** Evolution of the displacement of the cupula at the very beginning of the imposed rotational motion.

**Figure 2.18.** Evolution of the velocity of the fluid in the slender part of the duct at the beginning of the rotational motion.

**Figure 2.19.** Fluid velocity and cupula displacement at the beginning of the rotation. Visualization in the ALE reference frame.

**Figure 2.20.** Fluid velocity and cupula displacement at the end of the rotation. Visualization in the ALE reference frame.

**Figure 2.21.** Displacement of the center of the cupula during a constant angular rotation which ends at time  $t=15$  s.

**Figure 2.22.** Rotation of the canal located 30 mm away from the axis of rotation. The arrows are oriented along the fluid flow.

**Figure 2.23.** Visualization of a three-dimensional single canal.

**Figure 2.24.** Fluid velocity in m/s and cupula displacement in m at time instant  $t=0.03$  s and  $t=1$  s.

**Figure 2.25.** Three-dimensional CAD model of the three SCCs + utricle +cupulae.

**Figure 2.26.** Mesh of the final three-dimensional model which consists of 111 quadratics elements that represents 111 degrees of freedom.

**Figure 2.27.** Results provided by the simulation of the final 3D model of the semicircular canals.

**Figure 3.1.** Schematic block diagram of the virtual reality simulink model

**Figure 3.2.** Visualization of the diagnosis procedure and definition of the different coordinate systems

**Figure 3.3.** Definition of head movements: pitch, roll, and yaw.

**Figure 3.4.** Orientation of the coordinate systems for a yaw head movement while the subject is rotated around an Earth vertical axis.

**Figure 3.5.** Orientation of the coordinate systems for a pitch head movement while the subject is rotated around an Earth vertical axis.

**Figure 3.6.** Orientation of the coordinate systems for a roll head movement while the subject is rotated around an Earth vertical axis.

**Figure 3.7.** Graphical user interface of the virtual reality model

**Figure 3.8.** First layer of the simulink model.

**Figure 3.9.** Detailed view of the block of the first layer titled “SCC”.

**Figure 3.10.** Detailed view of the block of the first layer titled “utricle-sacculle”.

**Figure 3.11.** Schematic block diagram of how the virtual reality world is created and controlled..

**Figure 3.12.** Displacement of the cupula of each canal due to rotation movement of the chair, and rotation movement of the chair and of the head

**Figure 3.13.** Visualization of a virtual scene: The state of each sensor can be visualized on real time during the test.

**Figure 4.1.** Principle outline of the internal model concept applied for the estimation of external physical variables like acceleration, velocity, and position.

**Figure 4.2.** Merfeld Observer model for a yaw rotation.

**Figure 4.3.** Merfeld Observer model showing pole/zero cancellation.

**Figure 4.4.** One-dimensional Borah’s Kalman filter model.

**Figure 4.5.** Kalman filter model for yaw rotation (left)

**Figure 4.6.** Observer and KF estimated angular velocity responses to a 100 deg/s angular velocity step.

**Figure 4.7.** Kalman gain  $K_{21}$  with respect to  $Q/V$  ratio and shaping filter bandwidth.

**Figure 4.8.** Somatogravic illusion.

**Figure 4.9.** 3D Observer model.

**Figure 4.10.** 3D *internal model used in the present Kalman filter model.*

**Figure 4.11.** Block diagram of the steady state Kalman filter for the somatogravic illusion.

**Figure 4.12.** Perception of linear acceleration and pitch angle in response to a forward linear acceleration of 0.2g provided by Merfeld Observer and Kalman filter model.

**Figure 4.13.** Perception of linear acceleration and pitch angle in response to a forward linear acceleration of 0.2g provided by the Kalman filter model for two different otolith dynamics.

**Figure 4.14.** Response of the Kalman filter model with Borah’s otolith transfer function for different bandwidths of linear acceleration

**Figure 4.15.** Head and world coordinate frame.

**Figure 4.16.** Coordinate system attached to the sensors

**Figure 4.17.** Sensors transfer functions used in the EKF and UKF models.

**Figure 4.18.** Philosophy of the nonlinear model of human spatial orientation perception.

**Figure 4.19.** Detailed view of the model of the real world

**Figure 4.20.** Detailed view of the model of the internal model of the CNS

**Figure 4.21.** Equivalent model of the low pass filter

**Figure 4.22.** Equivalent representation of the transfer functions of the semicircular canal dynamics.

**Figure 4.23.** Equivalent representation of the transfer functions of the otolith dynamics.

**Figure 4.24.** Graphical user interface of the EKF/UKF models.

**Figure 4.25.** Scheme of the yaw rotation experiment in darkness.

**Figure 4.26.** Model response to a step in yaw angular velocity.  
**Figure 4.27.** Model response to a step in yaw angular velocity of the surrounding environment.  
**Figure 4.28.** Model response to a step in forward linear acceleration of 2 m/s  
**Figure 4.29.** Description of the Coriolis illusion.  
**Figure 4.30.** Simulation of vestibular Coriolis effect I  
**Figure 4.31.** Simulation of vestibular Coriolis effect II  
**Figure 4.32.** Description of the pseudo-Coriolis illusion.  
**Figure 4.33.** Simulation of the pseudo-Coriolis illusion.  
**Figure 4.34.** Influence of the bandwidth in angular velocity on the estimated yaw angular velocity in darkness.  
**Figure 4.35.** Influence of the bandwidth in linear acceleration on the estimated linear acceleration (a) and perceived pitch angle (b) in darkness.  
**Figure 4.36.** Influence of the linear acceleration process noise on the estimated linear acceleration (a) and perceived pitch angle (b) in response to a forward acceleration in darkness.  
**Figure 4.37.** Influence of bandwidth in head angular velocity on the estimated yaw angular velocity (a) and perceived pitch angle (b) in response to a Coriolis stimulation in darkness.

## List of tables

**Table 1.1.** Validation cases for Observer and KF / EKF models

**Table 2.1.** Summary of the values of the pressure-volume coefficient along with its relation to the long time constant of the cupula. See nomenclature for definition of parameters.

**Table 2.2.** Relationship between the Young's modulus of the cupula and the pressure-volume coefficient K.

**Table 2.3.** Expression of the prescribed displacements for a head rotation.

**Table 2.4.** Boundary conditions of the two-dimensional finite-element model of the horizontal semicircular canal.

**Table 5.1.** Dimension of the physical parameters that influences fluid flow within a semicircular canal in terms of fundamental units.

**Table 5.2.** Matrix form of the Buckingham Pi theorem.

**Table 5.3.** Matrix form of the Buckingham Pi theorem applied to our similitude problem.

**Table 5.4.** Required experimental values for cupula material Young's modulus and maximum simulated head angular velocity

**Table 5.5.** Quantitative estimation of possible configurations that keep constant all the dimensionless parameters.

**Table 6.1.** Summary of the sensitivity study of some of the parameters of the UKF model.

# General introduction

Daily human activity includes complex orientation, postural control, and movement coordination. All these tasks depend upon his perception of motion. The non-auditory section of the human inner ear, the vestibular system, is recognized as the prime motion sensing center. It represents an inertial measuring device which allows us to sense, in the absence of external sensory cues (vision, etc) self-motion with respect to the six degrees of freedom in space (three rotational and three translational).

The information from the vestibular apparatus is used in three ways:

- To provide a subjective sensation of movement in three-dimensional space
- To maintain upright body posture (balance)
- To control the muscles that move the eyes, so that in spite of the changes in head position which occur during normal activities such as walking or running, the eyes remain stabilized on a point in space.

Several scenarios illustrate these points. For instance, if a cat is dropped upside down, it will land right side up on all four paws. If a newborn infant is tilted backward, its eyes will roll downward so that its gaze remains fixed on the same point. If, as you read this report, you shake your head rapidly from side to side, the print nonetheless will stand still. Each of these scenarios is an example of how a healthy balance (vestibular) system compensates for daily changes in our spatial orientation.

The vestibular system is comprised of two primary sense organs:

- The semicircular canals (SCCs), which detect angular accelerations of the head
- The otolith organs, which respond to linear accelerations of the head and to gravity.

Thus, vestibular sensors provide information to the brain regarding our body's position and acceleration in space with sensing capabilities that are compatible with everyday movements of man relative to his surroundings, and hence play central role in spatial orientation.

Spatial orientation can be defined as one's perception of body position in relation to a reference frame. This process involves two main sensory modalities, the vestibular system and vision, but proprioceptive and auditory inputs also come into play. The control of spatial orientation during navigational tasks and locomotion requires a dynamic updating of the representation of the relations between the body and the environment, i.e. spatial orientation normally entails both the subconscious integration of multisensory cues and the conscious interpretation of external information. Therefore, the Central Nervous System (CNS) uses information coming from multiple sensors to come up with a representation of how the body is moving and is oriented in space.

The results of this "spatial orientation" process are usually satisfactory in most everyday life situations. However, when technology achievements began to expose humans to new and artificial situations such as sustained accelerations in fighter airplanes or micro-gravity environment in spacecrafts, our ability to correctly estimate our position and motion became

limited. As a matter of fact, as the number of fighter airplane accidents due to technical failure keeps decreasing, human errors have been proven to be a safety limiting factor. That is, the advent of aeronautics flight has not only involved a new demand on human organism but also the ability for pilots to deal with a high workload environment and a complex instrument panel. Furthermore, in some circumstances, for instance when flying in clouds or at night, pilots may not have the possibility of seeing external references. As a result, pilots are constantly liable to introduce conflict between their internal feeling of orientation and the true orientation, and hence to experience a case of spatial disorientation which is a phenomenon attributed to 15 to 30% of all aircraft fatalities in flight (Braithwaite et al. 1998, Knapp et al. 1996). Thus, all these considerations have lead number of researchers to model human spatial orientation.

Mathematical models for three-dimensional human spatial orientation have continued to evolve over the past four decades. Several models exist and have been developed using multiple computational approaches such as linear systems analysis, the concept of internal models, observer theory, Bayesian theory, Kalman filtering and particle filtering. A review of these approaches has recently been written by MacNeilage (2008). Different features can be distinguished among these models: some of them are restricted to one-dimensional space, whereas others take into account motions in three-dimensional space; some incorporate visual cues, whereas others only model vestibular response in the dark; and some work for large head tilts whereas others do not.

## **Contributions of this work**

The scope of the work presented in this thesis concerns on one hand the modeling of the vestibular sensors, and more particularly the semicircular canals, and on the other hand nonlinear models for human spatial orientation perception.

Since the 30's, numerous models of the semicircular canal macromechanics have been suggested using different approaches. W. Steinhausen (1933) formulated a classical torsion pendulum model for the dynamic behavior of a single SCC. This model, which has been the benchmark for subsequent works, consists of a single-degree of freedom overdamped spring-mass-damper system subject to mass-proportional inertia forcing. Several notable extensions have then been made to enhance this original model by relating the geometry and structure of the SCC to mass, stiffness, and damping parameters appearing in the model (e.g. Van Egmond et al. 1949, Groen et al. 1952, Van Buskirk 1976, Oman et al. 1987, Rabbitt et al 2004). Other models were based on the resolution of the fluid flow equation within the canal (Van Buskirk 1977, Van Buskirk 1988, Steer 1967, Oman et al. 1987, Damiano et al. 1996, Rabbitt et al. 1999). The three-dimensional model of Oman et al. (1987), in which the non-uniform geometry of the canal was considered, probably constitutes the most compatible biophysical single-degree of freedom model of the SCC. Some of these models are formulated in one dimension, while few of them consider a three-dimensional geometry. Moreover, all of these models consider a single canal and most of them do not take into account the fluid-structure interaction but rather consider the influence of the cupula by a punctual elasticity.

→ Therefore, the first goal of the present thesis is to provide a three-dimensional model of the entire set of canals using fluid-structural finite-elements simulations. To achieve this goal, we first develop a two dimensional finite-elements model of a single canal. Second, this

model is extended to a three-dimensional case. Finally, the 3D model is extended to the case where the three semicircular canals are considered.

In order to build these numerical models, one needs to know the physical properties of the fluid that fills the canals and the elastic properties of the cupula - a membrane located within the duct that acts as a coupling between the fluid flow and sensory hair cells. The properties of the fluid, i.e. its density and viscosity, are well known (Steer, 1967). However, it is hard to find in the literature values for the elastic properties of the human semicircular canal cupula, and more especially its Young's modulus, as most models represent the cupula as a linear spring-like element of stiffness  $K = \Delta P / \Delta V$ , where  $\Delta V$  is the volume displaced upon application of a pressure difference  $\Delta P$ .

→ Thus, the second goal of this doctoral work is to estimate the Young's modulus of the human semicircular canal cupula using thick plate theory and also finite-elements (FE) models. In addition, cupula FE models are also used to study the influence of different cupula shapes on its motion and to analyse both the shear strain distribution and evolution near the sensory epithelium.

As we move in our surrounding in space, our vestibular sensors provide information to the brain regarding our body's position and acceleration in space. However, the way each sensor behaves for any angular or linear acceleration is not obvious, especially for complex head motion. In particular, in order to find out what are the semicircular canals sensing when a subject is doing head movements on a centrifuge Adenot (2002) developed a model that was able to compute the state of each cupula during the imposed motion. However, this model was limited to SCC sensors, considered a head centered set of sensors, and the implementation of successive head movements was not possible.

→ Consequently, the third goal of this thesis is to extend this model: 1) by considering not only the angular but also the linear sensors, 2) by taking into account the position of the inner ear away from head vertical axis, 3) by implementing a three-dimensional animation of the sensors, and 4) by developing a virtual reality model of the experiment. As an application, we have chosen to model a medical procedure called the rotary chair testing that is commonly used during a vestibular diagnosis rather than a centrifuge experiment. However, the developed model can be easily extended to the case of a centrifuge paradigm as the distance between the position of the inner ear and the axis of rotation is a parameter of the model.

→ In addition to this virtual model, we propose a similitude study, a choice of adequate materials, and a set of parameters so as to build a large scale model of the system SCC / cupula that has a similar dynamic behavior of the biological system for a specific imposed angular velocity.. Both models (virtual and scale model) can be used as a demonstrating and learning tool, for instance for the training of medical students, as the theoretical state of each sensor can be observed in real time for any kind of head rotation.

Regarding to the models of human spatial orientation, two principle model families can be distinguished: Observer class models and Kalman filter class models. Although both approaches are apparently based on different assumptions, they produce similar responses, at least for the set of empirical parameters derived in the literature.



→ The fourth goal of this thesis is to demonstrate why the Observer and Kalman filter model families are dynamically equivalent from an input-output perspective. Furthermore, we investigate the physical meaning of the KF model parameters that were previously chosen as free parameter of the model and were derived empirically.

The first Observer model developed by Merfeld et al. (1993) has then been extended by several authors till the last contributions of Newman (2009). Despite this model is able to simulate different kinds of sensory illusions, it is limited to deterministic signals as it does not consider process noise and sensor noise. Furthermore, the gains used in the model that drive the responses in term of position, velocity, and acceleration perception are empirical. In order to derive a set of optimal gains and to take into consideration stochastic signals, Pommellet (1990) applied the extended Kalman filter (EKF) to this problem. However, his filter exhibited important numerical oscillations.

→ Therefore, the fifth goal of this thesis is first to modify Pommellet's model so as to improve numerical stability and second to develop another nonlinear model based on a novel estimation technique called the unscented Kalman filter (UKF). It has been shown that in many applications this technique outperforms the EKF in terms of stability, accuracy, and computation time.

## **Objectives of the thesis**

The main objectives of the presented thesis are summarized as follows:

- Estimation of the elastic properties of the human semicircular canal cupula – a membrane located in each canal that functions as a coupling between the fluid flow within the ducts and the sensory hair cells –using thin and thick bending membrane theory and also finite-element simulations based on more realistic morphology
- Develop of a three-dimensional model of the set of semicircular canals based on fluid-structural finite-elements simulations
- Develop of a three-dimensional dynamic virtual reality model of the vestibular sensors in order to propose both a demonstrating and a learning tool of this system
- Propose a similitude study so as to build a large scale model of the semicircular canals
- Demonstrate why the widely known “Observer” and “Kalman filter” model families for human spatial orientation perception – despite apparently different assumptions – are dynamically equivalent from an input-output (“black box”) perspective
- Develop two nonlinear models for human spatial orientation estimation with the help of the extended Kalman filter and the unscented Kalman filter, respectively. Both models are formulated in three-dimensional space and take into account vestibular and visual cues.

Based on the work of this thesis, the author has so far succeeded in publishing the following works:

- International peer-reviewed journals:
  - *Development of a dynamic virtual reality model of the inner ear sensory system as a learning and demonstrating tool.* Modelling and Simulation in Engineering, volume 2009.
- International conference with proceedings:
  - A Matlab/simulink model of the inner ear angular accelerometers sensors. ASME, International Design Engineering Technical Conferences & Computers and Information in Engineering Conference, August 30 – September 2<sup>nd</sup>, San Diego, California, USA.
- Manuscripts under progress:
  - *Mechanical properties and motion of the cupula of the human semicircular canal.* Journal of Vestibular Research.
  - *Relationship between Observer and Kalman filter models for human dynamic spatial orientation.* Journal of Neurophysiology.
  - *Nonlinear models for human spatial orientation.* Journal of Biology Cybernetics.
  - *A three-dimensional finite-element model of the human semicircular canals.* Computer Modeling in Engineering & Sciences.

## Thesis organization

The presented thesis is organized in six chapters.

- Chapter 1. – Background: Provides a background on the anatomy and physiology of the vestibular system, on the history of spatial orientation modeling, and on state estimation techniques of dynamic state-space models.
- Chapter 2. – Finite element modeling: Presents finite-element models for the cupula and finite-element fluid-structural interaction model of the semicircular canals. Introduces the history on cupula attachment, bending mode, stiffness, and modeling. Estimates the Young's modulus of the cupula using thin and thick bending membrane theory, finite-element simulations, and estimates of a pressure-volume coefficient taken from the literature. Presents a three-dimensional finite-element model of the semicircular canals.
- Chapter 3. – Virtual reality model: Presents the development of a virtual reality model of the vestibular sensors. The kinematics problem is first formulated. The resolution of the equation of motions and the computation of the state of each sensor are achieved using a Simulink model. Finally, a virtual world is linked to the Simulink file so as to visualize in real time the behavior of the sensory system. Note that a graphic user interface is specifically developed to simplify the use of the model.
- Chapter 4. – Models for human spatial orientation perception: Demonstrates why the "Observer" and "Kalman filter" model families are equivalent from an input-output perspective. Introduces the idea that the motion disturbance and sensor noise spectra employed in the Kalman Filter formulation may reflect human perceptual thresholds and prior motion exposure history. Describes the structure of the EKF and UKF models through the modeling of the sensors and the definition of the central process in terms of suboptimal estimation. Discusses implementation in Matlab. Presents predictions of the model for usual experimental cases. Performs a sensitivity analysis on the parameters of the model.
- Chapter 5. – Scale model of the semicircular canals: a similitude study for the semicircular canal is presented, and potential materials for the manufacturing of the large scale model are proposed.
- Chapter 6. – Conclusion: Summarizes the key findings of this study and makes recommendations for future work.

The work related to the development of models for human spatial orientation estimation and to finite-elements modeling of the cupula has been carried out while the author was a visiting student at Massachusetts Institute of Technology.

# Chapter I: Background

## 1.1. Vestibular physiology

The inner ear is divided into two parts: the cochlea serving auditory function, and the vestibular system - which is phylogenetically the oldest part of the inner ear - that contains the sensors providing information of body orientation and balance in three-dimensional space. Any motion of the body are thus detected by the vestibular system, encoded as an electrical signal, and transmitted to the brain through the vestibular nerve. The brain then integrates vestibular, visual, and somatosensory inputs to estimate the orientation and motion of the body, and consequently elicit eye, head, or body movements that will stabilize gaze and maintain balance.

There is one vestibular system on each side of the head, in close approximation to the cochlea. Due to its specific structure, this system is also called the labyrinth (Fig. 1.1). One distinguishes between the bony labyrinth and the membranous labyrinth. The bony labyrinth is a complex cavity tunneled in the temporal bone of the skull. Its structure forms three ducts - the semicircular canals - that converge toward a larger central part called “the vestibule”. The membranous labyrinth is enclosed in this osseous labyrinth, and is suspended in a fluid called “the perilymph” (Sauvage, 1999). In birds and mammals, fine connective tissue filaments suspend the membranous duct within the osseous canal. The filaments serve to anchor the membranous labyrinth to the temporal bone such that the gravito-inertial acceleration experienced by the sensory organs could be expected to be nearly identical to that experienced by the temporal bone. To date, there are no experimental data to suggest significant relative motion between the temporal bone and the membranous labyrinth (Rabbitt, 2004). The membranous labyrinth is also filled with fluid known as “the endolymph”, physically a water-like liquid. Each side of this bilateral system consists of two types of sensors: a set of three semicircular canals sensing rotation movement, and two otolith organs (the saccule and utricle) which sense linear movement and head tilt.

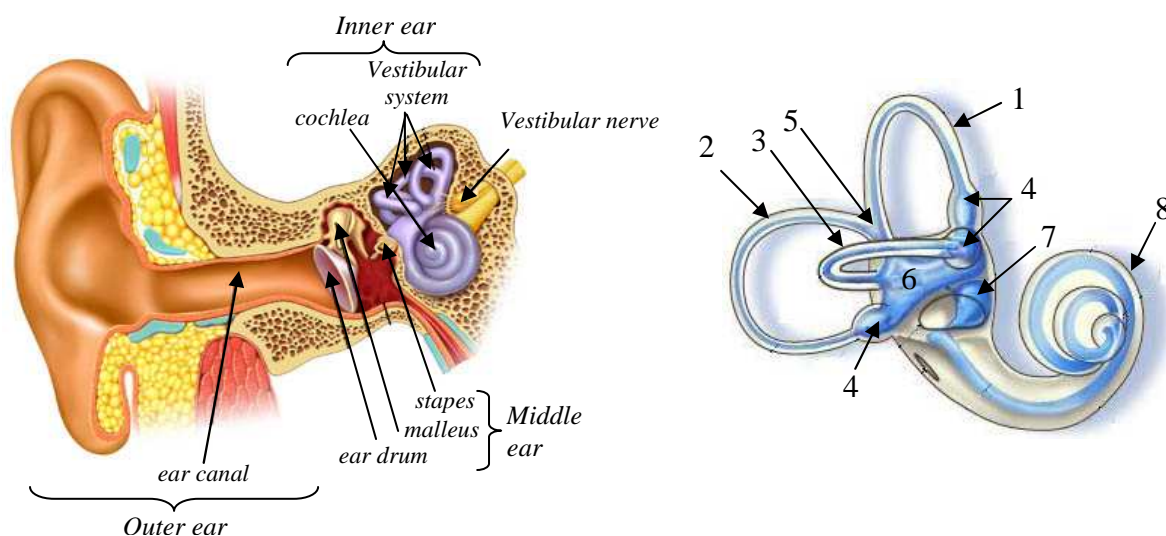


**Figure 1.1.** Visualization of the inner ear. 1) Anterior canal, 2) posterior canal, 3) lateral canal, 4) ampulla of each canal, 5) common crux, 6) utricle, 7) saccule, 8) cochlea.

### 1.1.1. The semicircular canals

The semicircular canals are commonly referred to as the lateral canal, also called horizontal canal, and the posterior and anterior canals, which constitutes the vertical canals. These latter have a common duct called the common crux for about 15% of their length. The canals are oriented in almost mutually orthogonal planes. The lateral canal lies in a plane elevated about 30 degrees from the horizontal plane, while the two others are arranged in diagonal planes which subtend roughly 45 degrees relative to the frontal and saggital planes of the skull (Fig. 1.2a). Thus, the anterior canal on one side of the head is parallel to the posterior canal on the other and vice versa, whereas the horizontal canals of both inner ears lie in the same plane. Because most head movements are not in a single SCC plane, and also because of the imperfect orthogonality of the three canals, the labyrinth usually resolves a given head rotation into three components. That is, endolymph motion in each canal measures component of the head's rotational velocity in the plane of that canal (Fig. 1.2b). It has also been shown that each canal admits a specific direction of stimulation, which maximizes the excitation: the lateral, anterior and posterior canals primarily sense yaw, roll and pitch respectively (Rabbitt, 1999).

The set of canals constitute a very small fluid-filled system the size of a pea. They approximately form a circular path of 3.2 mm radius and have a cross section radius along their slender part of about 0.16mm (Curthoys et al., 1987). The study of Curthoys and Oman probably constitutes the most thorough investigation concerning the dimensions of the human semicircular canals. From microdissected specimens, they were able to provide measurements of the sizes, cross-sectional shapes and areas all around the path of fluid flow through the horizontal semicircular duct, ampulla, and utricle. The results of this study are presented in more detail in Chapter II.

At one location in each canal, and more precisely in the vicinity of the utricle, the canal cavity swells to form a bulbous expansion known as the ampulla that contains a transverse ridge of sensory epithelium, the crista. The epithelial surface of the crista contains thousands of sensory hair cells and surrounding supporting cells (Fig. 1.3). Hair cells and supporting cells are found not only atop the ridge (crest) of the crista, but also down its sloping flanks. Hair cell sensory cilia project a short distance into tiny channels in the cupula, a gelatinous structure that extend upward from the surface of the crista all the way to the vault (roof) of the ampulla. The channels in the cupula material may be created as cupula material is secreted upwards from the supporting cells surrounding the each hair cell. The cupula effectively forms a thick diaphragm that completely occludes the canal lumen above the crista, and covers the entire sensory surface on the crest and both flanks. As detailed later, it is now believed that the cupula appears attached to the ampulla around its entire periphery.

When the head is subjected to an angular acceleration, endolymph inertia creates a hydrostatic pressure that deforms the cupula (Fig. 1.4). Bending of hair cell stereocilia then initiates a complex transduction process in hair cells and vestibular afferent neurons. The nervous signal is finally transmitted to the brain and a sensation of motion results. At a constant rotation rate, the endolymph in the canals tends to catch up with the rotation of the head due to the viscosity, eliminating the relative movement. Eventually, as long as the rotation rate remains constant, the cupula returns to a vertical position due to its elastic properties and the sensation of motion eventually ceases.

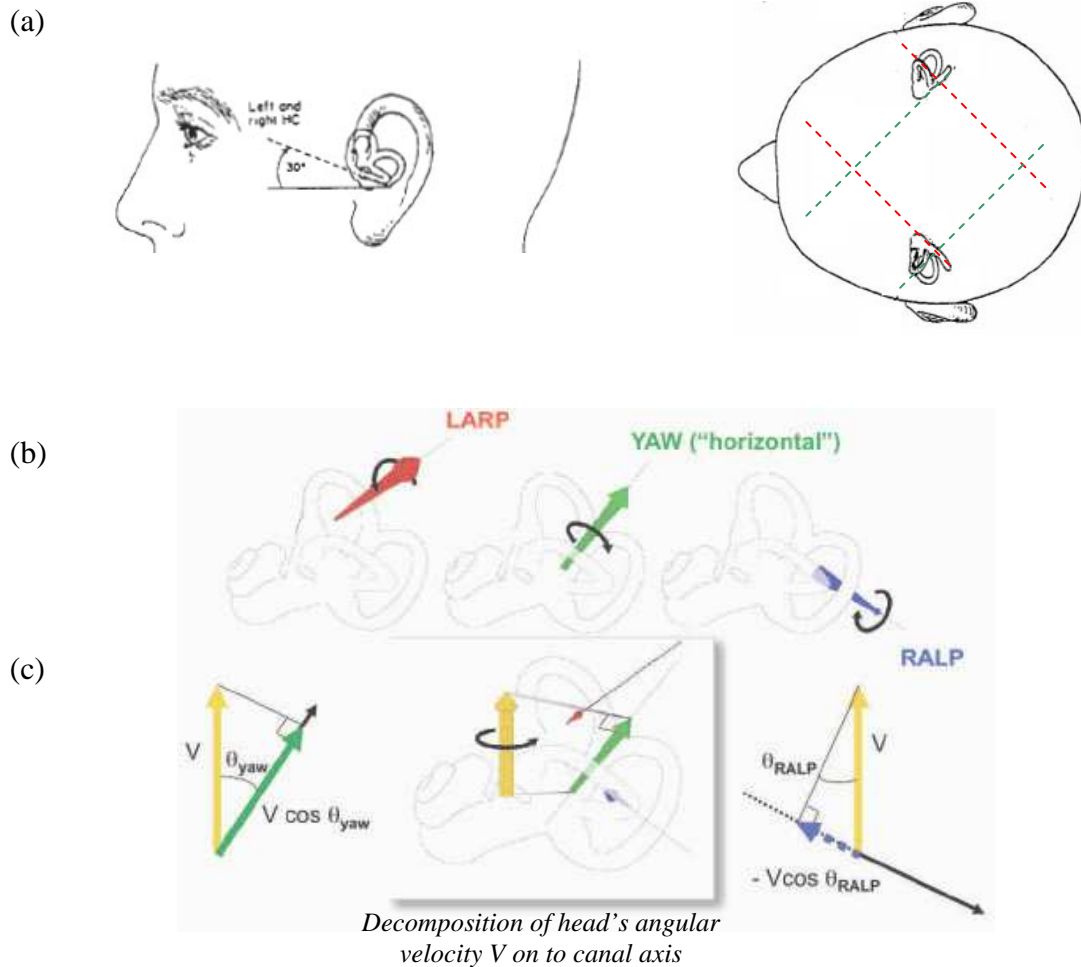


**Figure 1.2.** Orientation of the semicircular canals. (a) Orientation of the semicircular canals within the head. (b) Definition of canal axis. (c) Resolving head's angular rotation into vector components. HC, horizontal canal; RA and LA, right and left anterior canal, respectively; RP and LP, right and left posterior canal, respectively.

All of the hair cells on a semicircular canal crista are oriented or “polarized” in the same direction. Their stereocilia all have the tall ends pointing the same way. As a result, endolymph motion that is excitatory for one hair cell will be excitatory for all of the hair cells on that crista. Horizontal and vertical canals have different direction of polarization. Hair cells in the horizontal canals are polarized to be excited by flow of endolymph toward the ampulla, whereas hair cells in the vertical canals are polarized to be excited by flow of endolymph away from the ampulla.

Experimental studies (e.g. Goldberg and Fernandez, 1971) have shown that afferent neurons exhibit slightly different dynamics in response to the same head angular acceleration stimulus. All neurons seem to show a response component proportional to cupula volume displacement, as estimated from fluid mechanical models. Differences between units in static sensitivity, rate sensitivity and adaptive characteristics are attributed to the hair cell transduction or afferent encoding processes.

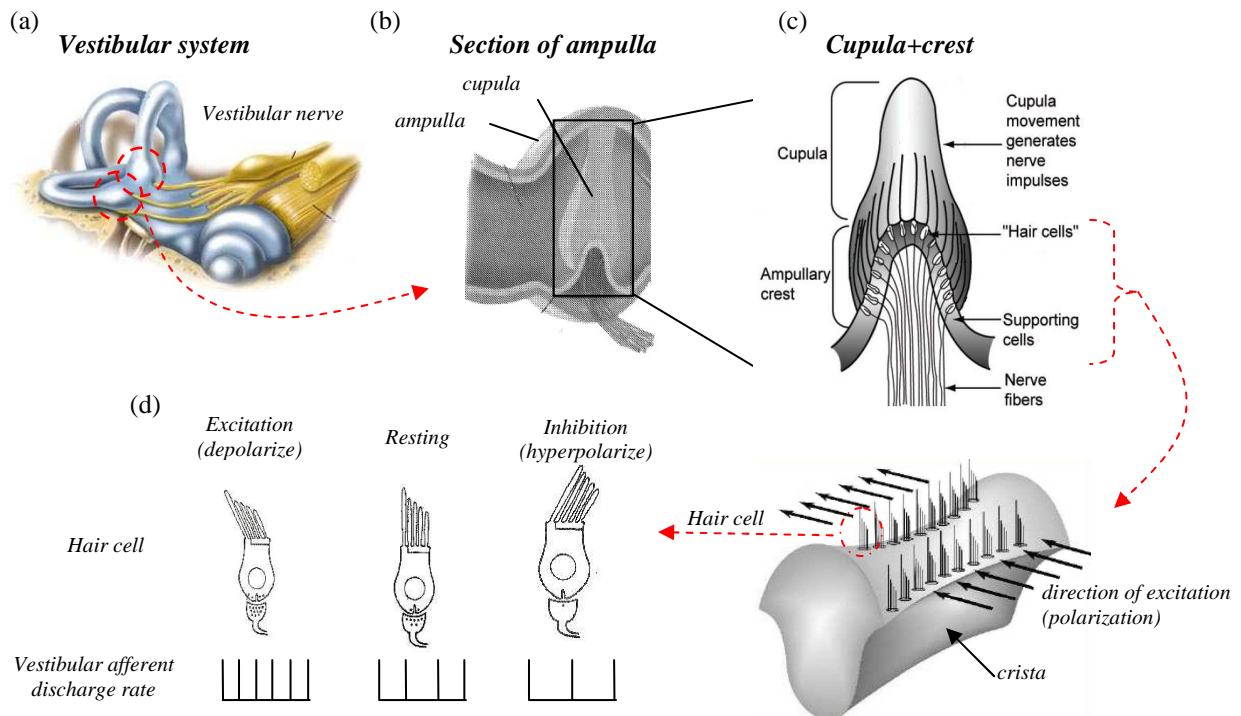


**Figure 1.3.** Cross-section of the ampulla and functioning of the hair cells. (a) Visualization of the vestibular system; (b) Section of ampulla showing how the cupula seals the duct; (c) Details of the crista and hair cells implantation; (d) Function of vestibular hair cells: when mechanical forces deviate the cilia toward the kinocilium, the hair cell depolarizes and the frequency of action potentials in the associated afferent vestibular neurons increases. When the cilia are deviated in the opposite direction, the hair cell hyperpolarizes and the frequency of action potentials decreases.

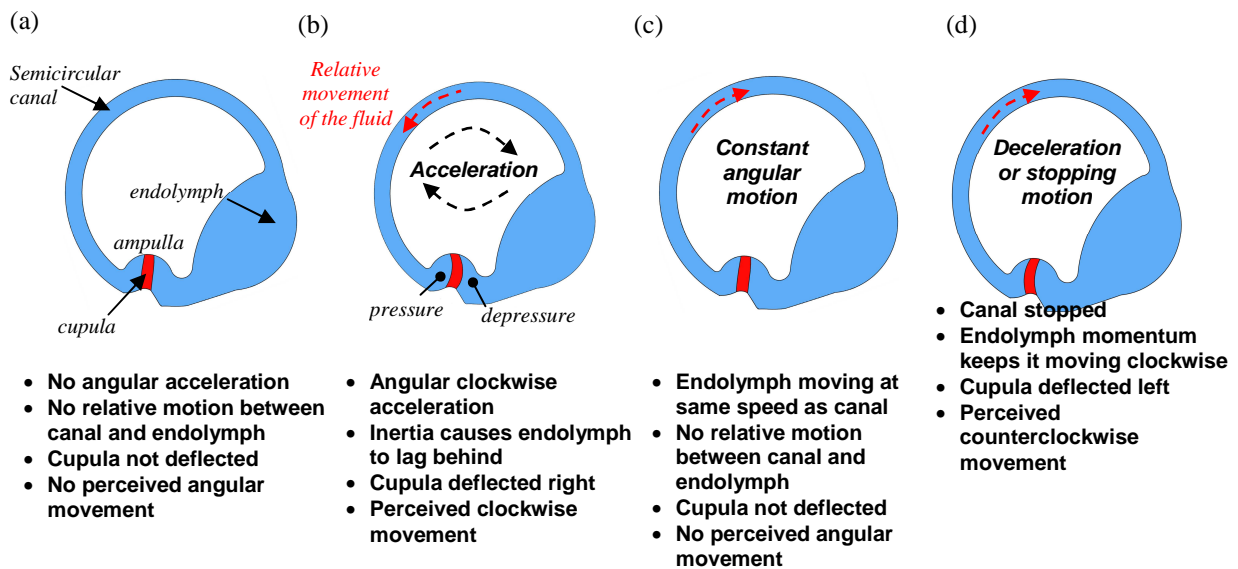


**Figure 1.4.** Detection of an angular acceleration of the SCC through inertia of the endolymph fluid relative to the canal motion. (a) At rest. (b) Clockwise head angular acceleration. (c) Constant angular motion. (d) Deceleration.



### 1.1.2. Otolith organs

The otolith organs, the saccule and utricle, are situated between the semicircular canals and the cochlea, and are approximately perpendicular to each other (Fig. 1.5a). They are the elements of the vestibular system that provide linear motion sensation in human and mammals. They are sensitive to the direction of the gravito-inertial force (GIF) applied to the head, and consequently respond to both linear acceleration and tilting of the head with respect to gravity. The saccule is dedicated to measuring primarily the vertical component of the GIF with respect to the head whereas the utricle measures primarily the horizontal component. As stated by Einstein's equivalent principle, all linear accelerometers must measure both linear acceleration and gravity (Einstein 1908). Therefore, the otolith organs cannot discriminate between acceleration and tilt, requiring additional sensory information to resolve this ambiguity.

Both the saccule and utricle are flat layered structures (Fig. 1.5b). The top layer, which is in contact with the endolymph, consists of calcium carbonate crystals called otoconia, the middle layer consists of a gelatinous matrix called the otolithic membrane, and the bottom layer consists of a bed of hair cells known as the macula that is rigidly attached to the skull and therefore moves with the head. The hair cells are anchored in the macula whereas their cilia extremities are embedded in the otolithic membrane.

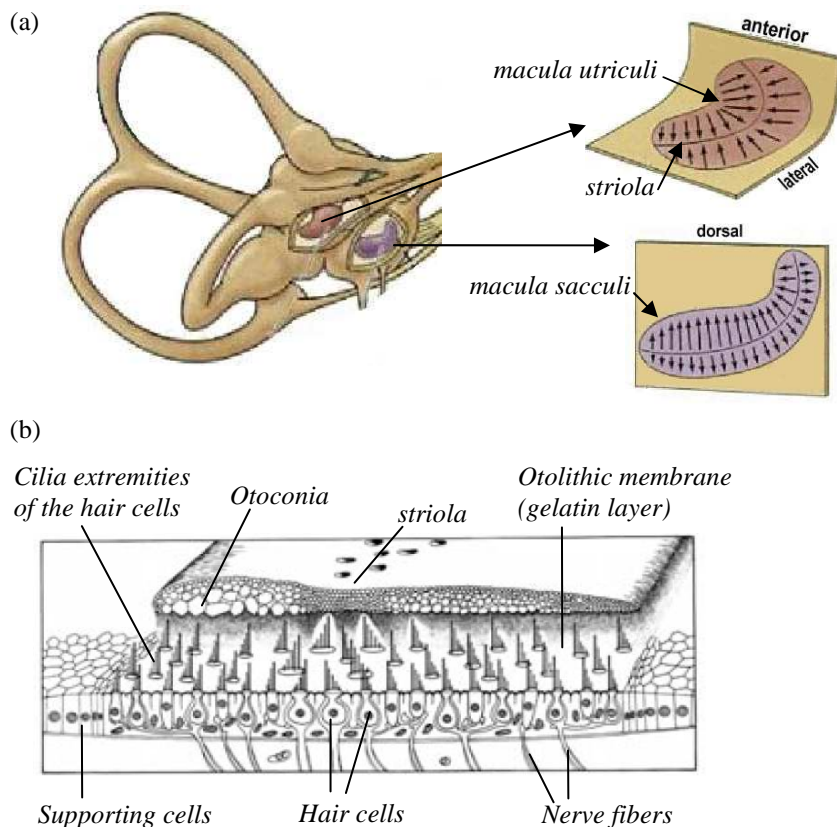


**Figure 1.5.** Physiology of the utricular macula. (a) Location of the utricle and saccule and orientation of the hair cells on the maculae of the otolith organs. The streamline represents the striola, and the arrows, the local direction of enhanced sensitivity of the hair cells. (b) 3D perspectives of a macula. Hair cells are embedded in the macula and measure the deformation of the otolith membrane caused by the motion of otoconia with respect to the head.



The orientation of the hair cell bundles is organized relative to a region called the striola, which demarcates the overlying layer of otoconia (Fig. 1.5). The striola forms an axis of symmetry such that hair cells on opposite sides of the striola have opposing morphological polarization. Thus, a tilt along the axis of the striola will excite the hair cells on one side while inhibiting the cells on the other side. Figure 1.5a illustrates the general morphological distribution of hair cell polarizations for the saccule and utricle where the arrows indicate the direction of movement that produces excitation.

The otoconia, which have a density of  $2.71\text{g/cm}^3$ , make the otolithic membrane considerably heavier than the structures and fluid surrounding it (Rabbitt et al., 2004). Thus, when the head experiences a linear acceleration, the membrane lags behind the sensory epithelium (Fig. 1.6). The resulting shearing motion between the otolithic membrane and the macula displaces the hair bundles, which are embedded in the lower gelatinous surface of the membrane. This displacement of the cilia generates a receptor potential in the hair cells. The same phenomenon also occurs when the head tilts, gravity causing the membrane to shift relative to the sensory epithelium.

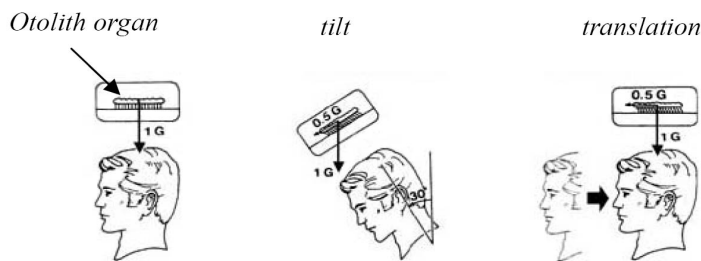


**Figure 1.6.** Mechanism of the otolith organs, showing their sensitivity to linear acceleration and head tilt. These drawings illustrate the shearing force in the plane of the utricular otolith membranes. For instance, a 30 degrees head-tilt elicits a force equivalent to 0.5G in the plane of the utricular macula. The same stimulus can be achieved using a linear acceleration of 0.5G with the head upright.

## 1.2. Mathematical modeling

### 1.2.1. Semicircular canals

The first model regarding the canals was proposed by W. Steinhausen (1931, 1933). He proposed a linear second order model of canal dynamics to explain the observed characteristics of vestibular-induced eye movements in fish (pike). This model was further refined by the “torsion pendulum” model of Van Egmond et al. (1949). They considered a canal as a thin torus having a constant large radius  $R$ , and a constant circular cross-section of radius  $r$ , and proposed that the angular displacement of the endolymph  $\xi(t)$  about the center of the canal was related to the angular acceleration of the head  $\alpha(t)$  by the differential equation of a heavily damped torsion pendulum:

$$\xi''(t) + \frac{\Pi}{\Theta} \xi'(t) + \frac{\Delta}{\Theta} \xi(t) = -\alpha(t) \quad (1.1)$$

where  $\xi(t)$ ,  $\dot{\xi}(t)$ , and  $\ddot{\xi}(t)$  denote respectively the angle, the angular velocity and acceleration of the fluid;  $\Theta$  is the endolymph moment of inertia;  $\Pi$  a viscous damping frictional drag of the endolymph, and  $\Delta$  a spring coefficient associated with cupula motion (Fig. 1.7).

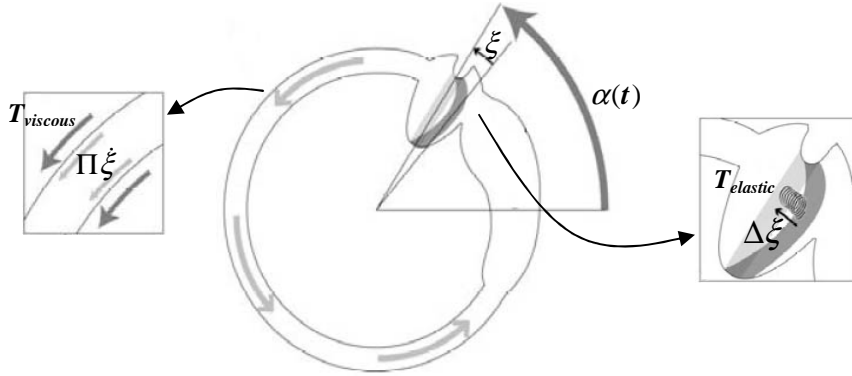


**Figure 1.7.** Mechanical model of a semicircular canal.

For a step of change  $\omega$  of angular velocity of the head, the exact solution for  $\xi(t)$  is given by:

$$\xi(t) = \frac{\omega \tau_1 \tau_2}{\tau_1 - \tau_2} \left( e^{-\frac{t}{\tau_1}} - e^{-\frac{t}{\tau_2}} \right) \quad (1.2)$$

where the two time constants are:  $\frac{1}{\tau_1}, \frac{1}{\tau_2} = \frac{-\Pi \pm \sqrt{(\Pi^2 - 4\Delta\Theta)}}{2\Theta}$ .

In all species studied to date, the semicircular canals are highly overdamped ( $4\Delta\Theta \ll \Pi^2$ ), which results in real-valued time constants (Groen, 1952; Rabbitt et al., 2004). In that case, a good approximation of the time constants is:

- $\tau_1 \approx \frac{\Pi}{\Delta}$ : long time constant (1.3)

- $\tau_2 \approx \frac{\Theta}{\Pi}$ : short time constant (1.4)

and equation (1.2) can be rewritten as:

$$\xi(t) \approx \frac{\omega \Theta}{\Pi} \left( e^{-\frac{\Delta t}{\Pi}} - e^{-\frac{\Pi t}{\Theta}} \right) \quad (1.5)$$

At the very beginning of the rotation of the head, the endolymph moves very quickly according to the short time constant. Afterwards the fluid will retreat slowly, according to the long time constant, controlled by the weak spring of the cupula and resisted by the high degree of friction

Parameters for man are, however, difficult to measure because direct afferent response of the semicircular canals cannot be obtained. Therefore, most early experiments to determine the torsion-pendulum model parameters were based on subjective response. For instance, Van Egmond (1949) determined both time constants according to the verbal response of humans

subjected to various motion inputs in a rotating chair. He reported that the long time constant  $\tau_1$  and short time constant  $\tau_2$  were close to 10 seconds and 0.1 seconds respectively. As discussed latter, values determined from subjective response do not truly represent the dynamics of cupula motion but rather constitute overall dynamics parameters representing the rotational sensation response to an angular velocity input. However, the basic operating principle of the canal is not impaired and is presented as follows.

The system endolymph-cupula being highly overdamped, a convenient and sufficiently accurate simplification of equation (1.1) in terms of Laplace transforms is:

$$\frac{\xi(s)}{\omega(s)} \approx \frac{\tau_1 \tau_2}{(\tau_1 s + 1)(\tau_2 s + 1)} \quad (1.6)$$

where  $\omega$  is the angular velocity of the head. The reason for expressing the transfer function between head angular velocity and cupula displacement is not obvious until one examines its frequency response. As noted by Mayne (1950, 1974), endolymph and cupula displacement are a measure of velocity rather than acceleration within a given frequency range of head angular velocity. This can be clearly seen on a Bode diagram (Fig. 1.8). Most head movements during normal body activity are in the range of frequencies where the canal response is flat, giving a nearly constant ratio between input and output and nearly zero phase shift. Clearly this implies that the canal's normal role is that of an angular velocity transducer. To explain this graph, Jones (1965) argued that the cutoff at high frequencies ( $\omega > 1/\tau_2$ ) is due to inertial force increasing with respect to viscous damping force, while the cupula spring force becomes negligible, and that the cutoff at low frequencies ( $\omega < 1/\tau_1$ ) is due to cupula spring force increasing with respect to viscous damping force, while inertial force becomes in turn negligible.

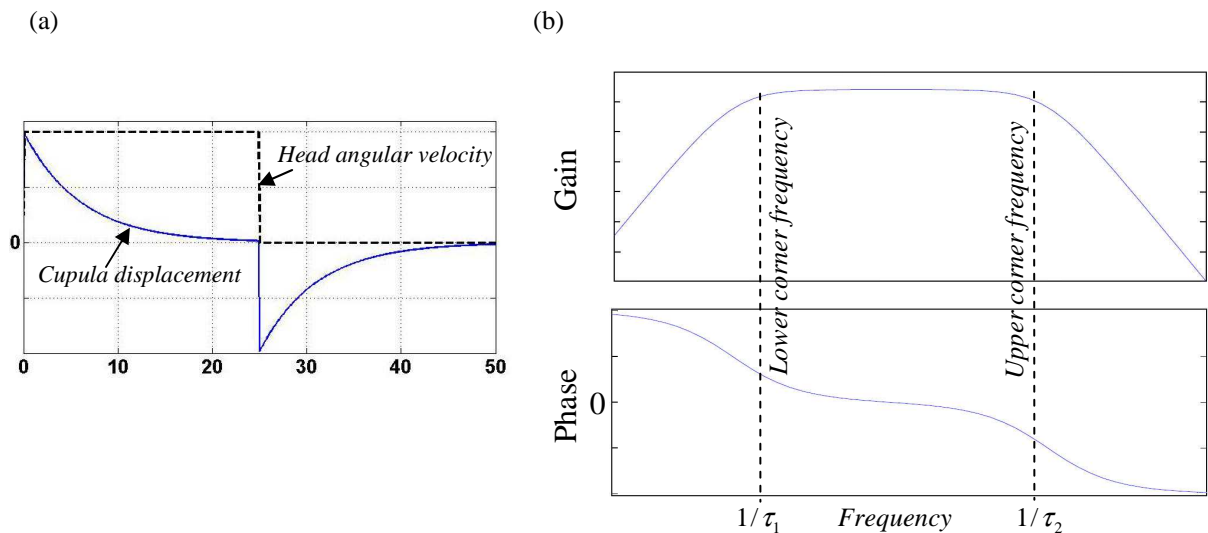


**Figure 1.8.** Curve of typical cupula displacement and Bode diagram of the transfer function between head angular velocity and cupula displacement. (a) Cupula deflection due to a step of angular velocity. (b) Theoretical frequency response of the semicircular canals based on the model of Van Egmond.

The torsion pendulum model has been the starting point for subsequent theoretical analyses of canal dynamics (Groen et al., 1952; Goren, 1956; Van Egmond et al., 1949; Njeugna et al.,

1986, Oman et al., 1987). Most of these studies were based on hydrodynamic considerations. Steer (Steer, 1967) solved the Navier-Stokes equations for flow in a toroidal duct, whereas Van Buskirk (1976, 1977, 1988) presented a more rigorous approach by considering the utricle as a semicircular segment, with a constant cross-section much larger than that of the duct. Oman et al. (1987) derived a more general two-segment model, and considered the effect of duct cross-section ellipticity on Poiseuille flow drag. He then extends his model to the case where the size, shape, and curvature of the canal lumen change continuously through the duct, utricle, and ampulla. He came up with a second-order differential equation that has three coefficients, unlike the equation of a torsion-pendulum, which has only two. He derived the following transfer function relating cupula volume displacement to head angular velocity:

$$\frac{V(s)}{\alpha(s)} = \frac{-2\rho\Lambda/K}{\frac{\rho L}{K}\left(\frac{1}{A}\right)s^2 + \frac{8\pi\mu L}{K}\left(\frac{S}{A^2}\right)s + 1} \approx \frac{G}{(\tau_1 s + 1)(\tau_2 s + 1)} \quad (1.7)$$

where  $\rho$  and  $\mu$  are the density and viscosity of endolymph, respectively,  $L$  is the total length of the central streamline,  $K$  is a stiffness coefficient representing the cupula as a linear spring-like element,  $\Lambda$  is the surface defined by the central streamline of the canal and projected into the plane of rotation,  $A$  is the cross-sectional area of the canal lumen,  $S$  is a wall shape factor, and  $G$  is the sensitivity of endolymph volume displacement to angular acceleration.

Based on anatomical data (Curthoys et al., 1987), Oman et al. (1987) estimated the short time constant of the system to be close to 4 ms. This value is two order of magnitude lower than previous values derived by a number of researchers (e.g. Van Egmond et al., 1949). That is, previous values were derived from subjective estimates of sensation of rotation and vestibular induced nystagmus. Therefore, these sensations are not representative of the response of the canal alone and are certainly influenced by the complicated physiology of the central vestibular pathways. As regards the determination of the long time constant, its calculation is not immediate as it requires the knowledge of the coefficient  $K$ . As it will be discussed in Chapter II, many researchers have attempted to estimate this parameter according to different experimental procedures, and thus several values have been suggested. Hence, estimated value for  $\tau_1$  is in turn different depending on the assumed value for  $K$ . Another way to approximate the long time constant is to record the response of peripheral afferent neurons. Indeed, it has been shown that the discharge of the afferent nerve fibers innervating the canals is proportional to cupular displacement. Fernandez et al. (1971) did record the discharge characteristics of peripheral vestibular afferents in the squirrel monkey under various angular acceleration inputs of different amplitudes and frequencies. They derived a transfer function relating the afferent firing rate of the vestibular nerve to the angular acceleration input of the form:

$$\frac{AFR(s)}{\alpha(s)} = \left[ \frac{\tau_a s}{1 + \tau_a s} \right] \left[ \frac{1 + \tau_1 s}{(1 + \tau_1 s)(1 + \tau_2 s)} \right] \quad (1.8)$$

The term  $\tau_a s / (\tau_a s + 1)$  results in a phase lead at low frequencies and is the frequency-domain representation of the Young-Oman adaptation operator (1969). The term  $(1 + \tau_1 s)$  is a lead component and reproduces the high frequency deviations from the torsion-pendulum model and implies that the system is sensitive both to cupular displacement and to the velocity of the

displacement. The values of the four time-constants were determined as:  $\tau_a = 80\text{ s}$ ,  $\tau_l = 0.049\text{ s}$ ,  $\tau_1 = 5.7\text{ s}$ , and  $\tau_2 = 0.003\text{ s}$ .

However, as noted by Merfeld et al. (1993), the transfer function derived by Fernandez et al. exhibits incorrect behaviors at high frequencies. First, the model predicts that the system response will increase as the frequency is increased from 3.25 Hz to 50Hz. Second, the model predicts that the system response will be constant for all frequencies greater than approximately 50 Hz. Neither of these predictions is likely. Consequently, Merfeld proposed a modified transfer function to represent the semicircular canals of the form:

$$\frac{AFR(s)}{\omega(s)} = \frac{\tau_1 \tau_a s^2}{(1 + \tau_1 s)(1 + \tau_a s)} \quad (1.9)$$

where  $\tau_1 = 5.7\text{ s}$  and  $\tau_a = 80\text{ s}$ .

Note that Merfeld considered the model inputs to be limited to low frequency disturbances, and that this simple model may thus not be used to make predictions beyond 1 Hz.

Finally, by assuming that the long time constant of the human semicircular canal cupula is close to that of the squirrel monkey, the computation of both the pressure-volume coefficient  $K$  and the sensitivity gain  $G$  of Oman's model can be performed. Indeed, the stiffness coefficient  $K$  and the gain  $G$  are related to the long time constant according to:

$$K \approx \frac{8\pi\mu L}{\tau_L} \left( \frac{S}{A^2} \right) \approx 6.8\text{ GPa}/\text{m}^3 \quad (1.10)$$

and

$$G = \tau_L A_c \frac{\bar{X}_c}{\gamma} \approx 1,85 \cdot 10^{-11} \text{ m}^3 \text{ s}^2 \quad (1.11)$$

where  $A_c$  is the cross-sectional area of the lumen occupied by the cupula and is equal to  $1.04\text{ mm}^2$  (Curthoys et al. 1987), and the ratio  $\bar{X}_c / \gamma$  defines the average displacement of the face of the cupula per unit head angular velocity and is equal to  $0.026\text{ }\mu\text{m}/\text{deg}/\text{s}$  (Oman et al. 1987).

## 1.2.2. Otolith organs

As with the semicircular canals, the first models regarding the dynamics of the otolith organs were based on subjective experiments. Meiry (1966) was probably the first to investigate subjective response to linear motion by using a cart to produce longitudinal sinusoidal motion. According to subjective indication of direction, he obtained a transfer function relating perceived velocity to stimulus velocity. Young and Meiry (1968) then noted that the proposed model correctly predicted the phase of perceived velocity for lateral oscillations, but failed to predict the otoliths response to sustained tilt angle as indicated by behavioral and physiological data. Therefore, they proposed a modified model, which related the perceived GIF to specific force stimulus, using a shorter long time constant and an additional lead term.

Despite this revised model was able to predict both perceived tilt and acceleration in response to acceleration input, it did not actually reflect the dynamics of the sensor alone, but rather the dynamics behavior representing the gravito-inertial sensation response to a GIF input.

A decade later, Zacharias (1977) noted that a lumped parameter model of otolith motion could be used to represent otolith dynamics, similar to the torsion-pendulum model for the semicircular canals. Ormsby (1974) first developed this model, and Grant et al. (1986, 1987, 1990, 1994) later proposed further refined versions. They first considered the gelatinous layer supporting the otoconial as an elastic solid (Fig. 1.9). By examining the maximum displacement of the otoconial layer in response to a step change in linear velocity, they approximated the short time constant of the system to be close to 0.002 s. However, they later demonstrated that this value turned out to be too large when reasonable values of the maximum otolith displacement are considered, and concluded that more damping was needed in the lumped parameter model. Therefore, Grant and Cotton (1990) proposed to introduce additional damping by considering in their mechanics model a viscoelastic gelatinous layer. They suggested a one dimensional analysis and treated the otoliths as a second-order spring-mass damper, where the otoconial layer was modeled as a rigid solid mass, the gel layer as an isotropic viscoelastic material, and the endolymph as a Newtonian fluid with uniform viscosity.

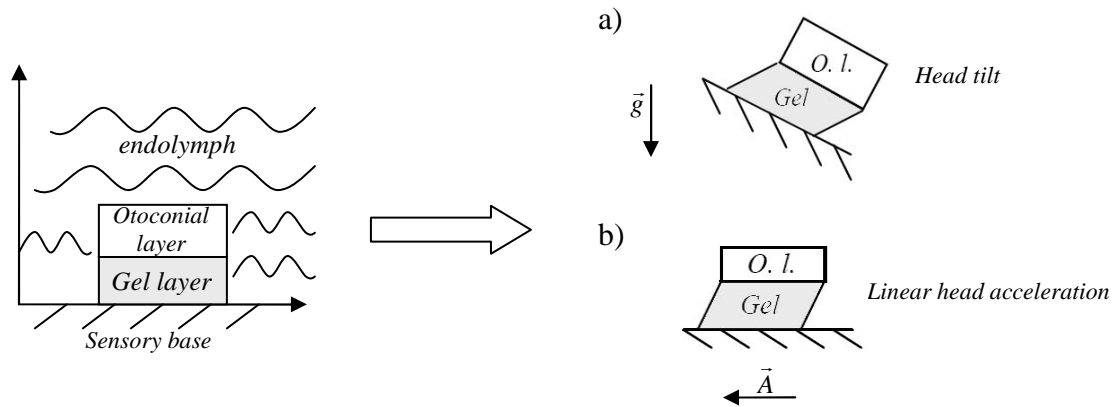


**Figure 1.9.** Schematic diagram of the functioning of the *Otolith organs*. (a) Schematic diagram of the otolith organ. (b) and (c) show two configurations illustrating the system under a purely tilt stimulus (b), and a purely inertial stimulus (c).

By applying Newton's second law of motion within the plane of the otoconial layer, they obtained the following transfer function:

$$\frac{x(s)}{f(s)} = \left(1 - \frac{\rho_e}{\rho_0}\right) \frac{\tau_{1oto} \tau_{2oto}}{(1 + \tau_{1oto}s)(1 + \tau_{2oto}s)} \quad (1.12)$$

where  $x$  is the relative displacement of the otoconial layer with respect to the head,  $\rho_e$  is the density of the endolymph, and  $\rho_0$  is the density of the otoconial membrane, with  $\rho_0 > \rho_e$ . As noted by Rabbitt et al. (2004), the fact that  $\rho_0 > \rho_e$  leads to the inertial force responsible for movement of the otolith mass relative to its substrate. Finally,  $\tau_{1oto}$  and  $\tau_{2oto}$  are the long and short time constant, respectively, that characterize the macromechanical temporal response dynamics of the otoconial layer. These time constants are analogous to those found in the semicircular canals but are shifted relative to the physiological time scales of motion present

in linear versus angular head movements. That is, the semicircular canals experience a wide range of angular motion stimuli at frequencies between the two characteristic times, whereas the otolith organs experience additional low-frequency stimuli arising primarily from slow head tilts relative to gravity. As with the semicircular canals, the otolith organs have been found to be highly overdamped (De Vries, 1950), and, in humans, the time constants are given by  $5 \mu s < \tau_{oto} < 40 \mu s$  and  $0.1 \mu s < \tau_{oto} < 4 \mu s$  (Grant and Cotton, 90; Grant .et al., 1994).

As regard the characterization of the physiology of the mammalian peripheral otolith system, the works of Fernandez and Goldberg (1976) probably constitutes to date the most comprehensive and thorough investigation. Indeed, before their studies, little was known about the spatial and temporal properties of these neurons, as all previous investigations had almost entirely dealt with primary otolith afferent responses to static tilts rather than dynamic linear accelerations. As they did few years after for the semicircular canals, they recorded the discharge of peripheral otolith neurons in response to various stimulations in the squirrel monkey. In particular, they described the response properties of primary otolith afferents to sinusoidal linear acceleration stimuli and provided the first quantification of the neurons response dynamics using system analyses techniques. They characterized the frequency responses of regular and irregular units with a transfer function of the form:

$$H(s) = \frac{1 + k_a \tau_a s}{1 + \tau_a s} \frac{1 + k_v (\tau_v s)^{k_v}}{1 + \tau_M s} = H_a(s) \frac{H_v(s)}{H_M(s)} \quad (1.13)$$

The term  $H_a$  is an adaption operator that contributes to low frequencies phase leads seen at and increases of gain from static to 0.006 Hz. The term  $H_v$  is a velocity-sensitive operator with a fractional exponent ( $k_v < 1$ ). The last term  $H_M$  is a first order lag operator that Fernandez and Goldberg noted might reflect the mechanics of otolith motion. Despite this transfer function provide an adequate representation of the dynamics behavior of most units, Hosman (1996) noted that this model is not easy to implement due to the fractional exponent in the lead term. He proposed a simplified model of the same form developed by Grant and Best (1987) which was then refined by Telban and Cardullo (2005). They came up with a transfer function relating the afferent otolith dynamics and the gravito-inertial force input of the form:

$$\frac{AFR(s)}{f(s)} = 33.3 \frac{(10s+1)}{(5s+1)(0.016s+1)} \quad (1.14)$$

By comparing the step response of the proposed afferent dynamics model (eq. 1.14) with the Fernandez-Goldberg model (eq. 1.13), they showed that both models were in good agreement.

### 1.3. History of spatial orientation

Spatial orientation refers to the natural ability to determine and maintain body position in relation to the surrounding environment, especially during motion. In order to achieve this goal, the brain has to integrate various sensory signals such as visual, vestibular, and proprioceptive inputs. A lot of studies have been focused on modeling the process of spatial orientation so as to understand how sensory signals are processed by the central nervous system as well as to model the phenomenon of spatial disorientation, which is attributed to 15-30% of all aircraft fatalities in flight (Braithwaite et al., 1998; Knapp et al., 1996).

Mathematical models for three dimensional human spatial orientation have continued to evolve over the past four decades. The earliest mathematical models for human orientation perception (e.g. Mayne, 1950) addressed rotation about an Earth vertical axis. Attenuation of sensations during prolonged rotation was attributed to semicircular canal (SCC) dynamics. However, in the 1970s, perspectives began to broaden: Validated models for primate semicircular canal (Goldberg et al., 1971) and otolith (Fernandez et al., 1976) afferent response dynamics became available. As a result, it became clear that the time course of perception was not entirely determined by end-organ dynamics. For example, animal vestibulo-ocular reflex (VOR) data indicated that central mechanisms somehow perpetuate SCC responses, broadening the dynamic range of motion perception, and lengthening the dominant VOR time constant - a phenomenon now generally referred to as "velocity storage". Alternative - but dynamically equivalent - mathematical models were proposed by Robinson (1977) and Raphan et al (1977, 1979). Similarly, it was recognized that relatively slow dynamics associated with somatogravic illusions - such as the sensation of pitching up during linear acceleration in the dark - were primarily not due to otolith end organ dynamics. Mayne (1974) noted that gravireceptors ambiguously respond to both gravity and linear acceleration, and proposed that somatogravic illusion dynamics resulted from central mechanisms which utilize both angular and linear acceleration cues to estimate the direction of "down". Mayne noted that keeping track of the direction of "down" is an essential step in inertial navigation, normally achieved by integrating angular velocity cues, and anchored by averaging the direction of net gravireceptor output over long periods of time. Mayne proposed a 3D orientation model where the central nervous system (CNS) estimated "down" and linear acceleration respectively via complementary low and high pass filtering of gravireceptor cues.

Meanwhile, aerospace guidance engineers developed formal mathematical methods for estimating the orientation and position of a vehicle for autonomous or assisted navigation based on information from a relatively small set of navigation sensor measurements. The vehicle trajectory is estimated in real time using an "internal model" for the vehicle dynamics. The trajectory estimate is continuously corrected by using internal models for the navigation sensors to predict what the current set of sensor measurements should be, provided the vehicle internal model prediction were correct. The difference between predicted and actual sensor measurements (termed the "residual") - appropriately weighted - is then used to correct the trajectory estimate. The general version of this scheme is referred to as a Luenberger Observer (Luenberger, 1963). For the case frequently encountered in engineering, where the entire system can be represented using linear models, and where "noise" disturbances to both the vehicle and sensor measurements can be well characterized, Kalman (1960) demonstrated how to calculate optimal residual weighting coefficients that minimize the stochastic error in the trajectory estimate. Where the residual weighting coefficients are computed in advance, such a system state estimator is referred to as a steady state Kalman Filter (KF). Oman (1982,



1991) noted that the “residual” signal in a KF corresponded to the putative sensory conflict signals thought to be the central neural stimulus triggering sensory motor adaptation and motion sickness.

Recognizing the potential utility of steady state KF techniques, Young and colleagues (Borah et al, 1979; Borah et al. 1988) applied them to model orientation perception by a human riding passively in a vehicle (Fig. 1.10). The estimator incorporated dynamic models for the semicircular canals and otoliths, as well as simple models of available visual angular and linear velocity cues. Simple 1-D and 3-D examples of Borah’s KF approach are presented in chapter 4. The transformation from world to head coordinates was mathematically linearized, so model predictions were restricted to small head deviations from the upright.

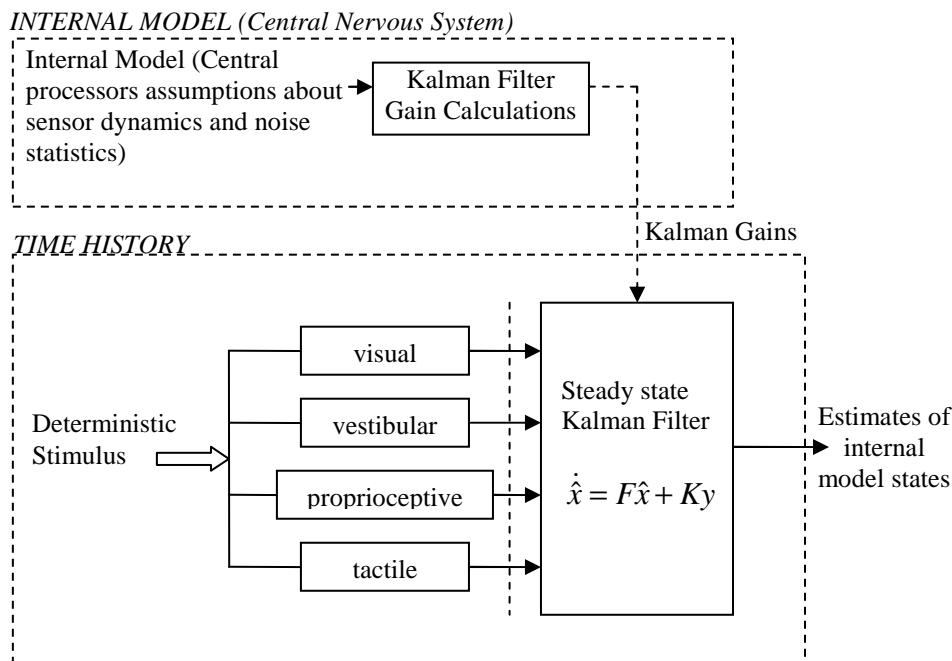


**Figure 1.10.** Borah et al. multisensory model using steady state Kalman filter to represent neural central processing.  $\hat{x}$  is the vector representing estimates of internal model states, e.g. estimates of angular velocity perception, orientation perception, etc.  $F$  is a function of  $K$  (Kalman gains) and internal model dynamics.

As noted by MacNeilage et al (2008), Borah et al regarded vehicle motion disturbance and sensor noise magnitude and bandwidth as free parameters in their model. They empirically determined values of these such that their KF model successfully mimicked angular velocity storage during rotation about the Earth-vertical, and somatogravic illusory tilts during linear acceleration in darkness. When visual stimuli were present, the model accounted for the “circularvection” and illusory tilt illusions resulting from scene rotation about vertical and horizontal axes, respectively.

Many aircraft accident, neuro-otological and laboratory spatial orientation research paradigms involve three dimensional, six-degree-of-freedom movements. Typically this results in head tilts (real or perceived) so large that the world-to-head coordinate transformation is nonlinear, and so a steady state KF model is not appropriate. Therefore, Pommellet (1990) generalized Borah’s model by using a nonlinear version of the KF known as the Extended Kalman Filter (EKF). In his model, the world-to-head coordinate transformation was represented using Quaternion mathematics. While Borah’s model responses qualitatively matched perceptions

for simple stimuli with the head near the erect position, the Pommelet EKF results exhibited numerical instabilities in quaternion estimation, particularly for the more complex profiles involving larger estimated tilts. A follow up EKF, which only considered the vestibular portions of Pommelet’s model, was developed by Bilién (1993). The resulting EKF was applied to a simple centrifuge paradigm in darkness, but, unfortunately, encountered similar difficulties, particularly when modeling Coriolis responses.

Meanwhile, Merfeld et al. (1993) proposed a nonlinear Observer model in which the relationship between head and world coordinate frame was also represented by quaternion mathematics (Fig. 11). In Merfeld’s model, this transformation was incorporated into the Observer’s internal model that estimated the direction of “down”. The residual corrections were applied in an ad-hoc fashion, and vehicle motion disturbance and sensor noise was not represented. However they showed that by appropriate choice of a single SCC residual weighting parameter, a one dimensional model could be tuned so its responses were identical to those of the Robinson/Raphan et al models for angular velocity storage. Adding three more Otolith measurement residual weighting factors as free parameters, the three dimensional version of the model predicted somatogravic illusions during lateral acceleration, centrifugation, and off-vertical-axis rotation. It also accounted for effects of head tilt on post-rotational sensations. Merfeld’s one and three-dimensional model are reviewed in chapter 4.

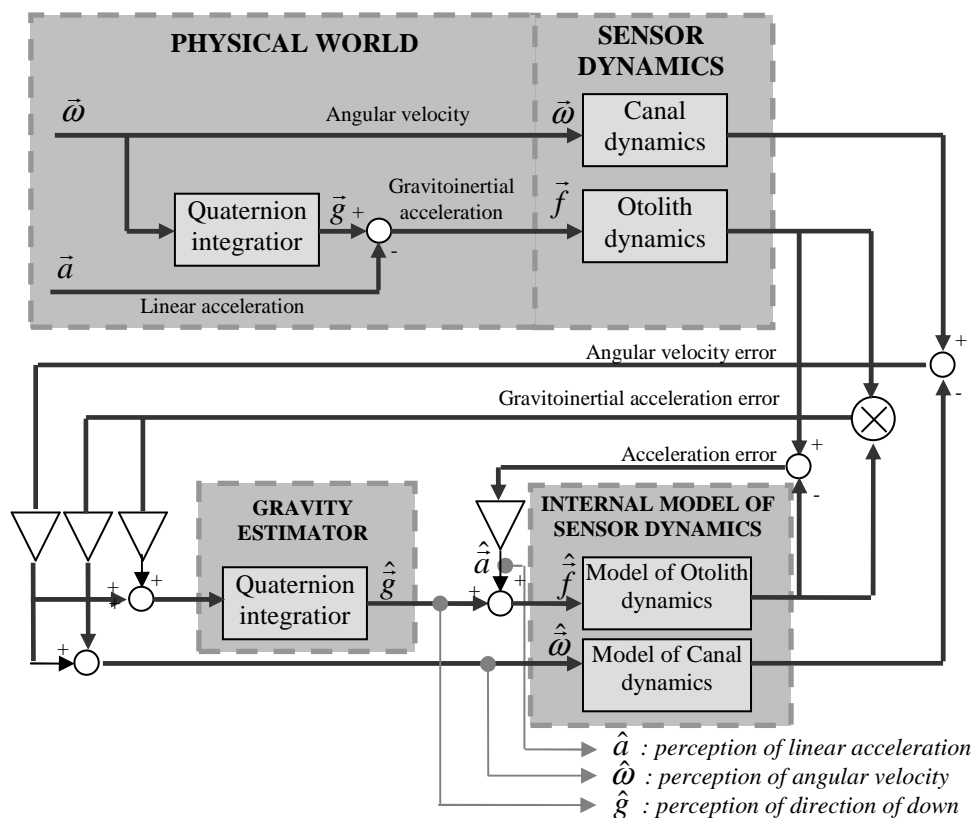


**Figure 1.11.** Outline of the three-dimensional model of Merfeld. The physical inputs, angular velocity and gravito-inertial acceleration are processed by the sensor dynamics, then compared to internal estimates either by subtraction or by means of a vector product. After scaling by gain factors (triangles), the error vectors are fed into the estimation process which contains internal models of sensor dynamics and physics.

Merfeld’s Observer model was further validated and extended by Haslwanter et al (2000), Merfeld and Zupan (2002), Vingerhoets et al (2006, 2007) and Newman (2009). Note that these models assumed that internal model estimates corresponded to perceptions. Table 1.1 summarizes these efforts and compares them against the alternate class of Kalman filter and extended Kalman filter models. Note also that, until Newman contributions, Observer models predicted orientation and linear acceleration, but did not predict position in space. In addition, previous Observer models were limited to SCC and otolith cue interaction. Newman contribution was in adding a “limbic” coordinate frame in which velocity and position path integration was assumed to take place, and in incorporating visual pathways. Results of this extended Observer model are in good agreement with the Borah KF model results for the simple visual-vestibular motion paradigms of linearvection, circularvection, rotation in the light and acceleration in the light.

	Stimuli used for validation						
	Earth Vertical Rotation	OVAR	Post- Rotational Tilt	Fixed Cab Centrifugation	Linear Acceleration	Roll Tilt	Pseudo Coriolis
<i>Observer Models</i>							
Merfeld 1993	×	×	×	-	-	-	-
Haslwanter 2000	-	×	-	-	-	-	-
Merfeld 2002	-	-	-	×	-	×	-
Vingerhoets 2006	-	×	-	-	-	-	-
Vingerhoets 2007	-	×	-	-	-	×	-
Newman 2009	×	×	-	×	×	-	×
<i>KF/EKF Models</i>							
Borah 1979	×	-	-	-	×	-	-
Pommellet 1990	×	-	-	×	×	-	-
Billien 1993	-	-	-	×	-	-	-

**Table 1.1.** Validation cases for Observer and KF / EKF models

## 1.4. State estimation of dynamic state-space models

### 1.4.1. Introduction

In daily life our sensors, such as vestibular and visual sensors, provide information of orientation, velocity, and acceleration to the brain. In addition, it is assumed that the central nervous system has an internal representation of the physical world which is defined in state space notation by a state vector  $x(t)$  and a system matrix  $A$ . The main idea of human spatial orientation estimation model is to estimate a state vector that contains variables of orientation, velocity and acceleration given a set of measurements provided by our sensors. It is assumed that some of the estimated states correspond to our perception of orientation, angular velocity, and linear acceleration. The principle of human spatial orientation model is presented in figure 1.12.

Different techniques such as Observer, linear Kalman filter, nonlinear Kalman filters, etc can be used to achieve this goal. In the following sections, we provide a background on state estimation techniques of dynamic state-space models. More particularly, we present in detail the linear Kalman filter algorithm as well as the extended and unscented Kalman filter techniques that will be used in chapter 4 to develop models for human spatial orientation.

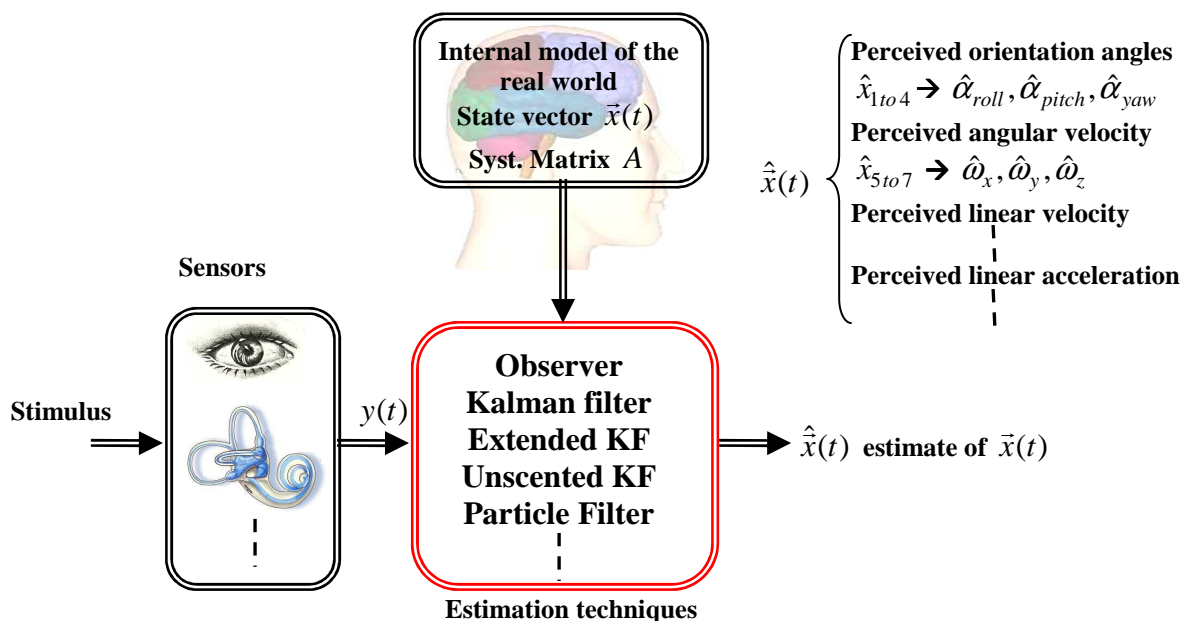


**Figure 1.12.** Principle of human spatial orientation estimation model. Sensors provide some measurements  $y(t)$ . The central nervous system is assumed to have an internal representation of the real world. Based on this model and on sensor measurements, estimation techniques can be used to provide an estimate state vector  $\hat{x}(t)$ . It is assumed that the estimated state variables correspond to perception of orientation, angular and linear velocity, and linear acceleration.

### 1.4.1.1. Probabilistic inference

Probabilistic inference is the problem of estimating the hidden variables (states) of a system in an optimal and consistent fashion as a set of noisy or incomplete observations of the system becomes available online. The optimal solution to this problem is given by the recursive Bayesian estimation algorithm which recursively updates the posterior density of the system state as new observations arrive. This posterior density constitutes the complete solution to the probabilistic inference problem, and allows us to calculate any “optimal” estimate of the state. Unfortunately, for most real-world problems, the optimal Bayesian recursion is intractable and approximate solutions must be used. Numerous approximate solutions to the recursive Bayesian estimation problem have been proposed over the last couple of decades in a variety of fields. These methods can be loosely grouped into the following three main categories:

- Gaussian approximate methods: these methods all model the pertinent densities in the Bayesian recursion by Gaussian distributions, under the assumption that a consistent minimum variance estimator (of the posterior state density) can be realized through the recursive propagation and updating of only the first and second order moments of the true densities.
  - Kalman filters: the celebrated Kalman filter is the optimal closed-form solution for linear, Gaussian dynamic state space models
  - Extended Kalman filter: the EKF applies the Kalman filter framework to nonlinear Gaussian systems, by first linearizing the dynamic state space model using a first order truncated Taylor series expansion around the current estimates.
- Direct numerical integration methods: these methods, also known as grid-based filters, approximate the optimal Bayesian recursion integrals with large but finite sums over a uniform N-dimensional grid that tiles the complete state space in the area of interest. For even moderately high dimensional state spaces the computational complexity quickly becomes prohibitively large, which all but preclude any practical use of these filters.
- Sequential Monte-Carlo methods: SMC methods make no explicit assumption about the form of the posterior density. They can be used for inference and learning in any general, nonlinear non-Gaussian dynamic state space models. These methods, like the grid-based filters, approximate the Bayesian integrals, with finite sum. Unlike grid-based filters however, the summation is done with sequential importance sampling on an adaptive “stochastic grid”. This grid, as defined by a set of weighted samples drawn from a proposal distribution that approximates the true posterior, is concentrated in high likelihood area of the state space.

### 1.4.1.2. Gaussian approximate methods

Due in part to their relative ease of implementation and modest computational cost, the group of Gaussian approximate solutions has received most attention for over the past 40 years. Under the assumption that the underlying dynamic state space model is linear and all the

probability densities are Gaussian, the celebrated Kalman filter is the optimal and exact solution to the recursive Bayesian estimation problem. If these assumptions hold, the achieved solution is optimal in the minimum mean-square-error (MMSE) sense. However, Kalman's original derivation of the Kalman filter did not require the underlying system equations to be linear or the probability densities to be Gaussian. The only assumption made are that consistent estimates of the system random variables can be maintained by propagating only their first and second order moments (means and covariances), that the estimator itself is a linear function of the prior knowledge of the system (summarized by  $p(x_k | y_{1:k-1})$ ) and the new observed information (summarized by  $p(y_k | x_k)$ ), and that predictions of the state and of the system observations can be calculated (these predictions are needed to approximate the first and second order moments of  $p(x_k | y_{1:k-1})$  and  $p(y_k | x_k)$ ). The fact that only means and covariances are maintained is why this method are (somewhat misleading) called Gaussian approximate solution. In other words, the densities are not required to be Gaussian, we simply only maintain the Gaussian components (mean and covariance) of the densities in the estimator. Predictions of the state and of the observations are optimally calculated by taking the expected value of the following equations:

$$\begin{aligned}x_k &= f(x_{k-1}, u_k, w_k) \\y_k &= h(x_k, v_k)\end{aligned}\tag{1.15}$$

where  $x_k$  is the hidden system state with initial probability density  $p(x_0)$  that evolves over time according to the conditional probability density  $p(x_k | x_{k-1})$ ,  $y_k$  are the observations that are generated according to the conditional probability density  $p(y_k | x_k)$ ,  $w_k$  is the process noise that drives the dynamic system through the nonlinear state transition function  $f$ , and  $v_k$  is the observation or measurement noise corrupting the observation of the state through the nonlinear observation function  $h$ . Note that the state transition density  $p(x_k | x_{k-1})$  is fully specified by  $f$ , whereas  $h$  and the observation noise distribution  $p(v_k)$  fully specify the observation likelihood  $p(y_k | x_k)$ . The dynamic state space model, together with the known statistics of the noise random variables as well as the prior distributions of the states, defines a probabilistic generative model of how the system evolves over time and how we partially observe this hidden state evolution.

It turns out that predictions of eq. (1.15) can in general only be calculated exactly for linear Gaussian random variables. This does not disallow the application of the Kalman framework to nonlinear systems. It just requires further approximations to be made. One such approximation is the linearization of the dynamic state space model through the use of a first order truncated Taylor series expansion around the current estimate of the system state. This algorithm known as the Extended Kalman filter will be presented in depth in section 1.4.3.2.

### 1.4.2. Linear state space estimation

The simplest of the state space models are linear models, which can be expressed with equations of the following form:

$$\begin{aligned}x_k &= Fx_{k-1} + w_k \\y_k &= Hx_k + v_k\end{aligned}\tag{1.16}$$

where:

- $x_k \in \mathbb{R}^n$  is the state of the system on the time step  $k$ .
- $y_k \in \mathbb{R}^m$  is the measurement on the time step  $k$ .
- $w_k \sim N(0, Q_k)$  is the process noise on the time step  $k$ .
- $v_k \sim N(0, V_k)$  is the measurement noise on the time step  $k$ .
- $F$  is the transition matrix, or the system matrix, of the dynamic model.
- $H$  is the measurement model matrix.
- The prior distribution for the state is  $x_0 \sim N(m_0, P_0)$ .

The model can also be equivalently expressed in probabilistic terms with distributions:

$$\begin{aligned} p(x_k | x_{k-1}) &= N(x_k | Fx_{k-1}, Q_k) \\ p(y_k | x_k) &= N(y_k | Hx_k, V_k) \end{aligned} \tag{1.17}$$

### 1.4.2.1. Kalman filtering

- Introduction

In 1960, R.E Kalman published his famous paper describing a recursive solution to the discrete data linear filtering problem (Kalman, 1960). At first sight, his ideas were met with some scepticism among his peers such that his second paper, on the time-continuous case, was once rejected because – as one referee put it – one step in the proof “cannot possibly be true”! Kalman persisted in presenting his paper and found a receptive audience in the fall of 1960 during a talk at the Ames Research Center of NASA in California (Mohinder et al., 2001). Kalman presented his recent results which had been recognized to be potentially applicable to the trajectory estimation and control problem for the Apollo project, a planned manned mission to the moon and back. In the mid-1960s, the Kalman filter became part of the Northrup-built navigation system for the C5A air transport, and then, in the early part of 1961, was made a part of the Apollo onboard guidance. Since that time, it has been an integral part of nearly onboard trajectory estimation and control system designed.

Theoretically the Kalman filter is an estimator for what is called the linear-quadratic problem, which is the problem of estimating the instantaneous state of a linear dynamic system perturbed by white noise – by using measurements linearly related to the state but corrupted by white noise. The resulting estimator is statistically optimal. Practically, it is certainly one of the greatest discoveries in the history of statistical estimation theory and possibly the greatest discovery in the twentieth century, at least for those involved in estimation and control problems. Many of the achievements since its introduction would not have been possible without it. It was one of the enabling technologies for the Space Age, in particular. The precise and efficient navigation of spacecraft through the solar system could not have been done without it. Its most immediate applications have been for the control of complex dynamic systems such as continuous manufacturing processes, aircraft, ships, or spacecraft. The Kalman filter is also used for predicting the likely future course of dynamic systems that people are not likely to control, such as the trajectories of celestial bodies, or the prices of traded commodities.

- Continuous version

The Kalman Filter is a linear Observer specifically designed to optimally estimate the state  $x$  of a linear system described by a set of difference equations:

$$\dot{x}(t) = Ax(t) + Bu(t) + Gw(t) \quad (1.18)$$

based on a set of noisy measurements  $y_k$  derived from certain components of the state  $x(t)$

$$y(t) = Cx(t) + v(t) \quad (1.19)$$

Here, the  $n$  dimensional vector  $x$  represents the state at time  $t$  of all the system variables - for example in our case the linear and angular positions and velocities of the head, SCC cupula and otolith displacements, and any other variables whose initial conditions must be known in order to predict future behavior. The  $n \times n$  matrix  $A$  defines the undisturbed dynamic behaviour of the system, since it relates how state at time  $t - \Delta t$  influences the rate of change of the state at the current time  $t$ . Some components of the system, defined by the matrix  $G$ , are disturbed by  $\ell$  continuous external “process noise” inputs,  $w(t)$  whose continuous covariance matrix is  $Q\delta(t)$  (where  $\delta(t)$  is the Dirac delta function). The system also responds to a deterministic external disturbance vector  $u(t)$ . Hence the  $n \times l$  matrix  $B$  describes how the deterministic inputs at time  $t - \Delta t$  disturb the rate of change  $x(t)$ .

It is assumed that sensors provide measurements  $y(t)$  of a subset of the system state  $x(t)$ , by an  $m \times n$  matrix  $C$ , that determines which states are being measured, and sensor sensitivity. The measurements are also corrupted by sensor noises  $v(t)$ , whose continuous covariance matrix is  $V\delta(t)$ . In our following models, this might correspond to the intrinsic variability in SCC and otolith afferent signals. Both the process and measurement noise processes are assumed uncorrelated, and each is independent, white, zero mean, and normally distributed i.e. :

$$w(t) \sim N(0, Q) \quad (1.20)$$

$$v(t) \sim N(0, V) \quad (1.21)$$

$$E[w(t)w^T(\tau)] = Q\delta(t - \tau) \quad (1.22)$$

$$E[v(t)v^T(\tau)] = V\delta(t - \tau) \quad (1.23)$$

$$E[w(t)v^T(\tau)] = 0 \quad (1.24)$$

Kalman (1960) showed that it is possible to derive an Observer that calculates  $\hat{x}(t)$ , an optimal estimate of  $x(t)$  that minimizes the mean of the squared error between the actual state  $x(t)$  and the estimated state  $\hat{x}(t)$ , as described by a state error covariance matrix  $P$ . The equations describing the continuous-time Kalman filter are:

$$\dot{\hat{x}}(t) = A\hat{x}(t) + Bu(t) + K(t)(y(t) - C\hat{x}(t)) \quad (1.25)$$

$$K(t) = P(t)C^T V^{-1} \quad (1.26)$$

$$\dot{P}(t) = AP(t) + P(t)A^T + GQG^T - P(t)C^T V^{-1} CP(t) \quad (1.27)$$



$$\hat{x}(0) = E[x(0)] \quad (1.28)$$

$$P(0) = E[(x(0) - \hat{x}(0))(x(0) - \hat{x}(0))^T] \quad (1.29)$$

Equation (1.25) is often called the “internal model” equation, since first three terms in equation (1.25) correspond exactly to those in equation (1.18). The Kalman filter “knows” the unforced dynamic characteristics of the system ( $A$  matrix), and can predict the effect on  $\hat{x}(t)$  of any deterministic inputs ( $B$  matrix), given an initial state estimate (eq. 1.28). It can use the internal model state estimate  $\hat{x}(t)$  and knowledge of sensor sensitivity to calculate  $C\hat{x}(t)$ , an estimate of what the sensor measurement should be if  $\hat{x}(t)$  were correct. The fourth term in equation (1.25) uses the difference between actual and anticipated sensor measurement,  $(y(t) - C\hat{x}(t))$ , usually called the “residual”, and weights it using a set of appropriately chosen weighting coefficients  $K$ , referred to as the “Kalman Gain” matrix. This fourth term in the internal model equation thus incorporates the unexpected component of sensor information, and continuously steers the internal model estimate  $\hat{x}(t)$  so it converges with reality. Kalman significant contribution was to show that the mean square state estimate is minimized if the weighting coefficients are computed using equation (1.26). This calculation requires a running estimate of state error covariance  $P$ , obtained by integrating equation (1.27), using an initial value provide by equation (1.29). However, in many practical situations,  $P$  soon reaches a steady state value, and it is possible to precompute  $P_\infty$  the cooresponding steady state value of  $P$ . In this case, equation (1.27) reduces to a nonlinear algebraic matrix Riccati equation:

$$0 = AP_\infty + P_\infty A^T + Q - P_\infty C^T V^{-1} C P_\infty \quad (1.30)$$

Equation (1.30) is readily solved for  $P_\infty$  using routines readily available, e.g. in Matlab. The two first terms in equation (1.30) represent the unforced state transition, i.e. the effect of the unforced system dynamics upon the covariance propagation. The third term increases the uncertainty due to the process noise, whereas the fourth term represents a decrease of uncertainty as a result of measurement.

Finally, the corresponding steady-state Kalman gain is given by:

$$K_\infty = P_\infty C^T V^{-1} \quad (1.31)$$

And the steady-state Kalman filter is given as:

$$\dot{\hat{x}}(t) = (A - K_\infty C)\hat{x}(t) + K_\infty y(t) \quad (1.32)$$

### 1.4.3. Nonlinear state-space estimation

As stated earlier, the Kalman filter calculates the optimal terms in the recursive form of the Gaussian approximate linear Bayesian update of the conditional mean of the state and its covariance exactly for linear dynamic state space models. This is a well known result for linear Gaussian systems, i.e. the linear transformation of a Gaussian variable stays Gaussian.

Many dynamic systems and sensors are however not absolutely linear. Even the simple  $I=V/R$  relationship of Ohm's law is only an approximation over a limited range. If the voltage across a resistor exceeds a certain threshold, then the linear approximation breaks down. Following the considerable success enjoyed by linear estimation methods on linear problems, extensions of these methods were applied to such nonlinear problems. The most widespread nonlinear extension of the Kalman filter is undoubtedly the extended Kalman filter, which is based on a direct linearization of the nonlinear system (Simon, 2006). However, this filter is usually limited to a first order accuracy of propagated means and covariances resulting from a first-order truncated Taylor-series linearization method. A way to reduce the linearization errors that are inherent in the EKF is to use "higher-order" approaches, e.g. a second-order extended Kalman filter. Estimation performance provided by these approaches is better than the first-order EKF, but they do so at the price of a higher complexity and computational expense. Recently, another technique called the unscented Kalman filter has been proposed in an attempt to address the EKF shortcomings. This is done through the use of novel deterministic sampling approaches to approximate the optimal gain and prediction terms in the Gaussian approximate linear Bayesian update of the Kalman filter framework. This filter can give greatly improved performance (compared with the EKF) and consistently outperforms the EKF in filter robustness and ease of implementation, for no added computational cost.

In the following sections, we first present how means and covariances propagate in nonlinear equations. Then, the first-order extended Kalman filter is introduced. Finally, after presenting the unscented transformation, which is a way to approximate how the mean and covariance of a random variable change when the random variable undergoes a nonlinear transformation, we introduce the unscented Kalman filter and completely specify its algorithmic implementation.

#### 1.4.3.1. Nonlinear transformation of random variables

- Multidimensional Taylor series

In order to apply tools from linear systems theory to nonlinear systems, the nonlinear system has to be linearized. In other words, a linear system that is approximately equal to the nonlinear system must be found. The usual approximation method of nonlinear function is the Taylor series expansion. For instance, if we consider a nonlinear function  $f$  of a scalar  $x$ , the expansion of  $f$  in a Taylor series around a linearization point  $\bar{x}$ , defining  $\tilde{x} = x - \bar{x}$ , is:

$$f(x) = f(\bar{x}) + \left. \frac{\partial f}{\partial x} \right|_{\bar{x}} \tilde{x} + \frac{1}{2!} \left. \frac{\partial^2 f}{\partial x^2} \right|_{\bar{x}} \tilde{x}^2 + \frac{1}{3!} \left. \frac{\partial^3 f}{\partial x^3} \right|_{\bar{x}} \tilde{x}^3 + \dots \quad (1.33)$$

Extending equation (1.33) to the general case in which  $x$  is a  $n \times 1$  vector, the expansion of  $f$  becomes:

$$f(x) = f(\bar{x}) + \left( \tilde{x}_1 \frac{\partial}{\partial x_1} + \dots + \tilde{x}_n \frac{\partial}{\partial x_n} \right) f \Big|_{\bar{x}} + \frac{1}{2!} \left( \tilde{x}_1 \frac{\partial}{\partial x_1} + \dots + \tilde{x}_n \frac{\partial}{\partial x_n} \right)^2 f \Big|_{\bar{x}} + \dots \quad (1.34)$$

where the term  $\left( \tilde{x}_1 \frac{\partial}{\partial x_1} + \dots + \tilde{x}_n \frac{\partial}{\partial x_n} \right) f \Big|_{\bar{x}}$  is the gradient of  $f$  times the displacement vector

and the term  $\left( \tilde{x}_1 \frac{\partial}{\partial x_1} + \dots + \tilde{x}_n \frac{\partial}{\partial x_n} \right)^2 f \Big|_{\bar{x}}$  represents the Hessian matrix times the displacement vector.

The advantage of this formulation is that it can be generalized to the case in which  $x$  is a  $n \times 1$  vector without using the usual tensor notation. Indeed, defining the operator  $D_{\tilde{x}}^k$  as:

$$D_{\tilde{x}}^k = \left( \sum_{i=1}^n \tilde{x}_i \frac{\partial}{\partial x_i} \right)^k f(x) \Big|_{\bar{x}} \quad (1.35)$$

the multidimensional Taylor series expansion of  $f$  can be re-written as:

$$f(x) = f(\bar{x}) + D_{\tilde{x}} f + \frac{1}{2!} D_{\tilde{x}}^2 f + \frac{1}{3!} D_{\tilde{x}}^3 f + \dots \quad (1.36)$$

- Mean transformation

Suppose that  $x$  is a random variable with mean  $\bar{x}$  and covariance  $P_x$ . A second random variable,  $y$  is related to  $x$  through the nonlinear function  $y = f(x)$ . The problem of predicting the future state of a system consists to calculate the mean  $\bar{y}$  and covariance  $P_{yy}$  of  $y$ . The statistic of  $y$  are calculated by determining the density function of the transformed distribution and evaluating the statistics from that distribution.

From equation (1.36)  $y = f(x)$  can be expanded in a Taylor series around  $\bar{x}$  as follows:

$$y = f(\bar{x}) + D_{\tilde{x}} f + \frac{1}{2!} D_{\tilde{x}}^2 f + \frac{1}{3!} D_{\tilde{x}}^3 f + \dots \quad (1.37)$$

The mean of  $y$  can thus be expanded as:

$$\bar{y} = f(\bar{x}) + E \left[ D_{\tilde{x}} f + \frac{1}{2!} D_{\tilde{x}}^2 f + \frac{1}{3!} D_{\tilde{x}}^3 f + \dots \right] \quad (1.38)$$

Assuming that the distribution of  $x$  is symmetrical, it can be shown that all odd-order moments of (1.38) are zeros (Simon, 2006). The expectation of the second order term can be written as:

$$\begin{aligned}
E\left[D_{\tilde{x}}^2 f\right] &= E\left[D_{\tilde{x}}(D_{\tilde{x}} f)^T\right] \\
&= E\left[(\nabla^T \tilde{x} \tilde{x}^T \nabla) f(x)\Big|_{x=\bar{x}}\right] \\
&= (\nabla^T P_x^T \nabla) f(x)\Big|_{x=\bar{x}}
\end{aligned} \tag{1.39}$$

Substituting this result into (1.38) gives the following form of the mean expression:

$$\bar{y} = f(\bar{x}) + \frac{1}{2} \left[ (\nabla^T P_x \nabla) f(x)\Big|_{x=\bar{x}} \right] + E \left[ \frac{1}{4!} D_{\tilde{x}}^4 f + \frac{1}{6!} D_{\tilde{x}}^6 f + \dots \right] \tag{1.40}$$

- Covariance transformation

In a similar fashion as the mean transformation calculation, the covariance of a variable that undergoes a nonlinear transformation can be calculated. By definition, the covariance of  $y$  is given by:

$$P_y = E \left[ (y - \bar{y})(y - \bar{y})^T \right] \quad (1.41)$$

By using equation (1.37) and (1.40), we can write  $y - \bar{y}$  as

$$y - \bar{y} = \left[ D_{\tilde{x}} f + \frac{1}{2!} D_{\tilde{x}}^2 f + \dots \right] - \left[ \frac{1}{2!} E \left[ D_{\tilde{x}}^2 f \right] + \frac{1}{4!} E \left[ D_{\tilde{x}}^4 f \right] + \dots \right] \quad (1.42)$$

Taking outer products and expectations, the transformed covariance is given by:

$$P_y = FP_x F^T - \frac{1}{4} \left[ FP_x F^T \right] \left[ FP_x F^T \right]^T + E \left[ \sum_{i=1}^{\infty} \sum_{j=1}^{\infty} \frac{1}{i! j!} D_{\tilde{x}}^i f \left( D_{\tilde{x}}^j f \right)^T \right] \quad \forall i, j \text{ such that } ij > 1$$

$$- \left( \sum_{i=1}^{\infty} \sum_{j=1}^{\infty} \frac{1}{(2i)!(2j)!} E \left[ D_{\tilde{x}}^{2i} f \right] E \left[ D_{\tilde{x}}^{2j} f \right]^T \right) \quad (1.43)$$

where  $F$  is the Jacobian matrix of  $f(x)$  evaluated at  $x = \bar{x}$ .

To sum up, the  $n$ th order term in the series for  $\bar{x}$  is a function of the  $n$ th order moments of  $x$  multiplied by the  $n$ th order derivatives of  $f$  evaluated at  $x = \bar{x}$ . If the moments and derivatives can be evaluated correctly up to the  $n$ th order, the mean is correct up to the  $n$ th order as well. Similar comments hold for the covariance equation as well. Since each term in the series is scaled by a progressively smaller and smaller term, the lowest order terms in the series are likely to have the greatest impact. Therefore, the prediction procedure should be concentrated on evaluating the lower order terms.

By the way, linearization – such as in the extended Kalman filter - assumes that the second and higher order terms of  $\tilde{x}$  can be neglected. Under this assumption:

$$\bar{y} = f(\bar{x}) \quad (1.44)$$

$$P_y = FP_x F^T \quad (1.45)$$

Comparing these expressions with equations (1.40) and (1.43), it is clear that these approximations are accurate only if the second and higher order terms in the mean and fourth and higher order terms in the covariance are negligible. Otherwise, linearization may introduce significant errors.

### 1.4.3.2. The extended Kalman filter

The most well known application of the Kalman filter framework to nonlinear inference problems is probably the extended Kalman filter (EKF). Indeed, the extended Kalman filter extends the scope of Kalman filter to nonlinear optimal filtering problem. This filter is based on a sub-optimal implementation of the recursive Bayesian estimation framework applied to Gaussian random variables. Basically, the EKF approximates the state distribution by a Gaussian random variable, and propagates the state analytically through a first-order linearization of the nonlinear system. As well as the Kalman filter, different versions of the EKF can be derived: continuous-time, discrete-time, and hybrid. We here present the hybrid EKF, which considers continuous-time dynamics and discrete-time measurements such as:

$$\dot{x} = f(x, u, w, t) \quad (1.46)$$

$$y_k = h_k(x_k, v_k) \quad (1.47)$$

$$w(t) \sim (0, Q_c) \quad (1.48)$$

$$v_k \sim (0, V_k) \quad (1.49)$$

where  $x(t) \in \mathbb{R}^n$  is the state,  $y_k \in \mathbb{R}^m$  is the measurement. The process noise  $w(t)$  is continuous-time white noise with covariance  $Q_c$ , and the measurement noise  $v_k$  is discrete-time white noise with covariance  $V_k$ . The state dynamics are modeled as continuous-time stochastic processes, and the measurements are obtained at discrete instances of time.

As the linear Kalman filter, the EKF has a prediction / correction structure. First, between measurement, the state estimate is propagated according to the known nonlinear dynamics from  $\hat{x}_{k-1}^+$  to the *a priori* estimate  $\hat{x}_k^-$  as well as the covariance  $P$  from  $P_{k-1}^+$  to the *a priori* covariance  $P_k^-$ . This propagation is performed by integrating the known nonlinear dynamics and the covariance of the estimation error  $P$ . Second, at each measurement time, the *a priori* state estimate and covariance are updated as derived in the discrete-time version of the EKF to get the *a posteriori* state estimate and covariance. The implementation of the hybrid EKF is given in algorithm 1.

**Algorithm 1: The hybrid extended Kalman filter**

1. The dynamic system is given by the following equations:

$$\dot{x} = f(x, u, w, t)$$

$$y_k = h_k(x_k, v_k)$$

$$w(t) \sim (0, Q_c)$$

$$v_k \sim (0, V_k)$$

2. Initialization

$$\hat{x}_0^+ = E(x_0)$$

$$P_0^+ = E[(x_0 - \hat{x}_0^+)(x_0 - \hat{x}_0^+)^T]$$

3. For  $k = 1, 2, \dots$

(a) Prediction step: integrate the state estimate and its covariance from time  $(k-1)^+$  to time  $k^-$  as follows:

$$\dot{\hat{x}} = f(\hat{x}, u, 0, t)$$

$$\dot{P} = AP + PA^T + LQ_cL^T$$

where  $A = \left. \frac{\partial f}{\partial x} \right|_{\hat{x}}$ ,  $L = \left. \frac{\partial f}{\partial w} \right|_{\hat{x}}$ . This integration begins with  $\hat{x} = \hat{x}_{k-1}^+$  and  $P = P_{k-1}^+$ . At

the end of this integration we have  $\hat{x} = \hat{x}_k^-$  and  $P = P_k^-$ .

(b) Correction step: at time  $k$ , incorporate the measurement  $y_k$  into the state estimate and estimation covariance:

$$K_k = P_k^- H_k^T (H_k P_k^- H_k^T + V_k)^{-1}$$

$$\hat{x}_k^+ = \hat{x}_k^- + K_k [y_k - h_k(\hat{x}_k^-, t)]$$

$$P_k^+ = (I - K_k H_k) P_k^- (I - K_k H_k)^T + K_k V_k K_k^T$$

where  $H_k$  is the partial derivatives of  $h_k(x_k, v_k)$  with respect to  $x_k$ , and is evaluated at  $\hat{x}_k^-$ .

Even though the hybrid EKF considers continuous-time systems, an important difference between the continuous-time EKF and the hybrid EKF appears in the expression of  $\dot{P}$ . In the case of the continuous-time EKF, its expression is given by:

$$\dot{P} = AP + PA^T + LQ_cL^T - PC^T R^{-1} CP \quad (1.50)$$

It can be observed that in the hybrid EKF the  $R$  term is not included. This can be explained by the fact that  $P$  is integrated between measurement times, during which any measurements are available.

Note that contrary to the Kalman filter,  $P_k$  and  $K_k$  cannot be computed offline because they depend on  $H$ , which depends on  $\hat{x}_k^-$ , which in turn depends on the noisy measurements.

- Limitation of the EKF

Even though the EKF is one of the most widely used approximate solutions for nonlinear estimation and filtering, it has a few serious drawbacks:

1. This technique is based on the linearization of the system around the current estimate using a first-order truncation of the multidimensional Taylor series expansion. Thus, it only achieves first-order accuracy in the calculation of both the posterior mean and covariance of the transformed random variables. Clearly, these approximations will only be valid if the higher order derivatives of the nonlinear functions are effectively zero. In other words, it requires the zeroth and first order terms of equation (1.40) to dominate the remaining terms, over the region of the state-space defined by the prior distribution of  $x$ .
2. The EKF does not take into account the inherent “uncertainty” in the prior random variable during the linearization process. That is, the linearization method employed by the EKF does not consider the fact that  $x$  is a random variable. This has large implications for the accuracy and consistency of the resulting EKF algorithm, and may sometimes lead to divergence of the filter.
3. In many cases the calculation of the Jacobian matrices can be a very difficult process and it also prones to human errors (both derivation and programming).

### 1.4.3.3. The unscented Kalman filter

The unscented Kalman filter (UKF) is a recursive MMSE estimator based on the optimal Gaussian approximate Kalman filter framework that addresses some of the approximation issues of the EKF. Because the EKF only uses the first order terms of the Taylor series expansion of the nonlinear functions, it often introduces large errors in the estimated statistics of the posterior distribution of the states. Unlike the EKF, the UKF does not explicitly approximate the nonlinear process and observation models. It uses the true nonlinear models and rather approximate the distribution of the state random variable. In the UKF the state distribution is still represented by a Gaussian random variable, but it is specified using a minimal set of deterministically chosen sample points. These sample points, called “Sigma-points”, completely capture the true mean and covariance of the Gaussian random variable, and when propagated through the nonlinear system, captures the posterior mean and covariance accurately to the 2<sup>nd</sup> order for any nonlinearity.

To present the UKF, we first start by explaining the deterministic sampling approach called the unscented transformation. Then, the implementation of the UKF is introduced.

- The unscented transformation

The unscented transformation (UT) is a method for calculating the statistics of a random variable which undergoes a nonlinear transformation (Julier et al., 1995, 1997, 2000). This technique is founded on the intuition that it is easier to approximate a Gaussian distribution than it is to approximate an arbitrary nonlinear function. The basic idea of the UT is:



1. A set of weighted samples (sigma points) are deterministically calculated using the mean and square-root decomposition of the covariance matrix of the prior random variable. As a minimal requirement the sigma point set must completely capture the first and second order moments of the prior random variable.
2. The sigma points are propagated through the nonlinear function using functional evaluations alone, i.e. no analytical derivatives are used, in order to generate a posterior sigma point set.
3. The posterior statistics are calculated using functions of the propagated sigma points and weights. Typically these take on the form of simple weighted sample mean and covariance calculations of the posterior sigma points.

For instance, let's consider the propagation of a  $n$  dimensional random variable  $x$  with mean  $\bar{x}$  and covariance  $P_x$  through a nonlinear function  $y = f(x)$ . In order to calculate the first two moments (mean and covariance) of  $y$  using the unscented transformation, the method is as follows. First, a set of  $2n+1$  weighted samples, called sigma points,  $S_i = \{w_i^m, w_i^c, X_i\}$  are deterministically chosen as follows:

$$\begin{aligned}
X_0 &= \bar{x} & w_0^m &= \lambda / (n + \lambda) & i &= 0 \\
X_i &= \bar{x} + \left( \sqrt{(n + \lambda)P_x} \right)_i & i &= 1, \dots, n & w_0^c &= \lambda / (n + \lambda) + (1 - \alpha^2 + \beta) & i &= 0 \\
X_i &= \bar{x} - \left( \sqrt{(n + \lambda)P_x} \right)_i & i &= 1, \dots, n & w_i^m &= w_i^c = 1 / (2(n + \lambda)) & i &= n + 1, \dots, 2n
\end{aligned} \tag{1.51}$$

where  $w_i^m$  and  $w_i^c$  are the weight associated with the  $i$ th sigma-point used for the computation of the predicted mean and covariance, respectively.  $\sqrt{(n + \lambda)P_x}$  is the matrix square root of  $(n + \lambda)P_x$  such that  $\left( \sqrt{(n + \lambda)P_x} \right)^T \sqrt{(n + \lambda)P_x} = (n + \lambda)P_x$ , and  $\left( \sqrt{(n + \lambda)P_x} \right)_i$  is the  $i$ th row (or column) of  $\sqrt{(n + \lambda)P_x}$ . The numerically efficient Cholesky factorization method is typically used to calculate the matrix square root.

The distance of the  $i$ th sigma point from  $\bar{x}$  is proportional to  $\sqrt{(n + \lambda)}$ , where  $\lambda$  is a scaling parameter defined as:

$$\lambda = \alpha^2(n + \kappa) - n \tag{1.52}$$

$\alpha$  and  $\kappa$  are two positive coefficients that provide extra degree of freedom to control the scaling of the sigma points without causing the resulting covariance to possibly become non-positive semidefinite.  $\alpha$  controls the size of the sigma-point distribution and is usually chosen as  $0 \leq \alpha \leq 1$ . The coefficient  $\kappa$  must be positive or null in order to guarantee positive semidefiniteness of the covariance matrix. The specific value of kappa is not critical though, so a good default choice is  $\kappa = 0$ . A third parameter  $\beta$  is introduced which affects the weighting of the zeroth sigma-point for the calculation of the covariance. It has been shown that for a Gaussian prior the optimal choice that reduces higher-order errors of the mean and covariance approximation errors is  $\beta = 2$  (Julier et al., 2002).

Finally, each sigma-point is propagated through the nonlinear function

$$Y_i = f(X_i) \quad i = 0, \dots, 2n \quad (1.53)$$

And the approximated mean, covariance and cross-covariance of  $y$  are computed as follows:

$$\bar{y} \approx \sum_{i=0}^{2n} w_i^m Y_i \quad (1.54)$$

$$P_y \approx \sum_{i=0}^{2n} w_i^c (Y_i - \bar{y})(Y_i - \bar{y})^T \quad (1.55)$$

$$P_{xy} \approx \sum_{i=0}^{2n} w_i^c (X_i - \bar{x})(Y_i - \bar{y})^T \quad (1.56)$$

These estimates of the mean and covariance are accurate to the third order (for Gaussian priors) of the Taylor series expansion of  $f(x)$  for any nonlinear function. For non-Gaussian inputs, approximations are accurate to at least the second-order, with the accuracy of third and higher order moments determined by the specific choices of scaling factors. In comparison, the EKF only calculates the posterior mean and covariance accurately to the first order.

- Implementation of the unscented Kalman filter

We here consider the hybrid version of the UKF (Simon, 2006). In this case, the system is described by continuous-time dynamics and discrete-time measurements such as equation (1.46) and (1.47). The implementation in matrix form is defined by the following recursive algorithm.

Algorithm 2: The hybrid unscented Kalman filter

Initialization

$$\hat{x}_0^+ = E(x_0)$$

$$P_0^+ = E[(x_0 - \hat{x}_0^+)(x_0 - \hat{x}_0^+)^T]$$

For  $k = 1, 2, \dots$

1. Calculate sigma-points:

$$X_{k-1} = [\hat{x}_{k-1} \ \cdots \ \hat{x}_{k-1}] + \sqrt{n + \lambda} \begin{bmatrix} 0 & \sqrt{P_{k-1}} & -\sqrt{P_{k-1}} \end{bmatrix}$$

2. Time update equations: integrate the state estimate and its covariance :

$$\dot{\hat{x}} = f(X(t))W^m$$

$$\dot{P}(t) = X(t)Wf^T(X(t)) + f(X(t))WX^T(t) + Q_c$$

$$\text{Where } \rightarrow W^m = [w_0^m \ \cdots \ w_{2n}^m]^T,$$

$$\rightarrow W = \left( I - [W^m \ \cdots \ W^m] \right) \times \text{diag} \left( w_0^c \ \cdots \ w_{2n}^c \right) \times \left( I - [W^m \ \cdots \ W^m] \right)^T.$$

The predicted mean and covariance are given as  $\hat{x}_k^- = \hat{x}(t_k)$  and  $P_k^- = P(t_k)$

3. Correction step: measurement update equations

(a) regenerate  $2n+1$  sigma points with appropriate changes since the current best guess for the mean and covariance of  $x_k$  are  $\hat{x}_k^-$  and  $P_k^-$

(b) Use the nonlinear measurement equation to transform the sigma-points into predicted measurements:

$$Y_k = h(X_k, t_k)$$

(c) Compute the predicted measurement vector from the transformed sigma-points:

$$\hat{y}_k^- = \sum_{i=0}^{2n} w_i^m Y_k^i$$

(d) Estimate the covariance of the predicted measurement

$$P_y = \sum_{i=0}^{2n} w_i^c (Y_k^i - \hat{y}_k^-)(Y_k^i - \hat{y}_k^-)^T$$

(e) Estimate the cross-covariance between  $\hat{x}_k^-$  and  $\hat{y}_k^-$ :

$$P_{xy} = \sum_{i=0}^{2n} w_i^c (X_k^i - \hat{x}_k^-)(Y_k^i - \hat{y}_k^-)^T$$

(f) The measurement update can be performed using the normal Kalman filter equations:

$$K_k = P_{xy} P_y^{-1}$$

$$\hat{x}_k^+ = \hat{x}_k^- + K_k (y_k - \hat{y}_k^-)$$

$$P_k^+ = P_k^- - K_k P_y K_k^T$$

- Accuracy of sigma-points approach

➤ Posterior mean accuracy

The unscented Kalman filter calculates the posterior mean from the propagated sigma-points. For the UKF, the sigma points are given by:

$$\begin{aligned} X_i &= \bar{x} \pm \sqrt{(n+\lambda)} p_{x_i} \\ &= \bar{x} \pm \tilde{p}_{x_i} \end{aligned} \quad (1.57)$$

where  $p_{x_i}$  denotes the  $i$ th column of the matrix square root of  $P_x$ . The propagation of each point through the nonlinear function as a Taylor series expansion about  $\bar{x}$  is given by:

$$Y_i = f(X_i) = f(\bar{x}) + D_{\tilde{p}_{x_i}} f + \frac{1}{2!} D_{\tilde{p}_{x_i}}^2 f + \frac{1}{3!} D_{\tilde{p}_{x_i}}^3 f + \dots \quad (1.58)$$

Using equations (1.51), (1.53), (1.54) and taking into consideration that the sigma-points are symmetrically distributed around  $\bar{x}$  (resulting in zero odd moment terms), the UKF calculated posterior mean is defined by:

$$\begin{aligned} \bar{y}_{UKF} &= f(\bar{x}) + \frac{1}{2(n+\lambda)} \sum_{i=1}^{2n} \left[ \frac{1}{2} D_{\tilde{p}_{x_i}}^2 f + \frac{1}{4!} D_{\tilde{p}_{x_i}}^4 f + \frac{1}{6!} D_{\tilde{p}_{x_i}}^6 f + \dots \right] \\ &= f(\bar{x}) + \frac{1}{2} (\nabla P_x \nabla) f(x) \Big|_{x=\bar{x}} + \frac{1}{2(n+\lambda)} \sum_{i=1}^{2n} \left[ \frac{1}{4!} D_{\tilde{p}_{x_i}}^4 f + \frac{1}{6!} D_{\tilde{p}_{x_i}}^6 f + \dots \right] \end{aligned} \quad (1.59)$$

By comparing equation (1.40) and (1.59), it can be clearly seen that the true posterior mean and the mean calculated by the UKF agrees exactly to the third order and that errors are introduced in the fourth and higher-order terms. The magnitude of these errors depends on the choice of the scaling parameter  $\lambda$  as well as the higher-order derivatives of  $f$ . In contrast, the linearization approach used in the EKF calculates the means as  $\bar{y}_{EKF} = f(\bar{x})$ , which only agrees with the true posterior mean up to the first order.

➤ Posterior covariance accuracy

The true posterior covariance is given in equation (1.43). By definition, the covariance of  $y$  is given by equation (1.55). Expanding (1.55) and using a similar approach used above to calculate the accuracy in the mean approximation, it is shown that the UKF calculated posterior covariance is:

$$\begin{aligned} P_y^{UKF} &= F P_x F^T - \frac{1}{4} [F P_x F^T] [F P_x F^T]^T + \frac{1}{2(n+\lambda)} \sum_{k=1}^{2n} \left[ \sum_{i=1}^{\infty} \sum_{j=1}^{\infty} \frac{1}{i! j!} D_{\tilde{p}_{x_i}}^i f \left( D_{\tilde{p}_{x_j}}^j f \right)^T \right] \\ &\quad - \left( \sum_{i=1}^{\infty} \sum_{j=1}^{\infty} \frac{1}{4(2i)!(2j)!(n+\lambda)^2} \sum_{k=1}^{2n} \sum_{m=1}^{2n} D_{\tilde{p}_{x_k}}^{2i} f \left( D_{\tilde{p}_{x_m}}^{2j} f \right)^T \right) \quad \forall i, j \text{ such that } ij > 1 \end{aligned} \quad (1.61)$$

Comparing equations (1.43) and (1.61), it is clear that the UKF calculates the posterior covariance accurately in the first two terms, with errors only introduced at the fourth and higher-order moments (Fig. 1.13). In contrast, the EKF truncates the Taylor series after the first term, that is:

$$P_y^{EKF} = FP_x F^T \tag{1.62}$$

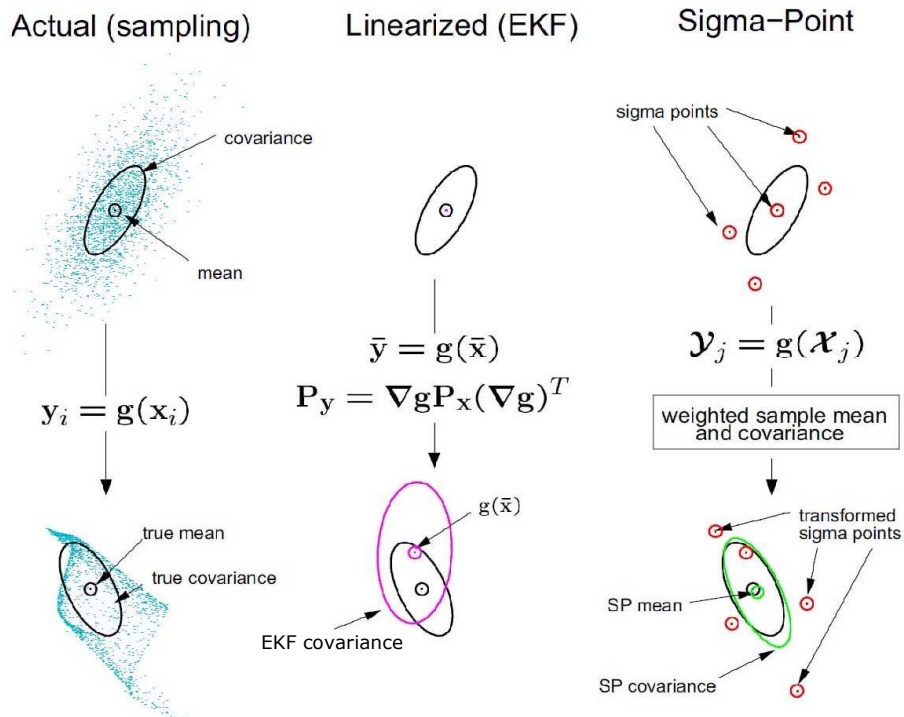


**Figure 1.13.** Demonstration of the accuracy of the unscented transformation for mean and covariance propagation. (a) Actual (Monte Carlo approach). (b) First-order linearization (EKF). (c) Sigma point transformation (UKF).

# Chapter II: Finite element modeling

## 2.1. Modeling of the cupula

The mathematical model for the dynamics of the cupula-endolymph system of the inner ear semicircular, as elaborated by numerous investigators, remains a fundamental tool in all of vestibular physiology. Most models represent the cupula as a linear spring-like element of stiffness

$$K = \Delta P / \Delta V \quad (2.1)$$

where  $\Delta V$  is the volume displaced upon application of a pressure difference  $\Delta P$ .  $K$  directly influences the long time constant of the cupula-endolymph system.

The following modeling addresses different objectives. The first goal is to determine the relation between the pressure-volume coefficient  $K$  of the cupula of the human semicircular canal which describes the cupula's behavior as a linear elastic element, and Young's modulus  $E$  of the cupula material. We model the cupula as a structurally homogeneous elastic diaphragm of constant thickness using the bending membrane theory. We consider two distinct cases, a thin and a thick diaphragm, and ask which model best matches numerical predictions from a finite-element model based on more realistic cupula morphologies. The second goal is to explore – using finite element models – the effect of regional cupula thickness on the shearing mechanical stimulus to underlying hair cells. We study two other different shapes for the cupula based on cupula measurements and quantify the impact on its transverse displacement. We then use one of the three-dimensional finite element models to analyze both the shear strain distribution and evolution near the sensory epithelium. The third goal is to quantify the impact of fluid filled vertical channels traditionally believed to be present in the cupula. To achieve this goal, we model a section of cupula material having vertical channels voids. We consider three distinct channel diameters, use finite element analysis, and compare the transverse displacement field to the one provided by a similar section of cupula material without channels. Finally, we discuss the properties of other biological materials that have similar elastic properties as the cupula, and potential implications.

### 2.1.1. Background

- Cupula attachment

The cupula is normally transparent, and therefore its shape and function was not appreciated by investigators prior to Steinhausen (1931) and Dohlman (1935). Since then, at least four modes of cupula displacement have been described:

1. Steinhausen (1931) and Dohlman (1935) cannulated pike semicircular canals, applied small pressures, and described the resulting cupula motion as that of a “swinging

gate”, wiping across the vault of the ampulla in the manner of a revolving door, maintaining a seal so no endolymph passed over the top.

2. Dohlman (1971) suggested that displacement of the endolymph caused the cupula to move as a sliding unit similar to a piston in a cylinder. Hence this model assumes no attachment of the cupula along its entire periphery. However, in light of present day knowledge of canal morphology and hair cell physiology, the displacements experimentally created by both Steinhausen and Dohlman appear unphysiologically large (Oman et al., 1972a and 1972b; Oman et al 1987).
3. Bélanger (1961) and Igarashi (1966) found some histological evidence that the cupula was functionally attached to the ampullary roof. Zalin (1967) then proposed a model which assumed that the cupula was suspended from the roof and the significant shearing motion took place at the surface of the crista. However, subsequent histology (Dohlman, 1971; Hillman, 1974, 1977) suggested strong attachment of the cupula to the crista via supporting cell filaments and receptor cell kinocilia.
4. Hillman (1972) hypothesized that the cupula adhered to the ampullary wall around its entire the circumference. To demonstrate this, Hillman studied cupula motion following the injection of a dye, compressing the canal wall. The cupula appeared stationary around the perimeter and displaced maximally in the central region. Hillman argued that in prior studies of cupula movement, the cupula attachment was likely traumatized. He argued that the intact cupula has mechanical properties of a elastic diaphragm. He argued the cupula is circumferentially attached to the ampullary wall, except alongside the crista where the cupula shears with the crista across subcupular space. These findings were confirmed by McLaren (1977) who analyzed the motion of opaque oil droplets placed within the cupula of the bullfrog. When endolymph was displaced by compression of the canal duct, McLaren observed that the line of droplets consistently flexed and bowed with maximal displacement near the center of the cupula rather than the apical edge. This “sealed diaphragm” hypothesis was confirmed by later studies of Hillman and McLaren (1979) and McLaren and Hillman (1979).

Therefore, in the following models, we will assume a pinned boundary condition both around the periphery of the cupula and at the crista, i.e. translation displacements at the boundary are set to zero. Note that a clamped boundary condition at the crista has no significant impact on the transverse displacement field as the material being very soft bends immediately above the crista. Note also that the subcupular space between the cupula and the sensory epithelium is here not taken into account.

- Cupula structure

The shape of the cupula has been described by several researchers, but detailed measurements are rarely published. The overall shape of the cupula in the plane of the crista in the frog is approximately that a semicircular disc with its base just above the crista and has a nonuniform thickness (Hillman, 1974; McLaren, 1977). McLaren (1977) described the cupula as having two thick columns of its mass arching along the wall of the ampulla that are separated by a thin region, which corresponds to the narrow portion of the crista. The base of the cupula is separated from the crista by a “subcupular space”, which is crossed by veils and a network of filaments, while the ampullar endolymph entrances are enclosed by drapes (Dohlman, 1971;

McLaren, 1977; Hillman and McLaren, 1979). Hence, it was suggested that the cupula is attached to the crista by connections across the subcupular space, i.e. kinocilia extend across the entire width of the subcupular space and are embedded directly in the base of the cupula. In addition, many studies have supported the fact that stereocilia and kinocilia appear to be inserted into channels running vertically within the cupula from the crista to the ampullary wall (Igarashi and Alford, 1969; Dolhman, 1971; Lim, 1971). Since the cupula is thought to be extruded upwards from supporting cells surrounding each hair cell, the channels are conventionally assumed to be “shadows” caused by the presence of hair cells.

However, a recent study of the cupula of the horizontal semicircular canal in the toadfish disputes these earlier results (Silver et al., 1998). Using confocal microscopy and a new histological technique so as to reduce shrinkage artifacts, Silver et al. examined the structure of the cupula and disputed previous interpretations. First, they found that the toadfish cupula has distinct internal organization composed of several different sections: lateral wings on both sides, a central “antrum” above the hair cells, and an asymmetric shell consisting of utricular and canal side “central pillars”. They described the antrum as an isotropic gel reinforced with collagen connective fibers running vertically. They argued that the presence of the antrum means there is no true subcupular space. Second, no tubes or channels, as described in earlier studies, were observed in the toadfish cupula, either in the antrum nor in the cupula. Finally, as regard the central portion of the cupula, they argued that the utricular-side pillar should be stiffer than other regions of the cupula perhaps due to its rich mucopolysaccharide content higher than any other portions of the cupula. Silver et al. speculate that the central section moves differently than the wings and that the utricular-side pillar might serve to limit the extent of cupula deformation during head displacement.

In order to model the cupula, it is clearly necessary to know the mechanical properties of each of its region. Unfortunately, as no physical data is available, one can only guess, for instance, what the Young’s modulus is for the various components. In our theoretical study we begin by modeling the cupula by an homogenous material of Young’s modulus  $E$ . (This assumption ignores regional differences in thickness, the possible presence of a subcupular space and/or differences in structure described by Silver et al. 1998). We then use finite-element models to assess the potential impact of regional thickness variations, and channels.

- Cupula stiffness  $K$

Beginning with the pioneering work of Steinhausen (1933), a succession of more physically detailed models have been proposed to describe the dynamics of the cupula-endolymph system (e.g. Groen et al. 1952; TenKate, 1973; Van Buskirk, 1977; Oman et al, 1987; Rabbitt et al, 1999; Rabbitt et al, 2004). A common feature of most studies is that the cupula is assumed to behave as a linear spring, and can therefore be characterized by an elastic coefficient which we define as  $K = \Delta P / \Delta V$  in order to describe the volume displacement of the cupula  $\Delta V$  when the latter experiences a transcupular pressure  $\Delta P$ . Different expressions and values for this parameter have been suggested (Van Buskirk, 1977; Oman et al., 1987; Rabbitt et al., 2004). The coefficient  $K$ , along with a second factor related to endolymph flow drag on the canal walls, determine the cupula-endolymph system long time constant  $\tau_L$ , which characterizes the return of the cupula to its rest position following a change in head angular velocity. In turn, the coefficient  $K$  is hypothesized to depend on the shape of the cupula, and the Young’s modulus  $E$  and the Poisson ratio  $\nu$  of the cupula material.



This following work explores the theoretical relationships between the morphology of the cupula of the semicircular canal, the stiffness  $K$ , and the cupula's material properties  $E$  and  $\nu$ . Fundamentally, there are three different approaches that can be used to estimate  $K$  of the cupula: Historically the first approach was to directly measure the pressure volume relationship. As noted earlier, the classic procedure (e.g. Dohleman, 1969) was to transect the canal, insert a micropipette containing stained fluid, administer a known pressure change, and measure the resulting volume displacement. However this procedure likely traumatized the cupula. A second, less direct method is to measure the cupula long time constant  $\tau_L$ , and then use a mathematical model of the cupula-endolymph system to estimate  $K$ . One technique used in animal models is to pinch the intact membranous duct, and to monitor the time course of return of the deflected cupula. Such displacements must be measured through the ampulla wall using a light microscope. However, the physiologic range of cupula deflections is at or below the limit of conventional light microscopy (Oman, et al 1987). The introduction of dye or particles to visualize the motion may also traumatize the attachments. Direct observation of  $\tau_L$  has not been attempted in humans. Instead, most estimates of  $\tau_L$  come from model based analysis of afferent responses (e.g. Goldberg and Fernandez, 1971) or eye movements (e.g. Dai et al 1999). Potentially, a third approach is to extract whole cupulae and directly measure their shape and material properties  $E$  and  $\nu$  using an appropriately designed micro-apparatus. This difficult experiment has not been attempted.

Almost all estimates of  $K$  are derived from the second approach, employing various mathematical models for the cupula-endolymph system. Table 2.1 shows estimates of  $K$  based on the theoretical relationships shown in the second column, and assumed values for  $\tau_L$  suggested by the individual authors are indicated. Values range from 2.2 - 13 GPa/m<sup>3</sup>. In the next modeling section, we will use Oman's model for endolymph hydrodynamics as it is probably the most detailed analytical model of endolymph volume displacement in one semicircular canal. Oman et al. extended the classic Steinhausen/Groen mathematical description of endolymph flow to the case where the size, shape, and curvature of the canal lumen change continuously through the duct, utricle and ampulla. As regard the long time constant of the system cupula / endolymph, we use a value of 6 s determined experimentally by recording the response of peripheral afferent neurons of the squirrel monkey (Goldberg et al, 1971).

	<b>Time constant (s)</b>	<b>K (GPa / m<sup>3</sup>)</b>	<b>Comments</b>
<b>Van Buskirk (1977)</b>	$\tau_L = \frac{8\mu R}{a^4 K}$	$K \approx 2.5$ if $\tau_L = 17$	Duct approximated as rigid toroidal duct of constant cross section and occupies one half of the circumference of a circle. Cupula modelled as a revolving door.
<b>Van Buskirk (1988)</b>	$\tau_L = \frac{8\mu\beta R}{\pi a^4 K}$	$K \approx 2.2$ if $\tau_L = 21$	Duct approximated as rigid toroidal duct of constant cross section and occupies 250° of the circumference of a circle. Cupula modelled as a revolving door.
<b>Oman et al. (1987)</b>	$\tau_L = \frac{8\pi\mu L}{K} \lambda$	$K \approx 6.8$ if $\tau_L = 6$ (Goldberg et al. 1971)	Rigid duct of length L with variations of cross section shape taken into account by $\lambda$ .
<b>Squires et al. (2004)</b>	$\tau_L = \frac{8\mu\beta R}{\pi a^4 K}$	$K \approx 13$ if $\tau_L = 4.2$ (Dai et al. 1999)	Same expression as Van Buskirk by considering a different time constant.
<b>Rabbitt et al. (2004)</b>	$\tau_L \approx \frac{c}{K} = \frac{\mu L A_c^2}{\gamma h A_d^2}$	$K \approx \frac{8\pi\gamma h}{A_c^2} \approx 1.33$ if $\tau_L = 13.3$	Parameters approximation based on morphological data.

**Table 2.1.** Summary of the values of the pressure-volume coefficient along with its relation to the long time constant of the cupula. See nomenclature for definition of parameters.

### 2.1.3. Analytical model using thin and thick bending membrane theory

The cupula is modeled as an isotropic circular elastic membrane of constant thickness with a pinned edge boundary condition along its entire periphery. In other words, the transverse displacement  $w(r)$  along the periphery is set to zero as well as the bending moment  $M_{rr}(r=R)=0$ . Thus, rotational degrees of freedom were allowed at the cupula attachment. We apply both thick and thin membrane theory - also referred to as the Love-Kirchhoff and Mindlin-Reissner theories respectively (Timoshenko, 1964; Ventsel et al., 2001) – and compare the results. The difference between thick and thin plate theories is principally due to the treatment of transverse shear in the membrane. In Kirchhoff (thin plate) theory, straight lines, initially normal to the middle plane before bending, are assumed to remain straight and normal to the middle surface during the deformation. This assumption means that the vertical shear strains are negligible and are not taken into account in the calculation of the strain energy. Therefore, this approach, also referred to as the “*hypothesis of straight normals*”, is a good approximation for thin plates. On the other hand, the Mindlin-Reissner (thick plate) theory supposes that the straight lines, initially normal to the middle plane before bending, are able to rotate as the plate deforms. Therefore the influence of the shear strains is not neglected in the derivation of the strain energy.

According to both theories, in the case of a pinned edge boundary condition, it can be shown that the deflection of a circular plate  $w(r)$  of radius  $R$  is given by:

$$w(r) = \frac{PR^4}{64D} \left(1 - \frac{r^2}{R^2}\right) \left(2 \frac{3+\nu}{1+\nu} - 1 - \frac{r^2}{R^2} + \phi\right) \quad (2.2)$$

Here  $P$  is a distributed load acting in the same direction of  $w$  and  $D$  is the bending rigidity of the plate defined as

$$D = \frac{Eh^3}{12(1-\nu^2)} \quad (2.3)$$

where  $E$  is the Young's modulus,  $\nu$  is the Poisson ratio of the plate material and  $h$  is the thickness of the plate. The coefficient  $\phi$  is defined as

$$\phi = \frac{16}{5} \frac{h^2}{R^2(1-\nu)} \quad (2.4)$$

and is therefore negligibly small in the case of the thin-plate assumption ( $h/R \ll 1$ ).

The volume displacement of the cupula is given by the integration of the transversal displacement so that

$$\Delta V = \int_0^R 2\pi r w(r) dr = \frac{3\pi P R^6 (1-\nu^2)}{8Eh^3} \left( \frac{3+\nu}{2(1+\nu)} + \frac{4h^2}{5R^2(1-\nu)} - \frac{1}{3} \right) \quad (2.5)$$

Finally, since  $K$  is the ratio  $\Delta P / \Delta V$ , a relation  $E = f(K)$  between the Young's modulus and the pressure-volume coefficient was derived for both theories (table 2.2).

	Thin plate theory	Thick plate theory
$\Delta V$	$\Delta V = \frac{\pi P R^6}{16Eh^3} (1-\nu)(7+\nu)$	$\Delta V = \frac{3\pi P R^6 (1-\nu^2)}{8Eh^3} \left( \frac{3+\nu}{2(1+\nu)} + \frac{4h^2}{5R^2(1-\nu)} - \frac{1}{3} \right)$
$E = f(K)$	$E = \frac{K\pi R^6 (1-\nu)(7+\nu)}{16h^3}$	$E = \frac{3K\pi R^6 (1-\nu^2)}{8h^3} \left( \frac{3+\nu}{2(1+\nu)} + \frac{4h^2}{5R^2(1-\nu)} - \frac{1}{3} \right)$

**Table 2.2.** Relationship between the Young's modulus of the cupula and the pressure-volume coefficient  $K$ .

## 2.1.4. Finite-element models

### 2.1.4.1. Computation of the Young's modulus

A three-dimensional finite-element model of the cupula is developed in order to check the thick and thin plate analytical models. The shape of the cupula is defined based on the 2D cross-section model of Njeugna et al. (1990). A pinned boundary condition is assumed all along the periphery of the cupula and at its base (crista). The thickness of the cupula was assumed to be 403  $\mu m$  based on the morphological study of Rabbitt et al. (2004) so that:

$$h = 0.7 \sqrt{A_c / \pi} \approx 403 \mu m \quad (2.6)$$

An elastic modulus of  $E = 10 \text{ Pa}$  was assumed, and for illustrative purposes a pressure of  $0.05 \text{ Pa}$  is applied (Fig. 2.1a). According to Oman and Young (1972a,b), the steady state relation of cupula pressure to head acceleration in the plane of the canal is given by:

$$P \approx 2\rho\pi Fa^2 R^2 B^{-2} \alpha \quad (2.7)$$

where  $\alpha$  is the angular acceleration of the head in  $\text{rad/sec}^2$  (See nomenclature for the definition of the other parameters). Therefore, a pressure of  $0.05 \text{ Pa}$  corresponds to an impulse of head angular acceleration of about  $400^\circ/\text{s}^2$ . Since the cupula is nearly incompressible, a Poisson ratio of  $0.48$  was considered (Kassem et al., 2005, Yamauchi et al., 2001). The solution shown in figures 2.1b was generated using Finite Element Analysis software (Abaqus v 6.5.1) on a 3D mesh with 4284 quadratic elements.

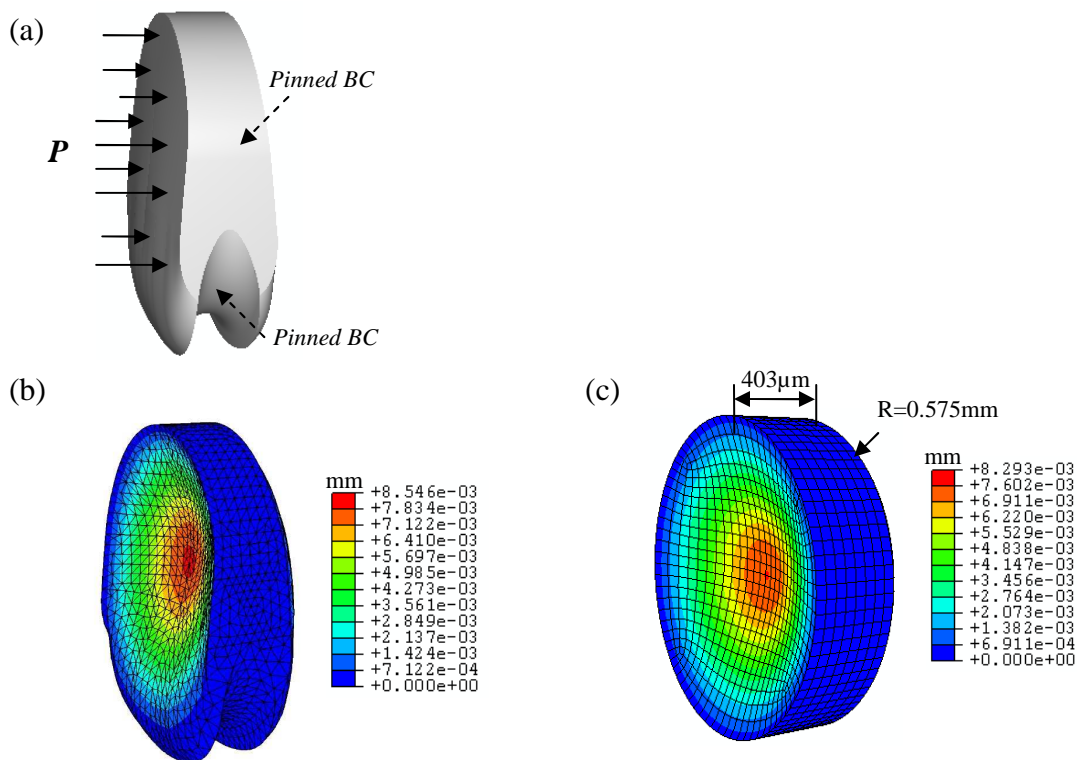


**Figure 2.1.** Three-dimensional model of the cupula. (a) 3D model of the cupula. (b) Transverse displacement field given by the FEM cupula model. (c) Transverse displacement field provided by a 3D FEM model of a circular plate.

The maximum transverse displacement occurs near the center of the cupula and is  $8.5 \mu\text{m}$ . We note that the displacement is almost identical to that of a completely circular plate of identical radius  $0.575 \text{ mm}$ , pinned along its entire boundary, shown for purposes of comparison in figure 2.1c. Therefore, we consider both models to be equivalent in terms of volume displacement.

The transverse displacements provided by the thin and thick plate theories and the numerical FE circular plate model are compared in figure for the case were  $E= 10 \text{ Pa}$ ,  $P= 0.05 \text{ Pa}$ ,  $R= 0.575 \text{ mm}$  and  $h=0.403 \text{ mm}$ . As can be seen, the thin-plate model yields results significantly different than either the thick-plate model or the 3D FE model, since it does not take into account the shear strain components within the strain tensor (Fig. 2.2). This illustrates that plate theory is not sufficiently accurate since thickness of the cupula is the same order of

magnitude as cupula radius. Therefore, the thick-plate model is more appropriate as it gives similar results as the 3D finite-element model.

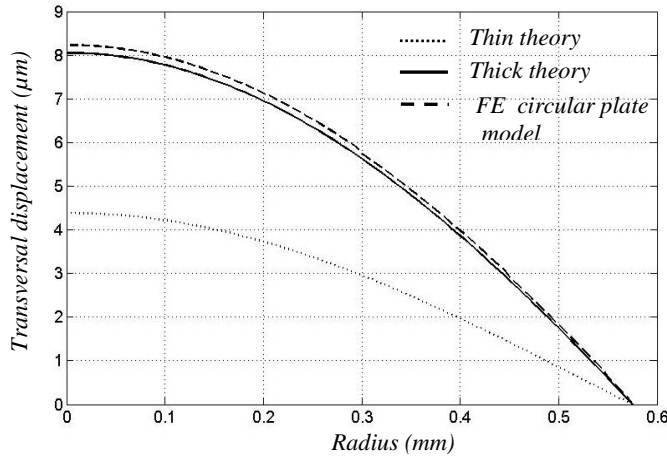


**Figure 2.2.** Transversal displacement  $w(r)$  provided by the thin and thick analytical membrane models, and the finite element circular plate model.

Using estimate of  $\kappa$  and  $\tau_L$  from the literature (Oman et al, 1987; Goldberg et al., 1971), using thick and thin plate theories (Table 2.2) it is possible to estimate the Young's modulus  $E$ . (Note that these relations are derived assuming the cupula is a circular bending plate, pinned along its entire periphery). A Poisson ratio of 0.48 was assumed. A value of  $K \approx 6.7 \text{ GPa} / \text{m}^3$  and a long time constant of 6 s yield a Young's modulus of 5.4 Pa for thick membrane theory. The value provided by the thick plate assumption is about five times lower than the Young's modulus given by Groen (1952).

Finally, note that the shorter the long time constant is assumed to be, the larger the theoretical prediction for Young's modulus. For instance, by considering Oman's model and the thick plate theory, we can derive the following relationship between  $E$  and  $\tau_L$ :

$$E = \frac{3\mu L \pi^2 R^6 (1-\nu^2) \lambda}{h^3 \tau_L} \left( \frac{3+\nu}{2(1+\nu)} + \frac{4h^2}{5R^2(1-\nu)} - \frac{1}{3} \right) = \frac{\kappa}{\tau_L} \quad (2.8)$$

where  $\kappa$  is constant that depends on numerous geometric factors.

#### 2.1.4.2. Comparison with other estimates

We compare our estimate of  $E$  with previous reports. Several authors proposed models the endolymph-cupula system for the fish, particularly the pike (De Vries, 1956; Ten Kate et al., 1969; Ten Kate et al., 1972). Although the pike's inner ear has different shape than that of the human, functionally it is similar. Ten Kate (1969) modeled the pike's cupula as a bending bar and was able to estimate the elastic or geometrical dimensions and Young's modulus as about 34.9 Pa. Other authors have focused on the modelling as well as direct measurements of the superficial neuromast in the fish lateral line system (Frishkopf et al., 1972; McHenry et al. 2007; McHenry et al. 2008). Superficial lateral line cupulae are structures that detect water flow on the surface body of fish and amphibians. These organs are closely related to

vestibular and auditory sensing organs, as the receptor cells of all these systems are morphologically similar. Water disturbance bends the cupulae which overlay hair cells, which results in stimulation of the organ. Oman et al (1972) experimentally measured cupula stiffness in the mudpuppy, and based on cupula morphology and cylindrical cantilevered beam theory estimated  $E = 10^3$  Pa. More recently, utilizing a more complex structural model, McHenry et al. (2007) estimated  $E = 21$  Pa for the zebrafish's freestanding cupula. This value is comparable to that originally estimated by Ten Kate for the pike, and is the same order of magnitude as that for the human's semicircular canals, which we estimated in the previous section.

### 2.1.4.3. Analysis of different cupula shapes

Detailed anatomical measurements of the shape of the cupula are rare in the literature. This is probably due to the fragility of the cupula, and the fact that it must be stained or the endolymph counterstained in order to visualize it. Left in-situ it is difficult to observe its shape through the wall of the semicircular canal. Extraction risks traumatizing the structure. Classic histological techniques have been optimized to preserve cellular structures, and e.g. alcohol dehydration and fixation for electron microscopy may damage or distort the cupula. Also, it is possible to misinterpret 2D micrographs of sectioned material unless the plane of sectioning is known. For instance, by looking closer at a classic 2D micrograph, one might assume that the cupula becomes thicker at the top. However, if the plane of sectioning was diagonal, the increased thickness may be on the sides.

As a result, notions of the three-dimensional shape of the cupula come mainly from various light micrographs obtained by certain investigators in animal preparations where the membranous labyrinth is easily accessed surgically (e.g. skate, pike, toadfish, frog) and photographed. Studies of isolated cupula of the skate (e.g. Oman et al., 1979) reveal that the cupula is thicker on the sides, and thin in the center all the way from the crista to the vault (Fig. 2.3).

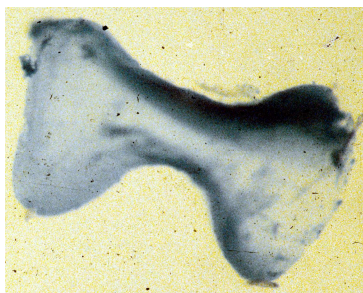


**Figure 2.3.** Top view of the skate cupula which is thicker on the sides and thin in the center (Oman et al, 1979).

Therefore, we have decided to use finite element modeling to investigate the influence of cupula shape on its transverse displacement for a standard transcupular pressure. We have studied the behaviour of two different models: one thicker around its entire periphery (Fig. 2.4a), the other thick only on the sides and with constant thickness in the center (Fig. 2.4b).

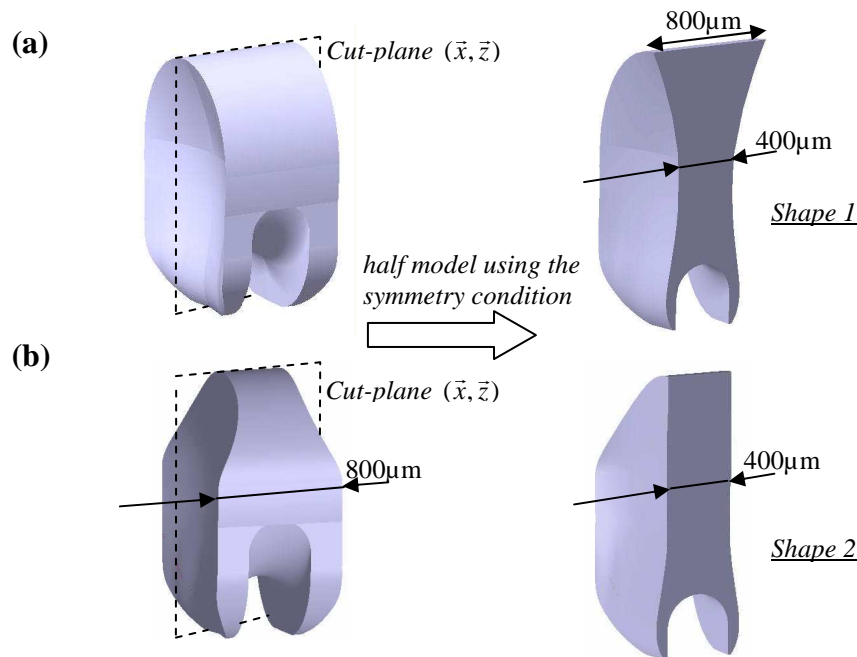


**Figure 2.4.** CAD models of the cupula considering different shapes. (a) Cupula with a thicker portion all around its periphery. (b) Cupula that is thin vertically with thick sides.

The first model has a 800  $\mu\text{m}$  thickness around its entire periphery, with a 400 micron thickness at its centre. The second model has a thin vertical center section 400  $\mu\text{m}$  thick, widening to 800  $\mu\text{m}$  on the sides in the region of the plana semilunata. The boundary conditions for the finite element analysis are: a clamped condition on the crista, and a pinned condition on the periphery of the cupula – plus a condition of symmetry relative to the cut-plane  $(\bar{x}, \bar{z})$ . For simulation purposes we apply a transcupular pressure of 0.05 Pa, and assume a Young's modulus of 10 Pa and a Poisson ratio of 0.48.

- Transverse displacement

The solution for the transverse displacement is shown for both models in figure 6. For both cases, the maximum transverse displacement is predicted to be smaller than that predicted for the simple 403 micron thick plate model by a factor of 2.8 for the first model and 1.8 for the second. . This is because the increased thickness effectively stiffens the cupula. We note that model 2.5b (cupula with fat sides and a thin vertical center) has a transverse displacement of about 55% larger than model in figure 2.5a (the cupula that was thick around its entire periphery). We also note that if the cupula is thicker along its entire periphery, the transverse displacement become vertically asymmetric as illustrated figure c. In that case the lower part of the cupula, precisely where the hair bundles are located, is the most deflected. This was not the case with model a, because the cupula is more symmetrical along a vertical axis.

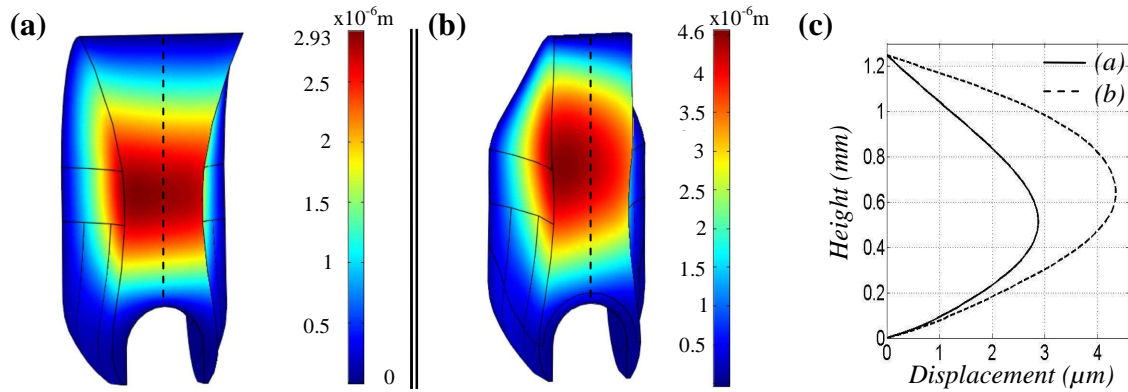


**Figure 2.5.** Transversal displacement of the human cupula provided by a finite element simulation in response to a static pressure of 0.05 Pa. (a) cupula with shape 1; (b) cupula with shape 2; (c) transversal displacement along the dashed line of both models (a) and (b).

- Predicted shear strain above the crista

The mammalian crista, which supports the cupula, contains two types of hair cells: cells of type one and two, respectively located at the top of the crista and down its sloping flanks. Hair cell sensory stereocilia, which range in height up to 35  $\mu\text{m}$  and even longer kinocilia, project into the cupula. It is generally assumed that the cilia are entrained with the cupula when the latter is deflected. Conversion of cupular volume displacement into bending of cilia initiates the transduction process in hair cells and vestibular afferent neurons. The mechanical stimulus of the stereocilia is determined by cupular shear strain that occurs close to the crista rather than cupular transverse displacement. Therefore, using the second three-dimensional finite element model of the cupula (Fig. 2.6), we analyse the shear strain at a surface located 50  $\mu\text{m}$  above the crista. First, we apply a static pressure of 0.05 Pa on the cupula and plot a map of the shear strain predicted by the model. Second, we perform a time dependent analysis in order to observe the evolution of the shear strain when the pressure increases. Results of both simulations are shown in figure 2.6.

The model predicts that the maximum shear strain occurs near the surface of the crista where the cilia are located. It is also notable that the shear strain at a surface 50  $\mu\text{m}$  above the crista is nonuniform. Indeed, the shear strain is predicted to be largest at the centre of the crista and to diminish both toward the periphery of the cupula and down the sloping flanks of the sensory epithelium as shown in the plots in figure 2.6. From the time dependent analysis, we determine that the shear strain first appears at the centre of the crista and then spreads out through time both toward the sides of the cupula and toward the bottom of the crista (Fig. 2.6d). Hence, the model predicts that hair cells of type 1 may be stimulated first, while hair cells of type 2 are progressively stimulated as the deflection of the cupula increases. This spatio-temporal variation in mechanical shearing stimulus to hair cells, as shown in the models, suggests that these two hair cell types could play different roles in encoding head movement.



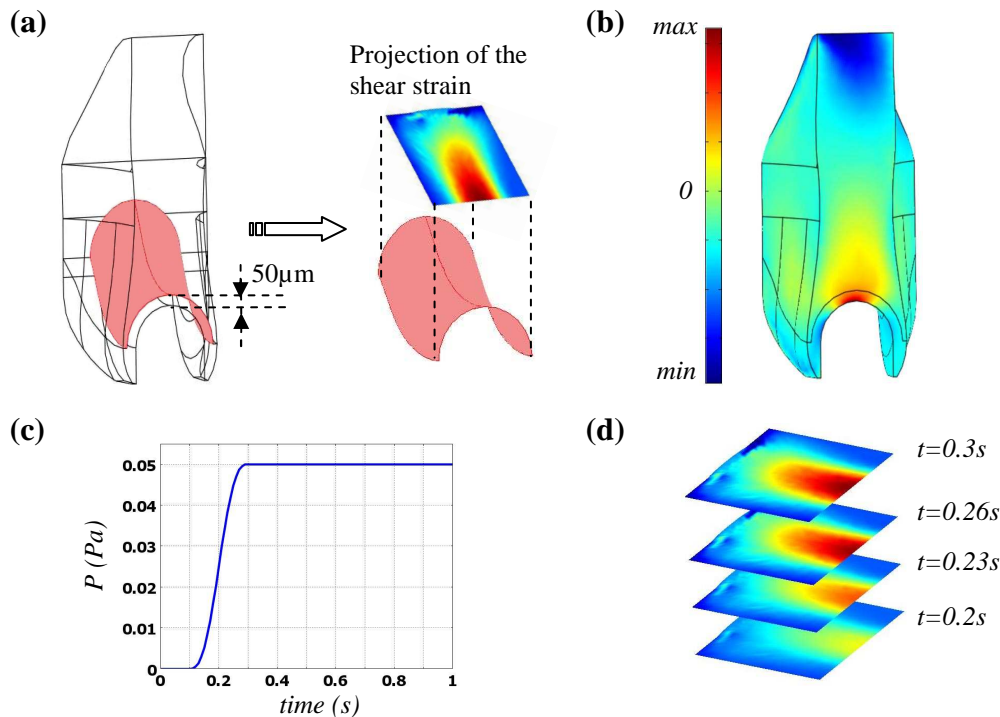


**Figure 2.6.** Analysis of the shear strain above the crista. (a) Definition of the surface located  $50\ \mu\text{m}$  above the crista and 2D map of the shear strain in response to a static pressure. (b) Shear strain in the cupula in response to a static pressure. (c) Pressure applied in the time dependent analysis. (d) Evolution of the shear strain at a surface  $50\ \mu\text{m}$  above the crista at different time instants.

#### 2.1.4.5. Mechanical influence of cupula channels

We have considered so far a homogenous material for the Young's modulus  $E$  of the cupula. However, according to Igarashi and Alford (1969), Dohlman (1971), and Lim (1971), the cupula has endolymph filled channels, of about  $10\ \mu\text{m}$  diameter, running vertically through it. Assuming that these channels exist, we use finite element models to investigate the influence of their presence on the cupula stiffness. For purpose of simplicity, we represent a volume of cupula material as a rectangular box of dimensions  $1\ \text{mm} \times 1\ \text{mm} \times 0.4\ \text{mm}$ . As we study the transverse displacement field of the cupula when the latter experiences a static pressure, the fluid within the tubes - being free to leave them - has therefore negligible effect on the cupula stiffness. Thus, we consider a rectangular box of cupula material having vertical empty channels positioned on a hexagonal matrix (Fig. 2.7a). Three channel diameters were successively taken into consideration:  $10\ \mu\text{m}$ ,  $20\ \mu\text{m}$ , and  $30\ \mu\text{m}$  (Fig. 2.7b,c). Note that each model involve a large number of degrees of freedom, and solution therefore demand significant computational resource as the tube diameters are two orders of magnitude smaller than the cupula dimensions. In addition, these channels need to be modeled by a fine mesh so as to provide accurate results. Figure 2.8a illustrates the transverse displacement provided by the simulation. Figure 2.8b shows the influence of the tubes diameter on the maximum transverse displacement of the cupula, and also compares these displacements to the one provided by a similar cupula material section without the tubes. It turns out that the higher is the tubes diameter, the larger is the displacement. For this tube spacing, it can be seen, however, that  $10\ \mu\text{m}$  diameter tubes have a very small effect while  $20\ \mu\text{m}$  and  $30\ \mu\text{m}$  diameter tubes involve larger transverse displacements of about 12.8 % and 28.6 %, respectively. The increase of displacement with respect to the tube diameters appears to be nonlinear. Since the cupula stiffness is clearly sensitive to channel size, it is important to

know whether they actually exist in specific species, and if they do, to determine their geometry, i.e. diameter and average spacing.

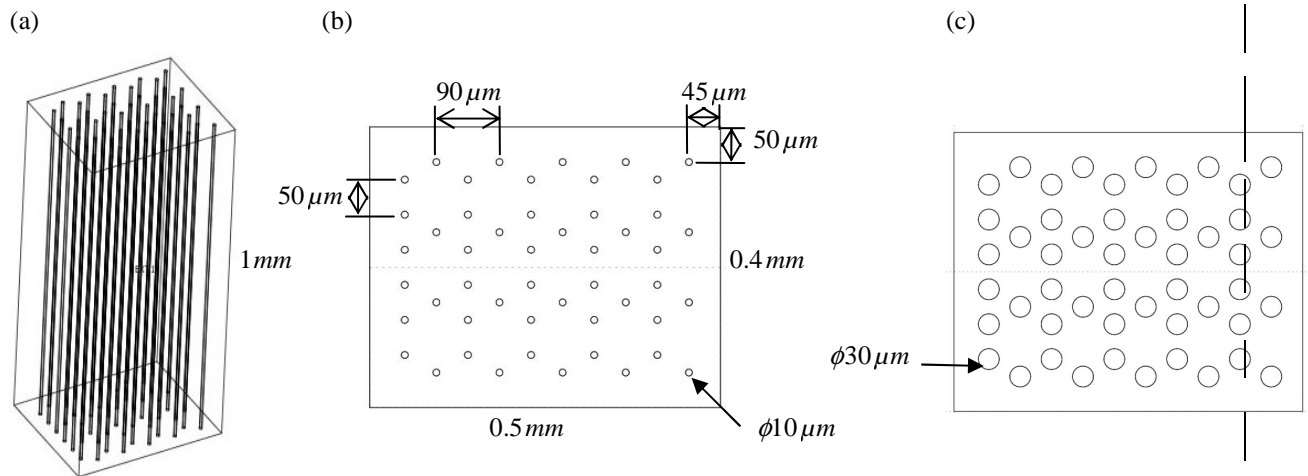


**Figure 2.7.** Modeling of a section of cupula material having vertical empty tubes. (a) 3D view of the box having vertical empty tubes; (b) top view with 10  $\mu\text{m}$  diameter tubes; (c) top view with 30  $\mu\text{m}$  diameter tubes.

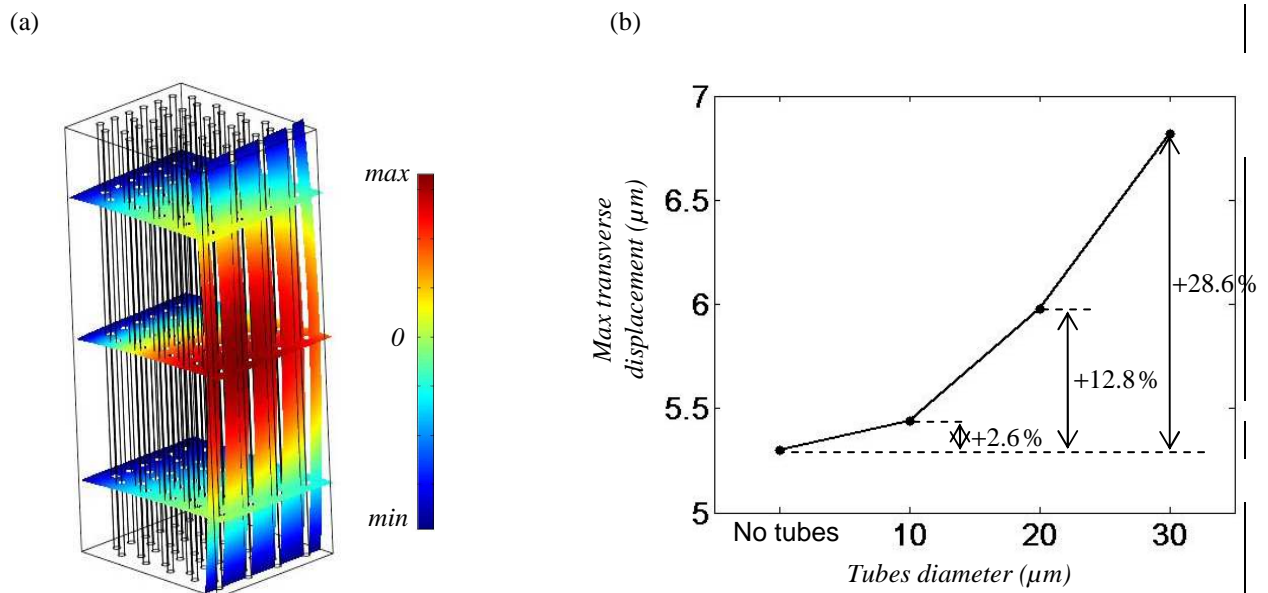


**Figure 2.8.** Results provided by the finite-element model of a section of cupula material having vertical empty tubes. (a) Transverse displacement of a box with 20  $\mu\text{m}$  diameter tubes; (b) Maximum transverse displacement at the center of the section for different tube diameters.

## 2.1.5. Biologically similar material

What biological materials have similar elastic properties as the cupula? We first consider biopolymers, a class of polymers produced by living organism such as cellulose or proteins for instance. Biopolymers are widely used as biomaterials and matrices in tissue engineering as they offer control of structure, morphology and chemistry as reasonable substitutes or mimics of extracellular matrix. They are also characterized by low values of mechanical properties in comparison with other classes of material. For example, alginate polysaccharide materials have an elastic modulus of 10-12 KPa (Velema et al., 2006). However, to our knowledge, measurements of the elastic modulus of biopolymers do not provide a Young's

modulus as low as the modulus of the cupula. Therefore, we considered hydrogel material properties.

Hydrogels are characterized by a network of polymer chains that contain a significant amount of water. These materials are viscoelastic so they are commonly characterized using dynamic mechanical analysis. The complex dynamic shear modulus  $G^*$  is used to represent their mechanical response. The parameter is composed of a real and imaginary part, so that:

$$G^* = G' + iG'' \quad (2.9)$$

The elastic modulus  $G'$  is a measure of the reversibly stored deformation energy, and the viscous modulus  $G''$  represents a measure of the irreversibly dissipated energy, and is proportional to the effective viscosity of the material. The elastic shear modulus is related to the Young's modulus according to:

$$G' = \frac{E}{2(1+\nu)} \quad (2.10)$$

With this relation, the value we derived for  $E=5.4$  Pa, correspond to a value for  $G'=1.8$  Pa. This range is similar to that reported for collagen hydrogels. Indeed, Raub et al. (2007) have demonstrated that the elastic shear modulus of collagen hydrogels varies between  $0.28 \pm 0.16$  Pa and  $23 \pm 3$  Pa, depending on the polymerization temperature (Fig. 2.9).

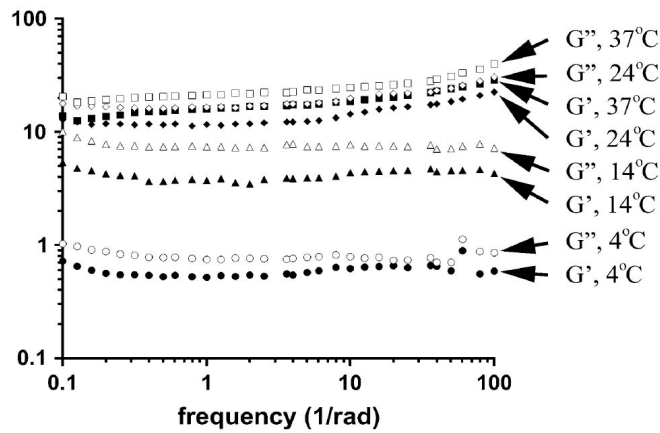


**Figure 2.9.** Representative frequency sweeps of  $G'$  (solid symbols) and  $G''$  (open symbols) for collagen hydrogels at each polymerization temperature (Raub et al., 2007).

## 2.2. Fluid structural interaction model

### 2.2.1. Introduction

When our head experience a movement of rotation, the fluid in the canal lags behind due to its inertia and produces a force across the cupula, deflecting it in the opposite direction of head movement. Therefore, the functioning of the system endolymph/cupula is a typical example of Fluid-Structure Interaction (FSI).

The aim of this section is to model the entire set of semicircular canals by taking into account fluid-structure interactions in order to investigate fluid flow and cupula motion during head rotation. To achieve this goal, we use the finite-element Comsol Multiphysics software as it permits to deal with different physics, and more particularly with FSI problems. The modeling strategy is as follows: first, we model a two-dimensional cross-section of the lateral semicircular canal using geometry and dimensions extracted from measured human data by Curthoys and Oman (1987); second, we extend this 2D model to a three-dimensional model of a single semicircular canal; and third, we develop a fully three-dimensional model by considering the three SCCs.

Before going in depth through the core of the model, we give a brief introduction to fluid-structure interaction problem and Arbitrary Lagrangian-Eulerian (ALE) method which is a common application in engineering used to solve problems pertaining to structure and fluid mechanics analysis. The ALE method employs the use of reference frames to represent the classical Lagrangian and Eulerian systems. The Lagrangian reference frame is used to study the structure problem while the Eulerian reference is used to study the fluid problem.

### 2.2.2. Fluid-structure interaction

Fluid-structure interaction is the interaction of some movable or deformable structure with an internal or surrounding fluid flow. As FSI problems and multiphysics problems in general are often too complex to solve analytically, they have to be analyzed by means of experiments or numerical simulations. Research in the fields of computational fluid dynamics and computational structural dynamics is still ongoing but the maturity of these fields enables numerical simulation of fluid-structure interactions. Typically in FSI, the fluid and solid components are modeled using different techniques to different levels of complexity, ranging from simple analytical solutions to three-dimensional numerical schemes with advanced physical models. Two main approaches exist for the simulation of FSI problems:

- Monolithic approach: the equations governing the flow and the displacement of the structure are solved simultaneously, with a single solver (e.g. Comsol Multiphysics).
- Partitioned approach: the equations governing the flow and the displacement of the structure are solved separately, with two distinct solvers.

The monolithic approach requires a code developed for this particular combination of physical problems whereas the partitioned approach preserves software modularity because an existing flow solver and structural solver are coupled. Although the integration of two software codes is possible in principle, the complexity and size of the software make, however, the partitioned approach quite unattractive. Furthermore, the computational overhead to run such codes is quite exorbitant as information has to pass from one code to the other in each time step, adding to the total overhead. Finally, data transfer for the coupling usually requires an extra program that acts as an interface between the two other codes, thus sacrificing the modularity of the method.

In addition to the range of techniques available for modeling the individual fluid and solid components, there is also the question of exchanging information, typically in the form of boundary conditions, at the interface. Different options can be considered and are classified on the basis of the level of coupling between fluid and solid as follows:

- One-way coupled FSI: in this case, the deformation of the solid is so small that its influence on the fluid flow is negligible. Therefore, only the fluid stresses need to be applied onto the structure and no iteration between the fluid model and the solid model is necessary.
- Two-way (or fully) coupled FSI: in this case, the response of the solid is strongly affected by the response of the fluid, and vice versa. In other words, fluid flow causes deformation of the structure. This deformation, in turn, changes the boundary conditions for the fluid flow.

In the following models, we adopt a monolithic approach – which is implemented in Comsol Multiphysics – and consider a fully coupled method between the solid and fluid. In other words, both fluid and solid equations are solved simultaneously and a two-way data transfer is performed such that the fluid exerts a force on the cupula, while the deformation of the solid affects the geometry of the fluid domain.

### **2.2.3. Arbitrary Lagrangian Eulerian methodology**

The algorithms of continuum mechanics usually make use of two classical description of motion: the Lagrangian description and the Eulerian description. The arbitrary Lagrangian Eulerian method was developed in an attempt to combine the advantages of the above classical kinematical description, while minimizing their respective drawbacks as far as possible.

The Lagrangian reference frame - also called physical coordinate system - is largely used most commonly in solid mechanics. It sets up a reference frame by fixing a grid to the material of interest then as the material deforms the grid deforms with it. Therefore, each individual node of the computational mesh follows the associated material particle during motion (Fig. 2.10b). For instance, a solid structure with little material flexibility uses the Lagrangian approach because as the grid deforms it maps out the deflection of the solid due to some load. The grid would also define the exact displacement of each particle. In this method conservation of mass is automatically satisfied because the individual sections of the grid always contain the same amount of mass. For structure motions with large deformation in

which the grid becomes excessively distorted, the integration time steps become smaller and smaller because they are based on the size of the smallest section of the grid.

The Lagrangian method typically is not the easiest solution for a fluid mechanics problem. The reason is that fluids are not cohesive and so the fluid particles do not stay closely together. So if a grid is mapped out onto a fluid, then no matter how small the initial grid sections the fluid particles will travel independent of each other and diverge in space. This will cause the grid to distort excessively and may overlap each other.

The Eulerian reference frame - also called spatial coordinate system - which is fixed in space, is the typical framework in the analysis of fluid mechanics problem (Fig. 2.10c). It allows for material with specified load or pressure to flow through the grid as it is with the Lagrangian frame, but this time without tracking the path of any of the individual particle. In other words the computational mesh is fixed and the continuum moves with respect to the grid. In order to predict the flow of the fluid across the grid, the Eulerian approach solves the problem by measuring the net flow through a certain area. While in the Lagrangian method conservation of mass is directly, in the Eulerian approach it is taken into account explicitly by measuring the flux in and out of each grid section. In the Eulerian description, large distortions in the continuum motion can be handled with relative ease. However, one of the disadvantages of the Eulerian system is that it does not track the path of any individual particle.

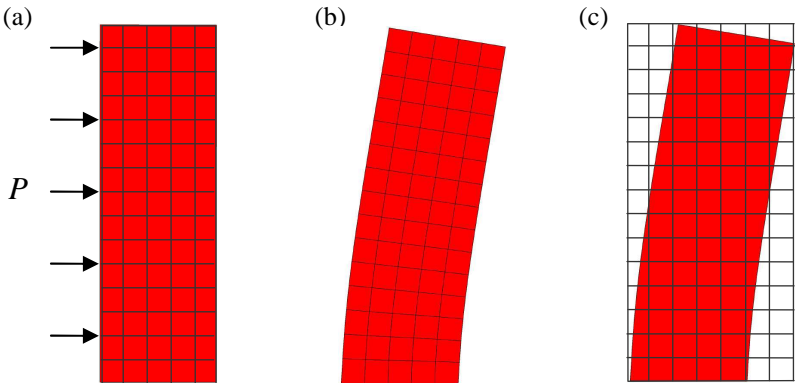


**Figure 2.10.** Comparison Lagrangian and Eulerian descriptions. 2D example of a beam that undergoes a pressure  $P$ . (a) initial grid and material. (b) Lagrangian description: the grid is attached to the material and deforms with it. (c) Eulerian description: the grid is fixed in space.

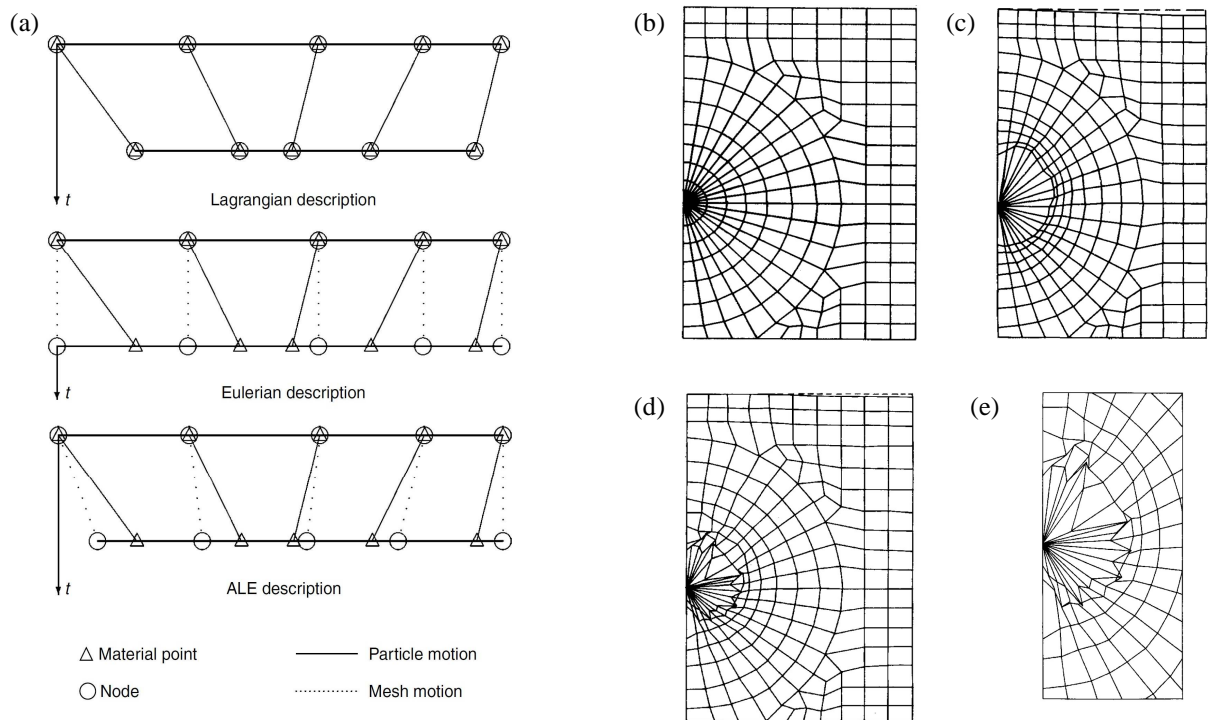


**Figure 2.11.** Comparison Lagrangian, Eulerian, and ALE descriptions. (a) One-dimensional example of Lagrangian, Eulerian and ALE mesh and particle motion. In the Lagrangian description each node of the mesh follows the associated material particle, whereas in the Eulerian description the mesh is fixed. In the ALE description, the nodes may either be moved or be held fixed depending on the distortion of the mesh. (b-e) Mesh used to model the detonation of an explosive charge in an extremely strong cylindrical vessel (from J. Donea et al., 2003). (b) Initial finite-element mesh; (c) ALE mesh at  $t=1$  ms; (d) Lagrangian mesh at  $t=1$  ms; (e) details of interface in Lagrangian description.

Because of the shortcomings of purely Lagrangian and purely Eulerian descriptions, the arbitrary Lagrangian Eulerian technique, which combines the best features of both the Lagrangian and Eulerian approaches, has been developed. In the ALE description, the nodes of the computational mesh may be moved with the continuum in normal Lagrangian fashion, or be held fixed in Eulerian manner, or be moved in some arbitrarily specified way to give a continuous rezoning capability (Fig. 2.11). Because of this freedom in moving the computational mesh offered by the ALE description, greater distortions of the continuum can be handled than would be allowed by a purely Lagrangian method, with more resolution than that afforded by a purely Eulerian approach. The example shown in figure 2.11 (b-e) illustrates the ability of the ALE description to accommodate significant distortions of the computational mesh.

In order to model effectively our FSI problem, we adopt the ALE approach. The corresponding subdomain and boundary conditions for the mesh will be presented later.

## 2.2.4. 2D model

### 2.2.4.1. Geometry of the 2D model



A two-dimensional cross-section of the lateral semicircular canal is modeled. The geometry and all the associated dimensions (Fig. 2.12) are extracted from measured human data by Curthoys and Oman (1987). The canal consists of three main regions: the semicircular canal, the ampulla, and the utricle. The canal is filled of a water-like fluid, known as endolymph. The model also considers the cupula (solid) located in the ampulla which completely seals the canal.

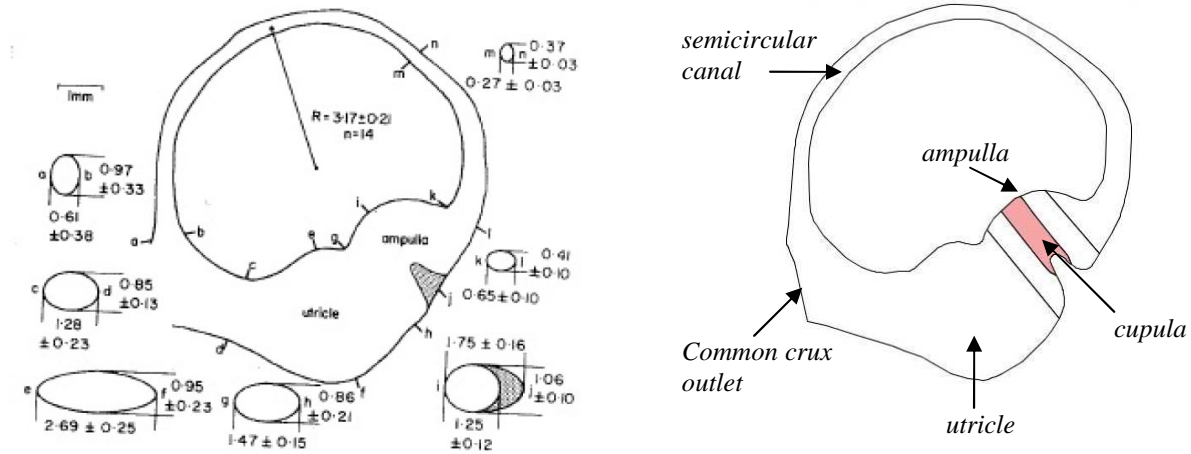


**Figure 2.12.** (Left) Dimensions of the human lateral semicircular canal (Curthoys et al., 1987) and (Right) reconstruction of a 2D model under Comsol Multiphysics. Note that the cupula is modeled by a 400  $\mu\text{m}$  thick section.

### 2.2.4.2. Governing equations

The equations describing the behavior of the cupula, considered as an elastic solid, and of the endolymph, modeled as an incompressible Newtonian fluid, are now presented. Typically, these equations are solved for displacement and for velocity and pressure respectively. This is due to the fact that the stress tensor in solids is defined in terms of displacement while, in fluids in terms of velocity and pressure.

- Fluid flow:

For an incompressible Newtonian fluid, the governing equations of fluid flow are described in terms of the two dimensional Navier-Stokes equations:

$$\rho_f \frac{\partial U_f}{\partial t} + \rho_f (U_f \cdot \nabla) U_f = F + \nabla \cdot \sigma_f \quad (2.12)$$

$$\nabla \cdot U_f = 0 \quad (2.13)$$

The first equation is the momentum transport equation, and the second is the equation of continuity for incompressible fluids. These equations describe how the velocity, pressure, and density of a moving fluid are related. The following variable and parameters appear in the equations:



- $\rho_f$  is the fluid density
- $F$  is the volume force affecting the fluid
- $\sigma_f$  is the stress tensor
- $U_f = (u_f, v_f)$  is the velocity field
- $p$  is the pressure

The Cauchy stress tensor is given by:

$$\sigma_f = -pI + \mu_f (\nabla U_f + (\nabla U_f)^T) = -pI + 2\mu_f \dot{\varepsilon} \quad (2.14)$$

where  $I$  is the unit diagonal matrix,  $\mu_f$  is the dynamic viscosity, and  $\dot{\varepsilon}$  is the rate of deformation tensor. We here assume no gravitation or other volume forces affecting the fluid, thus equation (2.12) can be written as:

$$\rho \frac{\partial U_f}{\partial t} + \rho (U_f \cdot \nabla) U_f - \nabla \left[ -pI + \mu_f (\nabla U_f + (\nabla U_f)^T) \right] = 0 \quad (2.15)$$

The Navier-Stokes equations (2.12) and (2.13) are solved in the spatial (deformed) coordinate system.

- Structural mechanics:

The structural deformations of the cupula are solved using an elastic formulation and a nonlinear geometry formulation to allow large deformations that may occur due to its very low stiffness. Neglecting body forces, the Navier equation of motion for the cupula can be written in terms of displacement vector  $U_s = (u_s, v_s)$  as:

$$\rho_s \frac{\partial^2 U_s}{\partial t^2} = \nabla \cdot \sigma_s \quad (2.16)$$

We consider an elastic isotropic material so that the generalized Hooke's law is obtained:

$$\sigma_s = 2\mu\varepsilon + \lambda \text{tr}(\varepsilon)I \quad (2.17)$$

where  $\mu$  and  $\lambda$  are Lamé's coefficients, which are related to Young's modulus of elasticity and Poisson's ratio  $\nu$ , by the following equations:

$$\mu = \frac{E}{2(1+\nu)} \quad (2.18)$$

$$\lambda = \frac{\nu E}{(1+\nu)(1-2\nu)} \quad (2.19)$$

- Interface fluid-structure

Due to the coupling between fluid and structure, conditions are needed to ensure that the fluid and structural domains will not detach or overlap during the motion (Fig. 2.13). For a viscous fluid, the coupling between fluid and structure requires that velocities coincide along the interface. In particular, the time derivatives of the structural displacements define the fluid's velocity so that:

$$U_f = \frac{dU_s}{dt} \quad (2.20)$$

In addition, the force exerted by the fluid on the solid boundary must be considered and is the negative reaction force on the fluid given by:

$$f = -n \cdot \left( -pI + \eta \left( \nabla u + (\nabla u)^T \right) \right) \quad (2.21)$$

where  $n$  is the outward normal vector to the boundary. This load represents a sum of pressure and viscous forces.

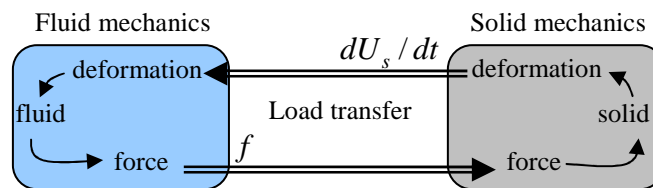


**Figure 2.13.** Concept of fluid-structure interaction (FSI). Load transfer from fluid side: nodal forces. Load transfer from solid side: nodal displacements and velocities.

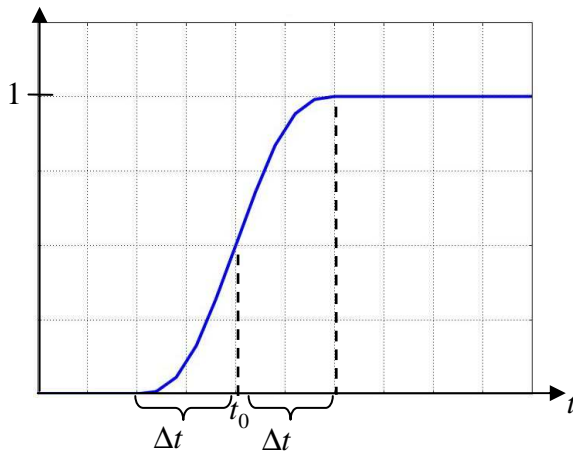
### 2.2.4.3. Boundary conditions

The aim of the model is to simulate a rotation of the head and investigate the dynamics of the fluid flow and cupula motion. In order to impose a constant rotational motion to the structure which starts at  $t = t_0$  and ends at instant  $t = t_1$ , we define the following variables:

Signification	Var. name	Expression
displacement $\bar{x}$	depx	$(X \cos(\omega t) + Y \sin(\omega t) - X) \times flc2hs(t - t_0, \Delta t) \times flc2hs(t_1 - t, \Delta t) + flc2hs(t - t_1, \Delta t) \times (X \cos(\omega t_1) + Y \sin(\omega t_1) - X)$
displacement $\bar{y}$	depy	$(-X \sin(\omega t) + Y \cos(\omega t) - Y) \times flc2hs(t - t_0, \Delta t) \times flc2hs(t_1 - t, \Delta t) + flc2hs(t - t_1, \Delta t) \times (-X \sin(\omega t_1) + Y \cos(\omega t_1) - Y)$
velocity $\bar{\dot{x}}$	vitx	$diff(depx, t)$
velocity $\bar{\dot{y}}$	vity	$diff(depy, t)$

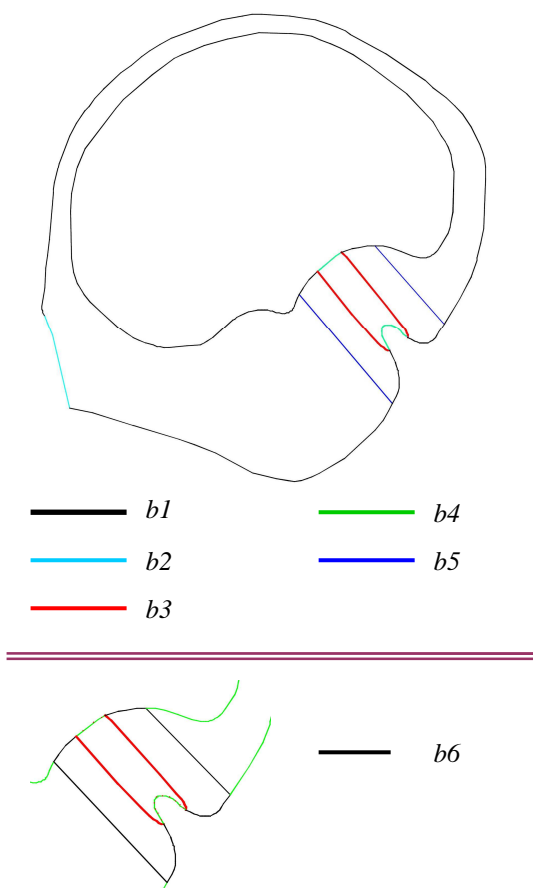
**Table 2.3.** Expression of the prescribed displacements for a head rotation that starts at  $t = t_0$  and ends at  $t = t_1$ .  $(X, Y)$  are the node coordinates in the reference frame,  $\omega$  is the pulsation of rotation,  $t$  is the current time, and  $diff(\dots)$  denotes the derivative operator.

Note that for time-dependent problems, the time-stepping algorithm can run into problem if any condition is imposed with a step function. In order to avoid problems with discontinuity, step functions are usually replaced with a smoothed switch function that emulates steps. Consequently, numerical reliability and convergence are improved. In the present case, we use a smoothed Heaviside function “*flc2hs*” (notation used in Comsol Multiphysics) with a continuous second derivative.



**Figure 2.14.** Smoothed Heaviside function  $flc2hs(t - t_0, \Delta t)$  with a continuous second derivative.

Boundary conditions are summarized in table 2.4.

<p><b>Solid domain</b></p> <ul style="list-style-type: none"> <li>→ b1, b2, b5: inactive boundaries</li> <li>→ b4: prescribed displacement (dep<sub>x</sub>, dep<sub>y</sub>)</li> <li>→ b3: fluid load <math>f</math></li> </ul> <p><b>Fluid domain</b></p> <ul style="list-style-type: none"> <li>→ b4, b5: inactive boundaries</li> <li>→ b1: imposed velocity (vit<sub>x</sub>, vit<sub>y</sub>). Consequently, the fluid at the wall of the canal rotates at the same velocity of the canal. This is locally equivalent as a no-slip condition.</li> <li>→ b2: open boundary so the nodal velocities are left free to accommodate inflow and outflow of endolymph between the LSCC and the other canals.</li> <li>→ b3: velocity of the cupula (<math>\dot{u}_s, \dot{v}_s</math>)</li> </ul> <p><b>ALE mesh</b></p> <ul style="list-style-type: none"> <li>→ b6: prescribed displacement (dep<sub>x</sub>, dep<sub>y</sub>)</li> <li>→ all other boundaries are inactive</li> </ul>	
---	---

**Table 2.4.** Boundary conditions of the two-dimensional finite-element model of the horizontal semicircular canal.

#### 2.2.4.4. Moving mesh

In order to model effectively the FSI problem, the moving mesh (ALE) approach is used to solve two problems; the fluid problem (i.e. the motion of the endolymph) and the structure problem (i.e. the movement of the cupula). Hence, the model combines the fluid flow with structural mechanics by using a moving mesh to make sure the fluid flow is deformed along with the cupula.

The model is divided into different parts so as to specify how the mesh displacement is computed in each subdomain (Fig. 2.15). The imposed conditions of mesh displacement are as follows:

- *Solid domain (cupula)*: the displacements ( $u_s, v_s$ ) provided by the computation of the structure mechanics equations are imposed. In other words, a Lagrangian method is used where the mesh movement follows the material motion.
- *Fluid domain near the cupula*: as cupula deformation may affect fluid flow in its vicinity we define a subdomain around the cupula where the mesh is free to move.

This means that the mesh is constrained only by the boundary conditions on the surrounding boundaries. The displacement in this subdomain is obtained by solving a PDE defined by a smoothing method, which is in the present case the “Winslow smoothing”. This equation smoothly deforms the mesh given the constraints on its boundaries.

- *Rest of the fluid domain:* the displacement of rotation imposed to the whole structure is also applied to this subdomain. In other words, the mesh is not deformed and follows the rotation of the canal.

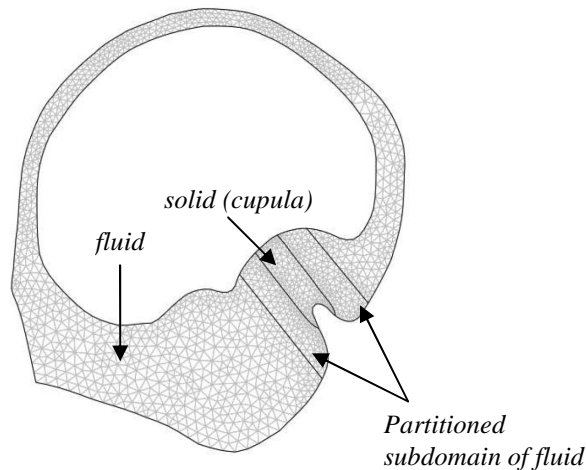


**Figure 2.15.** Visualization of the subdomains that have different conditions for mesh displacement.

#### 2.2.4.5. Simulations

Numerical solutions of the governing system of coupled nonlinear system partial differential equations (PDEs) are generated using finite-element analysis software (Comsol Multiphysics 3.5a). This PDEs system contains both dynamic PDEs (with time derivatives) and stationary PDEs (without time derivatives). Therefore the corresponding space-discretized system is a differential-algebraic equations (DAE) system, which means that it includes both differential and algebraic equations. For instance, the incompressible Navier-Stokes equations give rise to a DAE system when discretizing the space because the equation of continuity turns into an algebraic relationship. A system of DAEs implies some constraints on the initial values, for instance, that an algebraic equation must be satisfied. Typically, the solver perturbs the given initial values so that they become consistent with these constraints. In the present case, we use the implicit backward Euler method so as the solver perturbs the initial values of all degrees of freedom by taking a backward Euler step, giving a small perturbation to the differential degrees of freedom.

Two different cases of simulation are considered:

- the center of the canal is located on the axis of rotation (case 1)
- the center of the canal is located 30 mm away from the axis of rotation (case 2)

For each simulation, a constant angular velocity of  $\pi/2$  rad/s that mimics a constant head rotation is applied during 15 s (Fig. 2.16). The computation is performed till  $t = 30$  s in order to investigate the fluid dynamics and cupula motion after the deceleration phase.

All the results were generated on a 2D mesh with 2663 quadratics triangular elements that represent 16985 degrees of freedom. According to the results of section, we consider a Young's modulus for the cupula of 5 Pa and a Poisson's ratio of 0.48.

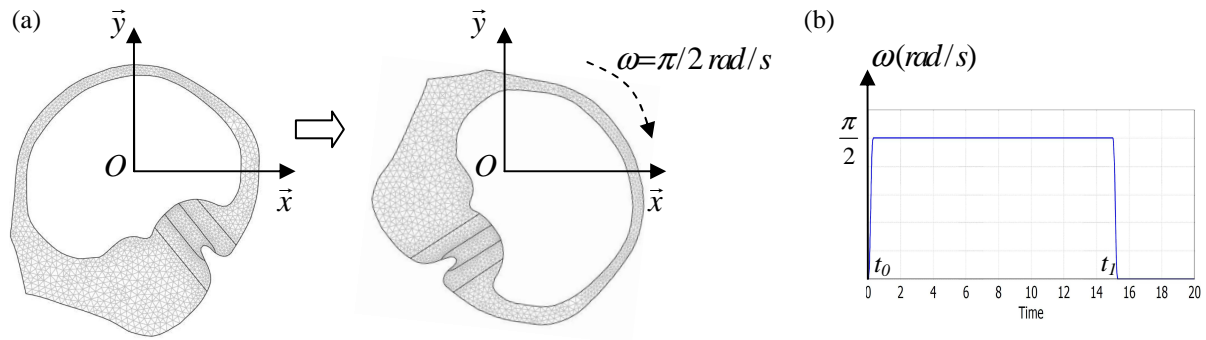


**Figure 2.16.** Rotational motion applied to the semicircular canal. (a) Moving mesh. (b) Profile of angular velocity applied to the structure.

### Case 1: Semicircular canal located at the center of the head.

- Cupula displacement at the very beginning of the imposed rotational motion:

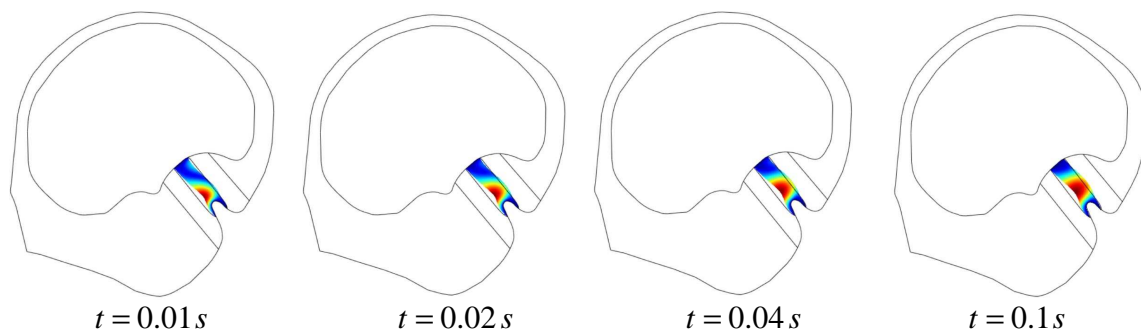


**Figure 2.17.** Evolution of the displacement of the cupula at the very beginning of the imposed rotational motion. The displacement of the cupula begins near the sensory epithelium and then spreads towards the center of the cupula.

The displacement of the cupula is shown in figure 2.17. It can be observed that displacement begins close to the crista, which suggests that initial movements of the cupula produce a shear type deformation right above the sensory epithelium. Thus, sensory hair cells are presumably stimulated as soon as head motion starts. After a certain limit is reached, about 0.1 s, maximal displacement spreads toward the center of the cupula. This behavior is consistent with previous studies of McLaren (1977) who measured the positions of oil droplets, which were injected in the cupula of the bullfrog, following the compression of the canal wall.

- Fluid flow in the slender part of the canal at the very beginning of the rotation:

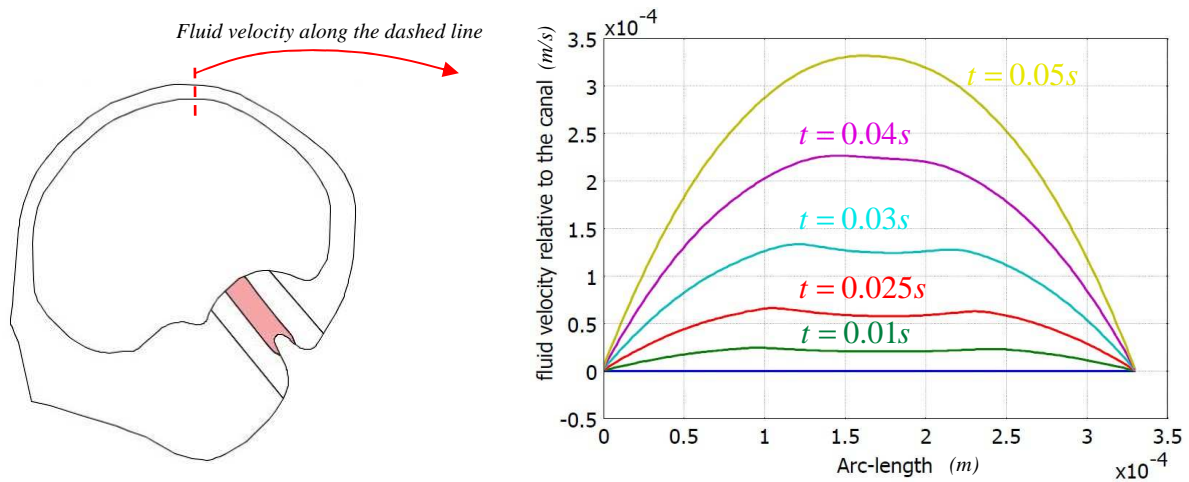


**Figure 2.18.** Evolution of the velocity of the fluid in the slender part of the duct at the beginning of the rotational motion.

Velocity profiles of the fluid flow in the slender part of the canal are plotted in figure 2.18. We see that in about 0.04 s – 0.05 s the fluid flow is analogous to a Poiseuille flow. Indeed, the velocity profile tends to a parabola, with the fluid in the center of the canal having the greatest speed. This result is consistent with previous analytical studies. For instance, Groen (1952) assumed a fully developed Poiseuille flow in a straight tube to investigate the dynamics of semicircular canal flow and cupula motion, while Van Buskirk et al. (1976) shown that endolymph volume displacement resulting from a step change in angular velocity under the non-steady state flow assumption can be approximate by the Poiseuille steady-state flow relation.

- Fluid flow in the canal and cupula motion

At the beginning of the rotation of the canal, the fluid lags behind due to its inertia. Therefore, fluid flow relative to the wall of the canal is oriented in the opposite direction of the imposed rotational motion during about 0.25 s (Fig. 2.19). Meanwhile, this flow, represented by the arrows in figure 2.19, exerts a pressure across the cupula, and thus deflects it in the opposite direction of rotation as well. The deflection of the cupula reaches a maximum value close to 15  $\mu\text{m}$  for the set of elastic properties retained. At time  $t=0.3$  s, even though the canal still experiences a rotational motion, the cupula starts to return to its rest position due to its elastic properties. In addition, because of the small diameter of the duct and the viscosity of the fluid, the latter tends to catch up with the rotation of the canal, eliminating little by little the relative movement between the fluid and the canal. One can notice that the maximum fluid velocity is decreased by a factor 20 between time instants 0.3 s and 0.6 s.

The canal experiences a constant angular velocity until  $t=15$  s, and then the movement of rotation is stopped in 0.3 s. At time  $t=15.1$  s, the fluid is still in motion within the canal due to its inertia. As a consequence, the cupula, which was returned to its rest position, is deflected in the opposite direction than previously (Fig. 2.20). Once again, we can note that cupula deflection starts near the sensory epithelium and then spread toward its center (Fig. 2.20). Finally, the cupula returns to its initial position which provokes a slight counter clockwise fluid flow.

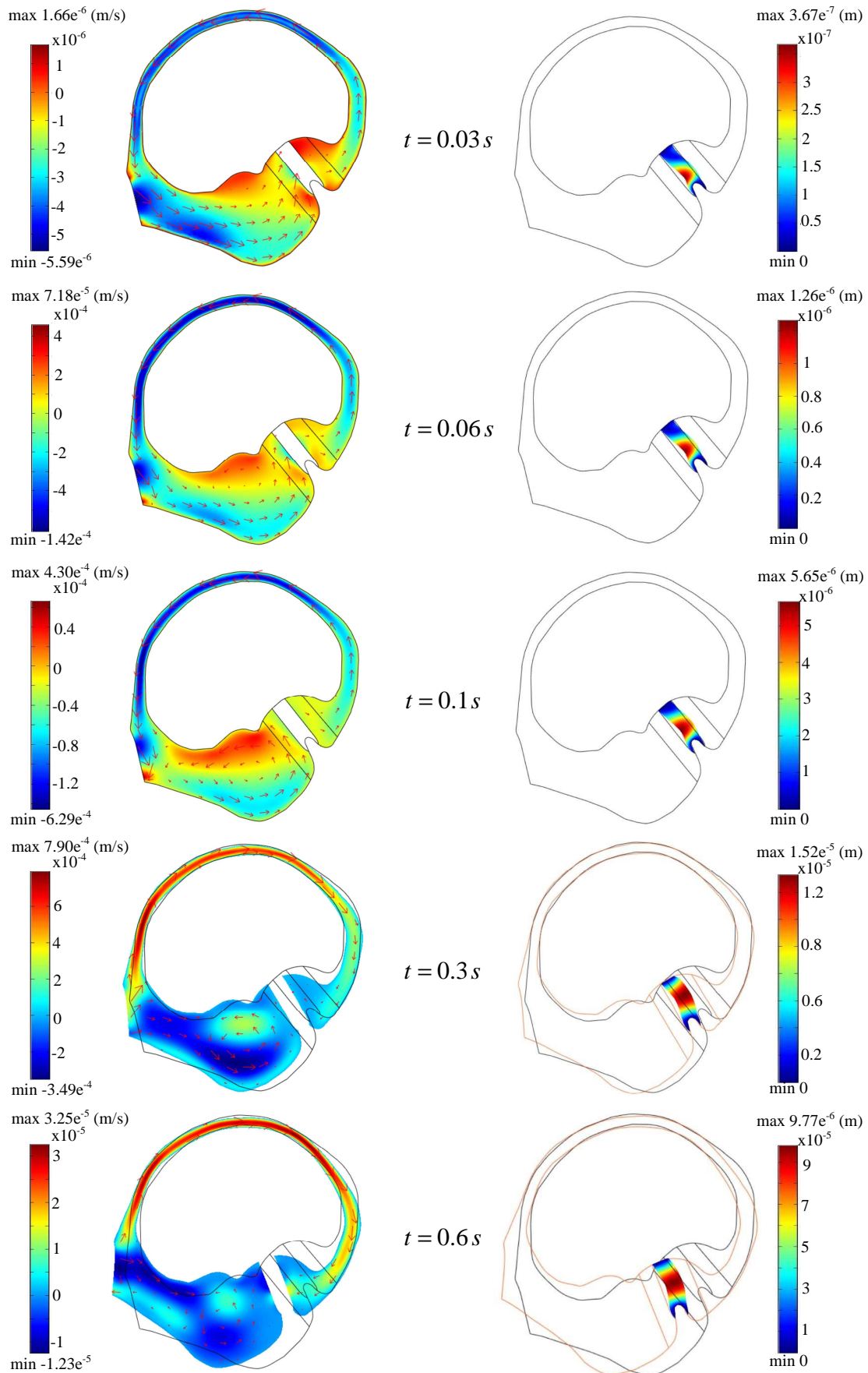


**Figure 2.19.** Fluid velocity (left) and cupula displacement (right) at the beginning of the rotation. Visualization in the ALE reference frame (moving mesh).



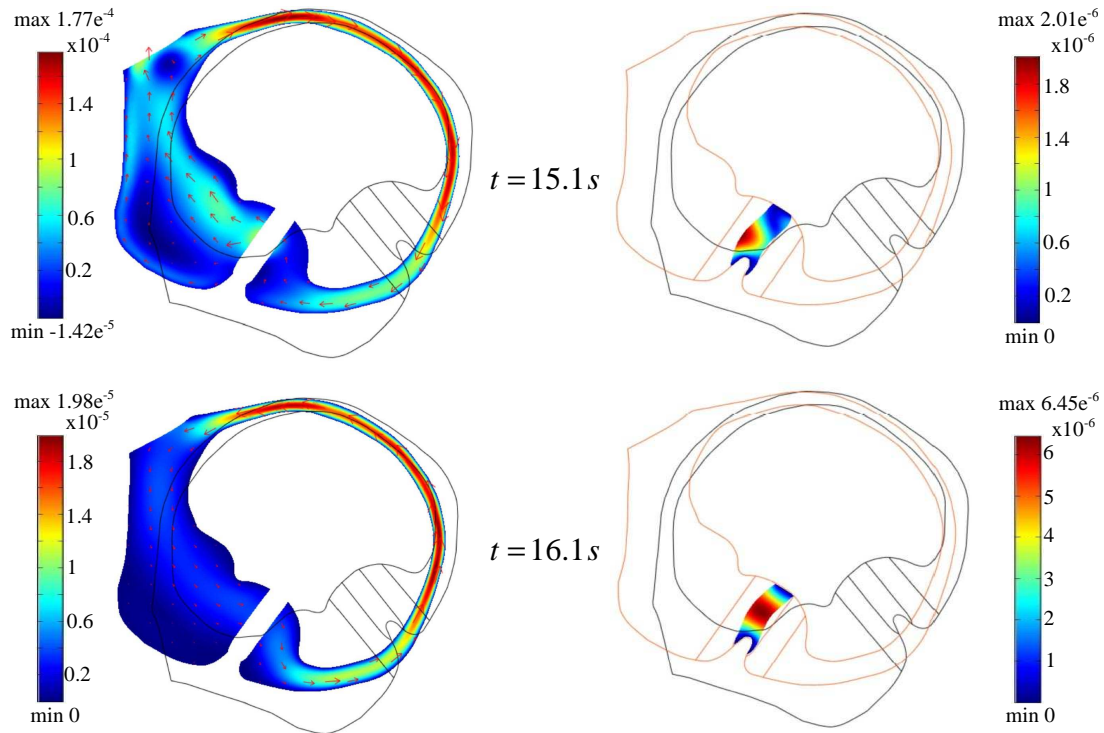


**Figure 2.20.** Fluid velocity (left) and cupula displacement (right) at the end of the rotation. Visualization in the ALE reference frame (moving mesh).

Figure 2.21 shows the time-dependent displacement of a point located at the center of the cupula. It can be seen that the cupula experiences two deflections in opposite directions that are due to the acceleration and deceleration phase of the motion.

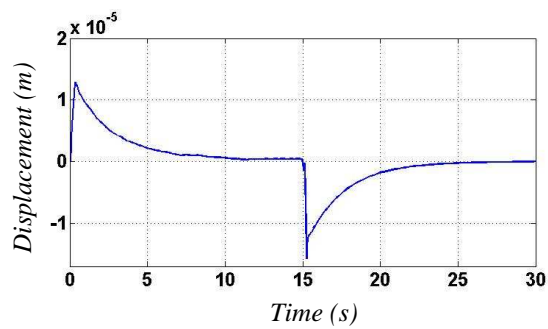


**Figure 2.21.** Displacement of the center of the cupula during a constant angular rotation which ends at time  $t=15$  s.

## Case 2: Semicircular canal located 30 mm away from the axis of rotation

The same simulation as previously is performed with the canal located 30 mm away from the axis of rotation. The behaviors of the cupula and of the fluid flow within the canal are similar to the centered canal model (Fig. 2.22). Figure 2.22 presents cupula motion and fluid flow at different instants. Following a deflection due to the angular acceleration of the canal, the cupula returns to its rest position through time. As regard the fluid flow, it is oriented clockwise because at time  $t=2$  s it has already caught up with the rotation of the canal.

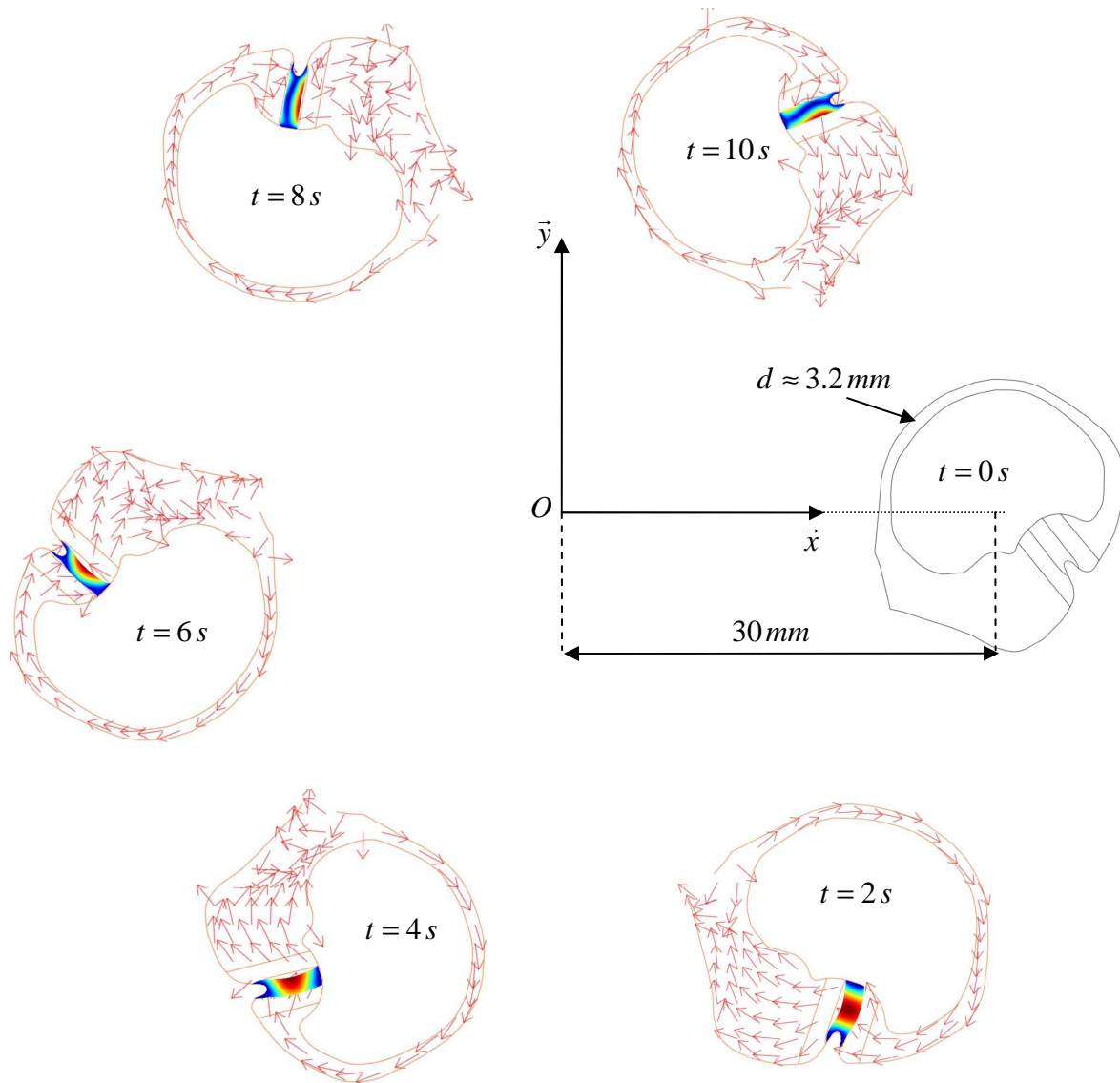


**Figure 2.22.** Rotation of the canal located 30 mm away from the axis of rotation (the physical scale is not respected). The arrows are oriented along the fluid flow.

## 2.2.5. Three-dimensional model of a single canal

Before modeling the entire set of semicircular canals, we have extended the previous 2D model to three-dimensional space. Once again, we have used dimensions and shape of the various cross sections provided by Curthoys and Oman (1987). Besides drawing a complex geometric model with the computer-aided design (CAD) tools built into Comsol Multiphysics, an alternative is to create it with a specialized and more appropriate CAD software application and save it to a file that can be, in turn, imported into Comsol Multiphysics. In the present case, we have chosen to develop the 3D canal under CATIA V5 (Fig. 2.23a). Then, the resulting geometry has been exported into a STEP file format, which is one of the most popular types of file used to exchange geometric models among CAD software applications. Finally, this STEP file, which contains the mathematical description of the object, has been imported into Comsol Multiphysics thanks to its CAD import module so as to perform the meshing (Fig. 2.23b) and run the simulations.

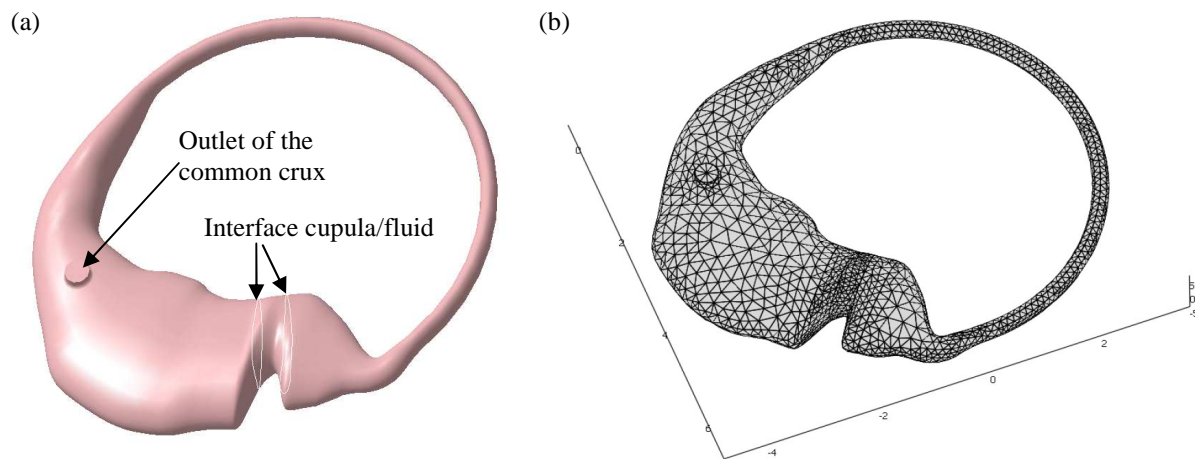


**Figure 2.23.** Visualization of a three-dimensional single canal. (a) CAD model under CATIA V5. (b) Tetrahedral mesh of the canal performed under Comsol Multiphysics.

As regard the simulation, we have only considered a rotation of the structure around a vertical axis passing through the center of the canal. Obviously, the size of the model is much higher than the two-dimensional version. The mesh is comprised of 15 408 quadratic tetrahedral elements that represent 133 112 degrees of freedom.

As one might expect, the solution provided by this 3D model is similar to the 2D model results previously computed (Fig. 2.24). Therefore, we only show few figures related to fluid velocity and cupula displacement. As already mentioned, at time instant 0.03 s the fluid lags behind due to its inertia. Therefore, fluid flow relative to the wall of the canal is oriented in the opposite direction of the imposed rotational motion which deflects the cupula. We can note that the maximum velocity of fluid flow is close to  $2.1 \mu\text{m/s}$  while the 2D model predicts a maximum value of  $1.6 \mu\text{m/s}$ . As regard cupula displacement, a maximum value of  $0.37 \mu\text{m}$  and  $0.44 \mu\text{m}$  are predicted by the 2D and 3D model, respectively (difference of about 20 %).

Due to the constant angular velocity applied to the canal and the elastic properties of the cupula, the latter returns to its rest position through time. At time instant  $t=1$  s, the maximum

displacement of the cupula is about  $1.7 \mu\text{m}$ . We can also observe that the fluid flow is oriented in the same direction as the imposed movement of rotation for the same reasons mentioned previously.

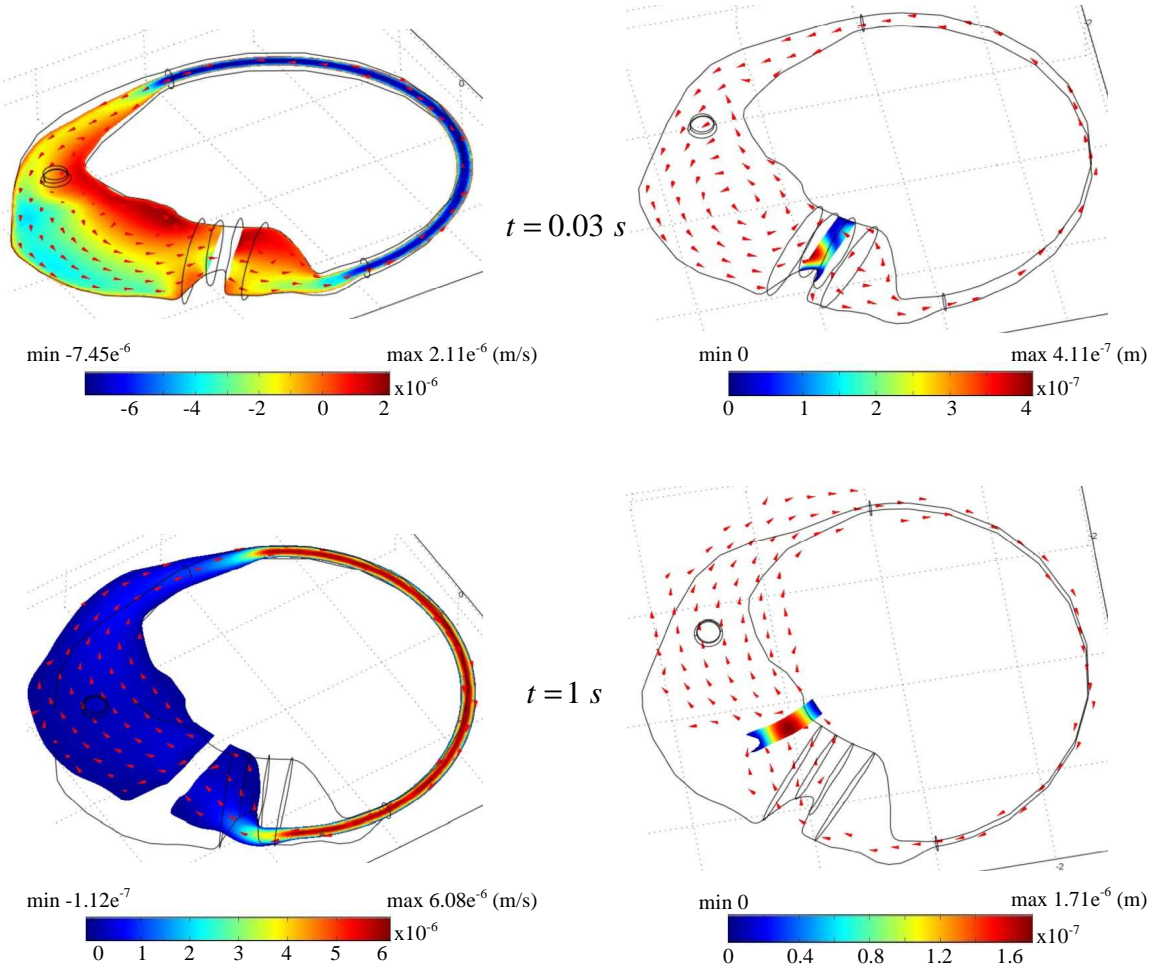


**Figure 2.24.** Fluid velocity in m/s (left) and cupula displacement in m (right) at time instant  $t=0.03 \text{ s}$  and  $t=1 \text{ s}$ . The fields of fluid velocity and cupula displacement are plotted on a cross-section of the 3D model located at the coordinate  $z = 0$  (midplane). Visualization in the ALE reference frame (moving mesh). The arrows are oriented along the fluid flow.

### 2.2.6. 3D model of the entire set of canals

The modeling of the entire set of semicircular canals + cupulae + utricle is now considered. As the previous 3D model, the geometry has been developed with the CAD software CATIA V5 and then has been imported into Comsol Multiphysics (Fig. 2.25). Dimensions of the vertical canals have been taken identical as the horizontal canal, and all the canals are assumed orthogonal.

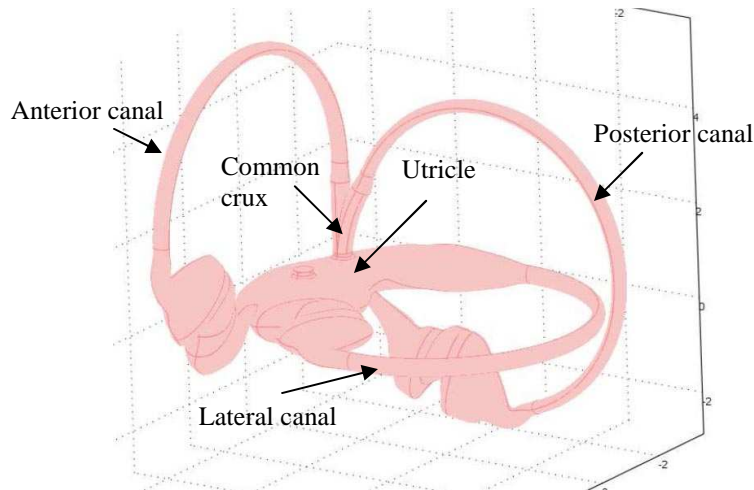


**Figure 2.25.** Three-dimensional CAD model of the three SCCs + utricle + cupulae.

Obviously the mesh of this model is much more complicated than the previous 3D model of a single canal because the connections between each canals and the utricle has to be meshed finely. The mesh is comprised of 45,408 quadratic tetrahedral elements that represent 498,112 degrees of freedom (Fig. 2.26).

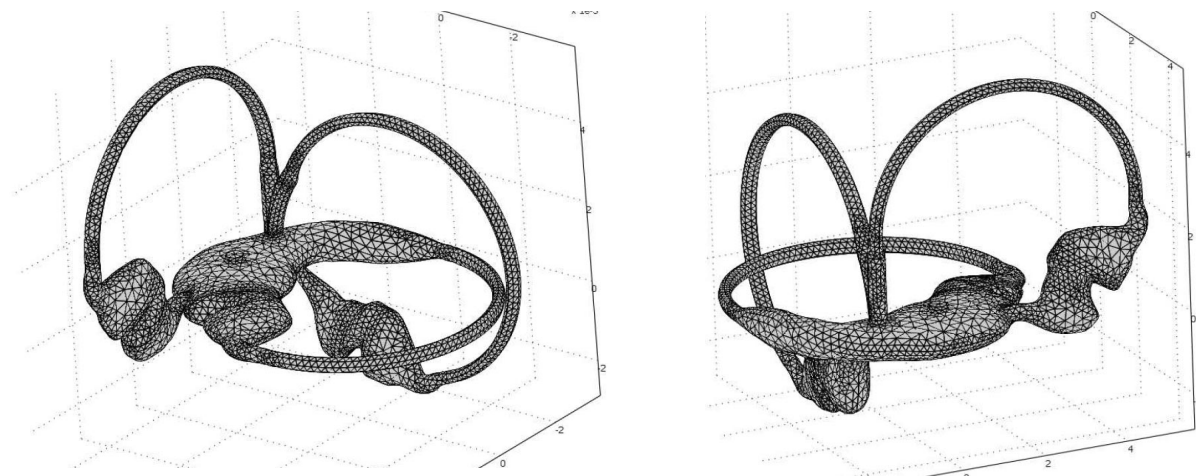


**Figure 2.26.** Mesh of the final three-dimensional model which consists of 45,408 quadratics elements representing 498,112 degrees of freedom.

The number of degrees of freedom (DOFs) conditioned the size of the model in terms of required computational resource, in particular Random-access memory (RAM). If the numbers of DOFs is very high so that the model requires a RAM quantity higher than that available in the computer, then the operating system is going to swap. Swapping is a useful technique that enables a computer to execute programs and manipulate data files larger than main memory. The operating system copies as much data as possible into main memory, and leaves the rest on the disk. When the operating system needs data from the disk, it exchanges a portion of data in main memory with a portion of data on the disk. In other words, if the size of the model is too high, the operating system will continuously exchange data between main memory and the disk, and computation time of the model will blow up. Therefore we have to make sure that memory required by the model is lower or at least equal to the available RAM. However, the size of the mesh also conditioned the accuracy of the solution. For instance, if the mesh is too coarse we may encounter problems of convergence of the solution because of inverted mesh. Thus, the model must be meshed as fine as possible as long as the available memory is sufficient.

In the present case, simulations of the model are run on a computer having two dual-core processors, 8Go RAM, and a 64-bit linux operating system. The available main memory implies a maximum number of DOFs close to 300,000.

Unfortunately, by running the model for a constant head angular velocity we encountered problems of convergence a time  $t=1.8s$  because of inverted mesh, which is probably due to the fact that the mesh was not fine enough. However, results of the simulation are promising as the overall behavior of the model at the beginning of the imposed rotation is similar to that of the models previously presented. Figure 2.27 shows displacement of the cupulae and fluid velocity at time  $t=0.1$  s and  $t=0.3s$ . At time  $t=0.1s$ , the fluid flow is in the opposite direction of the imposed clockwise rotational motion. The cupula of the lateral is thus deflected. Note that cupula of the anterior canal also experiences a slight deflection due to the gravity field. Cupula of the posterior canal remains at its rest position as there is no fluid flow within this canal and as this cupula is almost aligned with the gravity vector. At time  $t=0.3$  s, fluid flow catches up with the rotation of the canal eliminating little by little the relative motion between endolymph and canal walls.



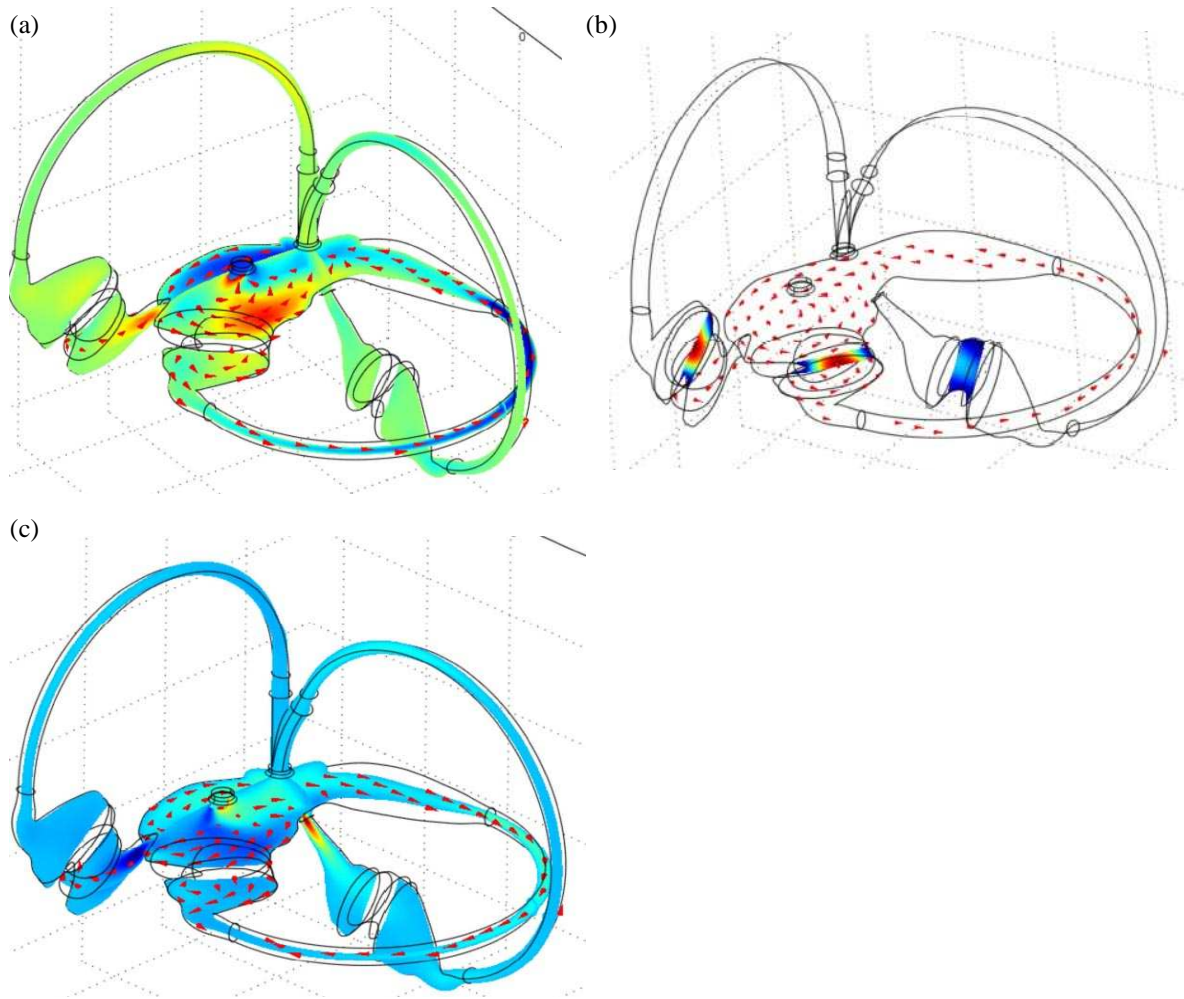


**Figure 2.27.** Results provided by the simulation of the final 3D model of the semicircular canals. (a) Field of fluid velocity at time  $t=0.1s$ . (b) Field of cupulae displacement at time  $t=0.1s$ . The cupula of the lateral canal is deflected because of the imposed motion of rotation of the canals. The cupula of the anterior canal is slightly deflected at the beginning of the simulation because of the gravitational field. Note that cupula of the posterior canal does not experience any deflection as there is no fluid flow within this canal and as this cupula is almost aligned with the gravity vector. (c) Field of fluid velocity at time  $t=0.3s$ .

# Chapter III: Virtual reality model

## 3.1. Virtual reality model

### 3.1.1. Introduction

As we move in our surrounding environment, our vestibular systems constantly provide information to the brain regarding our head's orientation and acceleration in space. As described in the background section, head angular motion induces cupula deflection which in turn provokes the bending of sensory hair cells bundles, and thus involves a stimulus on the semicircular canals' afferent nerve fibers. In the same way, both head linear acceleration and head tilts cause a displacement of the otolithic membrane relative to its sensory base, provoking bending of hair cell cilia that generates signal on the otolith afferent nerve fibers.

The way each cupula and otolithic membrane behaves for any angular or linear acceleration is, however, not obvious, especially for complex head motion. Therefore, a virtual reality model of the vestibular sensors is designed in our work. The primary advantage of this model is that it can be used as a demonstrating and learning tool as the theoretical state of each sensor can be observed in real time. As a result, it offers the possibility to get a better overall understanding of the vestibular apparatus.

This numerical model, developed in Matlab/Simulink, takes into account both the angular and linear sensors. However, the three-dimensional animation only considers the semicircular canals. While a previous model considered a head centered vestibular system (Adenot, 2002), we here assume that the sensors are located 30 mm away from the head vertical axis. Consequently, during any rotational head movement, the otolith organs experience both tangential and normal acceleration components.

As a practical demonstration, the model simulates the rotating chair test which is one of the procedures usually performed by specialists during a diagnosis of the vestibular system. Basically, this experiment consists of strapping the patient onto a rotating chair, applying different rotational motion profiles (trapezoidal, sinusoidal, etc), and recording - using two miniaturized infrared cameras mounted in a mask - an ocular reflex, which is the consequence of the stimulation of his vestibular systems, so as to detect any vestibular deficiencies. In order to simulate this experience and to compute numerically the state of each sensor, the model follows different steps (Fig. 3.1). First, it resolves the equations of motion in three distinct reference frames: earth, chair, and head coordinate system. Second, it computes the angular acceleration vectors projected on each canal axis and the linear acceleration vectors projected on the surface of the otolith organs. Third, the displacement of each sensor is derived using their transfer function. Fourth, these data, which constitute the inputs of the virtual scene, are transferred to the virtual model. Note that a Graphical User Interface (GUI) has been developed in order to simplify the use of this model.



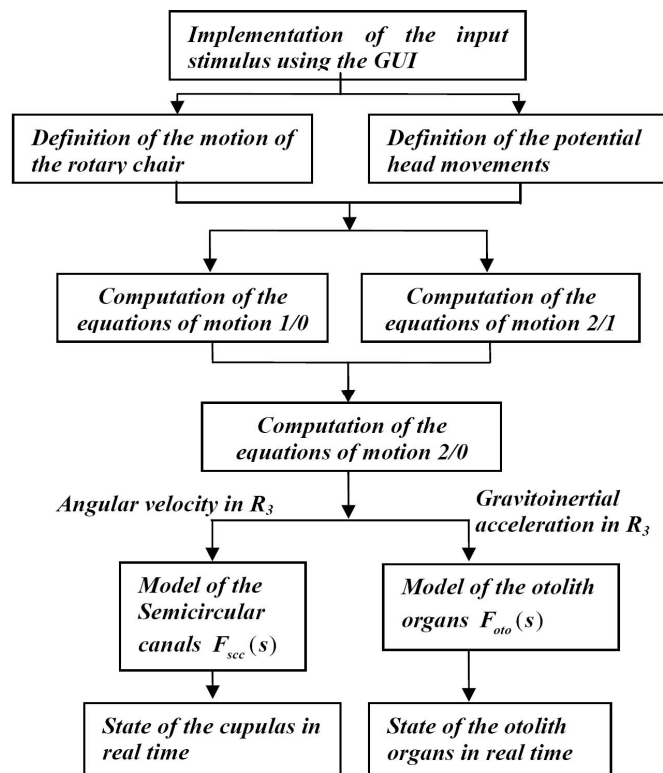


**Figure 3.1.** Schematic block diagram of the virtual reality model simulink model. The computation of the model is divided in several steps. First, the user implements the motions. Then, as soon as the simulation is run, 1) equations of motion are solved; 2) angular velocity and gravitoinertial acceleration are applied to the sensors models; 3) the state of each sensor is determined in real time.

The model is based on different assumptions:

- the orientation of the semicircular canals is derived according to a recent study performed by Della Santina (2005)
- the utricle has an elevation of  $30^\circ$  from the horizontal plane
- the saccule is assumed vertical
- a semicircular canal is normally excited by rotation in the plane of the canal
- the response to simultaneous canal stimuli is approximately the vector sum of the responses to each stimulus alone
- the canals are totally uncoupled
- the utricle is stimulated by horizontal components of gravito-inertial forces, whereas the saccule senses the vertical component.

### 3.1.2. Formulation of the kinematic problem

The different coordinate frames are defined as follows (Fig. 3.2b):

- $R_0$ :  $(O, \vec{X}_0, \vec{Y}_0, \vec{Z}_0)$  fixed orthogonal coordinate system
- $R_1$ :  $(O, \vec{X}_1, \vec{Y}_1, \vec{Z}_1)$  orthogonal coordinate system attached to the rotating chair

- $R_2: (A, \vec{X}_2, \vec{Y}_2, \vec{Z}_2)$  orthogonal coordinate system attached to the head
- $R_3: (B, \vec{X}_3, \vec{Y}_3, \vec{Z}_3)$  non-orthogonal coordinate system defined by the 3 perpendiculars of the semicircular canals

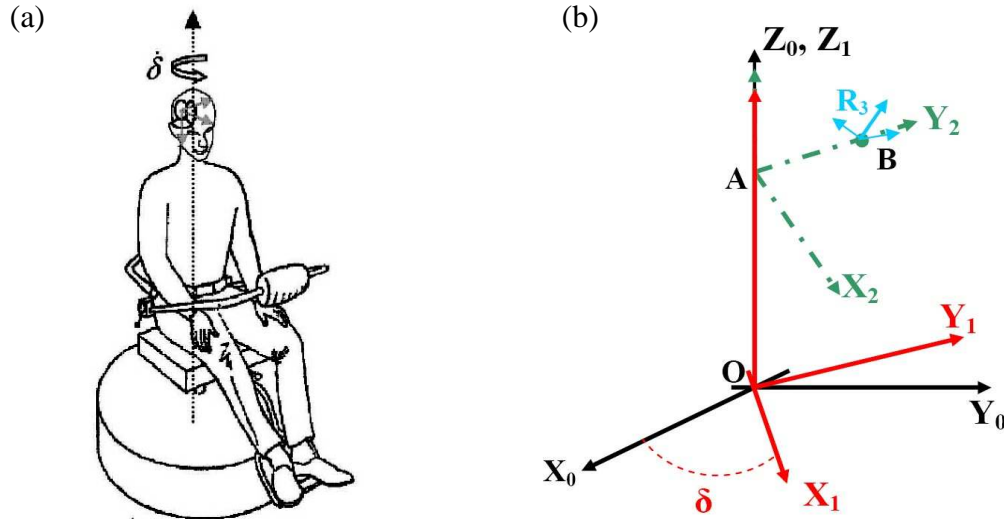


**Figure 3.2.** (a) Visualization of the diagnosis procedure, (b) Different coordinate systems :  $R_0: (O, \vec{X}_0, \vec{Y}_0, \vec{Z}_0)$  fixed orthogonal coordinate system,  $R_1: (O, \vec{X}_1, \vec{Y}_1, \vec{Z}_1)$  orthogonal coordinate system attached to the rotating chair,  $R_2: (A, \vec{X}_2, \vec{Y}_2, \vec{Z}_2)$  orthogonal coordinate system attached to the head,  $R_3: (B, \vec{X}_3, \vec{Y}_3, \vec{Z}_3)$  non-orthogonal coordinate system defined by the 3 perpendiculars of the semicircular canals.

During the experiment, the head of the patient is usually kept fixed so as to investigate his lateral semicircular canals. However it is interesting to have the possibility to simulate head rotations during the imposed chair motion. First, this would imply the stimulation of the vertical canals. Second, head-movements in a rotating environment create Coriolis cross-coupled stimuli that introduce problematic vestibular response. This phenomenon has been the topic of many researches. In particular, in order to prevent the serious deconditioning associated with prolonged exposure to weightlessness, scientists suggested using short-radius centrifugation in order to create artificial gravity. Unfortunately, out-of-plane head-turns on a centrifuge provoke unexpected illusory sensations of motion. As the present model permits to simulate any head rotations in a rotating environment, it can simply be extended to the case of a centrifuge experiment by modifying the position of the head coordinate frame from the axis of rotation.

For clarity purpose, the head movements of the subject are named (Fig. 3.3):

- pitch movement: for a head tilt toward the shoulders
- roll movement: for a downward or upward head rotation
- yaw movement: for a head rotation to the left or to the right.

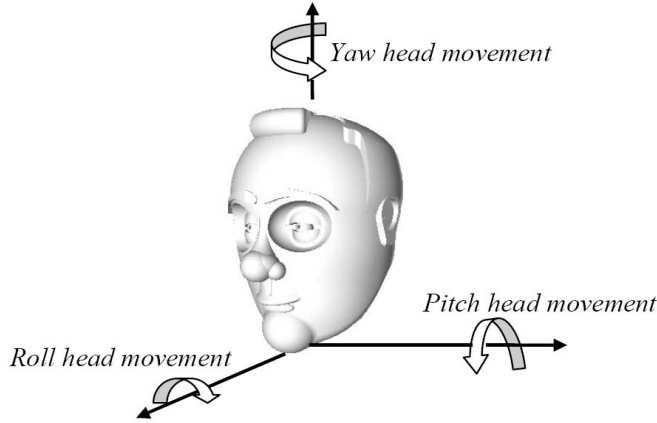
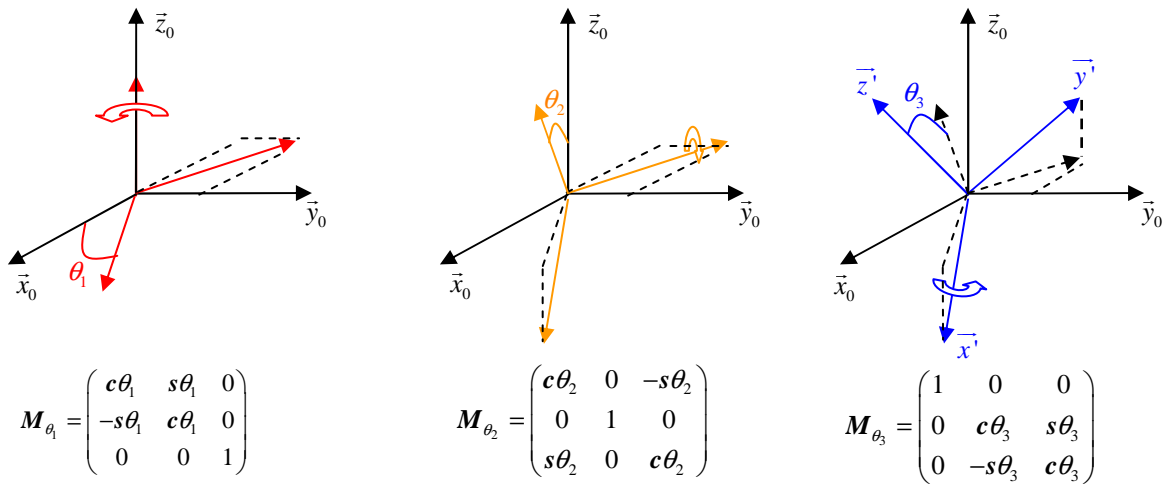


**Figure 3.3.** Definition of head movements: pitch, roll, and yaw.

### 3.1.2.1. Rotation of reference frames

The angular orientation of the reference frame is described by the Euler angle. This method involves successive rotation about the principle axes, and has a solid link with the intuitive notions of roll, pitch, and yaw. Needless to say, there are many valid Euler angle rotation sets possible to reach a given orientation. We consider here the sequence of yaw, pitch, and roll rotation that transforms the original coordinate frame into an arbitrary orientation.



The axes of the transformed coordinate frame  $R'$  are defined by the following matrix

multiplication: 
$$\begin{pmatrix} \bar{x}' \\ \bar{y}' \\ \bar{z}' \end{pmatrix} = M_{\theta_3} M_{\theta_2} M_{\theta_1} \begin{pmatrix} \bar{x}_0 \\ \bar{y}_0 \\ \bar{z}_0 \end{pmatrix} \quad (3.1)$$

### 3.1.2.2. Orientation of the SCC coordinate system

The model takes into account a coordinate frame attached to the SCC in which the components of angular acceleration will be projected. This coordinate system is defined by the normal of each canal plane  $\bar{n}_l$ ,  $\bar{n}_a$ ,  $\bar{n}_p$  (lateral, anterior and posterior respectively). The

problem that arises is to know accurately the absolute orientation of these perpendiculars with respect to the head coordinate frame. Apart from a widely cited study of 10 human skulls by Blanks et al. (1975, Curthoys et al. 1977), majority of the studies of human labyrinth morphology have related SCC orientations to accessible skull landmarks. Indeed, most of the studies have dealt with inter-SCC angles of isolated human labyrinths using high-resolution radiographic reconstructions (Archer et al. 1988, Tagaki et al. 1989, Harada et al. 1990, Hashimoto et al. 2003). In addition, Blanks et al. concluded that the horizontal and anterior SCC are not mutually orthogonal ( $111 \pm 7.6^\circ$ ) while multiple studies of isolated labyrinths have shown the inter-SCC angles are close to  $90^\circ$ . As noted by Della Santina et al., this difference is probably due to the small number of skull samples that Blanks et al. have considered. Therefore, in order to unify all the values proposed in the literature and to provide accurate data of orientation and position of SCC, Della Santina et al. have measured SCC orientations with respect to accessible skull landmarks using three-dimensional multiplanar reconstructions of high-resolution computed tomography scans of 44 labyrinths in 22 human subjects. They concluded that the angle between the anterior and posterior SCC is  $94.0 \pm 4.0^\circ$ , that the angle between the anterior and horizontal SCC is  $90.6 \pm 6.2^\circ$ , and that the angle between the horizontal and posterior canal is  $90.4 \pm 4.9^\circ$ . These angles are considered in the present model.

These values clearly show that the canals do not define an orthogonal coordinate system. In a physical sense that means if the head turn around the normal of one canal plane, not only this canal but the others will be stimulated. Thus, for any rotation of the head all the angular sensors should provide a stimulus. A vector defined in  $R_2$  is projected into the coordinate system  $R_3$  attached to the canals with the transformation matrix:

$$\mathbf{M} = \mathbf{M}_\varphi \mathbf{M}_\theta \mathbf{M}_\psi = \begin{pmatrix} c\theta_a c\psi_a & c\theta_a s\psi_a & -s\theta_a \\ -c\varphi_p s\psi_p & c\varphi_p c\psi_p & s\varphi_p \\ c\varphi_l s\theta_l & -s\varphi_l & c\varphi_l c\theta_l \end{pmatrix} \text{ with } c = \cos, s = \sin.$$

where  $\theta, \psi,$  and  $\varphi$  are the Euler angles defining the normal of each canal plane (lateral, posterior, anterior).

### 3.1.2.3. Expression of the angular velocity vectors

*Convention for notations:*

The symbol  $\overline{\omega_{i/j}}$  represents the angular velocity of a body moving in frame  $i$  as seen in frame  $j$ . Correspondingly  $\overline{\dot{\omega}_{i/j}}$ ,  $\overline{V_{B_i/j}}$ , and  $\overline{A_{B_i/j}}$  represent the angular acceleration, linear velocity, and linear acceleration of a body moving frame  $i$  as seen in frame  $j$ , respectively.

- Head / Chair

Head movements are separated into three non-simultaneous distinct motions:

- Case 1: yaw motion defined by the angle  $\gamma$ , so that  $\overline{\omega_{2/1}} = \dot{\gamma} \vec{Z}_2 = \dot{\gamma} \vec{Z}_1$
- Case 2: pitch motion defined by the angle  $\beta$ , so that  $\overline{\omega_{2/1}} = \dot{\beta} \vec{Y}_2 = \dot{\beta} \vec{Y}_1$
- Case 3: roll motion defined by the angle  $\alpha$ , so that  $\overline{\omega_{2/1}} = \dot{\alpha} \vec{X}_2 = \dot{\alpha} \vec{X}_1$ .

The axes of  $R_2$  are expressed in  $R_0$  according to:

$$\begin{pmatrix} X_2 \\ Y_2 \\ Z_2 \end{pmatrix} = M_\alpha M_\beta M_\gamma M_\delta \begin{pmatrix} X_0 \\ Y_0 \\ Z_0 \end{pmatrix} \text{ with } M_\delta = \begin{pmatrix} c\delta & s\delta & 0 \\ -s\delta & c\delta & 0 \\ 0 & 0 & 1 \end{pmatrix}$$

This yields the following expressions:

$$\triangleright \quad \bar{X}_2 = (c\beta c\gamma c\delta - s\delta c\beta s\gamma)\bar{X}_0 + (s\delta c\beta c\gamma + c\delta c\beta s\gamma)\bar{Y}_0 - s\beta\bar{Z}_0 \quad (3.2)$$

$$\triangleright \quad \bar{Y}_2 = [c\delta(s\beta c\gamma s\alpha - c\alpha s\gamma) - s\delta(s\alpha s\gamma s\beta + c\alpha c\gamma)]\bar{X}_0 \\ + [s\delta(s\alpha s\beta c\gamma - c\alpha s\gamma) + c\delta(s\alpha s\gamma s\beta + c\alpha c\gamma)]\bar{Y}_0 + c\beta s\alpha\bar{Z}_0 \quad (3.3)$$

$$\triangleright \quad \bar{Z}_2 = [c\delta(c\gamma c\alpha s\beta + s\alpha s\gamma) - s\delta(s\gamma c\alpha s\beta - s\alpha c\gamma)]\bar{X}_0 \\ + [s\delta(c\gamma c\alpha s\beta + s\alpha s\gamma) + c\delta(c\alpha s\gamma s\beta - s\alpha c\gamma)]\bar{Y}_0 + c\beta c\alpha\bar{Z}_0 \quad (3.4)$$

Thus, for each case of head rotation, the angular velocity vector  $\bar{\omega}_{2/1}$  is defined in  $R_0$  by:

$$\triangleright \quad \text{Case 1: } \bar{\omega}_{2/1} = \dot{\alpha}\bar{X}_2 = \dot{\alpha}c\delta\bar{X}_0 + \dot{\alpha}s\delta\bar{Y}_0 \quad (3.5)$$

$$\triangleright \quad \text{Case 2: } \bar{\omega}_{2/1} = \dot{\beta}\bar{Y}_2 = -\dot{\beta}s\delta\bar{X}_0 + \dot{\beta}c\delta\bar{Y}_0 \quad (3.6)$$

$$\triangleright \quad \text{Case 3: } \bar{\omega}_{2/1} = \dot{\gamma}\bar{Z}_2 = \dot{\gamma}\bar{Z}_0 \quad (3.7)$$

- Head / earth

The angular velocity of the head with respect to the earth coordinate frame is given by:

$\bar{\omega}_{2/0} = \bar{\omega}_{2/1} + \bar{\omega}_{1/0}$ . Therefore for each case of head rotation:

$$\triangleright \quad \text{Case 1: } \bar{\omega}_{2/0} = \dot{\alpha}\bar{X}_2 + \dot{\delta}\bar{Z}_0 = \dot{\alpha}c\delta\bar{X}_0 + \dot{\alpha}s\delta\bar{Y}_0 + \dot{\delta}\bar{Z}_0 \quad (3.8)$$

$$\triangleright \quad \text{Case 2: } \bar{\omega}_{2/0} = \dot{\beta}\bar{Y}_2 + \dot{\delta}\bar{Z}_0 = -\dot{\beta}s\delta\bar{X}_0 + \dot{\beta}c\delta\bar{Y}_0 + \dot{\delta}\bar{Z}_0 \quad (3.9)$$

$$\triangleright \quad \text{Case 3: } \bar{\omega}_{2/0} = \dot{\gamma}\bar{Z}_2 + \dot{\delta}\bar{Z}_0 = (\dot{\gamma} + \dot{\delta})\bar{Z}_0 \quad (3.10)$$

### 3.1.2.4. Expression of the angular acceleration vector

The angular acceleration of the head relative to the earth reference frame is given by:

$$\dot{\bar{\omega}}_{2/0} = \dot{\bar{\omega}}_{2/1} + \dot{\bar{\omega}}_{1/0} \quad (3.11)$$

If the chair rotates at a constant angular velocity, the vector  $\dot{\bar{\omega}}_{1/0}$  is null. Let us consider the following rotation rate vector:  $\bar{\omega}_{2/1} = \omega_x\bar{x}_2 + \omega_y\bar{y}_2 + \omega_z\bar{z}_2$  so that its first derivative is:

$$\dot{\bar{\omega}}_{2/1}\Big|_{R_0} = \dot{\omega}_x\bar{x}_2 + \dot{\omega}_y\bar{y}_2 + \dot{\omega}_z\bar{z}_2 + \omega_x\left(\frac{d\bar{x}_2}{dt}\right)_{R_0} + \omega_y\left(\frac{d\bar{y}_2}{dt}\right)_{R_0} + \omega_z\left(\frac{d\bar{z}_2}{dt}\right)_{R_0} \quad (3.12)$$

According to the formulas of differentiation of a vector in a moving frame, we have the following relations:

$$\left(\frac{d\vec{x}_2}{dt}\right)_{R_0} = \left(\frac{d\vec{x}_2}{dt}\right)_{R_1} + \vec{\omega}_{1/0} \wedge \vec{x}_2 = \vec{\omega}_{2/1} \wedge \vec{x}_2 + \vec{\omega}_{1/0} \wedge \vec{x}_2 \quad (3.13)$$

$$\left(\frac{d\vec{y}_2}{dt}\right)_{R_0} = \left(\frac{d\vec{y}_2}{dt}\right)_{R_1} + \vec{\omega}_{1/0} \wedge \vec{y}_2 = \vec{\omega}_{2/1} \wedge \vec{y}_2 + \vec{\omega}_{1/0} \wedge \vec{y}_2 \quad (3.14)$$

$$\left(\frac{d\vec{z}_2}{dt}\right)_{R_0} = \left(\frac{d\vec{z}_2}{dt}\right)_{R_1} + \vec{\omega}_{1/0} \wedge \vec{z}_2 = \vec{\omega}_{2/1} \wedge \vec{z}_2 + \vec{\omega}_{1/0} \wedge \vec{z}_2 \quad (3.15)$$

Finally, injecting (3.13), (3.14), and (3.15) into (3.12), the angular acceleration vector of the head relative to the earth coordinate frame is:

$$\dot{\vec{\omega}}_{2/1} \Big|_{R_0} = \dot{\omega}_x \vec{x}_2 + \dot{\omega}_y \vec{y}_2 + \dot{\omega}_z \vec{z}_2 + \vec{\omega}_{1/0} \wedge \vec{\omega}_{2/1} \quad (3.16)$$

### 3.1.2.5. Expression of the linear acceleration vectors

Due to their position from the head vertical axis, both vestibular systems experience normal and tangential acceleration components during any rotation of the head. The further is the head from the axis of rotation, the higher are these acceleration components. We assume here that these components stimulate the otolith organs. For each case of head movement – roll, pitch, and yaw rotation – the derivation of the absolute linear acceleration of the origin of the coordinate system  $R_3$  attached to the canals is given by:

$$\vec{A}_{B,2/0} = \vec{A}_{B,2/1} + \dot{\vec{\omega}}_{1/0} \wedge \vec{AB} + \vec{\omega}_{1/0} \wedge (\vec{\omega}_{1/0} \wedge \vec{AB}) + \vec{A}_{coriolis} \quad (3.17)$$

This expression describes linear acceleration in a rotating environment. The first term is due to the acceleration of B within the moving frame  $R_1$ . The second term is the result of the rotational acceleration of  $R_1$ . The third term constitutes the centripetal acceleration which is due to the rotation of the moving frame. The last term is due to the motion of B within the moving frame and is known as the Coriolis acceleration.

- Case 1: yaw head movement

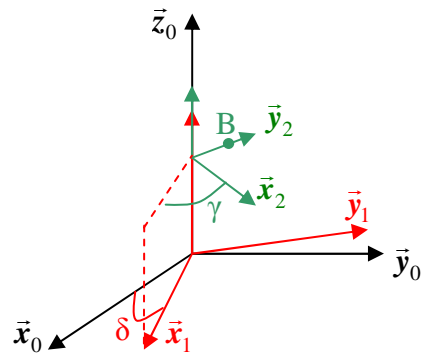


**Figure 3.4.** Orientation of the coordinate systems for a yaw head movement while the subject is rotated around an Earth vertical axis.

➤ Linear velocity

The velocity of B relative to the moving frame  $R_1$  is given by:

$$\overline{\mathbf{V}}_{B,2/1} = \overline{\mathbf{V}}_{A,2/1} + \overline{\omega}_{2/1} \wedge \overline{\mathbf{AB}} = \overline{\omega}_{2/1} \wedge \overline{\mathbf{AB}} \quad (3.18)$$

$$\Rightarrow \overline{\mathbf{V}}_{B,2/1} = \begin{matrix} -\dot{\gamma}d \\ 0 \\ 0 \end{matrix}_{R_2} = \begin{matrix} -\dot{\gamma}dc\gamma \\ -\dot{\gamma}ds\gamma \\ 0 \end{matrix}_{R_1} = \begin{matrix} \dot{\gamma}d(-c\gamma c\delta + s\gamma s\delta) \\ -\dot{\gamma}d(s\gamma c\delta + s\delta c\gamma) \\ 0 \end{matrix}_{R_0}$$

➤ Linear acceleration

- ✓ Acceleration of B relative to  $R_1$

$$\overline{\mathbf{A}}_{B,2/1} = \left( \frac{d}{dt} \left( \overline{\mathbf{V}}_{B,2/1} \right) \right)_{R_1} = \left( \frac{d}{dt} (-\dot{\gamma}d\overline{\mathbf{x}}_2) \right)_{R_1} = -\ddot{\gamma}d\overline{\mathbf{x}}_2 - \dot{\gamma}d \left( \frac{d\overline{\mathbf{x}}_2}{dt} \right)_{R_1} = \begin{matrix} -\ddot{\gamma}d \\ -\dot{\gamma}^2d \\ 0 \end{matrix}_{R_2} \quad (3.19)$$

- ✓ Coriolis acceleration

$$\overline{\mathbf{A}}_{coriolis} = 2\overline{\omega}_{1/0} \wedge \overline{\mathbf{V}}_{B,R_2/R_1} = 2 \times \begin{matrix} 0 \\ 0 \\ \dot{\delta} \end{matrix}_{R_2} \wedge \begin{matrix} -\dot{\gamma}d \\ 0 \\ 0 \end{matrix}_{R_2} = \begin{matrix} 0 \\ -2\dot{\delta}\dot{\gamma}d \\ 0 \end{matrix}_{R_2} = \begin{matrix} 2\dot{\delta}\dot{\gamma}ds\gamma \\ -2\dot{\delta}\dot{\gamma}dc\gamma \\ 0 \end{matrix}_{R_1} \quad (3.20)$$

- ✓ Absolute acceleration of B

$$\vec{A}_{B,2/0} = \vec{A}_{B,2/1} + \dot{\vec{\omega}}_{1/0} \wedge \overline{AB} + \vec{\omega}_{1/0} \wedge (\vec{\omega}_{1/0} \wedge \overline{AB}) + \overline{A_{coriolis}} = \begin{matrix} \left. \begin{array}{l} -\dot{\gamma}d - \delta\dot{d} \\ -\dot{\gamma}^2d - \delta^2\dot{d} - 2\dot{\delta}\dot{\gamma}d \\ 0 \end{array} \right|_{R_2} \end{matrix} \quad (3.21)$$

The green, red, and blue terms represent the acceleration of B relative to R<sub>1</sub>, the rigid body acceleration of B in R<sub>0</sub>, and the Coriolis acceleration, respectively.

- Case 2: pitch head movement

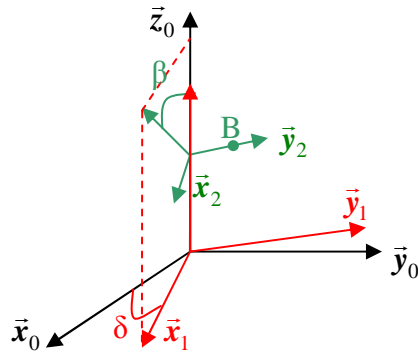


**Figure 3.5.** Orientation of the coordinate systems for a pitch head movement while the subject is rotated around an Earth vertical axis.

- Linear velocity

The velocity of B relative to the moving frame R<sub>1</sub> is null because it is located right on the axis of rotation  $\vec{y}_2$ . Therefore, both the acceleration of B relative to R<sub>1</sub> and the Coriolis acceleration are equal to zero.

- Linear acceleration

- ✓ Absolute acceleration of B

$$\vec{A}_{B,2/0} = \dot{\vec{\omega}}_{1/0} \wedge \overline{AB} + \vec{\omega}_{1/0} \wedge (\vec{\omega}_{1/0} \wedge \overline{AB}) = \begin{matrix} \left. \begin{array}{l} -\delta\dot{d} \\ -\delta^2\dot{d} \\ 0 \end{array} \right|_{R_1} = \begin{matrix} \left. \begin{array}{l} -\delta\dot{d}c\beta \\ -\delta^2\dot{d} \\ -\delta\dot{d}s\beta \end{array} \right|_{R_2} \end{matrix} \quad (3.22)$$



- Case 3: roll head movement

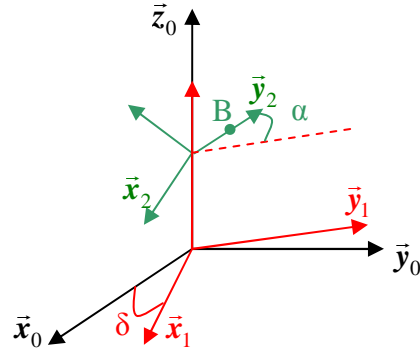


**Figure 3.6.** Orientation of the coordinate systems for a roll head movement while the subject is rotated around an Earth vertical axis.

- Linear velocity

The velocity of B relative to the moving frame  $R_1$  is given by:

$$\overrightarrow{V}_{B,2/1} = \begin{vmatrix} \dot{\alpha} & 0 & 0 & 0 \\ 0 \wedge & d & 0 & 0 \\ 0 & 0 & \dot{\alpha}d & \dot{\alpha}dc\alpha \end{vmatrix}_{R_2} = \begin{vmatrix} 0 & 0 & 0 \\ 0 & 0 & -\dot{\alpha}ds\alpha \\ \dot{\alpha}d & \dot{\alpha}dc\alpha & 0 \end{vmatrix}_{R_1} \quad (3.23)$$

- Linear acceleration

- ✓ Acceleration of B relative to  $R_1$

$$\overrightarrow{A}_{B/R_1} = \overrightarrow{A}_{B,R_2/R_1} + \dot{\omega}_{2/1} \wedge \overrightarrow{AB} + \omega_{2/1} \wedge (\omega_{2/1} \wedge \overrightarrow{AB}) = \begin{vmatrix} 0 & 0 \\ -\dot{\alpha}^2d & 0 \\ \ddot{\alpha}d & -\dot{\alpha}^2ds\alpha + \ddot{\alpha}dc\alpha \end{vmatrix}_{R_2} = \begin{vmatrix} 0 & 0 \\ -\dot{\alpha}^2dc\alpha - \ddot{\alpha}ds\alpha & 0 \\ -\dot{\alpha}^2ds\alpha + \ddot{\alpha}dc\alpha & 0 \end{vmatrix}_{R_1} \quad (3.24)$$

- ✓ Coriolis acceleration

$$\overrightarrow{A}_{coriolis} = 2\omega_{1/0} \wedge \overrightarrow{V}_{B,R_2/R_1} = 2 \times \begin{vmatrix} 0 & 0 \\ 0 \wedge & -\dot{\alpha}ds\alpha \\ \dot{\delta} & \dot{\alpha}dc\alpha \end{vmatrix}_{R_1} = \begin{vmatrix} 0 & 2\dot{\delta}\dot{\alpha}ds\alpha \\ 0 & 0 \\ 0 & 0 \end{vmatrix}_{R_1, R_2} \quad (3.25)$$

- ✓ Absolute acceleration of B

$$\overrightarrow{A}_{B,2/0} = \overrightarrow{A}_{B,2/1} + \dot{\omega}_{1/0} \wedge \overrightarrow{AB} + \omega_{1/0} \wedge (\omega_{1/0} \wedge \overrightarrow{AB}) + \overrightarrow{A}_{coriolis} = \begin{vmatrix} -\dot{\delta}dc\alpha + 2\dot{\alpha}\dot{\delta}ds\alpha \\ -\dot{\delta}^2d(c\alpha)^2 - \dot{\alpha}^2d \\ \dot{\delta}^2dc\alpha\alpha + d\ddot{\alpha} \end{vmatrix}_{R_2} \quad (3.26)$$

### 3.1.3. Programming and implementation

The entire model has been developed in Matlab/Simulink. A graphical user interface has been programmed in order to simplify the use of the model, the implementation of the simulation parameters, and the analysis of the results (curves plot, 3D animation, and virtual reality). This GUI is linked to the core of the model, implemented in Simulink, where the equations of motion and the state of the sensors are computed. In addition, a virtual reality world is linked to the kinematics and vestibular model using the virtual reality toolbox available in Matlab. This toolbox represents an interface between Matlab and Simulink data on one hand, and virtual reality graphics on the other hand.

Basically the model follows different steps:

1. the user implements the motion undertaken by an actual patient, i.e. the motion profile of the chair (continuous, trapezoidal, or sinusoidal) and the potential head rotations
2. the user runs the simulation: the kinematics and the state of each sensor are computed
3. the user analyses the results: data processing is performed from the GUI. The user has the possibility to plot the displacement of each sensor, to run a three-dimensional dynamic animation showing the state of the cupulae, or to run a virtual reality animation of the experiment.

#### 3.1.3.1. Graphical user interface

Figure 3.7 shows the GUI developed under Matlab. This interface is comprised of four main sections:

- Section I concerns the implementation of the motion of the rotating chair. The user can choose between a continuous, trapezoidal or sinusoidal rotation. The parameters of the imposed rotation are the angular velocity of the chair, the duration of acceleration and deceleration, the duration of the motion profile, and, in the case of a sinusoidal motion, the frequency of the rotation.
- Section II offers the possibility to consider translational motion. In that case, however, both the three-dimensional animation and the virtual reality model become useless as they only represent the rotating chair experiment. Nonetheless, the displacement of the otolithic membrane can still be analyzed through the different plots.
- Section III concerns the implementation of head movements. For each head rotation, the parameters are the starting and return time of the motion, and the magnitude and duration of each rotation.
- Section IV comprises the push buttons for running the simulation and for data processing (curves plots, animation, etc).

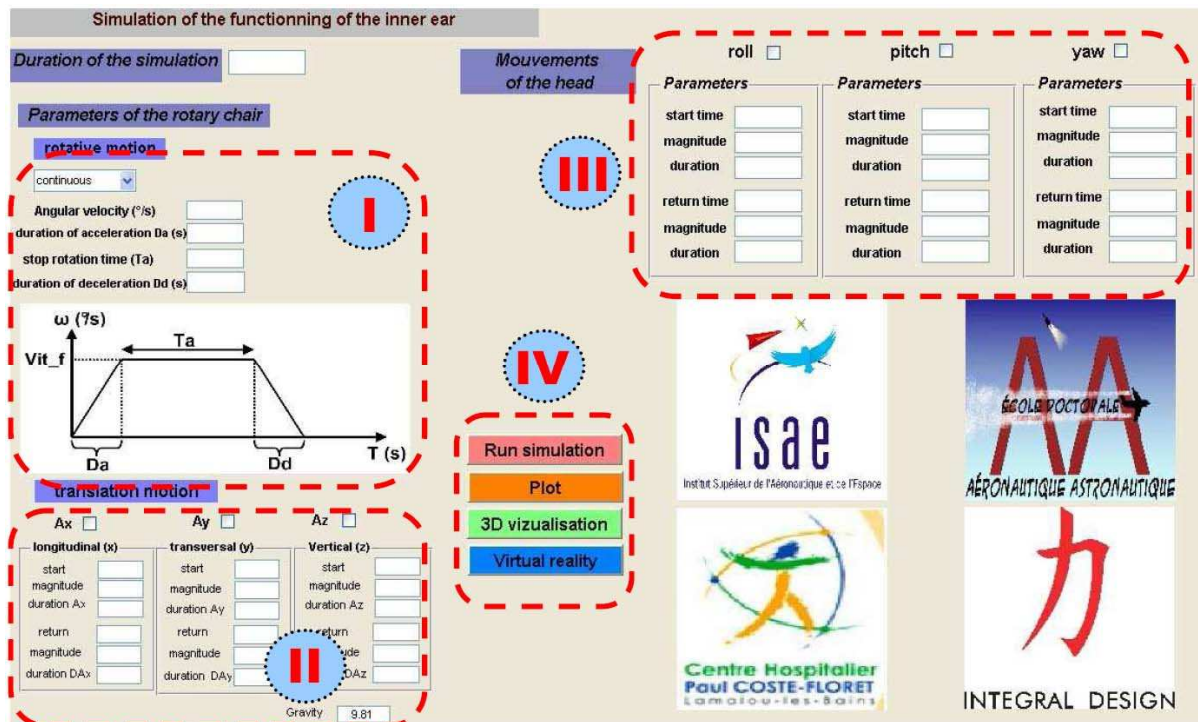


**Figure 3.7.** Graphical user interface of the virtual reality model. I: parameters of the rotary chair; II : parameters of exterior linear accelerations; III : parameters of head movements; IV : simulation, results and virtual reality push buttons.

### 3.1.3.2. Simulink model

The architecture of the core of the model is presented in figures 3.8. The first box titled SCC, computes the kinematics problem regarding the rotational motion, i.e. the angular velocity, angular acceleration, and linear acceleration components due to the movement of rotation. This block also performs the projection of the angular acceleration vectors into the coordinate frame attached to the canals. A variable permits to switch between the angular acceleration - either defined in  $R_2$  or  $R_3$  - that is applied to the SCC. In other words, the user can choose between an orthogonal head-centered vestibular system and a set of SCC that are oriented according to experimental angles. Hence, he can study the impact of a non-orthogonal coordinate frame on the stimulation of the SCCs. Assuming that the SCCs are totally uncoupled, the  $\bar{x}$ ,  $\bar{y}$ , and  $\bar{z}$  angular acceleration components are then sent to the transfer function of the posterior, anterior, and lateral canal, respectively. Note that the semicircular canals are supposed to have the same dynamic behavior, which is defined by equation (1.9).

The block titled Utricule-sacculé performs merely the sum of the linear acceleration vector due to the rotational motion, the linear acceleration vector of a potential translational motion, and the gravity vector. Each component is then passed through each otolith organ transfer function defined by equation (1.14). The  $\bar{x}$  and  $\bar{y}$  components are assumed to be sensed by the utricle, while the  $\bar{z}$  component stimulates the saccule.

Finally, the block named VR Vizualisation, which contains all the data relative to the virtual reality world, performs the virtual animation.

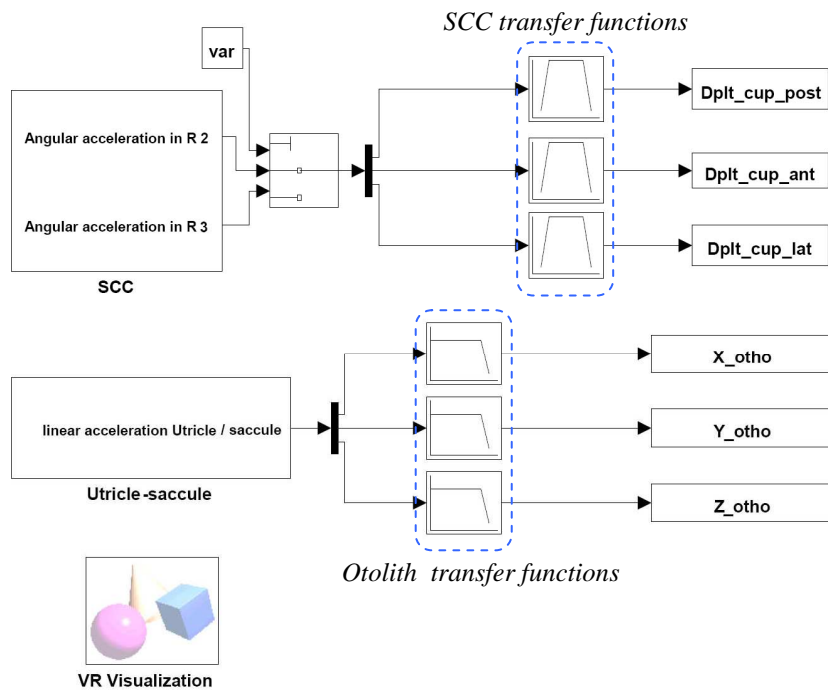


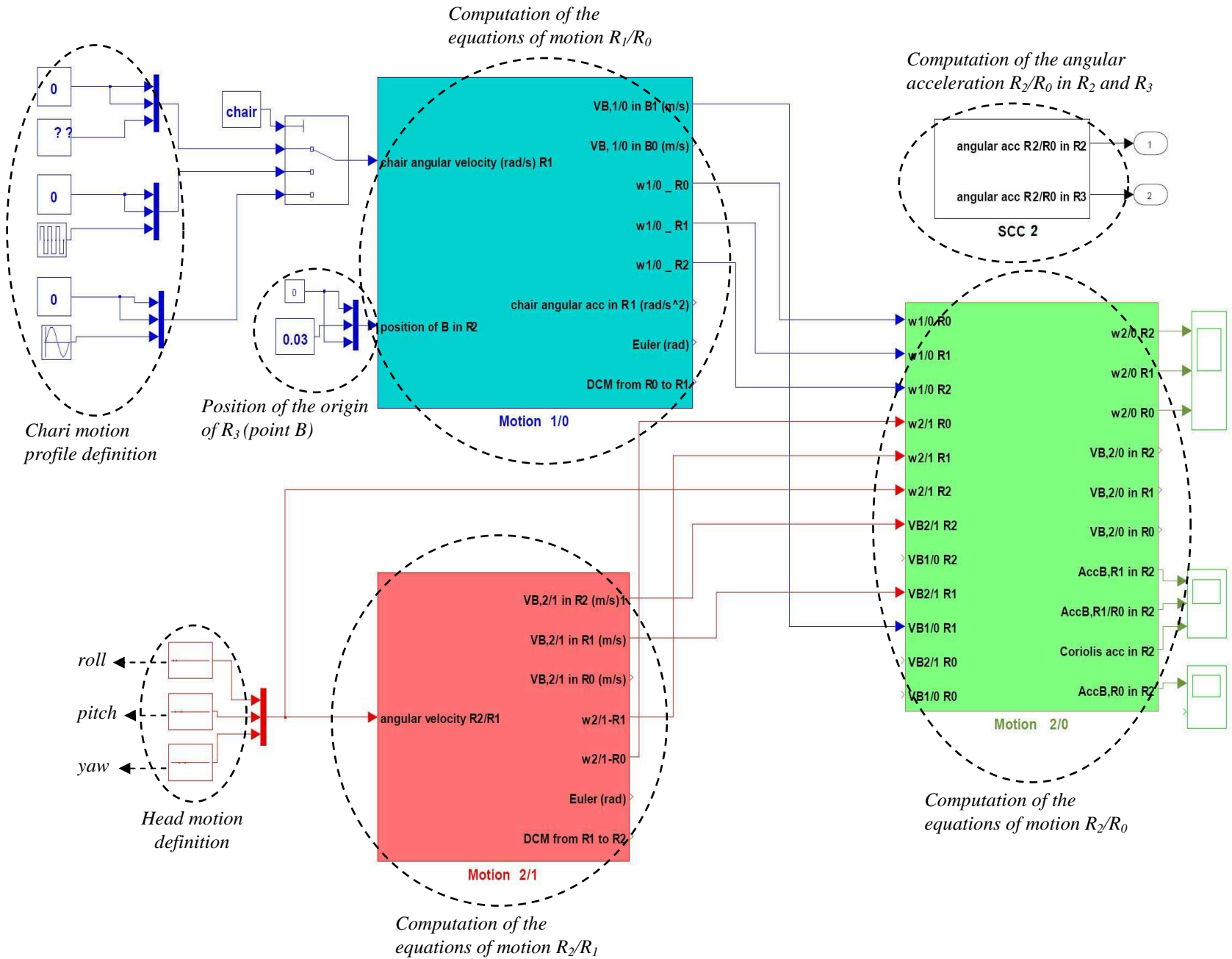
**Figure 3.8.** First layer of the simulink model.

The block “SCC” is detailed in figure 3.9. The kinematics problem is solved in four successive steps:

1. Blue block: calculation of the motion  $R_1/R_0$  (angular and linear velocity, Euler angles, rotation matrix from  $R_0$  to  $R_1$ , etc)
2. Red block: Calculation of the motion  $R_2/R_1$  (angular and linear velocity, Euler angles, rotation matrix from  $R_1$  to  $R_2$ , etc)
3. Green block: Calculation of the motion  $R_2/R_0$  (angular and linear velocity, linear acceleration, Euler angles, rotation matrix from  $R_0$  to  $R_2$ , etc)
4. White block: Calculation of the angular acceleration in  $R_2$  and  $R_3$ .

The block “Utricle-saccule” first sums up the potential linear acceleration imposed by the user and the gravity vector, and projects the resulting vector into the head coordinate frame  $R_2$ . Then, this vector is added to the linear acceleration of the origin of the coordinate frame  $R_3$  that is due to the rotational motion of the chair and of the head (Fig. 3.10).

Figure 3.9. Detailed view of the block of the first layer titled "SCC".



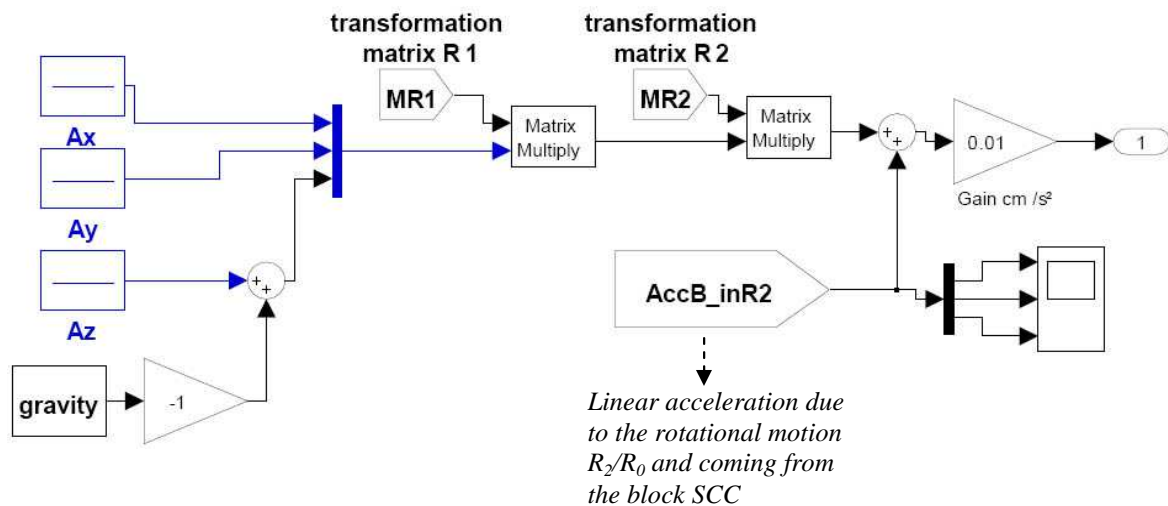
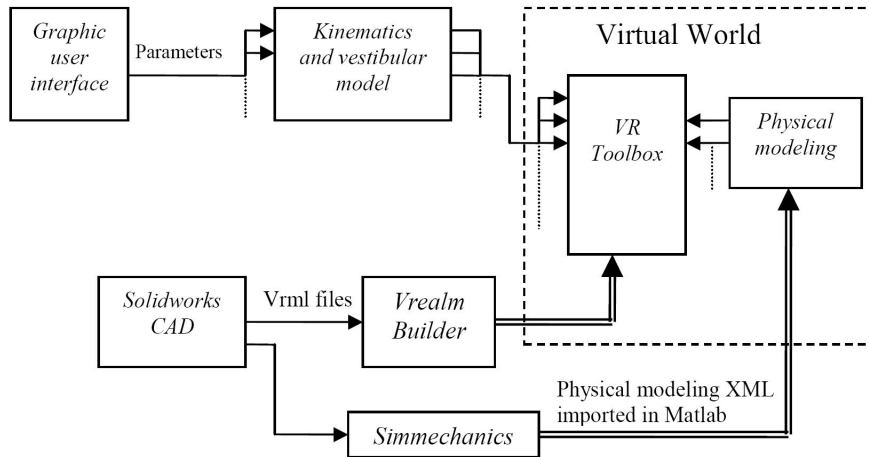


Figure 3.10. Detailed view of the block of the first layer titled “utricle-sacculle”.

### 3.1.3.4. Virtual reality model

A virtual reality world is linked to the kinematics and vestibular model using the virtual reality toolbox available in Matlab (Natick, 2007). This toolbox represents an interface between Matlab and Simulink data on one hand and virtual reality graphics on the other hand. Virtual reality graphics are based on VRML, an open standard for describing 3-D scenes (Carey et al., 1997). Virtual Reality Toolbox has been successfully used in multiple applications for visualizing results of Simulink simulations. However, it has been observed that system and control engineers who are unfamiliar with VRML find it difficult to create a VRML file describing a 3-D scene they would like to visualize. The solution to simplify the VRML file creation process is to start the design with CAD assemblies. In this modeling, the different parts of the virtual world are created using Solidworks (CAD software), which is very useful for specifying detailed three-dimensional design of a component (Solidworks User’s guide, 2007). The CAD models are then exported into Virtual Reality Modeling Language (VRML) files. The final virtual environment is created using the “V-Realm Builder” software where the VRML files are imported. In order to simulate the dynamics of the system, the CAD-to-SimMechanics translator from the MathWorks is used (SimMechanics User’s Guide, 2007). It enables to translate CAD assemblies from a CAD platform into a Physical Modeling XML file compatible with SimMechanics. Then a SimMechanics block diagram model is generated from this file to simulate the dynamics of the CAD assembly in the Simulink environment. In order to achieve this, Simulink and SimMechanics use a block diagram approach to model control systems around mechanical devices and simulate their dynamics. The block diagram approach does not include full geometric information, nor do CAD assemblies typically incorporate controllers or allow to perform dynamic simulations. Using this technique of CAD translation, the power of CAD and SimMechanics are combined.

Finally, this Simulink model is connected to the virtual scene in order to create a realistic high-quality animation. The outputs of the kinematics and vestibular model are linked to the inputs of the virtual reality toolbox in order to bring about progress in the virtual world (Fig. 3.11).



**Figure 3.11.** Schematic block diagram of how the virtual reality world is created and controlled. The VRML files are created using a CAD software. The Simmechanics module permits to represent and keep the physics of the modeling. All the data are imported into a Matlab/Simulink model where the virtual reality toolbox is used. This Simulink file is controlled by the kinematics of the simulation and the vestibular model.

### 3.1.3.5. Simulation and visualization

- *Rotation movement of the chair*

This experiment mimics the usual diagnosis procedure of the lateral semicircular canal. During this first experiment the patient sits down on the rotary chair. His head is kept fixed relatively to the device and tilted downward of  $30^\circ$  to bring the lateral semicircular canal in the plane of rotation. Then, a constant angular velocity of  $\dot{\delta} = 100^\circ/s$  is imposed to the chair. This motion starts at  $t_0 = 1s$  and achieves its steady state in  $1s$ . This simulation lasts 40 seconds. The volume displacement of the cupula is shown on figure 3.12. If the canals are considered to be orthogonal, the endolymph in the lateral canals lags behind - at the beginning of the rotation - due to its inertia. Consequently, the cupula of the lateral semicircular canal is deflected in the opposite direction of head movement (Fig. 3.12a). This deflection causes a sensation of motion. The angular velocity of the chair being constant, the endolymph in the lateral canal tends to catch up with the rotation of the head eliminating the relative movement. Therefore, the cupula returns to a vertical position due to its elastic properties, and the sensation of motion ceases.

Figures 3.12a and 3.12b enable us to show the influence of the non-orthogonality of the canals. From these plots, a slight displacement of the anterior and posterior cupula is observed that does not appear in the case of an orthogonal system. However, the lateral canal is the most stimulated as its plane is quasi-perpendicular to the axis of rotation. The displacement of the lateral cupula generates a sensation of rotation which lasts about thirty seconds at a constant angular velocity.



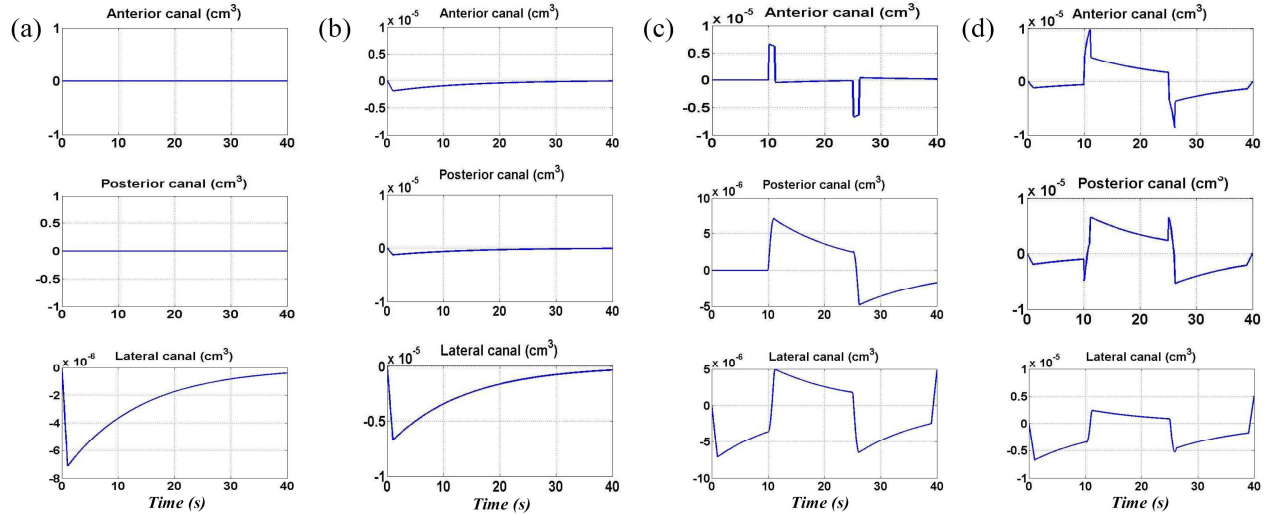


**Figure 3.12.** Displacement of the cupula of each canal due to: (a) and (b) rotation movement of the chair, (c) and (d) rotation movement of the chair and of the head. The graphics (a) and (c) correspond to an orthogonal coordinate system  $R_3$ , whereas (b) and (d) correspond to a non-orthogonal coordinate system  $R_3$ . The non-orthogonality of  $R_3$  entails a slight response of the verticals canals. This kind of response might be similar in the case of the existence of coupling terms between the canals due to fluid flow.

- *Rotation movement of the chair and then of the head*

The rotation movement of the chair is the same as above. In this case the subject does a downward and an upward head rotation at time  $t = 10s$  and  $t = 25s$  respectively. For the sake of simplicity, the amplitude of these movements is equal to  $90^\circ$  here. This kind of head motion during a constant angular velocity of the chair involves the stimulation of the other canals. The displacements of the cupulas can be observed on figures 3.12c and 3.12d. Until  $t$  being equal to 10s, the movement of the cupulas is the same as the previous experiment. At time 10s, the subject does a downward head rotation of  $90^\circ$  from the previous head position. In the case of an orthogonal set of canals, this head motion brings the posterior canal into the plane of rotation. Therefore the cupula of the posterior canal is in turn deflected whereas the cupula of the lateral canal bends in the opposite direction as the fluid keeps moving relatively to the wall of the lateral canal. At time  $t = 25s$ , the reverse phenomenon is produced as the subject makes an upward head rotation of the same magnitude.

It can be noticed that the succession of head movements during a constant rotation of the body, creates erroneous motion sensations known as the Coriolis Effect in aeronautic terms. For example, at  $t = 5s$  the downward motion of the head engenders a positive displacement of the lateral cupula. This means that during a few seconds the subject has a sensation of rotation opposite to the rotation of the chair. This is due to the inertia of the fluid which is still in motion inside the canal. The resulting sensory illusion will be presented in depth in chapter 4.

- *Virtual reality as a demonstration tool*

The aim of showing virtually the diagnosis test undertaken by the specialist is to allow a better comprehension of what happens inside the inner ear during a specific head movement. The state of each sensor is computed and visualized during the experimental protocol. Figure 3.13 illustrates the patient sitting on the rotary chair and experiencing a downward movement



of his head. The displacement of the cupula of each canal can be observed. For clarity purposes, a video of this simulation is available at the link: <http://personnel.supaero.fr/morlier-joseph/Inner%20ear.html>

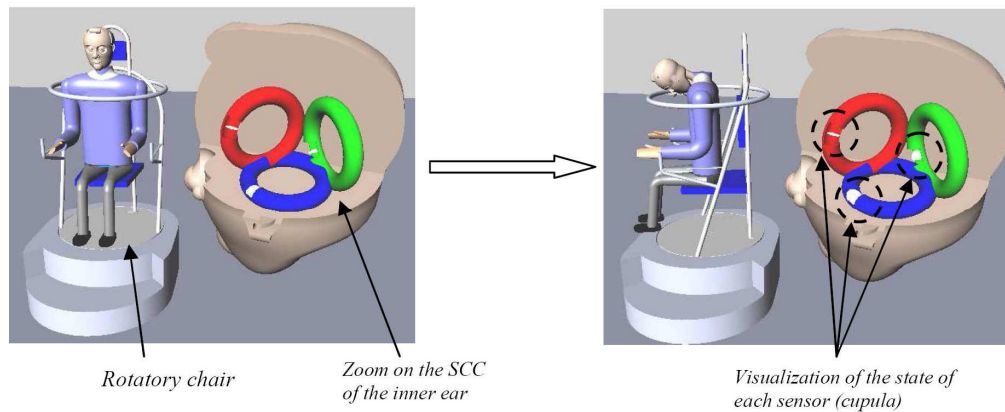


**Figure 3.13.** Visualization of a virtual scene: The state of each sensor can be visualized on real time during the test. The learning process is enhanced using user interactivity.

### 3.1.3.6. Conclusion

The model presented above simulates the rotating chair test which is one of the usual procedures carried out during a vestibular diagnosis. In addition, this model offers the possibility to simulate several head rotations.

All the parameters that define the experiment can be entirely specified by the user through a graphical user interface. Regarding data processing, the user has the choice between plotting the displacement curve of each sensor, visualizing a dynamic three-dimensional animation of the SCC, and visualizing a dynamic virtual scene of the experiment. Both the 3-D animation and the virtual reality environment are very convenient as the user can observe what theoretically happens at the level of each sensor during any head rotation. This model also provides a better understanding of different kinds of erroneous motion sensations which may appear during combined rotation motions.

The core of the model computes in real time equations of motion in earth, chair, and head coordinate system, and then project angular acceleration vectors into a reference frame attached to the semicircular canals. The orientation of the axes of this coordinate system has been defined according to a recent study based on 3-D multiplanar reconstructions of computerized tomography scans (Della Santina et al. 2005). The resulting non-orthogonal system underlines the fact that all the canals are stimulated for any rotation.

# Chapter IV: Models for human spatial orientation

## 4.1. Introduction

Models for human spatial orientation perception are based on the concept of *internal model* representation. This concept assumes that the central nervous system (CNS) has an internal model of the physical world. In other words, based on past motion experiences the CNS has somehow learnt the dynamics of the sensors (vestibular sensors, visual sensors, etc) which sense position and motion, as well as some physical relations.

This idea of *internal model* was developed in the 60's in the field of guidance engineering to estimate the orientation and position of a vehicle for autonomous or assisted navigation. An internal model (not to be confused with the overall model) is an integral component of estimation techniques like observer theory and optimal estimation theory (i.e., Kalman filters). The purpose of internal models is to estimate external variables (like gravity, acceleration, velocity etc.) by mimicking the physical relationships between those variables and the sensory systems and thereby predicting their time-course from incomplete, noisy, and/or inaccurate sensory information (Fig. 4.1). Since the 70's, this concept has attracted interests in neuroscience from motion sickness models (e.g. Reason, 1977, 1978; Oman, 1982, 1991) to model of human spatial orientation (Merfeld et al., 1993; Borah et al., 1979 and 1988; Zupan et al., 2002; Newman, 2009).

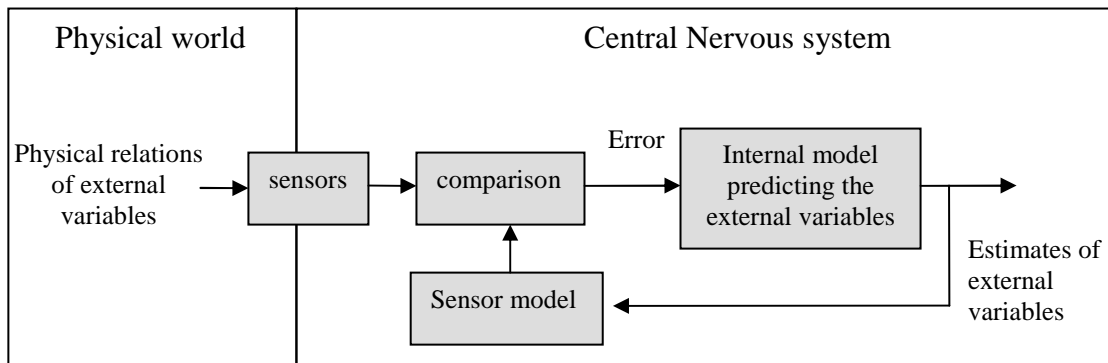


**Figure 4.1.** Principle outline of the internal model concept applied for the estimation of external physical variables like acceleration, velocity, and position.

As regard models for human spatial orientation estimation, two main model families can be distinguished: the Observer and the Kalman Filter model families. As already mentioned in the background section, Borah et al. were presumably the first to apply steady state Kalman filtering techniques to model orientation perception by a human riding passively in a vehicle. Their model considered dynamic models for vestibular and visual sensors, and the transformation from head to world coordinate system was linearized about the upright position. By empirically choosing sensor noise magnitude and bandwidth they show that their Kalman filter model successfully mimicked angular velocity storage during rotation about the Earth-vertical, somatogravic illusory tilts during linear acceleration in darkness, and angular vection and illusory tilt illusions resulting from scene rotation about vertical and horizontal axes, respectively.

A decade later, Merfeld et al. implemented a series of models using Observer theory. These models were developed to help explain perceived spatial orientation as well as the vestibulo-ocular reflexes elicited by complex motion paradigms. Obviously, Merfeld et al. applied the concept of internal model and assumed that internal model estimates corresponded to perceptions of acceleration, velocity, and position. The most well known Observer model refers probably to Merfeld's original paper (1993) in which a one-dimensional model and a three-dimensional model were proposed. Both of these models considered only vestibular sensors, and a nonlinear transformation from head to world coordinate system using quaternion mathematics was taken into account in the 3D model.

The first goal of this chapter is to investigate why the widely known "Observer" and "Kalman Filter" model families – despite their apparently different assumptions - are dynamically equivalent from an input-output ("black box") perspective. Obviously the Borah KF model incorporates some visual cues, whereas Merfeld Observer only described vestibular cue interaction in darkness. Borah assumed the sensory dynamics of the otoliths were relatively slow (5 seconds dominant time constant), whereas Merfeld was aware that otolith dynamics were much faster. Structurally, the models are somewhat different: In the Borah KF model, weighted sensor residuals determine the rates of change of model outputs, whereas in the Merfeld Observer model, SCC residuals simply add to the outputs. The vestibular portions of the Borah KF model postulate 16 SCC and Otolith residual weighting factors - each of which adds a potential decaying exponential or sinusoidal mode to the model's responses. By comparison the Merfeld Observer model utilizes only four ad hoc parameters. The Merfeld model works for large head tilts, whereas the Borah model does not. Nonetheless even for the head upright attitude, the angular velocity storage and somatogravic illusion responses of the Borah KF and Merfeld Observer are almost identical. Therefore, in the following section we ask: What are the reasons for the dynamic equivalence of the two models? How did Borah et al's choice of motion disturbance and sensor noise magnitude and bandwidth impact the KF model's dynamics? Is the Merfeld Observer model a lower-order-equivalent-system (LOES) for the Borah KF model, at least for the head upright condition? The Borah KF model residual weighting factors are optimal for the particular motion disturbance and sensor noise magnitude and bandwidth assumptions made. However, Borah et al considered these free parameters, equivalent to the four free parameters in the Merfeld observer model, and determined them by fitting data on illusory rotation and tilt perception. Shouldn't the appropriate external motion disturbance characteristics represented in the Borah et al model be determined by a person's motion exposure history? Do human thresholds for angular and linear motion correspond to the equivalent sensor noise implied by the Borah et al model coefficients?

The second goal of this chapter is to extend Borah's steady state Kalman filter model to a general time-continuous three-dimensional model that works for any head attitude. In order to achieve this goal, we use suboptimal filtering techniques such as the extended Kalman filter and the unscented Kalman filter. The first developed model is closely based on Pommellet's EKF model but differs in the sense that first, we use different dynamics for the otolith, second we add some fictitious process noise to the quaternion in order to address the issue of instabilities of the filter, and third we solve some implementation errors especially for the noise measurement. We then develop the first nonlinear model for human spatial orientation based on the hybrid unscented Kalman filter. This technique is fundamentally different than the EKF as it relies on the propagation, through the nonlinear dynamics of the system, of a set of points to approximate the mean and variance of the states instead of directly truncating the

nonlinear functions to a first or second order. In addition, its inherent properties involve a better accuracy and a faster computation time than the EKF. Finally, we simulate different motion paradigms and present modeling results for several vestibular and visual – vestibular illusions including for instance Coriolis and pseudo-Coriolis illusions.

## 4.1. Relationships between Observer and Kalman filter models for human dynamics spatial orientation

### 4.1.2. Observer and KF model comparison: yaw rotation in darkness

Here we compare the Merfeld Observer and Borah Kalman filter models for the simple one dimensional case where a human subject is rotated in yaw about an Earth vertical axis in the dark, stimulating only the horizontal semicircular canals. The system input is a step of angular velocity  $\omega_z$ . The subject reports perception of head angular velocity.

#### 4.1.2.1. Merfeld 1-D Observer model

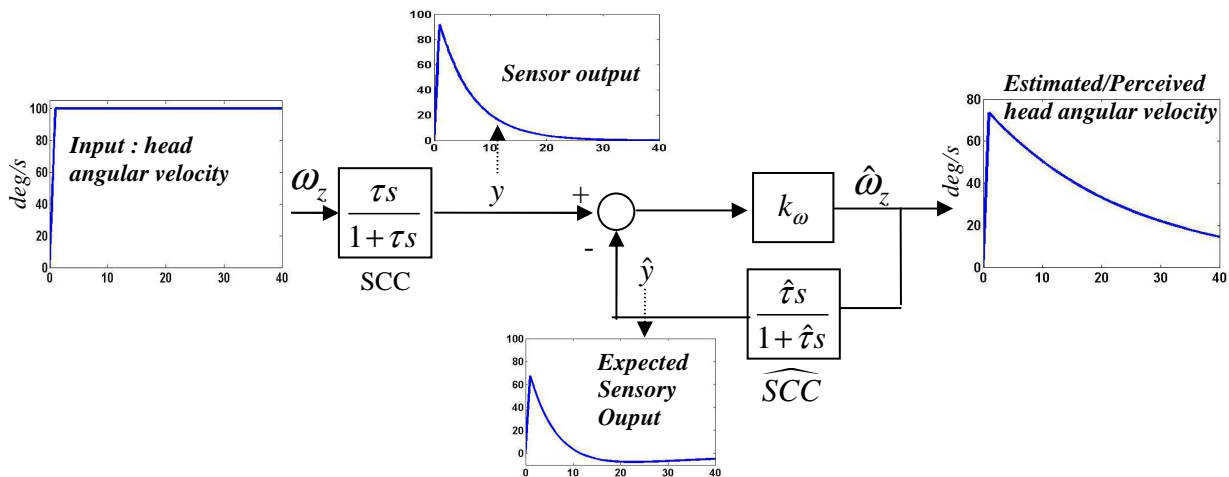


**Figure 4.2.** Merfeld Observer model for a yaw rotation. Hat variables refer to as the estimated variables. SCC: model of semicircular canal dynamics.  $\widehat{SCC}$ : model of semicircular canal dynamics assumed by the internal model of the central nervous system. The model predicts that in response to a constant head angular velocity, perception of angular velocity decays through time.

Merfeld et al's Observer model for this simple yaw rotation case is shown schematically in figure 4.2. Input to the system is head angular velocity  $\omega_z$ . The SCC sensory afference  $y$  was modelled assuming first order high-pass filter SCC dynamics with a time constant  $\tau$  of 6 s. Merfeld assumed that CNS neurons maintain an internal estimate of head angular velocity  $\hat{\omega}_z$ . Using this estimate, and an internal dynamic model for the SCC with time constant  $\hat{\tau}$  of 6 s, the CNS predicts SCC sensory afference  $\hat{y}$ , and computes a residual, and subtracts it from actual SCC afference. The residual is weighted by gain  $k_\omega = 3$  and set equal to the current velocity estimate  $\hat{\omega}_z$ . Note that this is a different estimation scheme than that used in the

Kalman observer (eq.1.25) where residual drives the rate of change of the estimated state, ensuring that the steady state residual approaches zero. Merfeld et al. chose this alternate scheme because the closed loop transfer function of the Observer is

$$\frac{k_\omega(1 + \hat{\tau}s)}{1 + (k_\omega + 1)\hat{\tau}s} \quad (4.1)$$

effectively cancelling the SCC pole, and replacing it with a time constant of  $(k_\omega + 1)\hat{\tau} = 24\text{ s}$ , matching empirical evidence for a “velocity storage” phenomenon (Fig. 4.3).

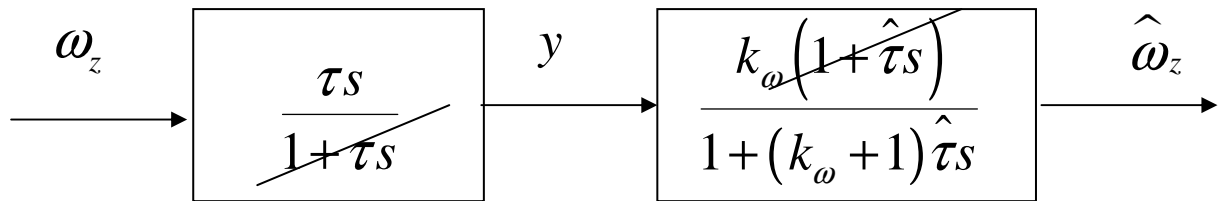


Figure 4.3. Merfeld Observer model showing pole/zero cancellation.

#### 4.1.2.2. Borah 1-D Kalman filter model

Next, we develop the corresponding Kalman filter model for yaw rotation. In the general Kalman filter formulation (section 1.4.2.1) the process and measurement noise are assumed white. However, the head angular velocity inputs encountered in daily life are band limited, so a low pass shaping filter of bandwidth  $\beta_\omega$  is incorporated into the system model, as shown in figure 4.4a. This also makes head angular velocity  $\omega_z$  a state of the system which the Kalman filter can then estimate.

(a)

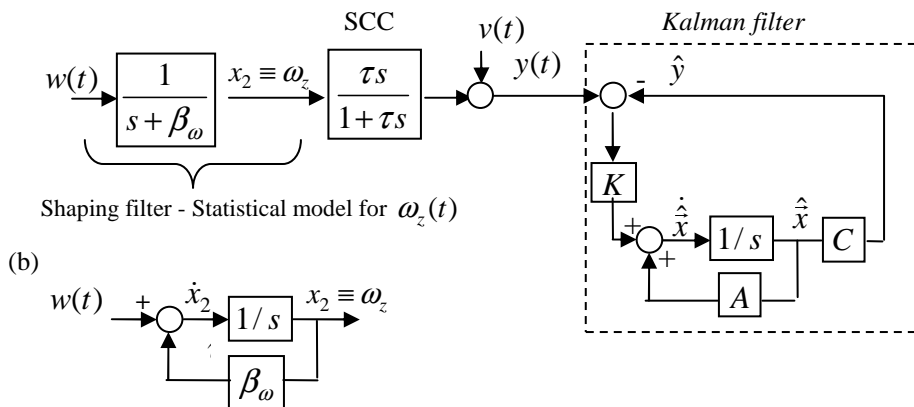


Figure 4.4. One-dimensional Borah's KF model. (a) Model for white noise shaping filter, SCC dynamics, and Kalman filter. (b) Equivalent representation for the shaping filter.

Therefore we represent the system using a state vector  $[x_c(t) \ \omega_z(t)]^T \equiv [x_1(t) \ x_2(t)]^T$  so the KF system equation is:

$$\begin{pmatrix} \dot{x}_1(t) \\ \dot{x}_2(t) \end{pmatrix} = A\bar{x}(t) + Gw(t) = \begin{pmatrix} -1/\tau & 1 \\ 0 & -\beta_\omega \end{pmatrix} \begin{pmatrix} x_1(t) \\ x_2(t) \end{pmatrix} + \begin{pmatrix} 0 \\ 1 \end{pmatrix} w(t) \quad (4.2)$$

And the measurement equation is:

$$y(t) = C\bar{x}(t) + v(t) = \begin{pmatrix} -1/\tau & 1 \end{pmatrix} \begin{pmatrix} x_1(t) \\ x_2(t) \end{pmatrix} + v(t) \quad (4.3)$$

Note that the shaping filter bandwidth  $\beta_\omega$  is a term in the system matrix  $A$ . The process noise, shaping filter, and measurement noise parameters Borah corresponding to those used by Borah were:

- $\beta_\omega = 200 \text{ rad/s}$
- $w(t) \sim N(0, 3.0 \times 10^5)$
- $v(t) \sim N(0, 0.75)$

Given these values, and assuming  $\tau = 6 \text{ s}$ , one can numerically solve the nonlinear algebraic Riccati equation (1.30) for  $P_\infty$  and then use equation (1.31) to compute the Kalman filter gain matrix  $K = [K_1 \ K_2]^T = (\approx 0, 463.5)^T$ . Note that for these parameter values,  $K_1$  is almost zero ( $10^{-13}$  or smaller). Defining the KF estimated state as  $\hat{x} = [\hat{x}_c(t) \ \hat{\omega}_z(t)] \equiv [\hat{x}_1(t) \ \hat{x}_2(t)]$ , the KF equations become:

$$\dot{\hat{x}}_1(t) = A\hat{x}_1(t) \quad (4.4)$$

$$\dot{\hat{x}}_2(t) = A\hat{x}_2(t) + 463.5(y(t) - C\hat{x}_2(t)) \quad (4.5)$$

The block diagram on the left side of figure 4.5 shows the structure of the resulting Kalman filter.

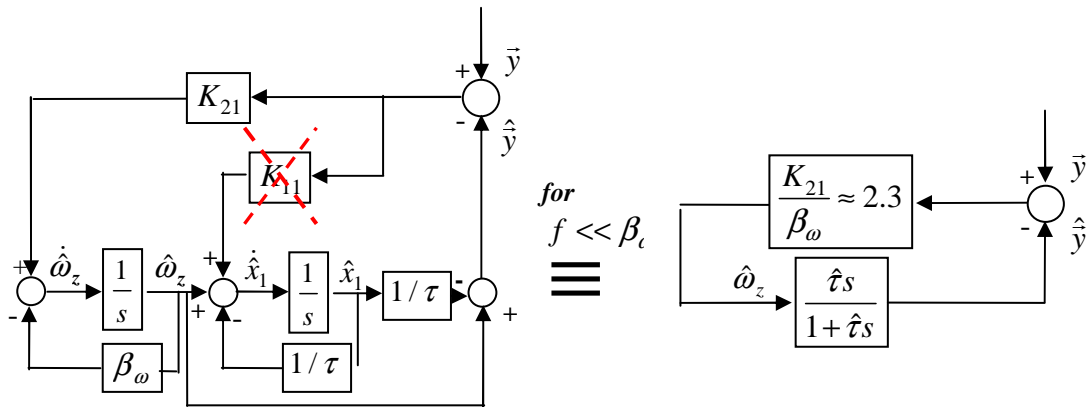


**Figure 4.5.** Kalman filter model for yaw rotation (left). Equivalent model for  $f \ll \beta_\omega$  (right).

Comparing this KF model with the Observer model described in section 4.1.2.1 and shown in figure 4.1, note that in the KF, the  $K_2$  weighted residual passes through “internal models” of the shaping filter and the SCC in series. This makes sense from a Bayesian perspective: the KF was designed based on the a priori assumption that components of the residual at frequencies  $f \gg \beta_\omega$  are unlikely, and should be filtered out since they are probably cues due to sensor noise. Note also that the shaping filter in the KF reduces the effect of the measurement noise on the KF yaw velocity estimate. The Merfeld Observer internal model has no explicit representation of the head movement spectrum and hence no internal model “shaping filter”. However for stimulus frequencies  $\ll \beta_\omega$  the transfer function of the shaping filter is simply  $1/\beta_\omega$ , so the KF dynamics can be approximated by the system shown on the right side of figure 4.5, which structurally is identical to the Merfeld Observer model. The KF residual pathway gain  $K_2/\beta_\omega = 463.5/200 = 2.3$  is very close to the  $k_\omega = 3$  of the Merfeld Observer model. As shown in figure 4.6, both models exhibit very similar dynamic responses to a deterministic 100 deg/s step change in head angular velocity. This is not surprising, since the parameters in both models were empirically tuned to match similar data.

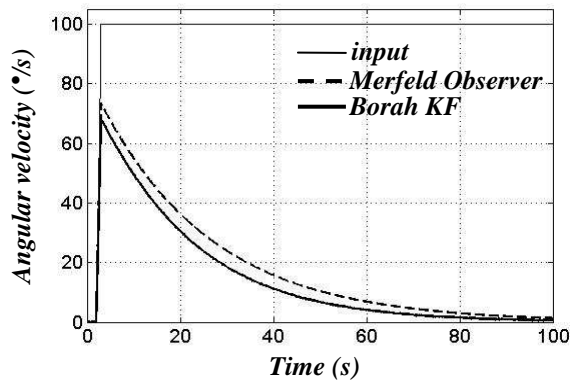


**Figure 4.6.** Observer and KF estimated angular velocity responses to a 100 deg/s angular velocity step.

We should note that to simplify the example and to facilitate comparison with Merfeld’s model, the KF model developed above used a first order SCC model and first order shaping filter. Borah actually employed a second order SCC model with a 10 s dominant time constant, and a second order shaping filter. The higher order models introduced additional complexity in Borah’s KF, due to the additional states. However the dynamic response of Borah’s model is almost identical to the example shown here.

We conclude that Merfeld’s Observer model is a lower order equivalent system to Borah’s KF, at least for the values of process and measurement noise and shaping filter bandwidths chosen by Borah.

#### 4.1.2.3. Ecologic basis for 1-D Kalman filter model parameters

Although Boral et al. (1978) considered  $Q$ ,  $V$  and  $\beta_\omega$  to be free parameters, they noted that the head motion input should be “a typical spectrum associated with walking and running or perhaps a typical average aircraft flight spectrum, however, neither of the above is well known”. They assumed measurement noise was simply an arbitrary fraction of the noise in the state estimate. However, we believe that KF parameters should not be considered entirely

free. Ecologically, it makes sense to think that the parameters of the process noise and shaping filter should reflect the spectrum of yaw head movements normally made in daily life. Similarly, we argue the measurement noise ought to determine the human perceptual threshold for motion detection when the subject is motionless. The bandwidth  $\beta_\omega$  of the shaping filter in the KF determines the relationship between  $Q$  (the covariance of the process noise  $w(t)$ ) and the covariance of the head angular velocity  $\omega_z(t)$  experienced by the subject. Passing a white noise  $w(t)$  with covariance  $Q$  through the shaping filter results in a signal  $\omega_z(t)$  whose spectral density function is given by:

$$\Phi_{\omega_z}(s) = Q \frac{1}{-s^2 + \beta_\omega^2} \quad (4.6)$$

And whose autocorrelation function is given by:

$$\phi_{\omega_z \omega_z}(\tau) = \frac{Q}{2\beta_\omega} e^{-\beta_\omega |\tau|} \quad (4.7)$$

Therefore, the variance of the signal  $\omega_z(t)$  is:

$$\sigma_{\omega_z}^2 = \phi_{\omega_z \omega_z}(0) = \frac{Q}{2\beta_\omega} \quad (4.8)$$

Hence, if we can estimate the variance of the head movement signal encountered in daily life, the variance of the associated white noise signal is  $Q = 2\beta_\omega \sigma_{\omega_z}^2$ .

The values of  $\sigma_{\omega_z}^2$  and  $\beta_\omega$  depend on the amplitude and frequency content of head motions made in daily life, which are biomechanically determined. Human locomotion typically occurs at frequencies up to 2-4 Hz. Active yaw head movements are usually in the range below 200 deg/s where the pursuit tracking and vestibule-ocular reflexes work well. Hence we estimate  $\beta_\omega = 25$ ,  $\sigma_{\omega_z}^2 = 12.2$  and so  $Q = 609$ .

Since  $K_1 \approx 0$  the shaping filter also determines how much measurement noise is expressed in the KF angular velocity estimate  $\hat{\omega}_z$  when the head is motionless. By similarity to equations , the measurement noise covariance is  $V = 2\beta_\omega \sigma_{\hat{\omega}_z}^2$ . We argue that  $\sigma_{\hat{\omega}_z}$  should correspond to the human perception threshold for passive angular motion perception, about 2 deg/s, so  $\sigma_{\hat{\omega}_z}^2 = 0.0012$ , and hence  $V = 0.061$ . Note that  $Q/V = \sigma_{\omega_z}^2 / \sigma_{\hat{\omega}_z}^2 = 10^4$ , more than an order of magnitude lower than the  $Q/V$  ratio assumed by Borah. Solving for the Kalman gains (eq. 1.31 ),  $K = [0 \ 78]^T$ . The KF residual pathway gain  $K_2 / \beta_\omega = 3.1$  is identical to Merfeld's proposed value of  $k_\omega$ , and close to Borah's model. As shown in figure 4.7, Riccati equation (1.30) solutions for other combinations of  $\beta_\omega$  bandwidth and  $Q/V$  yield values of KF gain  $K_2$  such that  $K_2 / \beta_\omega$  remains close to that of Merfeld Observer model. However, we argue that  $\beta_\omega = 25$  and  $Q/V = \sigma_{\omega_z}^2 / \sigma_{\hat{\omega}_z}^2 = 10^4$  can be ecologically justified based on human



movement and threshold characteristics. This allows us to suggest that human angular velocity estimates appear optimal in a mean square error stochastic sense. Borah et al. and Merfeld et al. could not make that assertion, since they offered empirical, rather than ecologic justification for their choice of model parameters.

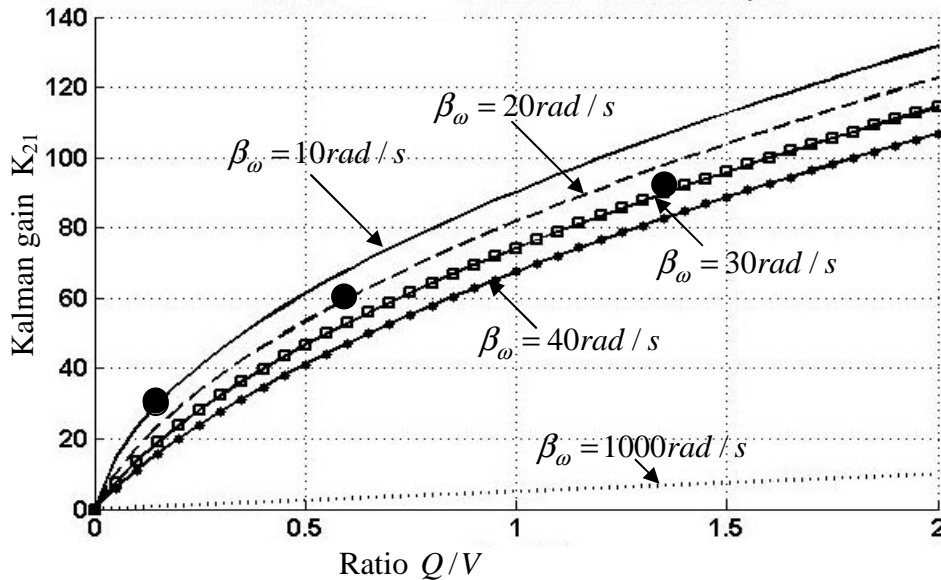


**Figure 4.7.** Kalman gain  $K_{21}$  with respect to  $Q/V$  ratio and shaping filter bandwidth. Black dots show parameter combinations where  $K_2 / \beta_\omega = 3$ , equivalent to the Merfeld and Borah models.

One could ask: what does a KF model response look like where  $Q/V = \sigma_{\omega_z}^2 / \sigma_{\hat{\omega}_z}^2 = 10^4$  but shaping filter has a much broader bandwidth (i.e.  $\beta_\omega \gg 25$ )? As shown in figure 4.7, as  $\beta_\omega$  increases, Kalman gain  $K_2$  decreases, and  $K_2 / \beta_\omega$  become less than 3. Both the magnitude and dominant time constant of the  $\hat{\omega}_z(t)$  response shorten compared to empirical values. There is some empirical evidence that prolonged occupational exposure to high motion environments (e.g. figure skating, gymnast, flying) reduces the gains and time constants of angular velocity perception (e.g. Groen 1962).

### 4.1.3. Observer and KF 3-D model for somatogravic illusion in darkness

In this section we model the somatogravic illusion which is elicited by sustained linear acceleration when no visual cues are available. This kind of illusion is well known in aviation and its most common form is the sense of pitching up when taking off into poor visibility. Basically the pilot undergoes a sustained forward linear acceleration which produces a backward inertial reaction force. When combined with the 1-G downward gravitational force, the net gravito-inertial force vector is rotated backward. This rotation might produce a pitch-up illusion (Fig. 4.8).

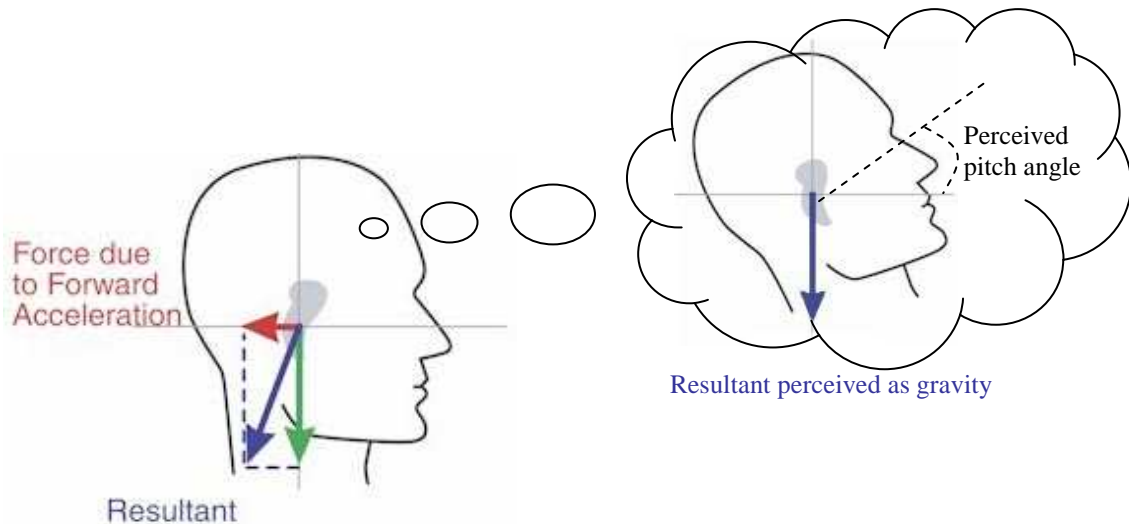


**Figure 4.8.** Somatogravic illusion. The subject experiences a sustained forward acceleration. The resulted sensation is an illusion of pitching up.

To model this phenomenon, the previous one-dimensional model needs to be extended to a three-dimensional version, and has to take into account the otolith organs which sense linear acceleration. In the following sections, the structures of the 3D Merfeld Observer model as well as the 3D Borah Kalman filter model are introduced. We then compare the response provided by both model and demonstrate why these two models are dynamically equivalent.

#### 4.1.3.1. Three-dimensional Merfeld Observer model for large tilts

The observer model has been extended to a three dimensional representation by replacing scalar values with vectors, and by replacing the transfer function of the sensory organs with 3x3 matrices transfer functions. The inputs of the model are angular velocity and linear acceleration (Fig. 4.9). In this configuration, three dimensional rotations change the orientation of the gravity relatively to the head coordinate frame. This point, which involves non-linearity in the model, has to be taken into account. This is what the block “rotate g” performs. Indeed, by knowing the current position of the gravity vector and the imposed angular velocity vector  $\vec{\omega}$ , the block “rotate g” keeps tracks in real time of the direction of down. To perform this, Merfeld used a quaternion integration.

According to Einstein’s equivalence principle, all linear accelerometers must measure both linear acceleration and gravity. Therefore, the otolith organs – which respond to translational motions and tilts of our body - must sense the gravitoinertial force  $\vec{f}$ . The gravitoinertial force is given by the difference between the gravity vector and the potential external linear acceleration; so that  $\vec{f} = \vec{g} - \vec{a}$ . The internal hypothesis suggests that the nervous system somehow knows these two physical effects, i.e the tracking of the gravity vector and the computation of the gravitoinertial force. To mimic these physical relationships, internal representations are implemented by assuming they have the same form. In particular, the perceived GIF is given by the difference between the internal estimates of gravity and linear acceleration such as  $\hat{f} = \hat{g} - \hat{a}$ .

The block diagram below shows the structure of the Observer model derived by Merfeld (Fig. 4.9). The angular velocity and the gravito-inertial force are respectively sent to the canals and the otolith organs. The internal model is composed of different loops to provide estimation of angular velocity, linear acceleration and gravity. Merfeld et al. arbitrarily considered four gains, one for each loop, that provide the only free parameter of the model. Double arrows show the pathway of the previous 1D model which yields angular velocity storage. In three-dimensional space, this path is affected by the otolith sensory afference through a gain  $k_{f\omega}$ . A feedback loop with a gain  $k_a$  is used to provide an estimate of linear acceleration whereas another loop with a gain  $k_f$  affects the computation of the estimated gravity vector. The transfer function of the SCC is the same as the 1D model. As regard the otolith dynamics, Goldberg and Fernandez (1976) experimentally determined a second order transfer function by recording the response of peripheral afferent neurons of the squirrel monkey. However, Merfeld considered a simplify model of otolith dynamics, in particular a lower order transfer function by considering the lowest pole, so as to reduce system stiffness for purposes of numerical stability. He chose to model the dynamics of the otolith organs by a low pass filter with cut-off frequency of 2Hz, so that the otolith transfer function is given by:

$$TF_{oto} = \frac{1}{s\tau_{oto} + 1} \quad (4.9)$$

with  $\tau_{oto} = 1/(2\pi f) \approx 0.08s$

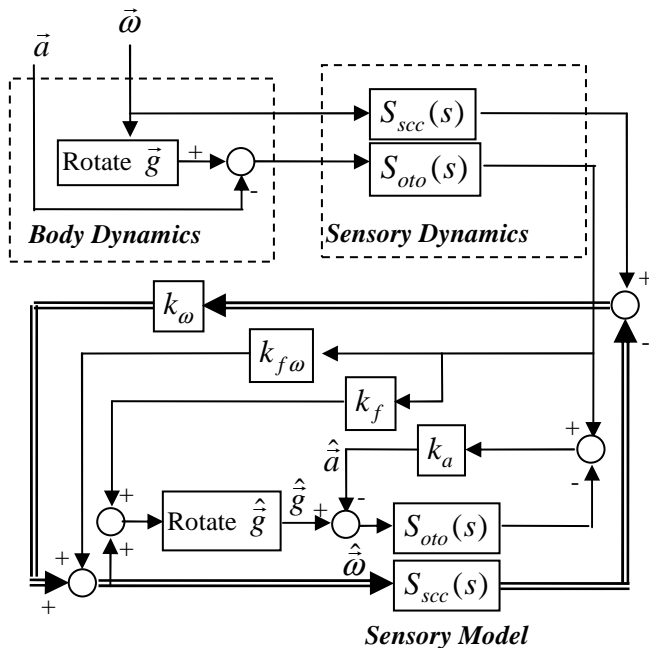


**Figure 4.9.** 3D Observer model. Double arrows show the 1D model pathways presented earlier.  $\hat{a}$ ,  $\hat{f}$ , and  $\hat{\omega}$  correspond to perception of linear acceleration, gravity, and angular velocity, respectively.

#### 4.1.3.2. Three-dimensional Borah steady state Kalman filter for small tilts

As the 3-D Borah's model was linearized near a head upright position, it only works for small head tilts. The three-dimensional internal model is presented in figure 4.10.

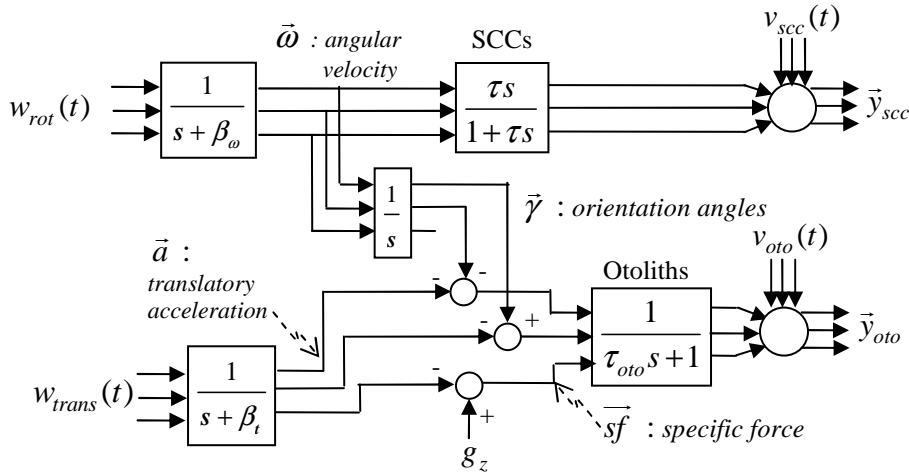


**Figure 4.10.** 3D internal model used in the present Kalman filter model. Note that Borah used a different transfer function for the otoliths. For comparison purposes, the transfer function used in Merfeld's model is also utilized in the following Kalman filter model.

White process noises  $w_{rot}(t)$  and  $w_{trans}(t)$  are passed through first order filters to generate angular velocity and linear acceleration. The angular velocity is then integrated to approximate orientation angle ( $\gamma$ ). The otolith organs are driven by the gravito-inertial acceleration equal to  $\vec{f} = \vec{g} - \vec{a}$ . The linearization about an upright position means that the orientation angle vector  $\vec{\gamma}$  has small components, so that the projection of the  $\vec{g}$  vector in the head coordinate frame is equal to  $g\vec{\gamma}$ . Finally, measurement noise is added.

The model is described in state space form by:

$$\frac{d\vec{x}(t)}{dt} = A\vec{x}(t) + Gw(t) \quad (4.10)$$

$$\vec{y}(t) = C\vec{x}(t) + v(t) \quad (4.11)$$

$$\text{With } A = \begin{pmatrix} 0 & 1 & 0 & 0 & 0 \\ 0 & -\beta_\omega & 0 & 0 & 0 \\ 0 & 1 & -1/\tau & 0 & 0 \\ 0 & 0 & 0 & -\beta_t & 0 \\ -1 & 0 & 0 & 1 & -1/\tau_{oto} \end{pmatrix}; E = \begin{pmatrix} 0 & 0 & 0 & 1 & 0 \\ 0 & 1 & 0 & 0 & 0 \end{pmatrix}^T; C = \begin{pmatrix} 0 & 1 & -1/\tau & 0 & 0 \\ 0 & 0 & 0 & 0 & 1/\tau_{oto} \end{pmatrix}.$$

Only five states are needed to model this experiment as only one component for both the linear acceleration and angular velocity are required. The states  $x_1$ ,  $x_2$  and  $x_4$  correspond to the pitch angle orientation, the angular velocity around the pitch axis and the forward linear acceleration respectively. The states  $x_3$  and  $x_5$  correspond to internal states of the sensors transfer function.

The process and measurement noises used in the simulation are:

$$w_{rot}(t) \sim N(0,120); w_{trans}(t) \sim N(0,0.1)$$

$$v_{rot}(t) \sim N(0, 10^{-3}); v_{trans}(t) \sim N(0, 10^{-4})$$

The initial conditions assumed by the filter are:

$$\hat{x}(0|0) = (0 \ 0 \ 0 \ 0 \ 0)^T \text{ and } P(0|0) = \begin{pmatrix} 10^{-3} & 0 & 0 & 0 & 0 \\ 0 & 10^{-3} & 0 & 0 & 0 \\ 0 & 0 & 10^{-3} & 0 & 0 \\ 0 & 0 & 0 & 10^{-4} & 0 \\ 0 & 0 & 0 & 0 & 10^{-3} \end{pmatrix}.$$

The steady state Kalman gain computation yields a 5x2 gains matrix. Each of these gains shapes the evolution of each state variable. However, it can be shown that four gains are required to capture the main behaviour of each state variable, the same number of gains used in the Observer. The minimum set of gains needed is  $(K_{21}, K_{12}, K_{32}, K_{42})$ . However, the structure of the Observer and the Kalman filter are different as the Kalman gains are applied to the rate of change of the state variables.

In the present case,  $K = \begin{pmatrix} 0.95 & -4.03 \\ 334.6 & -0.83 \\ 0.95 & -3.16 \\ 0.005 & -18.95 \\ -0.002 & 1.16 \end{pmatrix}$ . The dominant terms are the one circled and

setting the other to zero does not affect the result of the simulation. The update state equations of the steady state continuous Kalman filter are thus given by:

$$\dot{\hat{x}}_1(t) = \hat{x}_2(t) + K_{12} \tilde{y}_{oto}(t) \quad (4.12)$$

$$\dot{\hat{x}}_2(t) = -\beta_\omega \hat{x}_2(t) + K_{21} \tilde{y}_{scc}(t) \quad (4.13)$$

$$\dot{\hat{x}}_3(t) = \hat{x}_2(t) - \frac{1}{\tau} \hat{x}_3(t) + K_{32} \tilde{y}_{oto}(t) \quad (4.14)$$

$$\dot{\hat{x}}_4(t) = -\beta_t \hat{x}_4(t) + K_{42} \tilde{y}_{oto}(t) \quad (4.15)$$

$$\dot{\hat{x}}_5(t) = -\hat{x}_1(t) + \hat{x}_4(t) - \frac{1}{\tau_{oto}} \hat{x}_5(t) \quad (4.16)$$

The resulting three-dimensional model is presented in figure 4.11.

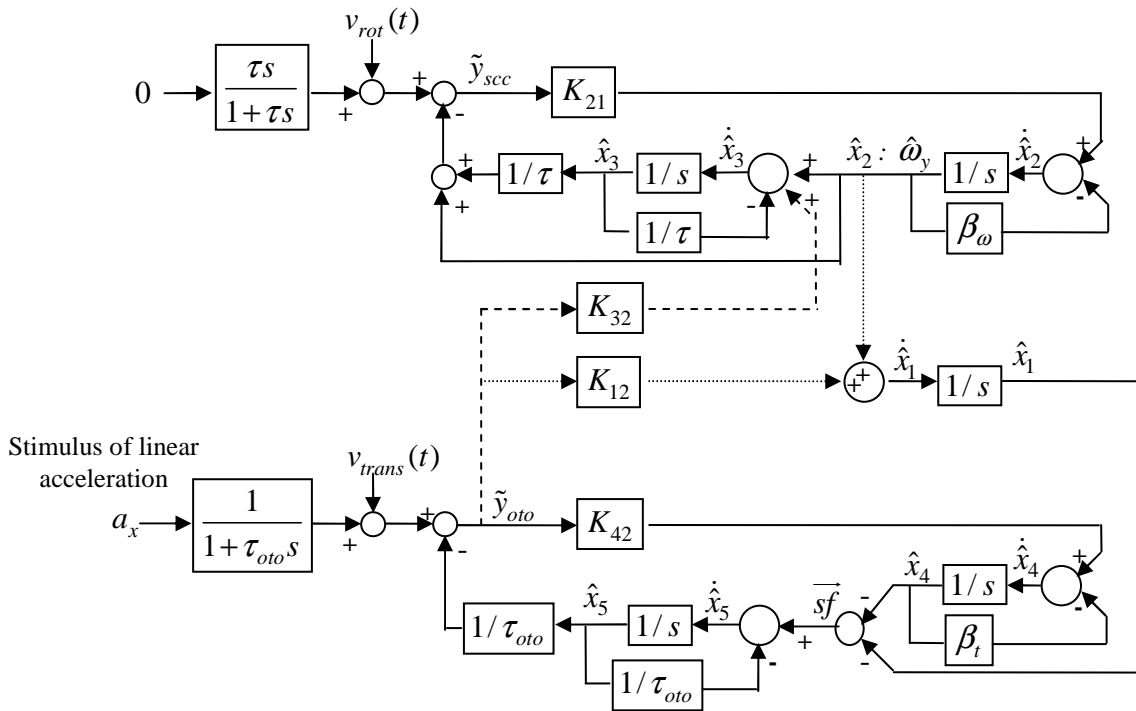


**Figure 4.11.** Block diagram of the steady state Kalman filter for the somatogravic illusion. The system corresponds to a KF with only the four necessary gains.  $\hat{x}_1$ ,  $\hat{x}_2$ , and  $\hat{x}_4$  correspond to perception of orientation, angular velocity, and linear acceleration, respectively.

Figure 4.12 shows the response of the Kalman filter model developed above and of the Merfeld Observer model. It can be seen that the perceived linear acceleration and the perceived pitch angle provided by both models are close, at least for the set of parameters assumed.

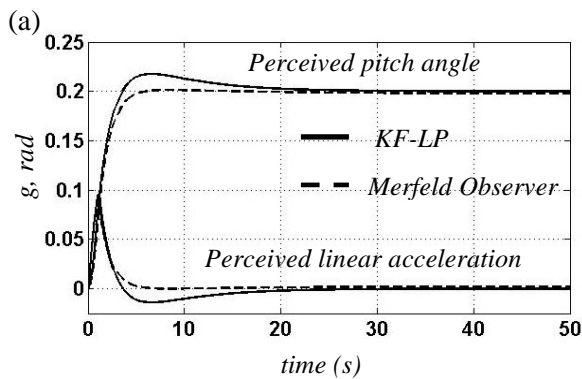


**Figure 4.12.** Perception of linear acceleration and pitch angle in response to a forward linear acceleration of 0.2g provided by Merfeld Observer and Kalman filter model. Both models consider a low pass filter of cut-off frequency 2Hz for otolith dynamics.

By the way, Borah used a much slower otolith dynamics than that considered by Merfeld. More particularly, Borah took into consideration a higher order transfer function of the form:

$$TF 2_{oto} = \frac{90(s+0.1)}{s+0.2} \quad (4.17)$$

Nevertheless, for the same values of bandwidths, both Kalman filters – one with the low pass filter and the other with Borah’s transfer function for otoliths dynamics – produce similar results (Fig. 4.13). One can note however that the outputs of the Kalman filter depend largely on the assumed bandwidths. As it can be seen on figure 4.14, the lower is the translational bandwidth: 1) the higher is the magnitude of perceived linear acceleration, 2) the longer is the duration of the perceived linear acceleration, 3) the slower is the perception of tilt around the pitch axis.

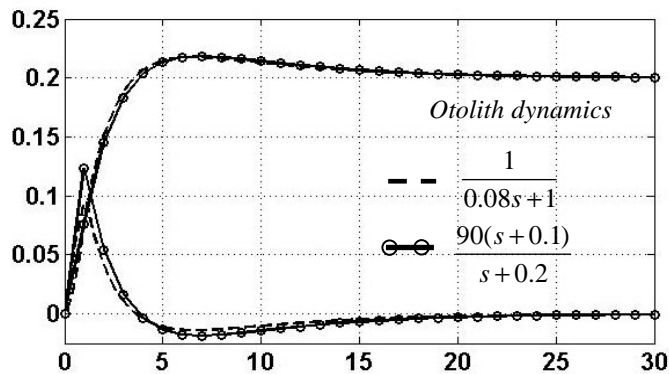


**Figure 4.13.** Perception of linear acceleration and pitch angle in response to a forward linear acceleration of 0.2g provided by the Kalman filter model for two different otolith dynamics.

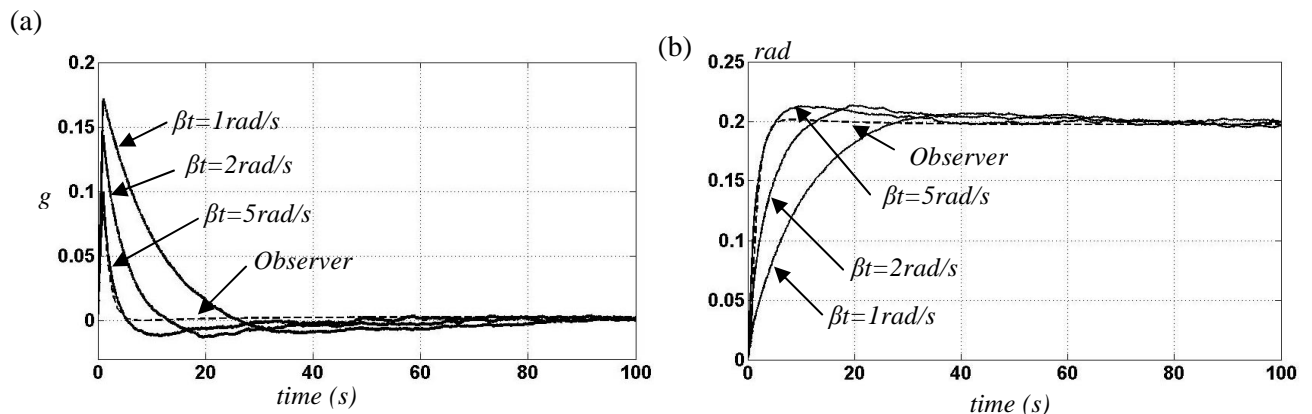


**Figure 4.14.** Response of the Kalman filter model with Borah’s otolith transfer function for different bandwidths of linear acceleration. (a) Perception of linear acceleration; (b) perception of pitch angle.

## Conclusion

Even though Merfeld’s model and Borah’s model are based on different approaches and assumed empirical data, we have shown that both models are dynamically equivalent from an input-output blackbox as they produce similar results in terms of perception (estimation) of head angular velocity, linear acceleration, and orientation.

We have argued that the presence of the low pass filters used to shape the process noise means that the brain expects head angular velocities and linear accelerations in a certain range of frequencies. We have supposed that these filters somehow reflect past motion history, i.e. kind of motion our head has encountered in the past and that the central nervous system might expect. Therefore, we have suggested that the bandwidths of these bandlimited filters should be determined by a person's motion exposure history.

We have also demonstrated that the shaping filter is also a mathematical device to augment the size of the state vector by adding one more state that corresponds either to head angular velocity or head linear acceleration. Thus, it gives us a mean to estimate perception of head angular velocity and head linear acceleration. Note also that they control the magnitude of the process noise covariance.

Finally, even if Borah used a slower otolith dynamics than that considered in Merfeld's Observer, we have shown that perception of motion and orientation provided by the Kalman Filter do not depend very much on the dynamics of the otoliths. For the same value of bandwidths, both Kalman filters look almost the same



## 4.2. Nonlinear models for human spatial orientation based on the hybrid extended and unscented Kalman filter

As previously described, Borah's Kalman filter model for human spatial orientation is valid only for a head orientation near the upright position. In order to develop a model for human spatial orientation that works for any head tilt, the transformation between head coordinate system and world reference frame must be considered. This transformation which can be defined either by Euler angles or quaternion parameters is nonlinear. Thus, a modified version of the Kalman filter has to be used to estimate the state variables of this nonlinear system. Different techniques apply the Kalman filter framework to nonlinear Gaussian systems, such as the Extended Kalman Filter or the Unscented Kalman Filter.

In the following sections, we first apply both the hybrid extended Kalman filter and the unscented Kalman filter to develop a model of human spatial orientation. First, we define the coordinate system as well as the sensors dynamics used in the model. Second, we present the "real world model" that permits to generate sensors measurement, and the "internal model" of the central nervous system. Third, by assuming that the central nervous system works as an optimal estimator, we formulate more precisely the internal model using state space representation. Finally, we simulate different motion paradigms and present modeling results for several vestibular and visual – vestibular illusions provided by both the EKF and the UKF models.

### 4.2.1. Coordinate system

We consider a (XYZ) coordinate system related to the Earth, and a (x,y,z) coordinate system related to the vehicle in which the pilot is flying.

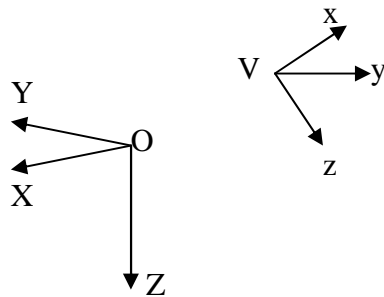
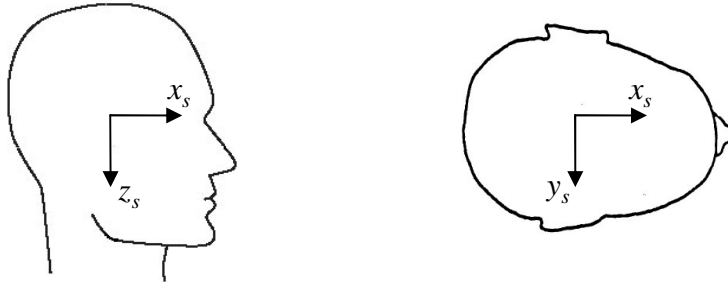


Figure 4.15. Head and world coordinate frame.

For modeling purposes, we take into consideration a cyclopean set of canals and otoliths located at the center of the head (Fig. 4.16). First, this assumption means that only one vestibular system is considered. This implicitly assumes that the subject has two healthy vestibular systems. Second, considering a cyclopean set of sensors implies that linear acceleration components (normal and tangential), which acts on the otolith organs, created by a rotational motion are not taken into account. In the present context, this simplification is sufficient to model the notion of perception of orientation, at least for a subject without vestibular disorder.

An input to our sensors model can thus be characterized by a function of time describing the movement of the vehicle ( $V, x, y, z$ ) in the inertial space. The orientation process consists in knowing at each time the transformation matrix between  $(x, y, z)$  and  $(X, Y, Z)$ . This is done by quaternion integration and then a transformation from quaternion parameters to Euler angles.



**Figure 4.16.** Coordinate system attached to the sensors

### 4.2.2. Modeling of the sensors

The model takes into account visual and vestibular cues. The visual-orientation process can be divided into two distinct categories: the focal vision which is related to object recognition, and the ambient vision for general spatial orientation. In this study, we consider only the ambient vision which provides both motion cues and position cues. For simplicity we assume that the visual sensory dynamics can be approximated as unity transfer function which responds to both angular and linear velocity of the visual environment. Since dynamic inputs illicit a sensation of motion in the opposite direction of the visual field (e.g. linearvection or angularvection) the dynamic sensors are modeled in three-dimensional space as a negative  $3 \times 3$  identity matrix.

As regard the vestibular system, the SCCs as well as the otolith organs are assumed located at the center of the head. We model the SCCs as a single set of three orthogonal canals. They are supposed identical, uncoupled, and can thus be modeled in three dimensional space by a set of three identical transfer functions. As mentioned in the background section, the dynamics of each SCC and otolith organ can be modeled by a second order filter. We here chose to use the Fernandez and Goldberg transfer function to represent the dynamics of the SCC and to retain the Telban and Cardullo transfer function to relate otolith afferent firing rate with the gravito-inertial force. These transfer function are reminded in figure 4.17.

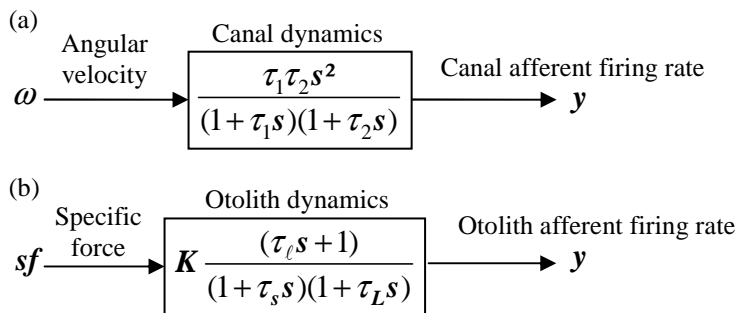


**Figure 4.17.** Sensors transfer functions used in the EKF and UKF models. (a) Semicircular canal model with  $\tau_1 = 6s$  and  $\tau_2 = 80s$  (Goldberg et al., 1971); (b) Otolith model with  $\tau_L = 5s$ ,  $\tau_s = 0.016s$ ,  $\tau_\ell = 10s$ , and  $K = 33.3$  (Telban RJ, 2005).

### 4.2.3. Description of the model

The philosophy of the developed model of human spatial orientation perception is presented in figure 4.18.

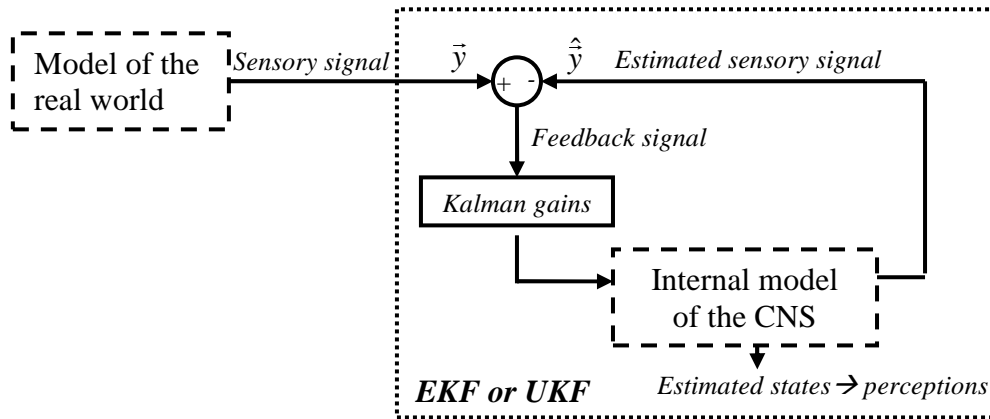


**Figure 4.18.** Philosophy of the model of human orientation perception. The model of the real world is used to generate the output of each sensor. It is assumed that the CNS has an internal representation of the real world denoted as “internal model”. Assuming that the CNS performs the estimation of the state vector in an optimal sense, the CNS is modeled as an Extended or Unscented Kalman filter (EKF or UKF). The estimated states of the internal model correspond to the subject perception of orientation, angular velocity and linear acceleration. The internal model provides an expected sensor signal vector which is compared with the actual sensory signal vector. The resulting feedback signal is then weighted by some Kalman gains which then drive the estimated states

A model of the real world, which will be detailed later, is used to generate a sensory output vector comprised of the signals provided by the semicircular canals, the otolith organs and the visual system. The true dynamics of the body and sensors of a passive subject that experiences angular velocity or linear acceleration can be described by:

$$\dot{\bar{x}}(t) = f(\bar{x}(t), \bar{u}) + w(t) \quad (4.18)$$

where  $\bar{x}$  is the state space vector containing variables of position, velocity, acceleration, and internal states of the sensors transfer function,  $\bar{u}$  is the external motion input applied to the body and  $w(t)$  is a zero mean white process noise. The measurement provided by the sensors are given by:

$$\bar{y}_k = h(\bar{x}, \bar{u}) + v_k \quad (4.19)$$

where  $y_k$  is the output vector coming out from the sensors, and  $v_k$  is a zero mean white noise modeling the biological noise corrupting the afferent neurons signals.

Models of spatial orientation are based on the idea that the central nervous system has an internal model of the real world. In other words, it somehow knows the dynamics of the sensors which sense position and motion as well as some physical equations. The idea for the central nervous system (CNS) having an internal model of the real world means that it knows

both functions  $f$  and  $h$ . The problem faced by the central nervous system consists in estimating the random state vector of the internal model given a set of noisy measurements which are computed by the real world model (Fig. 4.18). It is assumed that these internal model estimates correspond to perceptions of orientation, angular and linear velocity, and linear acceleration.

To achieve this goal, the CNS is modeled by a nonlinear suboptimal estimator. Both the hybrid extended Kalman filter and the hybrid unscented Kalman filter are applied to this estimation problem. Hybrid version of these two filters means that the system is modeled by continuous-time dynamics and measurements are obtained at discrete-time instants.

#### 4.2.3.1. Real world model

The model of the real world, which permits to generate the sensors measurements vector, is presented in figure 4.19. The blocks “Canals dynamics” and “Otolith dynamics” are composed of three SCC transfer functions and three otoliths transfer functions respectively, one for each component of angular velocity and gravito-inertial acceleration. Angular velocity is passed through the semicircular canals transfer function to produce sensory afferent signals as well as the visual transfer functions to get information of the visual field rotation. In order to keep track of the direction of down when our head rotates, we have to be able to compute our orientation relatively to the earth coordinate frame. This task is performed by quaternion integration rather than a classic Euler representation as quaternions eliminate gimbal lock, reduce numerical storage from 9 to 4 digits, and increase computational stability. The quaternion equations and the transformation between quaternion parameters and Euler angles are defined in appendix 2. The gravito-inertial force, defined as the difference between the gravity and the linear acceleration, is passed through the otolith transfer function to get a three-dimensional otolith afferent rate vector. Finally, linear velocity obtained from the direct integration of linear acceleration is applied to a negative identity transfer function to get the visual field translation velocity. The computation of the sensor output vector  $\bar{y}$  can be performed using the Simulink model presented in appendix 3.

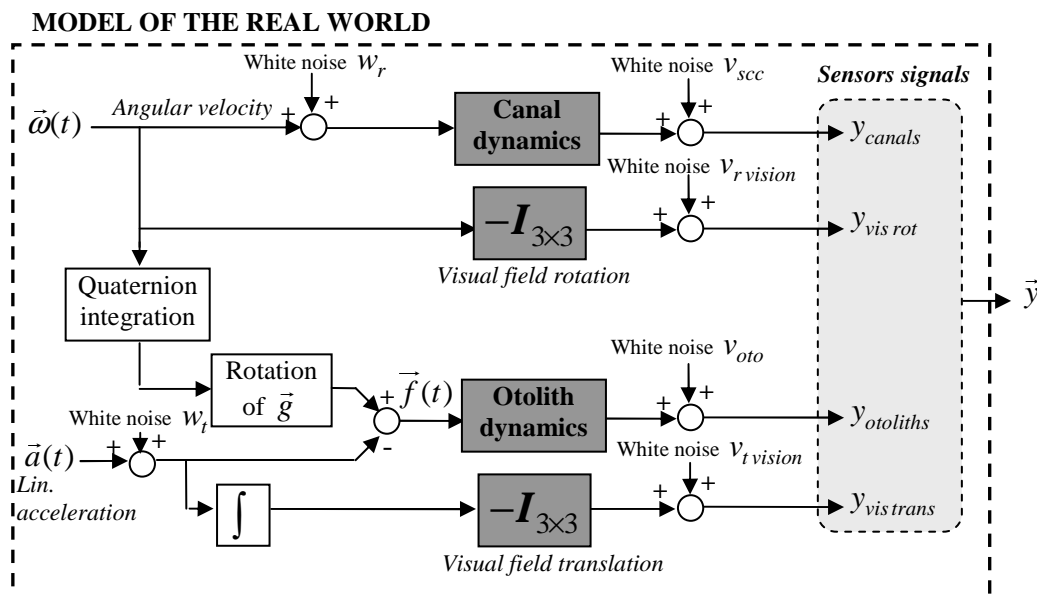


Figure 4.19. Detailed view of the model of the real world.

### 4.2.3.2. Internal model of the CNS

The internal model of the central nervous system is presented in figure 4.20. It is different than the real world model in the sense that the CNS does not know which motion the subject is going to experience. This means the CNS does not know the input, which is a part of what it has to estimate. Nevertheless, it can be assumed that the CNS has some expectation about the frequency range of the motion the body is going to encounter. In other words, the CNS expects a certain bandwidth of angular velocity and linear acceleration. Therefore, we use two low pass filters – as in Borah model (1988) – to generate angular velocity and linear acceleration (figure 4.20).

The nervous system is also facing other problems that arise when one tries to use the sensor output to compute position and orientation in space:

- As stated by various researchers, the otoliths alone are not sufficient to distinguish between gravity and linear acceleration. This physical fact is a problem faced by any linear accelerometer, and is commonly referred to as gravito-inertial force (GIF) resolution.
- Correct implementation of rotational kinematics requires a three-dimensional angular velocity to orientation integration.

These two problems must be considered by the CNS when attempting to process ambiguous motion cues.

As already mentioned in section 4.1.3.1, linear accelerometers (including the otoliths) respond similarly to inertial and gravitational accelerations (Einstein's equivalence principle, Einstein 1908). The otoliths can only measure the sum of both as follows:

$$\vec{f} = \vec{g} - \vec{a} \quad (4.20)$$

where  $\vec{f}$  denotes the total linear acceleration measured by the otoliths, which is composed of gravitational acceleration  $\vec{g}$  and other translational acceleration  $\vec{a}$ . Thus, otolith afferent provide inherently ambiguous sensory information, given that the encode acceleration could have been generated during either actual translation or a head reorientation relative to gravity (Angelaki and Dickman, 2000). Therefore, the problem of GIF resolution has to be solved by the CNS using other information.

A lot of studies (e.g. Zupan et al. 2004) have supported the hypothesis that the CNS knows the physical relationships between gravity, translational acceleration and gravito-inertial force. In other words, the neural representation of gravity  $\hat{g}$  minus the neural representation of linear acceleration  $\hat{a}$  equals the neural representation of GIF, consistent and mimicking the real world physics such as:

$$\hat{f} = \hat{g} - \hat{a} \quad (4.21)$$

where  $\hat{f}$  is the estimate of the total acceleration,  $\hat{g}$  is the current estimate of gravity, and  $\hat{a}$  is the current estimate of translatory acceleration.

Similarly, transformation between head coordinate system and world reference frame requires a three-dimensional angular velocity to orientation integration. This integration is performed using quaternion mathematics. We hypothesized that the CNS also performed this integration so as to provide an internal estimate of the direction of down, i.e. an estimate of the gravity vector, as well as internal estimates of orientation angles.

Finally we assume that the brain has an exact knowledge of the sensors dynamics, so that the transfer functions of the SCC and otolith organs have the same form as in the real world model.

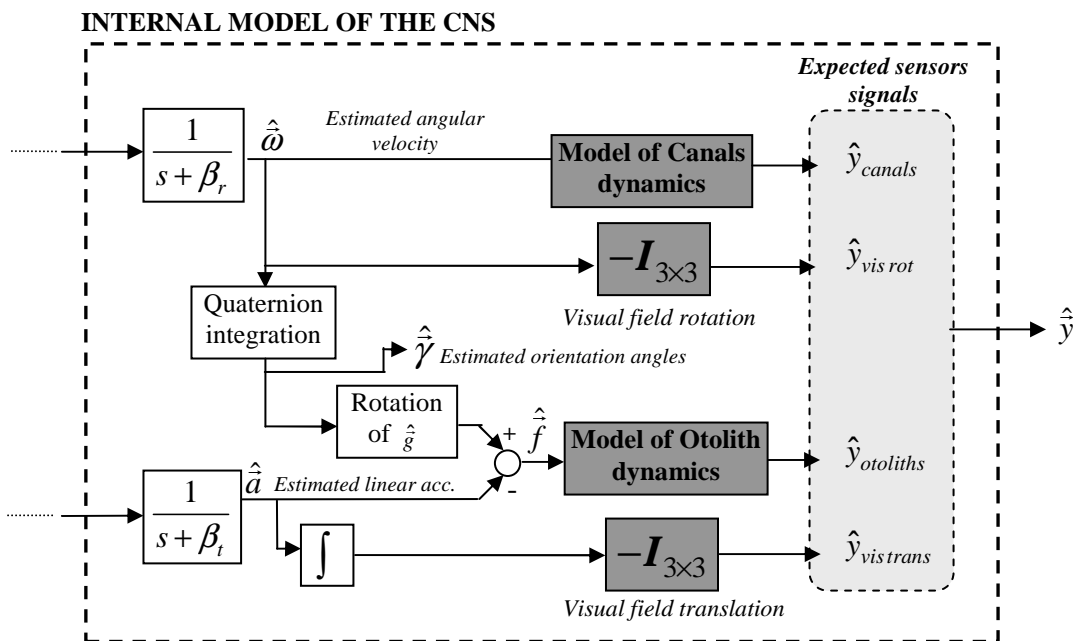


**Figure 4.20.** Detailed view of the internal model of the CNS. This block is a part of figure 4.18. We assume that the CNS expects angular velocity and linear acceleration in a certain frequency range. Thus, two low pass filters with cut-off frequency  $\beta_r$  and  $\beta_t$  respectively are used. It is also supposed that the CNS performs a quaternion integration to provide an internal estimate of the direction of down and computes the difference between the estimated gravity  $\hat{g}$  and linear acceleration  $\hat{a}$  vectors to produce an estimate of the gravito-inertial force  $\hat{f}$ . The transfer functions of the sensors have the same form as in the real world model.

## 4.2.4. Estimation process

### 4.2.4.1 State vector update

The model can be written in a state-space differential equation of the form:

$$\dot{\bar{x}}(t) = f(\bar{x}(t)) + \bar{w}(t) \quad (4.22)$$

$\bar{x}$  is a state vector of dimension 25, expressed in the head reference system and partitioned as follows:

- ( $x_1, x_2, x_3, x_4$ )	quaternion parameters ( $q_0, q_1, q_2, q_3$ )
- ( $x_5, x_6, x_7$ )	angular velocity ( $\omega_x, \omega_y, \omega_z$ )
- ( $x_8, x_9, x_{10}$ )	linear velocity ( $V_x, V_y, V_z$ )
- ( $x_{11}, x_{12}, x_{13}$ )	linear acceleration ( $a_x, a_y, a_z$ )
- ( $x_{14}, x_{15}, x_{16}, x_{17}, x_{18}, x_{19}$ )	variables of SCCs transfer function
- ( $x_{20}, x_{21}, x_{22}, x_{23}, x_{24}, x_{25}$ )	variables of otoliths transfer function

- Quaternion differential equations

In order to update the quaternion vector as we rotate in inertial space the initial quaternion must be integrated with respect to the angular velocity input  $\vec{\omega}(t) = (\omega_x, \omega_y, \omega_z)$ . The integration of the rate of change of the quaternion vector is given below. The gain  $\lambda$  drives the norm of the quaternion to 1.0. The value of this gain must be chosen with care, because a large value improves the decay rate of the error in the norm, but also slows the simulation. A value of 0.9 worked best for our sample rate.

$$\begin{pmatrix} \dot{q}_0 \\ \dot{q}_1 \\ \dot{q}_2 \\ \dot{q}_3 \end{pmatrix} = \frac{1}{2} \begin{pmatrix} 0 & -\omega_x & -\omega_y & -\omega_z \\ \omega_x & 0 & \omega_z & -\omega_y \\ \omega_y & -\omega_z & 0 & \omega_x \\ \omega_z & \omega_y & -\omega_x & 0 \end{pmatrix} \begin{pmatrix} \dot{q}_0 \\ \dot{q}_1 \\ \dot{q}_2 \\ \dot{q}_3 \end{pmatrix} + \lambda \varepsilon \begin{pmatrix} \dot{q}_0 \\ \dot{q}_1 \\ \dot{q}_2 \\ \dot{q}_3 \end{pmatrix} \quad \text{with } \varepsilon = 1 - (q_0^2 + q_1^2 + q_2^2 + q_3^2) \quad (4.23)$$

According to (4.23), quaternion equations in terms of state space variables are given by:

$$\dot{x}_1 = \frac{1}{2}(-x_5x_2 - x_6x_3 - x_7x_4) + 0.9x_1(1 - (x_1^2 + x_2^2 + x_3^2 + x_4^2)) \quad (4.24)$$

$$\dot{x}_2 = \frac{1}{2}(x_5x_1 + x_7x_3 - x_6x_4) + 0.9x_2(1 - (x_1^2 + x_2^2 + x_3^2 + x_4^2)) \quad (4.25)$$

$$\dot{x}_3 = \frac{1}{2}(x_6x_1 - x_7x_2 + x_5x_4) + 0.9x_3(1 - (x_1^2 + x_2^2 + x_3^2 + x_4^2)) \quad (4.26)$$

$$\dot{x}_4 = \frac{1}{2}(x_7x_1 + x_6x_2 - x_5x_3) + 0.9x_4(1 - (x_1^2 + x_2^2 + x_3^2 + x_4^2)) \quad (4.27)$$

Therefore, the update of the corresponding estimated state variables is given by:

$$\dot{\hat{x}}_1 = \frac{1}{2}(-\hat{x}_5\hat{x}_2 - \hat{x}_6\hat{x}_3 - \hat{x}_7\hat{x}_4) + 0.9\hat{x}_1(1 - (\hat{x}_1^2 + \hat{x}_2^2 + \hat{x}_3^2 + \hat{x}_4^2)) + \sum_{i=1}^r K_{1i}\tilde{y}_i \quad (4.28)$$

$$\dot{\hat{x}}_2 = \frac{1}{2}(\hat{x}_5\hat{x}_1 + \hat{x}_7\hat{x}_3 - \hat{x}_6\hat{x}_4) + 0.9\hat{x}_2(1 - (\hat{x}_1^2 + \hat{x}_2^2 + \hat{x}_3^2 + \hat{x}_4^2)) + \sum_{i=1}^r K_{2i}\tilde{y}_i \quad (4.29)$$

$$\dot{\hat{x}}_3 = \frac{1}{2}(\hat{x}_6\hat{x}_1 - \hat{x}_7\hat{x}_2 + \hat{x}_5\hat{x}_4) + 0.9\hat{x}_3(1 - (\hat{x}_1^2 + \hat{x}_2^2 + \hat{x}_3^2 + \hat{x}_4^2)) + \sum_{i=1}^r K_{3i}\tilde{y}_i \quad (4.30)$$

$$\dot{\hat{x}}_4 = \frac{1}{2}(\hat{x}_7\hat{x}_1 + \hat{x}_6\hat{x}_2 - \hat{x}_5\hat{x}_3) + 0.9\hat{x}_4(1 - (\hat{x}_1^2 + \hat{x}_2^2 + \hat{x}_3^2 + \hat{x}_4^2)) + \sum_{i=1}^r K_{4i}\tilde{y}_i \quad (4.31)$$

where  $r$  is the dimension of the measurement vector  $\vec{y}$  and  $\tilde{y}_i = y_i - \hat{y}_i$  is the difference between the actual measurement and the expected measurement.  $K_{ji}$  corresponds to the element of the  $j^{\text{th}}$  row and  $i^{\text{th}}$  column of the Kalman gain matrix.

- Angular velocity

We assume that the subject expects a certain bandwidth  $\beta_\omega$  of angular velocity. This signal is represented in the internal model by the output of a first order shaping filter driven by the feedback signal  $(\vec{y} - \hat{\vec{y}})$  weighted by the Kalman gain matrix.

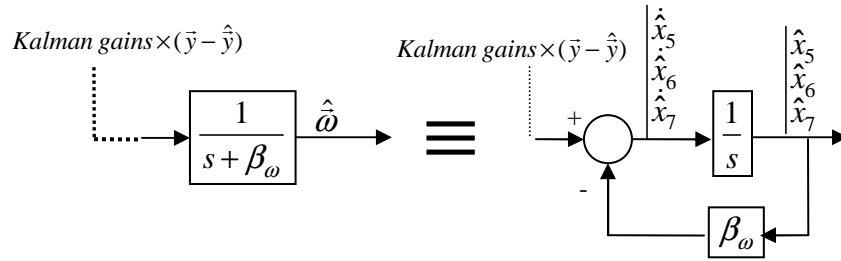


**Figure 4.21.** Equivalent model of the low pass filter.

Therefore we have the following differential equations for the update of angular velocity:

$$\dot{\hat{x}}_5 = -\beta_\omega\hat{x}_5 + \sum_{i=1}^r K_{5i}\tilde{y}_i \quad (4.32)$$

$$\dot{\hat{x}}_6 = -\beta_\omega\hat{x}_6 + \sum_{i=1}^r K_{6i}\tilde{y}_i \quad (4.33)$$

$$\dot{\hat{x}}_7 = -\beta_\omega\hat{x}_7 + \sum_{i=1}^r K_{7i}\tilde{y}_i \quad (4.34)$$

- Linear velocity and linear acceleration

Linear velocity is obtained by integration of linear acceleration, so that its update is given by:

$$\dot{\hat{x}}_8 = \hat{x}_{11} + \sum_{i=1}^r K_{8i}\tilde{y}_i \quad (4.35)$$

$$\dot{\hat{x}}_9 = \hat{x}_{12} + \sum_{i=1}^r K_{9i}\tilde{y}_i \quad (4.36)$$



$$\dot{\hat{x}}_{10} = \hat{x}_{13} + \sum_{i=1}^r K_{10i} \tilde{y}_i \quad (4.37)$$

As angular velocity, linear acceleration is expected to be the output of a first order shaping filter driven by the feedback signal  $(\bar{y} - \hat{y})$  weighted by the Kalman gain matrix , so that:

$$\dot{\hat{x}}_{11} = -\beta_t \hat{x}_{11} + \sum_{i=1}^r K_{11i} \tilde{y}_i \quad (4.38)$$

$$\dot{\hat{x}}_{12} = -\beta_t \hat{x}_{12} + \sum_{i=1}^r K_{12i} \tilde{y}_i \quad (4.39)$$

$$\dot{\hat{x}}_{13} = -\beta_t \hat{x}_{13} + \sum_{i=1}^r K_{13i} \tilde{y}_i \quad (4.40)$$

- Semicircular canals dynamics

Semicircular canal dynamics is defined by the transfer function presented in figure 4.22. This transfer function can be redrawn as:

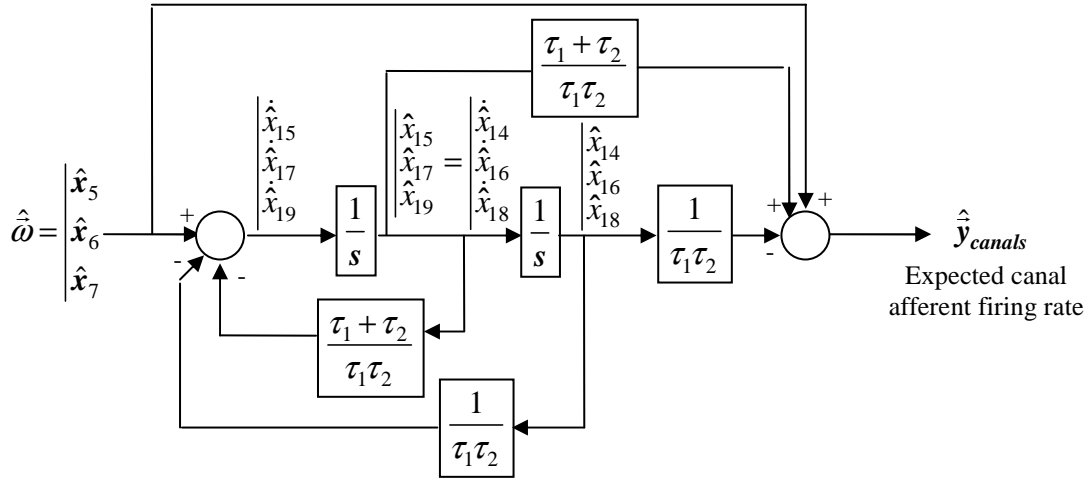


**Figure 4.22.** Equivalent representation of the transfer functions of the semicircular canal dynamics of the internal model.

Therefore, the semicircular canal states update is given by the following set of differential equations:

$$\dot{\hat{x}}_{14} = \hat{x}_{15} + \sum_{i=1}^r K_{14i} \tilde{y}_i \quad (4.41)$$

$$\dot{\hat{x}}_{15} = -\frac{\tau_1 + \tau_2}{\tau_1 \tau_2} \hat{x}_{15} - \frac{1}{\tau_1 \tau_2} \hat{x}_{14} + \hat{x}_5 + \sum_{i=1}^r K_{15i} \tilde{y}_i \quad (4.42)$$

$$\dot{\hat{x}}_{16} = \hat{x}_{17} + \sum_{i=1}^r K_{16i} \tilde{y}_i \quad (4.43)$$

$$\dot{\hat{x}}_{17} = -\frac{\tau_1 + \tau_2}{\tau_1 \tau_2} \hat{x}_{17} - \frac{1}{\tau_1 \tau_2} \hat{x}_{16} + \hat{x}_6 + \sum_{i=1}^r K_{17i} \tilde{y}_i \quad (4.44)$$

$$\dot{\hat{x}}_{18} = \hat{x}_{19} + \sum_{i=1}^r K_{18i} \tilde{y}_i \quad (4.45)$$

$$\dot{\hat{x}}_{19} = -\frac{\tau_1 + \tau_2}{\tau_1 \tau_2} \hat{x}_{19} - \frac{1}{\tau_1 \tau_2} \hat{x}_{18} + \hat{x}_7 + \sum_{i=1}^r K_{19i} \tilde{y}_i \quad (4.46)$$

- Otolith dynamics

The internal model of otoliths respond to the estimated gravito-inertial force  $\hat{f} = \hat{g} - \hat{a}$ . The orientation of  $\hat{g}$  relative to head coordinate system is defined by:

$$\hat{g} = M \begin{pmatrix} 0 \\ 0 \\ 9.81 \end{pmatrix} = \begin{pmatrix} 19.62(\hat{x}_2 \hat{x}_4 - \hat{x}_1 \hat{x}_3) \\ 19.62(\hat{x}_3 \hat{x}_4 - \hat{x}_1 \hat{x}_2) \\ 9.81(\hat{x}_1^2 + \hat{x}_4^2 - \hat{x}_3^2 - \hat{x}_2^2) \end{pmatrix} \quad (4.47)$$

where  $M$  is the transpose of the direction cosine matrix define in appendix 2. Thus the gravito-inertial force is given by:

$$\hat{f} = \begin{pmatrix} 19.62(\hat{x}_2 \hat{x}_4 - \hat{x}_1 \hat{x}_3) - \hat{x}_{11} \\ 19.62(\hat{x}_3 \hat{x}_4 - \hat{x}_1 \hat{x}_2) - \hat{x}_{12} \\ 9.81(\hat{x}_1^2 + \hat{x}_4^2 - \hat{x}_3^2 - \hat{x}_2^2) - \hat{x}_{13} \end{pmatrix} \quad (4.48)$$

Otolith dynamics is defined by the transfer function presented in figure 4.23. This transfer function can be redrawn as:

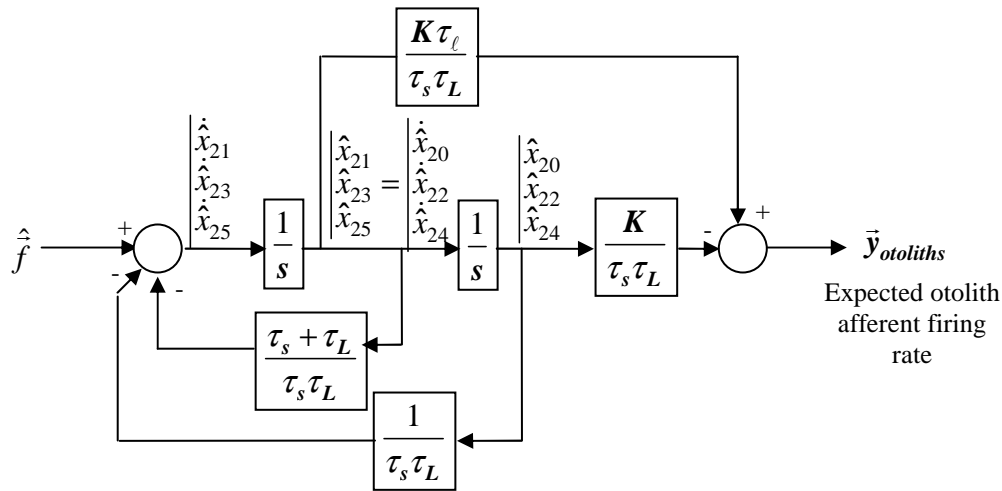


**Figure 4.23.** Equivalent representation of the transfer functions of the otolith dynamics of the internal model.

Therefore, the states update is given by the following differential equations:

$$\dot{\hat{x}}_{20} = \hat{x}_{21} + \sum_{i=1}^r K_{20i} \tilde{y}_i \quad (4.49)$$

$$\dot{\hat{x}}_{21} = -\frac{\tau_s + \tau_L}{\tau_s \tau_L} \hat{x}_{21} - \frac{1}{\tau_1 \tau_2} \hat{x}_{20} + 19.62(\hat{x}_2 \hat{x}_4 - \hat{x}_1 \hat{x}_3) - \hat{x}_{11} + \sum_{i=1}^r K_{21i} \tilde{y}_i \quad (4.50)$$

$$\dot{\hat{x}}_{22} = \hat{x}_{23} + \sum_{i=1}^r K_{22i} \tilde{y}_i \quad (4.51)$$

$$\dot{\hat{x}}_{23} = -\frac{\tau_s + \tau_L}{\tau_s \tau_L} \hat{x}_{23} - \frac{1}{\tau_1 \tau_2} \hat{x}_{22} + 19.62(\hat{x}_3 \hat{x}_4 + \hat{x}_1 \hat{x}_2) - \hat{x}_{12} + \sum_{i=1}^r K_{23i} \tilde{y}_i \quad (4.52)$$

$$\dot{\hat{x}}_{24} = \hat{x}_{25} + \sum_{i=1}^r K_{24i} \tilde{y}_i \quad (4.53)$$

$$\dot{\hat{x}}_{25} = -\frac{\tau_s + \tau_L}{\tau_s \tau_L} \hat{x}_{25} - \frac{1}{\tau_1 \tau_2} \hat{x}_{24} + 9.81(\hat{x}_1^2 + \hat{x}_4^2 - \hat{x}_2^2 - \hat{x}_3^2) - \hat{x}_{13} + \sum_{i=1}^r K_{25i} \tilde{y}_i \quad (4.54)$$

#### 4.2.4.2. Measurement equations: outputs of the real world model

The measurement equations are derived from the state space representation of the canals, otoliths, and visual transfer functions. According to each transfer function we have:

$$y_1 = -\frac{1}{\tau_1 \tau_2} x_{14} - \frac{\tau_1 + \tau_2}{\tau_1 \tau_2} x_{15} + x_5 + v_{scc} \quad (4.55)$$

$$y_2 = -\frac{1}{\tau_1 \tau_2} x_{16} - \frac{\tau_1 + \tau_2}{\tau_1 \tau_2} x_{17} + x_6 + v_{scc} \quad (4.56)$$

$$y_3 = -\frac{1}{\tau_1 \tau_2} x_{18} - \frac{\tau_1 + \tau_2}{\tau_1 \tau_2} x_{19} + x_7 + v_{scc} \quad (4.57)$$

$$y_4 = -x_5 + v_{r\,vision} \quad (4.58)$$

$$y_5 = -x_6 + v_{r\,vision} \quad (4.59)$$

$$y_6 = -x_7 + v_{r\,vision} \quad (4.60)$$

$$y_7 = -x_8 + v_{t\,vision} \quad (4.61)$$

$$y_8 = -x_9 + v_{t\,vision} \quad (4.62)$$

$$y_9 = -x_{10} + v_{t\,vision} \quad (4.63)$$

$$y_{10} = -\frac{K}{\tau_s \tau_L} x_{20} - \frac{K \tau_\ell}{\tau_s \tau_L} x_{21} + v_{oto} \quad (4.64)$$

$$y_{11} = -\frac{K}{\tau_s \tau_L} x_{22} - \frac{K \tau_\ell}{\tau_s \tau_L} x_{23} + v_{oto} \quad (4.65)$$

$$y_{12} = -\frac{K}{\tau_s \tau_L} x_{24} - \frac{K \tau_\ell}{\tau_s \tau_L} x_{25} + v_{oto} \quad (4.66)$$

In addition, we consider one more measurement equation in order to keep the norm of the quaternion equal to unity, which is fundamental in the quaternion formulation. Thus, we have:

$$y_{13} = x_1^2 + x_2^2 + x_3^2 + x_4^2 \quad (4.67)$$

#### 4.2.5. Implementation consideration

The algorithms of the EKF and UKF defined in the background section are implemented in the MATLAB software (code available in appendix 4). As the central nervous system is modelled as a continuous system, the differential equations for the state vector  $\hat{x}$  and the error covariance matrix  $P$  have to be integrated between each measurement time step. For the EKF, a fourth-order Runge-Kutta integration is used with an integration time step of 0.01s. Note that in this case Euler integration would provide very bad and oscillatory results. However, Euler integration with a time step of 0.01s is convenient for the UKF and provides similar results as if a Runge-Kutta scheme would be used, for a computation time about five times faster. For both models, a time-step of 0.04 s is used to update the state vector.

A graphical user interface is also developed and provides users with complete control over all model parameters - such as bandwidths and covariance of process and measurement noise - and data output without a need for advanced programming skills or optimal filtering knowledge (Fig. 4.24). The user has the choice to run different motion paradigms:

- Yaw rotation in darkness: the subject is strapped into a rotating chair and experiences a movement of rotation at a constant angular velocity in darkness.
- Forward acceleration in darkness: the subject experiences a constant forward linear acceleration in darkness.
- Yaw angular vection: vection is defined as the compelling sensation of self-motion elicited by a moving visual stimulus. In this experiment the subject is stationary and placed inside a rotating drum which rotates at a constant angular velocity around a vertical axis.
- Pitch angular vection: the subject is stationary and placed inside a rotating drum which at a constant angular velocity around the pitch axis.
- Roll angular vection: the subject is stationary and placed inside a rotating drum which at a constant angular velocity around the roll axis.
- Backward linear vection: the subject is stationary. His surrounding environment translates backward at a constant linear velocity.
- Coriolis stimulation: the subject sits head erect in a chair which rotates around a vertical axis. When angular velocity perception has effectively decayed to zero, the subject makes a head tilt.
- Pseudo-Coriolis stimulation: the subject is stationary with his head erect. His surrounding environment rotates about an Earth vertical axis at a constant angular velocity. When the subject experiences an illusory sensation of rotational motion in the opposite direction of the surrounding motion, he makes a head tilt.

- Off-vertical axis rotation (OVAR): the subject sits on a rotating char tilted from the Earth vertical axis. He then experiences a rotation around a tilted axis in darkness.

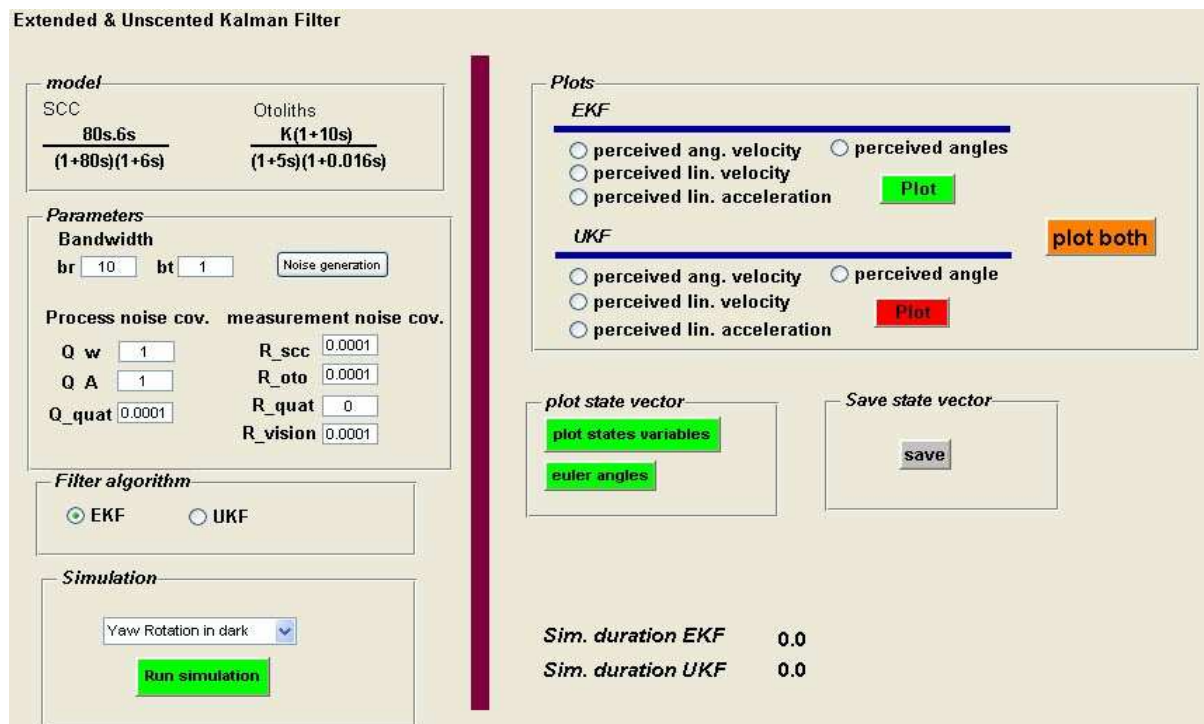


**Figure 4.24.** Graphical user interface of the EKF/UKF models. The “parameters” panel allow the user to define the bandwidths as well as the process noise covariance and measurement noise covariance. The “filter algorithm” panel permits to switch between the EKF and the UKF. The “Simulation” panel proposes different kind of motion paradigms such as yaw rotation in darkness, forward linear acceleration in darkness, Coriolis stimulation, etc. Then the user can plot any of the state variables and save the state vector. Computation-times are displayed at the end of each simulation.

## 4.2.6. Simulation results

### 4.2.6.1. Parameters

The following set of parameters is used in the following simulations:

- Bandwidths:  $\beta_\omega = 25$  and  $\beta_t = 1$
- Process noise covariance matrix:  $Q$  is a 25x25 diagonal matrix with:
  - $Q(1,1) = Q(2,2) = Q(3,3) = Q(4,4) = Q_{quat} = 1e^{-5}$
  - $Q(5,5) = Q(6,6) = Q(7,7) = Q_r = 609$
  - $Q(11,11) = Q(12,12) = Q(13,13) = Q_t = 1$
  - All the other diagonal elements are set to zero

- Measurement noise covariance matrix for experiments performed in darkness:  $V$  is a 7x7 diagonal matrix with:
  - $V(2,2) = V(3,3) = V(4,4) = V_{scc} = 0.001$
  - $V(5,5) = V(6,6) = V(7,7) = V_{oto} = 0.001$
  - $V(1,1) = 0 \rightarrow$  assumed there is no measurement noise for the quaternion norm computation
  
- Measurement noise covariance matrix for experiments performed in light:  $V$  is a 13x13 diagonal matrix (3 angular and 3 translational visual information are added) with:
  - $V(1,1) = V(2,2) = V(3,3) = V_{scc} = 0.001$
  - $V(4,4) \dots \dots V(9,9) = V_{vision} = 0.001$
  - $V(10,10) = V(11,11) = V(12,12) = V_{oto} = 0.001$
  - $V(13,13) = 0 \rightarrow$  assumed there is no measurement noise for the quaternion norm computation

In order to integrate the state vector and the error covariance matrix  $P$ , the extended Kalman filter model uses a 4<sup>th</sup> order Runge-Kutta integration scheme with a time-step of 0.01s, while the unscented Kalman filter uses a Euler integration scheme with an identical integration time-step. Both models update the estimated state vector  $\hat{x}(t)$  every 0.04 s.

#### 4.2.6.2. Constant velocity rotation about an earth vertical axis

In this simulation the subject is strapped into a rotating chair and experience a rotation about an Earth vertical axis at a constant angular velocity. Two different experiments are considered: 1) rotation of the subject in the dark around an Earth vertical axis; 2) the subject is stationary and his surrounding rotates at a constant angular velocity (circularvection). An angular velocity of 60 °/s is chosen for the stimulation.

When the subject experiences a yaw rotation, the information is registered by the horizontal semicircular canals. Several seconds after the beginning of the rotational motion, the horizontal semicircular canals signal a steadily reduced yaw rate, which finally drops below subjective threshold. The yaw rate sensation begins at the original yaw rate and decays exponentially (Fig. 4.26). The sensation of rotation eventually ceases. As the yaw rate sensation decays over time, the associated perception of yaw angle to achieve a complete rotation lasts longer (Fig. 4.25). Note that the EKF predicts a longer decay of yaw rate sensation, and thus perception of yaw angle is faster than that predicted by the UKF.

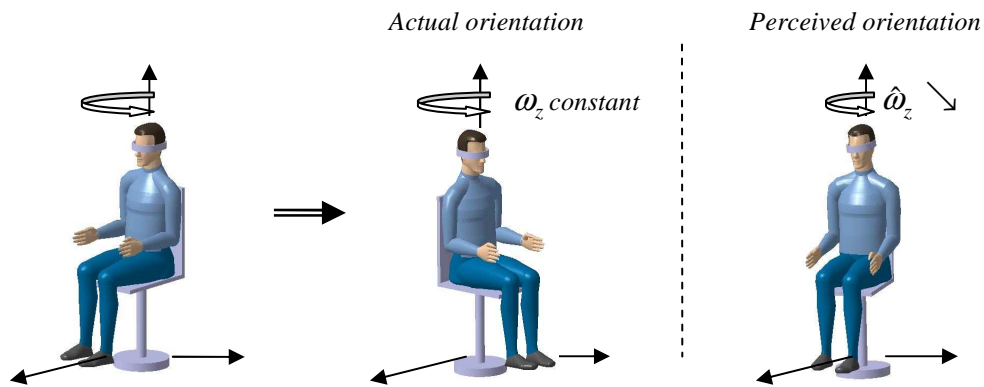


**Figure 4.25.** Scheme of the yaw rotation in darkness experiment. The subject is rotated at a constant angular velocity  $\omega_z$ . However, his perception of angular velocity  $\hat{\omega}_z$  decays to zero. If the rotation is sustained long enough, the subject will feel motionless.

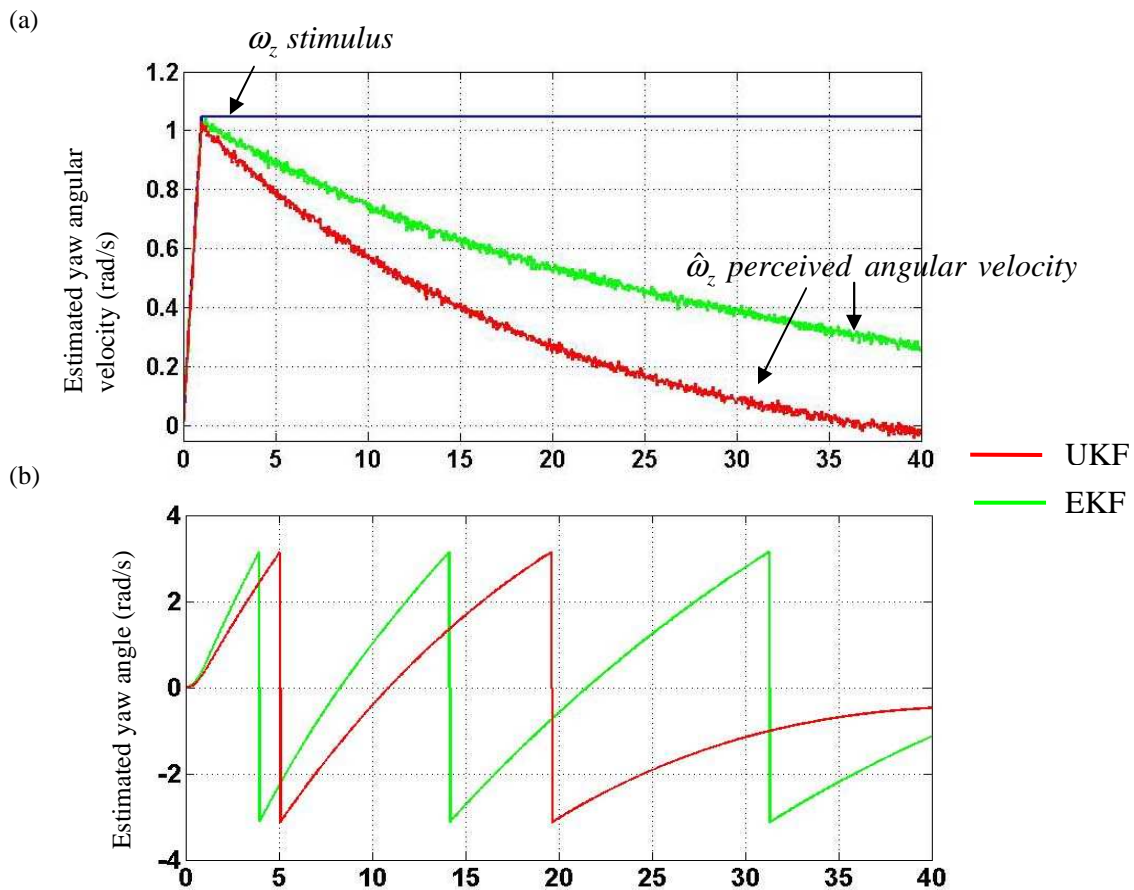


**Figure 4.26.** Model response to a step in yaw angular velocity. The subject is seated upright in the dark and is rotated around an Earth vertical axis (a) Perceived angular velocity in darkness. (b) Perceived yaw angle in darkness. Green and red curves are the results provided by the EKF and UKF

If the subject is stationary and placed inside a rotating drum so that his surrounding environment rotates at a constant angular velocity, the model predicts a sustained sensation of rotation in the opposite direction of the visual field which tends toward a value close to the input stimuli. This illusory sensation of rotation is commonly referred as “angular vection”. The curve of perceived angular velocity shows two distinct components associated with the time course of the perceived self motion: a fast rising component responsible for the quick initial onset followed by a slow rising component (Fig. 4.27).

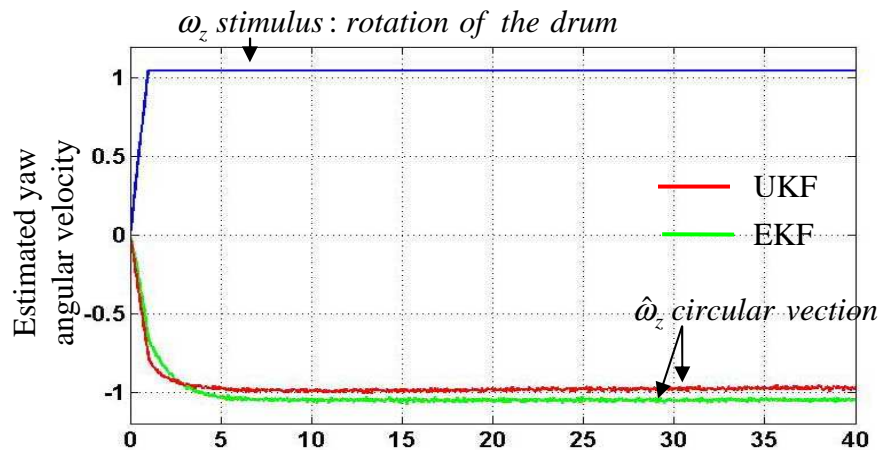


**Figure 4.27.** Model response to a step in yaw angular velocity of the surrounding environment. The subject is stationary, eyes opened and placed in a rotating drum. His surrounding environment is rotated around an Earth vertical axis at a constant angular velocity. After few seconds, the subject feels that he is rotating in the opposite direction the visual stimulation. This illusion is referred to as “circular vection”.



### 4.2.6.3. Forward linear acceleration in darkness

In this experiment, the subject is sat on a sled and experiences a forward linear acceleration in darkness. The forward acceleration creates a backward inertial force that combines with gravity to produce a resultant gravito-inertial vector rotated backward from the subject (Fig. 4.8). Hence, the subject experiences an illusion of pitching up. This illusion has been well documented experimentally (Cohen et al. 1973, Graybiel 1966). This illusion known as the “somatogravic illusion” is a common illusion in aviation that is believed to have caused a large number of mishaps over the years. This illusion of pitching up excessively is experienced by pilots when taking off into poor visibility or even more extremely during a catapult-assisted takeoff from an aircraft carrier. This false climb illusion demonstrates the limitation of the otoliths in providing accurate information to the brain, when there is insufficient visual information to correct the misinformation.

Figures 4.28 shows the perceived linear acceleration and the perceived pitch angle in response to a step of linear acceleration of  $2 \text{ m/s}^2$ . Both the EKF and UKF predict a pitch angle of about  $11.5^\circ$ . Note that results provided by the EKF are less stable than that predicted by the UKF.

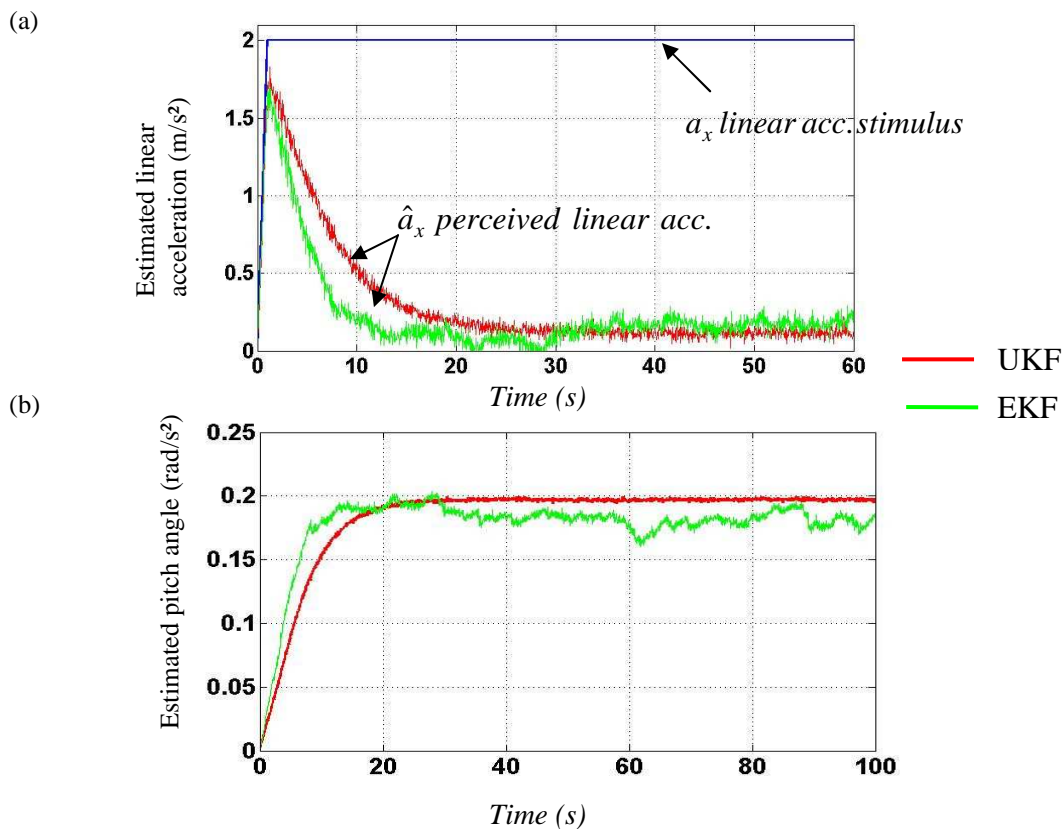


**Figure 4.28.** Model response to a step in forward linear acceleration of  $2 \text{ m/s}^2$ . The subject is seated upright and accelerated forward. (a) Perceived linear acceleration. (b) Perceived pitch angle. Green and red curves are the results provided by the EKF and UKF

#### 4.2.6.4. Vestibular “Coriolis” Cross-coupling

Head-movements in a rotating environment create a disturbing stimulus called the Coriolis cross-coupled stimulus. These head movements out of the plane of rotation provoke unexpected illusory sensations of motion and motion sickness. This phenomenon is commonly experienced in flight when a pilot in a turn looks down to adjust some navigation setting.

In order to simulate this phenomenon, the subject is seated upright in a chair that is rotated in yaw about an Earth vertical axis at a constant angular velocity of  $100^\circ/\text{s}$ . At 60 seconds, angular velocity perception of the simulated subject has decayed to zero because the horizontal canal has been in the plane of rotation long enough for its cupula to return to its rest position and thus signals no rotation to the brain. At this instant ( $t=60\text{ s}$ ), the simulated subject makes a rolling head tilt of  $+20^\circ$  towards the right shoulder (Fig. 4.29). The surprising sensation is an illusion of angular motion and tilt about a third axis of rotation which can be highly nauseogenic (Guedry and Benson, 1972).

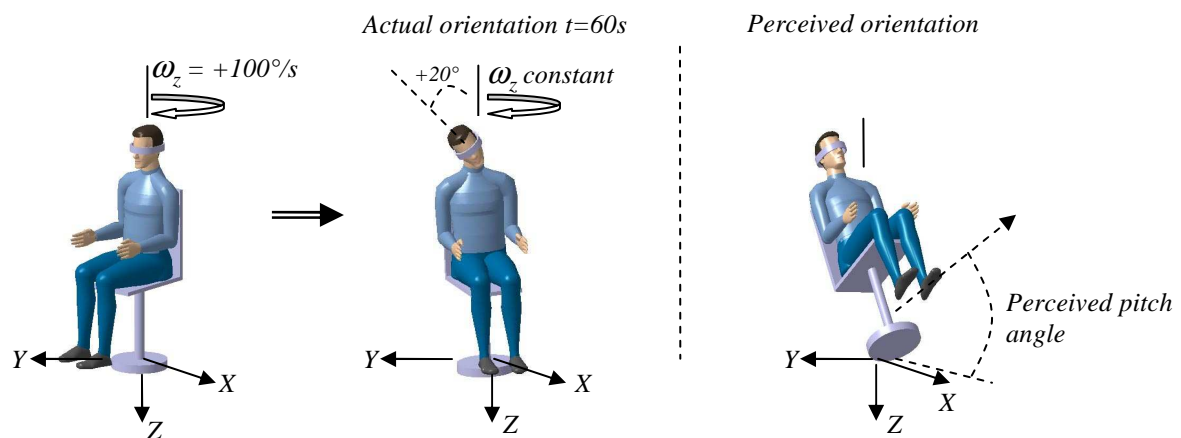


**Figure 4.29.** Description of the Coriolis illusion. The subject is rotated in darkness around an Earth vertical axis. At time 60s, the subject makes a roll head tilt towards his right shoulder. The resulting illusion is a sensation of pitching up.

This illusion can be explained by considering the torques acting on each semicircular canal. When the head is rolled towards the right shoulder, the horizontal canals are suddenly removed from the plane of chair rotation. Therefore they experience a deceleration, leading to cupula deflection in a direction opposite to the original sense, with the consequent decaying sense of rotation about the head’s z-axis, which now lies horizontal. Meanwhile, the anterior canal is suddenly exposed to a step change in angular velocity as it is rolled into the plane of rotation. Its cupula is deflected and slowly returns to its rest position. Therefore, the subject perceives a pitch angular velocity that decays slowly to zero (Fig. 4.30a).

In addition, a sensation of pitch up is predicted by the model. Note that the EKF predicts a pitch up sensation of  $17^\circ$  while the UKF gives a value of  $23^\circ$  (Fig. 4.31a).

As the perception of yaw angular velocity become negative at  $t=60\text{ s}$ , the simulated has the perception of turning in the opposite direction of the imposed rotation. This can be seen in figure 4.31c in which the estimated yaw angle changes in direction.

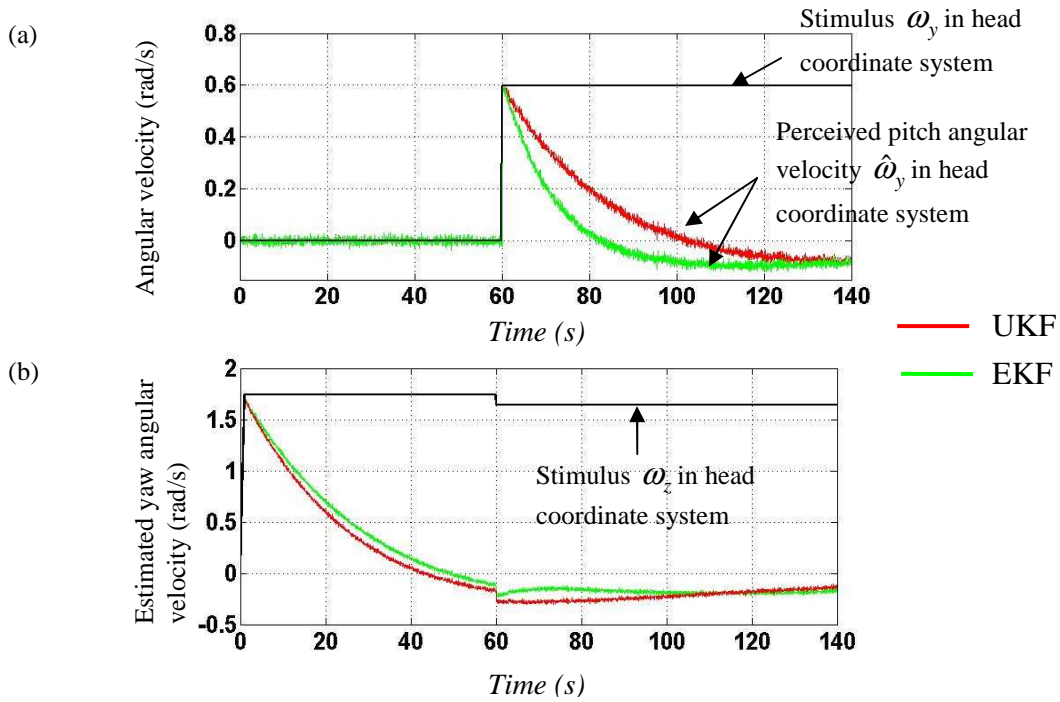


**Figure 4.30.** Simulation of vestibular Coriolis effect I. (a) Perceived roll angular velocity. (b) Perceived yaw angular velocity. Green and red curves are the results provided by the EKF and UKF, respectively. The head is rolled at  $t=60$  s.

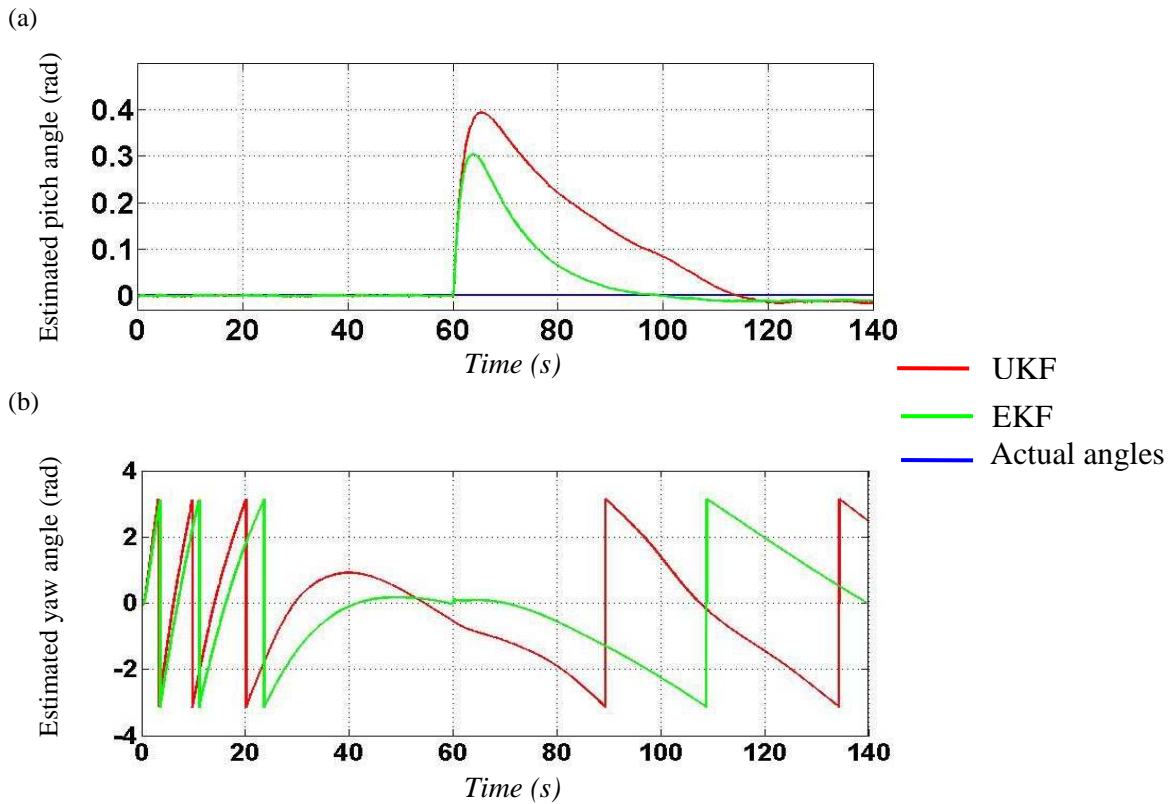


**Figure 4.31.** Simulation of vestibular Coriolis effect II. (a) Perceived roll angle. (b) Perceived yaw angle. Green and red curves are the results provided by the EKF and UKF, respectively. Blue curve is for the actual angles. The head is rolled at  $t=60$  s.

#### 4.2.6.5. Pseudo-Coriolis illusion

Numerous studies mention that pitching or rolling head movements during pure wide field of optokinetic rotational stimulation about a vertical axis produce illusions of disorientation as well as nausea (Dichgans et al. 1973, Bles, 1998, Johnson et al. 1999). This illusion is referred to as the pseudo-Coriolis illusion.

In this simulation, the subject is stationary and seated upright inside a rotating drum which rotates around a vertical axis at a constant angular velocity of 100 °/s. When the subject experiences an illusion of self-motion in the opposite direction of the rotation of the drum, he makes a head tilt of 20 ° towards his right shoulder (Fig. 4.32). Note that the stimulation is chosen to correspond to the previous Coriolis illusion simulation. In other words, while the subject was rotated in a positive direction relative to the world coordinate frame in the case of Coriolis, the drum (visual scene) is here rotated in a negative direction so that the subject experiences an illusion of self-motion in the same direction of the physical stimulation applied in the Coriolis experiment.

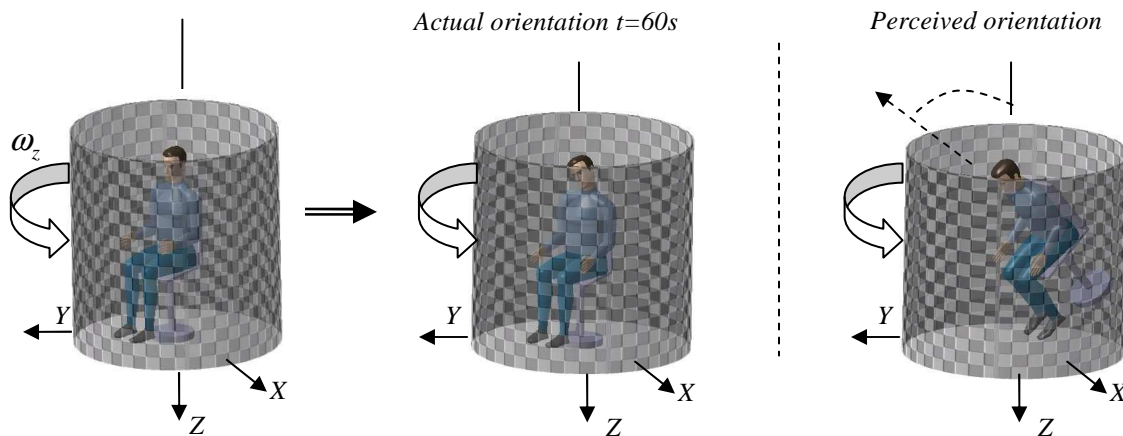


**Figure 4.32.** Description of the pseudo-Coriolis illusion. The subject is stationary and placed inside a rotating drum. The drum is rotated in a negative direction relative to the world coordinate frame so the subject experiences a self-motion illusion in the same direction of the physical stimulation used previously in the Coriolis experiment. At time 60 s, the subject makes a roll head tilt towards his right shoulder. Even though the stimulation is mainly visual, the subject experiences the illusion of pitching down. Note that this illusion is opposite to the direction of the Coriolis illusion.

Both the EKF and UKF predict a transient pitch-up sensation (Fig. 4.33c). Note that the direction of the illusory pitch sensation is opposite to the direction of the classic Coriolis illusion. The UKF predicts a maximum pitch angle of -11.5 ° while the EKF predicts a smaller pitch angle of -5.6 °. Note also that pseudo-Coriolis illusion is not induced from a cross-coupling of the semicircular canals. As noted by Newman (2009), the pseudo-Coriolis illusion is a result of fundamentally different neurological mechanism which could be described as “visual velocity storage”.

Coriolis and pseudo-Coriolis motion paradigms are completely different. In the Coriolis simulation, the subject is physically rotated, and thus his horizontal canals provide angular information to the brain. On the contrary, during pseudo-Coriolis stimulation the subject is stationary, and his illusion of self-motion is produced by a rotating visual field. Therefore, his

semicircular canals do not provide any information of angular velocity to the central nervous system.

In the Coriolis stimulation, when the head is rolled away from the gravitational vertical, the horizontal semicircular canal experiences a sudden deceleration, and the vertical canals experience a corresponding acceleration. As noted by Guedry and Benson (1978), the resultant angular velocity components ( $\hat{\omega}_y, \hat{\omega}_z$ ) combine to generate the pitch-down sensation. However, in the pseudo-Coriolis stimulation, when the head rolled away from the Earth vertical axis, the horizontal canal does not register any inertial deceleration as the subject is stationary. The model suggests that the visual system does not respond instantaneously to the change in relative orientation of the visual field. Instead, as the head is rolled towards the shoulder, it seems that the visual system stores the angular velocity estimate with respect to the head reference frame and rotates this vector in the new  $20^\circ$  orientation. As a consequence, the model predicts a pitch-up illusion along with a continued sensation of rotational motion.

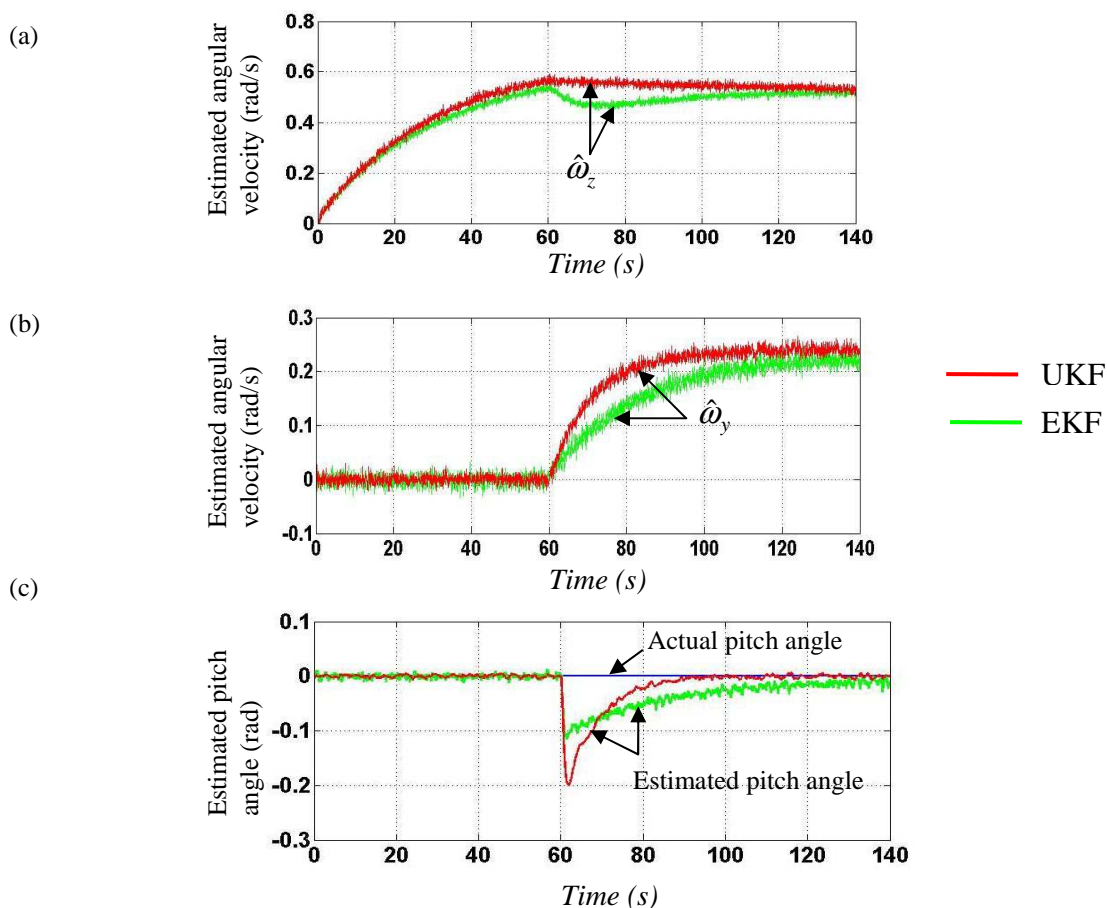


**Figure 4.33.** Simulation of pseudo-Coriolis illusion. (a) Perceived z-head axis angular velocity. (b) Perceived y-head axis angular velocity. (c) Perceived and actual pitch angle. Green and red curves are the results provided by the EKF and UKF, respectively.

In order to make sure that the illusory pitch is opposite to the classic Coriolis response, a simple pilot study was conducted in the MIT Man Vehicle Lab (MVL). Four subjects (ages 23 to 65) with no history of vestibular abnormality were used. Each subject was seated upright in a stationary chair and positioned so that their head and upper torso were encased in a rotating optokinetic drum 50 cm in diameter. The drum was rotated counter-clockwise at 36 °/s. Subjects were instructed to look straight ahead and were told to make an approximate 20 degree left ear down (LED) roll head tilt as soon as they experienced a sensation of self-motion around an Earth vertical axis. Then, they were asked to report the direction (pitch-up / pitch-down) of any pitching sensation. The experimental procedure was then repeated for a right ear down (RED) roll tilt.

All four subjects reported a pitch up sensation for the head tilt towards the right shoulder and a pitch down illusion for the head tilt towards the left shoulder. These responses match the predictions of both the EKF and UKF, and are also consistent with the Newman's Observer model (2009). These results support the fact that the direction of illusory pitch for the pseudo-Coriolis illusion is indeed opposite to the classic Coriolis response.

## 4.2.7 Sensitivity study

The results of the various simulations depends on the parameters assumed for the bandwidths of head angular velocity and head linear acceleration, and the process and measurement noise covariance matrices. Therefore we propose a sensitive study in order to investigate the impact of these parameters on the predicted perceptions of orientation, velocity, and linear acceleration. All the following results are provided by the UKF model. The default parameters chosen for each simulation are:  $\beta_\omega = 25$ ,  $\beta_l = 1$ ,  $Q_\omega = 609$ ,  $Q_l = 1$ ,  $V_\omega = V_l = 0.001$ .

### 4.2.7.1. Yaw angular velocity in darkness

The simulated subject is strapped into a chair that is rotated at a constant angular velocity of 60 deg/s. The experiment is performed in darkness.

- Influence of the bandwidth in angular velocity  $\beta_\omega$

Figure 4.34 show the influence of the expected frequency bandwidth for head angular velocity of the CNS. It turns out that the lower is the bandwidth, the longer is the perception of angular velocity. For instance, the model predicts that if a bandwidth of 40 rad/s is assumed the perception of angular velocity decays to zero in about 30 s, whereas a bandwidth of 20 rad/s yield a perception of angular velocity that lasts 40 s.



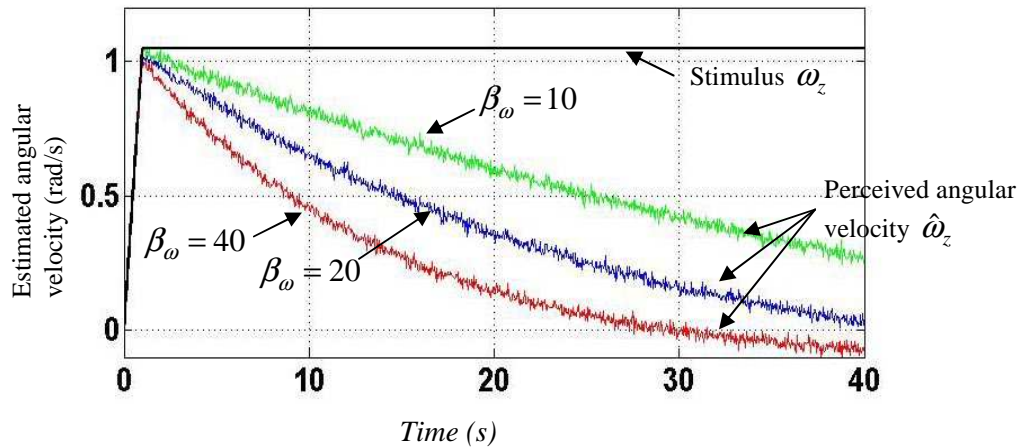


**Figure 4.34.** Influence of the bandwidth in angular velocity on the estimated yaw angular velocity in darkness.

#### 4.2.7.2. Forward linear acceleration in darkness

- Influence of the bandwidth in head linear acceleration

Figure 4.35 shows the responses predicted by the UKF for different bandwidths in linear acceleration. It can be seen that the higher if the bandwidth  $\beta_t$ , the shorter is the perception of linear acceleration and the smaller is the magnitude of the perceived acceleration. Note that considering a value  $\beta_t = 0.3$  the model predicts a constant perception of linear acceleration close to  $0.5 \text{ m/s}^2$  in response to a stimulus of  $2 \text{ m/s}^2$ . This result is inconsistent with the dynamics of the otolith organs as they provide a sensory signal that decays toward zero in response to a constant linear acceleration. The residual value of  $0.5 \text{ m/s}^2$  is presumably due to the integration method which constitutes in the present case a limit of the model.

Regarding the estimated pitch angle, the onset of the pitch-up illusion is much faster for a high value of bandwidth (Fig. 4.35b). For instance, if a bandwidth  $\beta_t = 5$  is considered the estimated pitch angle reaches a maximum value in about 5 s, whereas a bandwidth of 1 gives a maximum value of perceived pitch angle reached in about 20s.

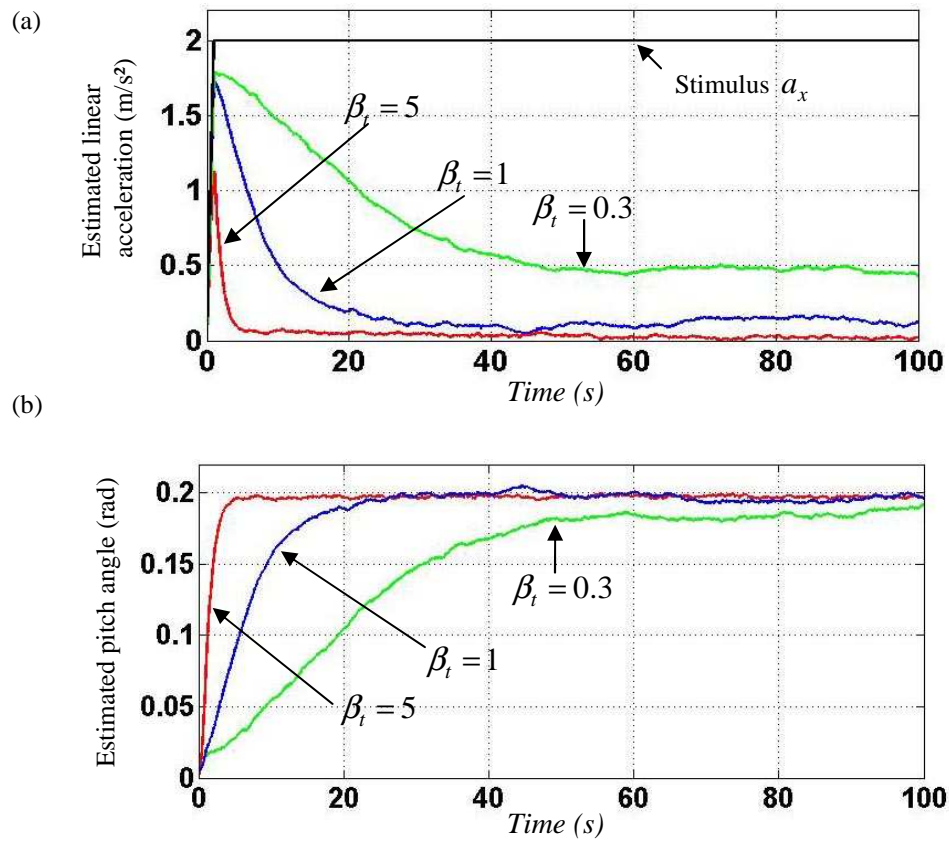


**Figure 4.35.** Influence of the bandwidth in linear acceleration on the estimated linear acceleration (a) and perceived pitch angle (b) in darkness.



- Influence of the process noise in head linear acceleration

Figure 4.36 shows the responses predicted by the UKF for different linear acceleration process noises. The model predicts that the smaller is the process noise, the shorter is the perception of linear acceleration and the smaller is the magnitude of the perceived acceleration. Once again, note that considering a high value for linear acceleration process noise the model predicts a constant perception of linear acceleration close to 0.5 m/s<sup>2</sup> in response to a stimulus of 2 m/s<sup>2</sup>.

As already observed in the case of a high value of bandwidth, the onset of the pitch-up illusion is here much faster for a small value of  $Q_t$ .

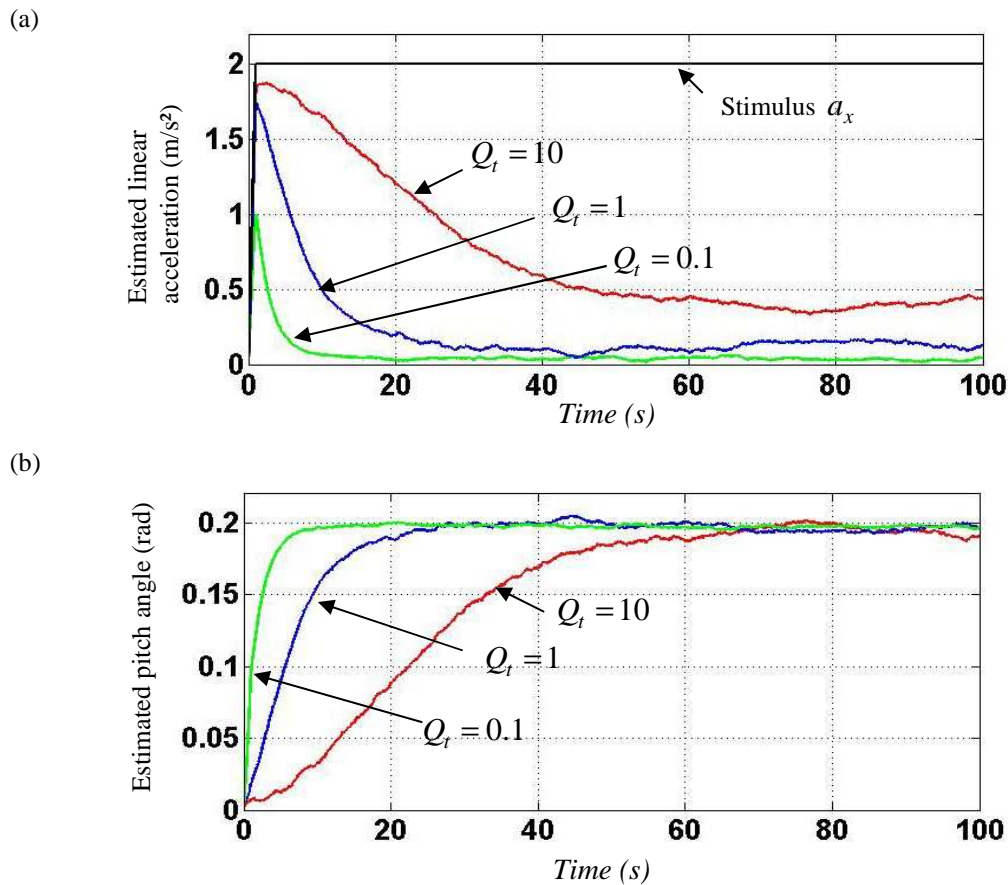


**Figure 4.36.** Influence of the linear acceleration process noise on the estimated linear acceleration (a) and perceived pitch angle (b) in response to a forward acceleration in darkness.

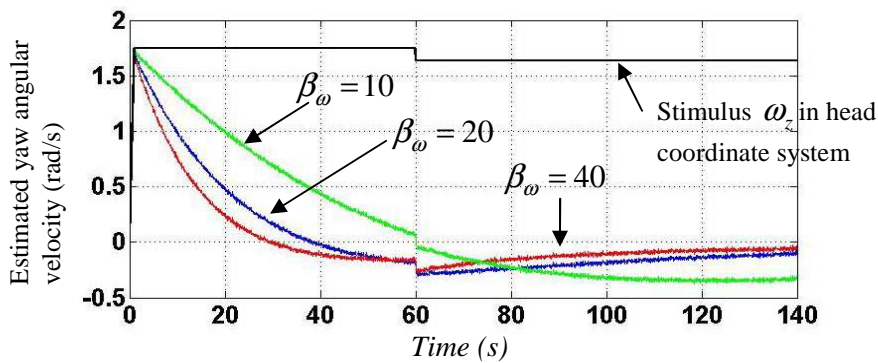
### 4.2.7.3. Vestibular Coriolis illusion

The subject experiences a rotation around an Earth vertical axis at a constant angular velocity of 100 deg/s in darkness. At time 60 s, while rotating, the subject makes a head roll tilt toward his right shoulder. An illusion of pitch-up is predicted by the model (Fig. 4.34b).

The impact of the bandwidth  $\beta_\omega$  on the perceived angular velocity  $\hat{\omega}_z$  is identical as the yaw angular velocity in darkness experiment. The model predicts a longer sensation of yaw angular velocity for smaller values of bandwidth (Fig. 4.37a).

For small values of bandwidth, the estimated pitch angle provided by the model is higher and the sensation of tilt lasts longer than that predicted for large bandwidths. For instance, if a bandwidth of 10 rad/s is considered the UKF model predicts a tilt illusion of about 28.6 ° that lasts 80 s, whereas a pitch-up angle of about 14.3 ° is produced by considering a bandwidth of 40 rad/s (Fig. 4.37b).

(a)



(b)

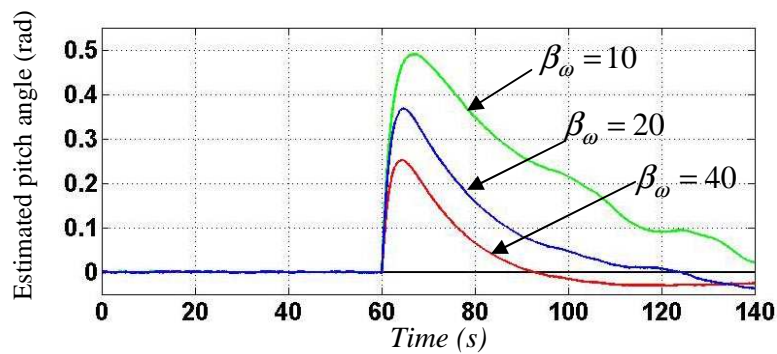


**Figure 4.37.** Influence of bandwidth in head angular velocity on the estimated yaw angular velocity (a) and perceived pitch angle (b) in response to a Coriolis stimulation in darkness.

## Chapter 5. Scale model of the semicircular canals

Before writing the final conclusion of the presented thesis, a detailed study is presented that establishes the design features for the construction of a physical model of the semicircular canals. To our knowledge this study is the first that considers dynamic similitude between the biological sensors and the scale model and that suggests potential and adequate materials for manufacturing of the mock-up.

The objective of this part is to construct a physically similar augmented model of one semicircular canal for both quantitative and qualitative testing. Price, construction simplicity and material availability have been determinant variables during this project. The project requirements are listed below:

- Size of the model large enough to be easily observed and recorded during the experiments. This restraint could be translated as a minimum scale factor of 20, considering the small dimensions of the vestibular system (e.g. 0.16 mm cross-section radius)
- Transparency of the fluid representing the endolymph, due to the visual experiments
- Low Manufacturing complexity
- Cupula Material Young's modulus non inferior to  $E = 0.005 \text{ GPa}$  (silicone rubber)
- Maximum angular velocity applied to the scale model limited by  $\omega_{\max} = 250^\circ / s$ , due to equipment restraints

### 5.1. Similitude study

Construction of a scale model must be accompanied by an analysis to determine what conditions it is tested under. While the geometry may be simply scaled, other parameters such as pressure, velocity and type of fluid may be altered. Similitude is achieved when testing conditions are created such that the results are applicable to real design. The following criteria are required to achieve similitude:

- Geometric similarity: the model is the same shape as the application, usually scaled
- Kinematic similarity: fluid flow of both the model and real application must undergo similar time rates of change motions.

In order to satisfy the above conditions and thus to ensure dynamic similitude between the scale model and the application, we perform a dimensional analysis to express the system with dimensionless parameters. The values of these dimensionless parameters are held to be the same for both the scale model and the real semicircular canal.

Given the fundamental units  $M$  (mass),  $L$  (length), and  $T$  (time), any physical parameters  $G$  may be written as:

$$G = M^{a_1} L^{b_1} T^{c_1} \quad (3.27)$$

where the exponents are rational numbers.

The fluid velocity  $\dot{y}$  within the canal is a function of:

- fluid density  $\rho$
- fluid dynamic viscosity  $\mu$
- cross-section radius of the duct  $r$
- canal length  $l$
- cupula Young's modulus  $E$
- angular velocity of the head  $\omega$ .

Therefore, each of these parameters has the following dimension:

Fluid density	$G_1 = \rho = \frac{M}{L^3}$	Canal length	$G_4 = l = L$
Fluid dynamic viscosity	$G_2 = \mu = \frac{M}{LT}$	Cupula Young's modulus	$G_5 = E = \frac{M}{LT^2}$
Cross-section radius	$G_3 = r = L$	Pulsation of head angular acceleration	$G_6 = \omega = \frac{1}{T}$

**Table 5.1.** Dimension of the physical parameters that influences fluid flow within a semicircular canal in terms of fundamental units.

The fluid velocity can be written as:

$$\dot{y} = f(\rho, \mu, r, l, E, \omega) = L^x M^y T^z = \frac{L}{T} \quad (3.28)$$

so that  $x = 1$ ,  $y = 0$ ,  $z = -1$ .

According to *Buckingham Pi* theorem (1914), which provides a method for computing sets of dimensionless parameters from given variables, a physical variable  $P_i$  can be expressed by the following equation:

$$P_i = G_1^{\alpha_1} G_2^{\alpha_2} \dots G_n^{\alpha_n} = L^x M^y T^z \quad (3.29)$$

where the  $G_i$  are  $n$  physical variables, and the exponents  $\alpha_i, x, y, \text{ and } z$  are rational numbers.

Equation (3.29) can be expressed in matrix form relative to the fundamental units as:

	$G_1$	$G_2$	$\dots$	$G_n$	$P$
$L$	$a_1$	$a_2$	$\dots$	$a_n$	$x$
$M$	$b_1$	$b_2$	$\dots$	$b_n$	$y$
$T$	$c_1$	$c_2$	$\dots$	$c_n$	$z$

**Table 5.2.** Matrix form of the Buckingham Pi theorem.

And  $\alpha_i$  are the solutions of the following linear system:

$$\begin{aligned}
 a_1\alpha_1 + a_2\alpha_2 + \dots + a_n\alpha_n &= x \\
 b_1\alpha_1 + b_2\alpha_2 + \dots + b_n\alpha_n &= y \\
 c_1\alpha_1 + c_2\alpha_2 + \dots + c_n\alpha_n &= z
 \end{aligned}
 \tag{3.30}$$

In this particular case, we have:

	$G_1 = \rho$	$G_2 = \mu$	$G_3 = r$	$G_4 = l$	$G_5 = E$	$G_6 = \omega$	$P$
$L$	-3	-1	1	1	-1	0	1
$M$	1	1	0	0	1	0	0
$T$	0	-1	0	0	-2	-1	-1

**Table 5.3.** Matrix form of the Buckingham Pi theorem applied to our similitude problem.

The correspondent linear system is:

$$\begin{aligned}
 -3\alpha_1 - \alpha_2 + \alpha_3 + \alpha_4 - \alpha_5 &= 1 \\
 \alpha_1 + \alpha_2 + \alpha_5 &= 0 \\
 -\alpha_2 - 2\alpha_5 - \alpha_6 &= -1
 \end{aligned}$$

So that

$$\begin{aligned}
 \alpha_1 &= \alpha_5 + \alpha_6 - 1 \\
 \alpha_2 &= -2\alpha_5 - \alpha_6 + 1 \\
 \alpha_3 &= -\alpha_4 + 2\alpha_5 + 2\alpha_6 - 1
 \end{aligned}$$

Finally,

$$\begin{aligned}
 \dot{y} &= G_1^{\alpha_1} G_2^{\alpha_2} G_3^{\alpha_3} G_4^{\alpha_4} G_5^{\alpha_5} G_6^{\alpha_6} \\
 \dot{y} &= \frac{\mu}{\rho r} \left( \frac{l}{r} \right)^{\alpha_4} \left( \frac{\rho r^2 E}{\mu^2} \right)^{\alpha_5} \left( \frac{\rho r^2 \omega}{\mu} \right)^{\alpha_6}
 \end{aligned}$$

$$\dot{y} = \frac{\mu}{\rho r} f \left( \left( \frac{l}{r} \right)^{\alpha_4}; \left( \frac{\rho r^2 E}{\mu^2} \right)^{\alpha_5}; \left( \frac{\rho r^2 \omega}{\mu} \right)^{\alpha_6} \right) \quad (3.31)$$

It is therefore required to keep constant the following dimensionless parameters so as to ensure dynamic similitude between the scale model and the semicircular canal:

- $\left( \frac{l}{r} \right)$  which is a geometric parameter
- $\left( \frac{\rho r^2 E}{\mu^2} \right)$  which relates fluid properties with the Young's modulus of the cupula
- $\left( \frac{\dot{y} \rho r}{\mu} \right)$  which is the Reynolds number
- $\left( \frac{\rho r^2 \omega}{\mu} \right)$  which is the Womersley number that represents the pulsatile flow frequency

in relation to viscous effects (1955). This dimensionless number is also equal to the product of the well known Reynolds and Strouhal number. In the present case, this number is small (less than 1) even for high frequency of head acceleration pulsation (e.g.  $f=10$  Hz). This means that in any case the frequency of pulsation will be sufficiently low so that a parabolic velocity profile will have time to develop during each cycle, and the flow will be given to a good approximation by Poiseuille's law.

In the present case, we consider a simple step of constant angular velocity rather than a sinusoidal rotation that will be applied to the scale model. Therefore, the first three dimensionless parameters are taken into consideration for the choice of potential materials suitable for the manufacturing of the scale model.

- First dimensionless number:  $\left( \frac{l}{r} \right)$

This geometrical parameter can be easily maintained by adjusting the correct canal length to a chosen cross-section radius.

- Second dimensionless number:  $\left( \frac{\rho r^2 E}{\mu^2} \right)$

The main restraint of the scale model resides in maintaining the second dimensionless number, because it requires an extremely Young's modulus for the cupula material. By considering a scale factor  $\Psi$  the new cross-section radius is given by  $r' = \Psi r$ . Then, for conserving the second dimensionless parameter, it may be written:

$$\left( \frac{\rho r^2 E}{\mu^2} \right) = \left( \frac{\rho' r'^2 E'}{\mu'^2} \right) \quad (3.32)$$

From which

$$E' = \left( \frac{\mu'}{A\mu} \right)^2 \left( \frac{\rho}{\rho'} \right) E = k.E \quad (3.33)$$

where  $E', \mu', \rho'$  are the parameters of the scale model.

The main limitation of the problem is that  $E$  is considerably small, namely close to 5 Pa. For this reason, the coefficient  $k$  has to be large as much as possible so that an adequate material can be found such that  $E' > E'_{\min} \approx 0.005 \text{ GPa}$ . In a practical approach, the density  $\rho'$  and the scale factor  $\Psi$  play a minor role in influencing  $k$  in comparison with the potential impact the viscosity may have. That is, fluids having a viscosity around  $10^6$  times higher than the endolymph can be found and retained for the scale model.

➤ Third dimensionless parameter:  $\text{Re} = \left( \frac{\dot{\gamma} \rho r}{\mu} \right)$

As long as  $\text{Re} = \text{Re}'$ , by choosing a large enough value for the viscosity  $\mu'$ , the velocity of the fluid is relatively larger in the scale model experiment when all other variables are kept constant. In other words, the simulation of a chosen head rotation requires an even large scale model rotation.

## 5.2. Choice of materials

- Endolymph: Polidimethylsiloxane Silicone Oil

For modeling the endolymph, an initial qualitative study with three different high viscosity fluids has been conducted. Results of this study are presented in table 5.4 for a maximum scale model rotation of 250 °/s. Red cells in the last column indicate that the criterion  $E' > E'_{\min}$  is satisfied.

The polydimethylsiloxane group has been chosen among the analyzed materials to represent the endolymph, inasmuch as it stands for a high enough cupula elasticity modulus and as it provides experiments with higher rotational rates. Equally, the commercial easiness to find it renders it an attractive choice. The fluid presents other interesting features such as: clear, colorless, fluid, extremely high kinematic viscosities covering a wide range, little viscosity change with temperature. It can also be pointed out that the mentioned fluid covers a wide range of possible kinematic viscosities (from less than 0.65 till 20 million cSt), while maintaining practically constant density ( $978 \text{ kg/m}^3$ ).

Fluid	Dynamic viscosity (Pa.s)	Density (kg/m <sup>3</sup> )	Scale factor	Angular Velocity (°/s)	Young's modulus E (GPa)
Glycerol	1.42	1260	20	75.4	5e-5
			40	301.7	1e-5
Peanut Butter	200	333	20	1.1	4.15
			40	4.3	1.04
			60	9.6	0.46
			80	17.1	0.26
			100	26.6	0.17
Silicone Polydimethylsiloxane	78.3	979	20	1.1	0.22
			40	4.3	0.054
			60	9.6	0.024
			80	17	0.014
			100	26.6	0.009
	88.0	978	20	0.9	0.274
			40	3.8	0.069
			60	8.5	0.030
			80	15.1	0.017
			100	23.6	0.011
	107.6	978	20	0.8	0.409
			40	3.1	0.102
			60	7.0	0.045
			80	12.4	0.026
			100	19.3	0.016

**Table 5.4.** Required experimental values for cupula material Young's modulus and maximum simulated head angular velocity.

- Cupula: silicone rubber

Regarding to the cupula, low elasticity modulus silicone rubbers with  $E' \approx E'_{\min} \approx 0.005 \text{ GPa}$  have been considered. A convenient material is the “*Super soft silicone rubber Ecoflex 10*”. Note that by choosing the material's lowest possible Young's modulus, higher viscosity can be utilized, minimizing the angular velocity that will be applied to the scale model.

### 5.3. Results

In order to maintain the dimensionless numbers and to respect the constraint on the minimum Young's modulus value, an Excel file was elaborated with a Visual Basic macro for a discrete set of scale factors as well as different fluid viscosities, and the Goal Seek optimization function was used. Results are shown in table 5.5.

It turns out that the maximum scale factor  $\Psi = 100$  is the most convenient, allowing higher simulated head rotations. The corresponding fluid kinematic viscosity is  $\nu' = 60000 \text{ cSt} = 0.06 \text{ m}^2/\text{s}$ . For this task of representing the endolymph, we propose the *polydimethylsiloxane Wacker AK 60,000 cSt Silicon Oil*.



Angular velocity applied to the scale model $\omega = 250^\circ/s$ Simulated head angular velocity $\omega = 25^\circ/s$		
Fluid kinematic viscosity (m <sup>2</sup> /s)	Scale factor	Young's modulus of the cupula (GPa)
0.01	30	0.0009
0.03	60	0.0024
0.05	80	0.0063
0.07	90	0.0079
0.08	100	0.0098
Angular velocity applied to the scale model $\omega = 250^\circ/s$ Simulated head angular velocity $\omega = 30^\circ/s$		
Fluid kinematic viscosity (m <sup>2</sup> /s)	Scale factor	Young's modulus of the cupula (GPa)
0.01	30	0.0006
0.03	60	0.0024
0.05	80	0.0043
0.06	90	0.0055
0.07	100	0.0068
Angular velocity applied to the scale model $\omega = 250^\circ/s$ Simulated head angular velocity $\omega = 35^\circ/s$		
Fluid kinematic viscosity (m <sup>2</sup> /s)	Scale factor	Young's modulus of the cupula (GPa)
0.01	30	0.0004
0.03	70	0.0024
0.05	90	0.0040
0.06	100	0.0050

**Table 5.5.** Quantitative estimation of possible configurations that keep constant all the dimensionless parameters. Red cells indicate that the criterion  $E' > E'_{\min} = 0.005 \text{ GPa}$  has been met.

# Chapter 6. Conclusion and future works

## 6.1. Overall conclusion

The thesis presents models of the human vestibular system, and more particularly of the semicircular canals, as well as models for human spatial orientation perception.

- In Chapter 2, the system endolymph / cupula has been modeled using finite-element simulations. In order to estimate the elastic properties of the human semicircular canal cupula, the latter has been modeled assuming it was attached around its periphery, and deformed according to thick and thin membrane theory. A three-dimensional finite-element model of the cupula has also been developed. Comparison with the finite-element model has confirmed that the thin-membrane model is not appropriate, because the thickness of the cupula has the same order of magnitude as the radius of the cupula. Based on thick bending membrane theory, a relation between the pressure-volume coefficient  $K$  and the Young's modulus of the cupula has been derived. A value for  $E$  has been computed based on the cupula radius and thickness and on the various estimates of the pressure-volume displacement coefficient  $K$  or the cupula long time constant of the cupula. We have estimated that the Young's modulus of the cupula is close to 5.4 Pa. It is notable that this value depends not only on the geometric dimensions of the cupula but also on the long time constant that we assumed. The shorter the long time constant, the larger the theoretical prediction for the cupula material's Young's modulus. However, our estimate is the same order of magnitude as a previous value derived by Groen et al. (1952), with values derived for the pike (Ten Kate, 1969), and with the Young's modulus of the cupula of the lateral-line organs of the fish (Mc Henry et al., 2007).

Using finite-element models, we have also studied two other shapes for the cupula: one with thick sides and a thin vertical center, the other being thick along its entire periphery. We have investigated their influence on the transverse displacement field of the cupula. It turns out that the cupula with thick sides along its entire periphery bends less as its stiffness is larger than the second model, and that the cupula having a thin vertical center exhibits a vertical asymmetrical transverse displacement. In that case, the lower part of the cupula, precisely where the hair cilia are located, is the most deflected. Since the mechanical stimulus of the stereocilia is determined by cupular shear strain that occurs near the crista, we have also used a finite-element model of the cupula so as to study the predicted shear strain right above the sensory epithelium. It turns out that first, the maximum shear strain occurs near the surface of the crista where the cilia are located, and, second, that the shear strain first appears at the center of the crista and then spread toward the periphery of the cupula and down the sides of the crista.

According to numerous authors (Igarashi and Alford, 1969; Dohlman, 1971; Lim, 1971) the cupula is in reality not a homogenous structure. Traditionally it is thought to contain endolymph-filled vertical channels although this has recently disputed. By modeling a section of cupula material having empty vertical channels positioned on a hexagonal matrix, we have shown that in the case of a static transcupular pressure the stiffness of the cupula is strongly sensitive to the diameter of the channels. In particular 10  $\mu\text{m}$  diameter channels have a small effect on the transverse displacement of the cupula while 30  $\mu\text{m}$  channels tubes increases the displacement by 28.6 %.

Then we have investigated the fluid-structural dynamics that takes place in the semicircular canals of the vestibular system using the Comsol Multiphysics software. The endolymph has been modeled as an incompressible Newtonian fluid while the cupula was considered as an elastic solid. The fluid-structure interaction problem has been treated with a strong coupling between the fluid flow and structural displacements. First, a two-dimensional as well as a three-dimensional model of a single semicircular canal have been considered. Results provided by both models were in good agreement with previous analytical studies as regard cupula displacement and fluid flow velocity field. We have shown that:

- in about 0.04 s fluid flow in the slender part of the semicircular canal can be approximated by a classic Poiseuille flow
- for a step change in head angular velocity cupula displacement begins near the sensory epithelium and then spreads towards its center
- displacement of the cupula through time is in good agreement with the classic torsion-pendulum model, i.e. described by two exponential terms

In addition, we have considered a head centered canal as well as a canal located 30 mm away from an Earth vertical axis and have shown that both models predict similar results.

Second, we have developed a three-dimensional finite-element model of the entire set of semicircular canals and cupulae. The associated geometry has been constructed using a CAD software (CATIA V5) which has then been imported into the finite-element Comsol Multiphysics software. Unfortunately, during the simulation convergence problems due to inverted mesh were encountered. This kind of problem usually occurs when the mesh is too coarse. In the present case, a finer mesh was not possible as we were limited by the available RAM (8Go) which in turns limits the size of the model. To explain more clearly, the size of the model is conditioned by the size of the mesh, i.e. the number of degrees of freedom. The finer is the mesh, the larger are the size of the model and the required RAM. Even if the model has been meshed as fine as possible according to the available RAM, it was not enough fine for the computation to converge. However the available solutions provided by the model at the beginning of the simulation were promising as they were in good agreement with the previous 2D and 3D models.

- In chapter 3, a virtual reality model that simulates the rotating chair test - one of the usual procedures carried out during a vestibular diagnosis – has been developed. This model also offers the possibility to simulate several head rotations while the simulated subject is rotated around an Earth vertical axis and to investigate in real time the state of each sensor. In addition, a Graphical User Interface has been developed and provides users with complete control over all model parameters and data processing. Regarding data processing, the user has the choice between plotting the displacement curve of each sensor, visualizing a dynamic three-dimensional animation of the SCC, and visualizing a dynamic virtual scene of the experiment. Both the 3-D animation and the virtual reality environment are very convenient as the user can observe what theoretically happens at the level of each sensor during any head rotation. This model also provides a better understanding of different kinds of erroneous motion sensations which may appear during combined rotation motions.

The core of this virtual reality model computes in real time equations of motion in earth, chair and head coordinate system, and then project angular acceleration vectors into a reference frame attached to the semicircular canals. The orientation of the axes of this coordinate

system has been defined according to a recent study based on 3-D multiplanar reconstructions of computerized tomography scans (Della Santina et al. 2005). The resulting non-orthogonal system underlines the fact that all the canals are stimulated for any rotation.

In addition, a similitude study has also been proposed in order to build a large scale model of the semicircular canals. It was found that four dimensionless parameters define the design features of the mockup, by considering a step change in head angular velocity, keeping constant the dimensionless parameters, and taking into account a minimum Young's modulus of the cupula equal to 0.005 GPa. Thus we have determined that a scale factor  $A=100$  is the most convenient, allowing higher simulated head rotations. We have also looked for potential materials that could be used to build the scale model. We have proposed to use a highly viscous fluid for the endolymph such as the *polydimethylsiloxane Wacker AK 60,000 cSt Silicon Oil*, and to use a super soft silicone rubber for the cupula, e.g. ECOFLEX 00-10.

- Chapter 4 has been devoted to models for human spatial orientation perception. First, we have investigated the Observer and Kalman filter model families and have shown why these two approaches are dynamically equivalent from an input-output blackbox. We have compared the Merfeld Observer model with the Borah Kalman filter model for a simple one-dimensional case, i.e. a subject who experiences a yaw rotation around an Earth vertical axis in dark (angular velocity storage), and for a three-dimensional case, i.e. a subject who experiences a forward acceleration in dark (somatogravic illusion). Both models are structurally different in the sense that:

1. Merfeld Observer model utilizes only four ad hoc parameters while the Borah Kalman filter model postulate 16 weighting factors
2. In Merfeld Observer model, residuals simply add to the output, whereas in Borah KF model the residuals determine the rate of change of model outputs
3. Merfeld Observer model work for large head tilts (nonlinear model), whereas Borah KF model is linearized near the upright position
4. Merfeld considered faster dynamics for the otoliths
5. Merfeld considered only vestibular cues while Borah took into consideration vestibular as well as visual cues.

However, despite all these differences, we have shown that both models predict similar results for perception of head angular velocity in the dark as well as perception of linear acceleration and pitch angle in response to a forward linear acceleration in darkness.

We have also discussed the presence of low pass filters, also called shaping filters, used to limit the band of the process noises. First, these filters constitute a mathematical device to augment the size of the state vector by adding one more state that correspond either to head angular velocity or head linear acceleration. Second, these shaping filters control the magnitude of the process noise covariance. Third, we have argued that the consideration of these filters means that the brain expects head angular velocities and linear acceleration in a certain range of frequencies. In other words, these low pass filters somehow reflect past motion history, i.e. kind of motion our head has encountered in the past and that the central nervous system might expect. Unlike Borah who considered bandwidths and noise covariances as free parameters of his model, we have argued that these parameters can be ecologically justified based on human movement and threshold characteristics.

Second, in order to extend Borah steady state Kalman filter model to a general time-continuous three-dimensional model that works for any head attitude, we have applied nonlinear estimation techniques to the problem of human spatial orientation perception. In particular, two models based on the extended and the unscented Kalman filters respectively, have been developed. The first model was based on Pommellet's 1990 extended Kalman filter model. Several modifications of Pommellet's model have been performed such as the consideration of different dynamics for the otolith organs, the use of fictitious process noise for the quaternion in order to reduce numerical instabilities of the filter, and correction of some implementation errors as regard measurement noise. The second model was developed according to the hybrid version of the unscented Kalman filter. This novel technique is fundamentally different from the EKF in the sense that the EKF approximates the nonlinear functions of the state space model, whereas the UKF propagates a set of sigma points through the nonlinear functions, and then estimates the mean and covariance of the states based on the transformed sigma points.

As the central nervous system is modeled as a continuous system, the differential equations for the estimated state vector  $\hat{x}$  and the error covariance matrix  $P$  have been integrated between each measurement time step. For the EKF, fourth-order Runge-Kutta integration has been used to avoid numerical instabilities, whereas an Euler integration scheme appeared to be sufficient in the UKF to obtain accurate results. The direct consequence was a computation time about 2-3 times faster in favor of the UKF.

Both models were successfully implemented and used to predict the responses to a number of vestibular, visual and visual-vestibular motion paradigms such as the somatogravic illusion, angular vection, vestibular Coriolis illusion and pseudo-Coriolis illusion. However, according to the results provided by both filters, it turned out that the UKF yields more accurate and less oscillatory responses than the EKF, for the same set of initial conditions and noise parameters. In addition, a sensitive study has been proposed so as to investigate the influence of the bandwidths and process noise covariance on the predicted perceptions of orientation, velocity, and acceleration for various motion paradigms. Results of this study are summarized in the table below:

	High values of $\beta_\omega$	High values of $\beta_t$	High values of $Q_t$
Yaw rotation in darkness	Shorter perception of head angular velocity	–	–
Forward linear acceleration in darkness	–	Shorter perception and lower magnitude of head linear acceleration Quicker illusion of tilt	Longer perception and higher magnitude of head linear acceleration Slower illusion of tilt
Vestibular Coriolis illusion	Shorter perception of head angular velocity Smaller and shorter perception of pitch angle	–	–

**Table 6.1.** Summary of the sensitivity study of some of the parameters of the UKF model.

It has been shown that a high value of bandwidth of angular velocity tends to shorten the perception of head angular velocity. In addition, in the case of the vestibular Coriolis illusion, the perception of pitch angle becomes smaller and the associated sensation is also shortened. In the case of a forward acceleration in darkness, a similar phenomenon is observed for a high value of bandwidth of linear acceleration. The perception of linear acceleration is shortened and the associated magnitude is diminished. This involves a fast illusion of tilt. The inverse effect is obtained if a high magnitude of linear acceleration process noise covariance is considered. Therefore, we can see that the behavior of the developed model really depends on the assumed parameters for the bandwidths and noise covariances. It is the reason why these parameters must be estimated as accurate as possible. In chapter four, we have tempted to approximate these parameters based on ecological assumptions. For instance, we have determined that a bandwidth of angular velocity of 25 rad/s should reflect the spectrum of yaw head movements normally made in daily life

## 6.2. Perspectives

- Regarding the proposed models of the human semicircular canal cupula, the latter has been described in terms of its pressure-volume elastic coefficient  $K$ . However, the cupula is composed of two components: filamentous material (proteins) and an amorphous mucopolysaccharide substance (Hillman et al., 1979). This kind of structure, which resembles specific biopolymers (biological polysaccharides) or hydrogels, is much more like a viscoelastic material. Therefore, viscoelasticity models, such as Maxell or Kelvin-Voigt model, should be considered in future studies. These models would help investigators to answer two questions: Do the viscoelastic properties of the cupula have a significant influence on the dynamic response of the system cupula/endolymph? Does the cupula behave more stiffly for fast deflections?

Furthermore, another limitation of the presented study is that the cupula was assumed homogeneous because of the lack of knowledge of its mechanical properties. In order to build a more detailed and accurate model based on the structural examination of Silver et al. (1998), future experiments to determine, or at least estimate, the mechanical properties of each region of the cupula may be ultimately needed.

Concerning the final three-dimensional fluid-structural finite-element model of the semicircular canals, we have obtained promising results. However a finer mesh needs to be considered in order to ensure the convergence of the simulation. Therefore, the size of the model - in terms of degrees of freedom – will increase and the simulations will have to be run on a supercomputer. Based on our 3-D simulations, we have estimated that at least 10-12 Go of RAM are required to avoid any swap between the main memory and the disk.

In the future, this model could be used to study different kind of vestibular disorders such as the Ménière's disease which is caused by an increase in pressure and volume of the endolymph.

- In case of the developed virtual reality model, its major limitation is that it does not entirely represent the real diagnosis procedure. Currently, the way to explore the vestibular component of the inner ear is to record the vestibulo-ocular-reflex (VOR) – a reflexive eye movement due to the stimulation of the vestibular sensors - using different experiments including the rotary chair test. By examining this ocular reflex relatively to the imposed rotational movements the specialists are able to detect any vestibular deficiencies. A potential future application of this model could be its use during such diagnosis in order to have a

comparison between clinical results and those of the model. To achieve this goal this first version has to be enhanced:

1) by taking into account the link between the vestibular sensors and the vestibulo-ocular-reflex, i.e. the transfer functions between these two components (Note that vestibulo-ocular reflex models exist in the literature, e.g. Zupan, 1995)

2) by incorporating eye movements in the virtual scene.

- Regarding models for human spatial orientation perception, both the presented EKF and UKF models assume Gaussian noises. While this assumption may be valid in many cases, it is not always justified (Faisal et al., 2008). Therefore, a prospect would be to apply the Particle Filter technique to the three-dimensional model here presented. The particle filter, which was invented to numerically implement the Bayesian estimator is a completely nonlinear estimator that does not assume any specific Gaussian noise. The particle filter has some similarities with the UKF in that it transforms a set of points via known nonlinear equations and combines the results to estimate the mean and covariance of the state. However, in the particle filter the points are chosen randomly using Monte Carlo simulations, whereas in the UKF the points are chosen on the basis of a specific algorithm. Because of this, the number of points used in a particle filter generally needs to be much greater than the number of points generated by the UKF. On the other hand, the estimation error in a particle filter does converge to zero as the number of particles (and hence the computational effort) approaches infinity, which is not the case for the UKF. Therefore, although the Kalman filter can be used in nonlinear systems for state estimation, the particle filter may give better results at the price of additional computational effort. A future study regarding the application of particle filtering to a 3-D model of human spatial orientation should help to answer the following questions: Does particle filtering improve the performance of the three-dimensional UKF model for human spatial orientation estimation? Does the improved performance worth the increased computational effort? How many particles should we consider to get at least the same accuracy as the UKF? In that case, is the computation time comparable with that of the UKF? Does the unscented Kalman filter provides a good balance between the low computational effort of the Kalman filter and the high performance of the particle filter?

However, a well known and fundamental problem in particle filters is “particle collapse” or “particle degeneracy” as a result of Bayes’ rule. Recently, F. Daum and J. Huang have solved this problem by developing a new filter that implements Bayes’ rule using particle flow rather than with a pointwise multiplication of two functions. This new nonlinear filter has been shown to be vastly superior to the classic PF and the EKF as the computational complexity of this filter is many orders of magnitude less than the PF with optimal estimation accuracy for problems with dimension greater than 4. Therefore, another prospect of this study would be to apply the nonlinear particle flow filter to the three-dimensional problem of human spatial orientation which would provide more accurate results as well as faster computation time than any other nonlinear estimation techniques.

## References

- Adenot, S., 2004. *Artificial gravity: changing the intensity of Coriolis cross-coupled stimulus with head-angle*. S.M. Thesis, Massachusetts Institute of Technology, Cambridge.
- Archer, C.R., Cooper, M.H., Kveton, J.F., 1988. *Correlation of high-resolution computed tomography and gross anatomic sections of the temporal bone*. II. Vestibular apparatus. *Am. J. Otol.*, 9, 276-281.
- Bélanger, L.F., 1961. *Observations of the intimate structure and composition of the chick labyrinth*. *The Anatomical Record*, 139, 5-45.
- Bilien, V., 1993. *Modeling human spatial orientation perception in a centrifuge using estimation theory*. S.M. Thesis, Massachusetts Institute of Technology, Cambridge, MA.
- Borah J., Young L.R., Curry R.E., 1979. *Sensory mechanism modelling*. AFHRL-TR-78-83, Wright-Patterson Air Force Base, OH.
- Borah J., Young L.R., Curry R.E., 1988. *Optimal estimation model for human spatial orientation*. *Ann. NY Acad. Sci.*, 545, 51-73.
- Braithwaite M.G., Durnford S.J., Groh S.L., Jones H.D., Higdon A.A., Estrada A., Alvarez E.A., 1998. *Flight simulator evaluation of a novel flight instrument display to minimize the risks of spatial disorientation*. *Aviation, Space and Environmental Medicine*, 69, 733-742.
- Buckingham, E., 1914. On physically similar systems: illustrations of the use of dimensional equations. *Phys. Rev.*, 4, 345-376.
- Canuto, C.M., Hussaini, Y., Quarteroni, A., Zang, T.A., 1988. *Spectral method in fluid dynamics*, Springer-Verlag.
- Carey, R., Bell, G., 1997. *The Annotated VRML 2.0 Reference Manual*. Addison-Wesley Publishing, Boston, MA.
- Curthoys, I.S., Oman, C.M., 1987. *Dimensions of the horizontal semicircular duct, ampulla, and utricle in the human*. *Acta Otolaryngol.*, 103, 254-261.
- Dai, M., Klein, A., Cohen, B., Raphan, T., 1999. *Model-Based study of the human copular time constant*. *J. Vestib. Res.*, 9, 293-301.
- Damiano, E.R., Rabbitt, R.D., 1996. *A singular perturbation model of fluid dynamics in the vestibular semicircular canal and ampulla*. *J. Fluid Mech.*, 307, 333-372.
- Daum, F., Huang, J., 2009. Nonlinear filters with particle flow induced by log-homotopy.
- De Vries, H.L., 1950. *Mechanics of the labyrinth organ*. *Acta Otolaryngol.*, 38, 262-273.
- De Vries, H.L., 1956. *Physical aspects of the sense organs*. *Progress in Biophysics and Biophysical Chemistry*, 6, 207-264.
- Della Santina, C.C., Polyagaylo, V., 2005. *Orientation of human semicircular canals measured by three dimensional multiplanar CT reconstruction*. *J. Assoc. Res. Otolaryngol.*, 6, 191-206.



- Dohlman, G.F., 1935. *Some practical and theoretical points in labyrinthology*. In Proceedings of Royal Society of Medicine 28, 65-78.
- Dohlman, G.F., 1969. *The shape and function of the cupula*. J. Laryngol., 83, 43-53.
- Dohlman, G.F., 1971. *The attachment of the cupulae, otolith and tectorial membranes to the sensory cell areas*. Acta Otolaryngol., 71, 89-105.
- Donea, J., Huerta, A., Ponthot, J.-Ph, Rodriguez-Ferran, A., 2003. *Arbitrary Lagrangian-Eulerian Methods*. www.wiley.co.uk/ecm/pdfs/Volume\_1\_Chapter\_14.pdf.
- Einstein, A., 1908. *Über das Relativitätsprinzip und die aus demselben gezogenen Folgerungen*. Jahrb. Radioakt., 4, 411-462.
- Faisal AA, Selen LP, Wolpert DM, 2008. *Noise in the nervous system*. Nat Rev Neurosci 9:292-303.
- Fernandez, C., Goldberg, J.M., 1971. *Physiology of peripheral neurons innervating semicircular canals of the squirrel monkey. II. Response to sinusoidal stimulations and dynamics of peripheral vestibular system*. J. Neurophysiol., 34, 661-675.
- Fernandez C and Goldberg JM., 1976. *Physiology of peripheral neurons innervating otolith organs of the squirrel monkey. I. Response to static tilts and to long-duration centrifugal force*. J. Neurophysiol., 39, 970-984.
- Fernandez C and Goldberg JM., 1976. *Physiology of peripheral neurons innervating otolith organs of the squirrel monkey. II. Directional selectivity and force-response relations*. J. Neurophysiol., 39, 985-995.
- Fernandez C and Goldberg JM., 1976. *Physiology of peripheral neurons innervating otolith organs of the squirrel monkey. III. Response dynamics*. J. Neurophysiol., 39, 996-1008.
- Frishkopf, L.S., Oman, C.M., 1972. *Structure and motion of cupulae of lateral line organs in Necturus maculosus*. Quarterly Progress Report, Research Laboratory of Electronics, Massachusetts Institute of Technology, 104, 326-343.
- Goldberg, J., & Fernandez, C., 1971. *Physiology of peripheral neurons innervating the semicircular canals of the squirrel monkey. I. Resting discharge and response to constant angular accelerations*. J. Neurophysiol., 34, 635-660.
- Grant, J.W., Best, W.A., 1986. *Mechanics of the otolith organ dynamic response*. Annals of Biomedical Engineering, 14, 241-256.
- Grant, J.W., Best, W.A., 1987. *Otolith organ mechanics: lumped parameter model and dynamic response*. Aviation Space and Environmental medicine, 58, 970-976.
- Grant, J.W., Cotton, J.R., 1990. *A model for otolith dynamic response with viscoelastic gel layer*. J. Vestib. Res., 1, 139-151.
- Grant, J.W., Huang, C.C., Cotton, J.R., 1994. *Theoretical mechanical frequency response of the otolithic organs*. J. Vestib. Res., 4, 137-151.
- Groen, J.J., Egmond, A.A.J. van, Jongkees, L.B.W., 1952. *The function of the vestibular organ*. Practica Oto-Rhino-Laryngologica, 14, 1-109.

- Groen, J.J., 1956. *The semicircular canal system of the organs of equilibrium*. Phys. Med. Biol., 103-117.
- Guedry, F.E., Benson, A.J., 1978. *Coriolis cross-coupling effects: Disorienting and nauseogenic or not?* Aviation, Space and Environmental. Medicine, 49, 29-35.
- Halswanter, T., Jaeger, R., Mayr, S., Fetter, M., 2000. *Three-dimensional eye-movement responses to off-vertical axis rotations in humans*. Exp. Brain Res., 134, 96-106.
- Harada, T., Ishii, S., Tayama, N., Sugasawa, M., 1990. *Computer aided three-dimensional reconstruction of the osseous and membranous labyrinths*. Eur. Arch. Otorhinolaryngol., 247, 348-351.
- Hashimoto, S., 2003. *Three-dimensional reconstruction and measurement of the human membranous semicircular canal*. Nippon Jibiin-koka Gakkai Kaiho, 106, 1-6.
- Hillman, D.E., 1972. *Observations on morphological features and mechanical properties of the peripheral vestibular receptor system in the frog*. Prog. in Brain Res., 37, 69-75.
- Hillman, D.E., 1974. *Cupular structure and its receptor relationship*. Brain, Behavior, and Evolution, 10, 52-68.
- Hillman, D.E., 1977. *Relationship of the sensory cell cilia to the cupula*. Scanning Electron Microscopy, 2, 415-420.
- Hillman, D.E., McLaren, J.W., 1979. *Displacement configuration of semicircular canal cupulae*. Neuroscience, 4, 1989-2000.
- Hosman, R.J., 1996. *Pilot's perception and control of aircraft motions*. Ph.D. Thesis, Delft University of Technology, Delft, The Netherlands.
- Igarashi M., 1965. *Architecture of the otolith end organ with some functional considerations*. NASA Report, N66-17272.
- Igarashi M., 1966. *A standard technique for temporal bone preparation*. Monograph 13, Naval Aerospace Medical Institute, Pensacola, Florida.
- Igarashi, M., Alford, B.R., 1969. *Cupula, cupular zone of otholitic membrane, and tectorial membrane in the squirrel monkey*. Acta Otolaryngol., 68, 420-426.
- Jedrzejewski, F., 2001. *Introduction aux méthodes numériques*, Springer-Verlag.
- Jones, G.M., Milsum, J.H., 1965. *Spatial and dynamics aspects of visual fixation*. IEEE transactions on Bio-Med. Eng., 54-62.
- Julier, S., Uhlmann, J.K., Durrant White, H., 1995. *A new approach for filtering nonlinear system*. In the Proceedings of the American Control Conference, Seattle, Washington, 1628-1632.
- Julier, S., Uhlmann, J.K., 1997. *A new extension of the Kalman filter to non-linear systems*. In Proc. SPIE – Int. Soc. Opt. Eng. (USA), 3068, 182-193.
- Julier S., Uhlmann, J.K., Durrant-White, H., 2000. *A new approach for non-linear transformation of means and covariances*. IEEE Transactions on Automatic Control, 45, 477-482.
- Kalman, R.E., 1960. *A new approach to linear filtering and prediction theory*. J. Basic Eng. 82, 33-45.

- Kalman, R.E., 1960. On the general theory of control systems. Proc of the first IFAC Moscow congress.
- Kassem, M., Deserranno, D., Oas, J.G., 2005. *Fluid-structural interactions in the inner ear*. Computers & Structures, 83, 181-189.
- Knapp C.J., Johnson R., 1996. *F-16 Class A mishaps in the U.S. Air Force, 1975-93*. Aviation, Space and Environmental Medicine, 67, 777-783.
- Lim, D.J., 1971. *Vestibular sensory organs. A scanning electron microscopic investigation*. Arch. Otolaryngol., 94, 69-76.
- Luenberger, D.G., 1963. *Observing the state of a linear system*. IEEE Transactions on Military Electronics, 74-80.
- MacNeilage P.R., Ganesan, N., Angelaki, D.E., 2008. *Computational approaches to spatial orientation: from transfer functions to dynamic Bayesian inference*. J. Neurophysiol., 100, 2981-2996.
- Mayne, R., 1950. *The dynamics characteristics of the semicircular canals*. J. Comp. and Physiol. Psychol., 43, 309-319.
- Mayne, R., 1974. *A systems concept of the vestibular organs*. In: Kornhuber H, editor. Handbook of Sensory Physiology. Vestibular system. Psychophysics, Applied Aspects and General Interpretations. Part 2. Berlin-New York: Springer-Verlag, 493-580.
- Meiry, J.L., 1966. *The vestibular system and human dynamic space orientation*. NASA report: NASA CR-628.
- Merfeld D.M., Young L.R., Oman C.M., Shelhamer M.J., 1993. *A multidimensional model of the effect of gravity on spatial orientation of the monkey*. J. Vestib. Res., 3, 141-61.
- Merfeld D.M., 1995. *Modeling the vestibule-ocular reflex of the squirrel monkey during eccentric rotation and roll tilt*. Exp. Brain. Res., 106, 123-134.
- Merfeld, D.M., Zupan, L., 2002. *Neural processing of gravito-inertial cues in humans. III. Modeling tilt and translation responses*. J. Neurophysiol., 87, 819-833.
- McHenry, M.J., van Netten, S.M., 2007. *The flexural stiffness of superficial neuromasts in the zebrafish lateral line*. J. Exp. Biol., 210, 4244-4253.
- McHenry, M.J., Strother J.A., van Netten, S.M., 2008. *Mechanical filtering by the boundary layer and fluid-structure interaction in the superficial neuromast of the fish lateral line system*. J. Comp. Physiol., 9, 795-810.
- McLaren, J.W., 1977. *The configuration of movement of the semicircular canal cupula*. Ph.D. thesis, University of Iowa, Iowa city, IA.
- McLaren, J.W., Hillman, D.E., 1979. *Displacement of the semicircular canal cupula during sinusoidal rotation*. Neuroscience, 4, 2001-2008.
- Mohinder S. Grewal, Angus P., 2001. *Kalman filtering : theory and practice using MATLAB*. Edited by Wiley-Interscience.
- Natick, *Virtual Reality Toolbox User's Guide*, The MathWorks, Inc., March 2007.

- Natick, *Simulink User's Guide*, The MathWorks, Inc., March 2007.
- Newman, M.C., 2009. *A multisensory Observer model for human spatial orientation perception*. S.M. Thesis, Massachusetts Institute of Technology, Cambridge.
- Njeugna, E., Kopp, C.M., 1986. *Modèles mécaniques d'un canal semi-circulaire*, J. Biophys. Biomécan., 10, 63-70.
- Njeugna, E., Kopp, C.M., Eichhorn, J.L., 1990. *Etude mécanique de la cupule du capteur de pression de l'oreille interne des vertébrés*. Innovation et Technologie en Biologie et Médecine, 11, 165-182.
- Obrecht, B., 1976. *Comportement dynamique de systèmes en régime non permanent. Etude d'un modèle théorique et d'un modèle hydraulique. Application à la biomécanique*. Ph.D. Thesis, Strasbourg, Université Louis Pasteur.
- Oman, C.M., Young, L.R., 1972a. *The physiological range of pressure difference and cupula deflections in the human semicircular canal*. Acta Otolaryngol., 74, 324-331.
- Oman, C.M., Young, L.R., 1972b. *Physiological range of pressure difference and cupula deflections in the human semicircular canal: Theoretical considerations*. Prog. Brain Res., 37, 529-539.
- Oman, C.M., Frishkopf, L.S., Goldstein, M.H., 1979. *Cupula motion in the semicircular canal of the skate, Raja erinacea*. Acta Otolaryngol., 87, 528-538.
- Oman C.M., 1982. *A heuristic mathematical model for the dynamics of sensory conflict and motion sickness*. Acta Otolaryngol. Suppl., 392, 1-44.
- Oman, C.M., Marcus, E.N., Curthoys, I.S., 1987. *The influence of semicircular canal morphology on endolymph flow dynamics*. Acta Otolaryngol., 103, 1-13.
- Oman, C.M., 1991. *Sensory conflict in motion sickness: an Observer theory approach. Pictorial communication in real and virtual environments*. S. Ellis. London, Taylor and Francis, 362-367.
- Ormsby C., 1974. *Model of Human Dynamic Orientation*. Ph.D Thesis, Massachusetts Institute of Technology, Cambridge, MA.
- Pommellet P.E., 1990. *Suboptimal Estimator for the Spatial Orientation of a Pilot*. S.M. Thesis, Massachusetts Institute of Technology, Cambridge.
- Poncin, H., 1940. *Etude d'une équation intégrale de l'hydrodynamique du fluide visqueux*. J. Math., 19, 163-195.
- Rabbit, R.D., 1999. *Directional coding of three-dimensional movements by the vestibular semicircular canals*. Biol. Cybern., 80, 417-431.
- Rabbitt, R.D., Damiano, E.R., Grant, J.W., 2004. *Biomechanics of the semicircular canals and otolith organs*. In: Highstein, S.M., Popper, A., Fay, R. (Eds), The Vestibular System. Springer, New York, 153-201.
- Raub, C.B., Suresh, V., Krasieva, T., Lyubovitsky, J., Mih, J.D., Putnam, A.J., Tromberg, B.J., Goerge, S.C., 2007. *Noninvasive assessment of collagen gel microstructure and mechanics using multiphoton microscopy*. Biophysical Journal, 92, 2212-2222.
- Raphan T., Matsuo V, Cohen B., 1977. *A velocity storage mechanism responsible for optokinetic nystagmus (OKN), optokinetic after-nystagmus (OKAN) and vestibular nystagmus*. In: Control of Gaze

by Brain Stem Neurons, Developments in Neuroscience, edited by Baker R, Berthoz A. Amsterdam: Elsevier/NorthHolland Biomedical, 1, 37-47.

Raphan T., Matsua V., Cohen B., 1979. *Velocity storage in the vestibule-ocular reflex arc (VOR)*. Exp. Brain. Res., 35, 229-248.

Robinson D.A., 1977. *Vestibular and optokinetic symbiosis: an example of explaining by modeling*, In: Control of Gaze by Brain Stem Neurons, Developments in Neuroscience, edited by Baker R, Berthoz A. Amsterdam: Elsevier/NorthHolland Biomedical, 1, 49-58.

Roman, S., 2000. *Physiologie vestibulaire*. Ency. Méd. Chirurg., Elsevier.

Sauvage, J.P., 1999. *Anatomie de l'oreille interne*. Ency. Méd. Chirurg. , Elsevier.

Silver, R.B., Reeves, A.P., Steinacker, A., Highstein, S.M., 1998. *Examination of the cupula stereocilia of the horizontal semicircular canal in the toadfish *Opsanus Tau**. J. Comp. Neurol., 402, 48-61.

Simon D., 2006. *Optimal State Estimation: Kalman,  $H_{\infty}$ , and Nonlinear approaches*. Edited by Wiley-Interscience.

SolidWorks Office Premium 2007, Software Package, SolidWorks Corporation, Concord, MA, 2007.

SolidWorks to SimMechanics Translator, Software Package, The MathWorks, Inc., Natick, MA, 2007.

SimMechanics, "SimMechanics User's Guide", The MathWorks, Inc., Natick, MA, March 2007.

Squires, T.M., Weidman, M.S., Hain, T.C., Stone, H.A., 2004. *A mathematical model for top-shelf vertigo: the role of sedimenting otoconial in BBPV*. J. Biomech., 37, 1137-1146.

Steer, R.W., 1967. *The influence of angular and linear acceleration and thermal stimulation on the human semicircular canal*. S.M. Thesis, Massachusetts Institute of Technology, Cambridge.

Steinhausen, W., 1931. *Über den Nachweis der Bewegung der Cupula in der intakten Bogengangsampulle des Labyrinthes bei der natürlichen rotatorischen und calorischen Reizung*. Pflug. Arch. 228, 322-328.

Steinhausen, W., 1933. *Über die Beobachtung der Cupula in den bogengansampullen des Lebenden Hechts*. Pflueger's Arch. ges. Physiol., 232, 500-512.

Tagaki, A., Sando, I., Takahashi, H., 1989. *Computer-aided three-dimensional reconstruction and measurement of semicircular canals and their cristae in man*. Acta. Otolaryngol., 107, 362-365.

Telban, R.J., Cardullo, F.M., 2005. *Motion cueing algorithm development: Human-centered linear and nonlinear approaches*. NASA report: NASA/CR-2005-213747.

Ten Kate, J.H., 1969. *The oculo-vestibular reflex of the growing pike. A biophysical study*. PhD Thesis, Groningen.

Ten Kate, J.H., 1973. *The mechanics of the growing semicircular canal*. J. Exp. Biol., 58, 351-366.

Timoshenko, S., 1964. *Theory of plates and shells*. Open University Press (Eds).

Van Buskirk, W.C., 1976. *The fluid mechanics of the semicircular canals*. J. Fluid Mech., 78, 87-98.

- Van Buskirk, W.C., 1977. *The effect of the Utricle on Fluid Flow in the Semicircular Canal*. *Annals of Biomed. Eng.*, 5, 1-11.
- Van Buskirk, W.C., 1988. *The biomechanics of the semicircular canals*. IEEE Engineering in Medicine and Biology Society, 10<sup>th</sup> Annual International Conference.
- Van der Merwe, R., Wan, E., Julier, S., Bodganov, A., Harvey, G., Hunt, J., 2004. *Sigma-point Kalman filters for nonlinear estimation and sensor fusion: applications to integrated navigation*. Proceedings of the AIAA Guidance Navigation & Control Conference, Providence RI, 1-30.
- Van Egmond, A.A.J., Groen, J.J., Jonkees, L., 1949. *The mechanics of the semicircular canal*. *J. Physiol.*, 110, 1-17.
- Velema, J., Kaplan, D., 2006. *Biopolymer-based biomaterials as scaffolds for tissue engineering*. *Advances in Biochemical Engineering / Biotechnology*, 102, 187-238.
- Ventsel, E., Krauthammer, T., 2001. *Thin plates and shells: Theory, analysis and applications*. CRC Publisher, New York.
- Vingerhoets, R.A.A., Medendorp, W.P., Van Ginsbergen, J.A.M., 2006. *Time course and magnitude of illusory translation perception during off-vertical axis rotation*. *J. Neurophysiol.*, 95, 1571-1587.
- Vingerhoets, R.A.A., Van Ginsbergen, J.A.M., Medendorp, W.P., 2007. *Vertically perception during off-vertical axis rotation*. *J. Neurophysiol.*, 97, 3256-3268.
- Womersley, J.R. 1955. *Method for the calculation of velocity, rate flow, and viscous drag in arteries when the pressure gradient is known*. *J. Physiol.*, 127, 553-563.
- Yamauchi, A., Rabbitt, R.D., Boyle, R., Highstein, S.M., 2001. *Relationship between inner-ear fluid pressure and semicircular canal afferent nerve discharge*. *J. Assoc. Res. Otolaryngol.*, 3, 24-44.
- Young, L.R., Meiry, J.L., 1968. *A revised dynamic Otolith model*. *Aerospace Med.*, 39, 606-608.
- Young, L.R., Oman, C.M., 1969. *Model of vestibular adaptation to horizontal rotations*. *Aerospace Med.*, 40, 1076-1080.
- Zacharias, G.L., 1977. *Motion sensation dependence on visual and vestibular cues*. Ph.D. Thesis, Massachusetts Institute of Technology, Cambridge, MA.
- Zalin, A., 1967. *On the function of the kinocilia and stereocilia with special reference to the phenomenon of directional preponderance*. *J. Laryngol.*, 81, 119-135.
- Zupan, L. 1995. *Modélisation du Réflexe Vestibulo-Oculaire et prédiction des cinétoses*, PhD Thesis, Ecole Nationale Supérieure des Télécommunications, ENST95-E004.
- Zupan L.H., Merfeld D.M., Darlot C., 2002. *Using sensory weighting to model the influence of canal, otolith and visual cues on spatial orientation and eye movements*. *Biol. Cybern.* 86, 209-230.

# Appendix 1:

## Numerical model for the resolution of the fluid flow within a single canal

At the beginning of our work, we were interested in studying fluid dynamics that takes place within each semicircular of the inner ear so as to understand the dynamic behavior of the system cupula/endolymph. Therefore we developed a numerical tool that solves, for different head motions, the governing equations of the fluid flow in the slender duct of the lateral semicircular canal, so that motions and volume displacements of the cupula can be approximated. This numerical tool based on a Chebyshev spectral collocation method has been validated according to an analytical solution for a specific head motion.

This work is not included in the core of this report as it does not really make any significant contribution. Indeed, modeling of the system endolymph/cupula based on the governing equations of fluid flow has already been investigated by many researchers (Van Buskirk, 1977; Ten Kate, 1969; Oman et al., 1987; Damiano et al., 1996). However, we have chosen to add this work as an appendix as it constitutes a useful numerical tool implemented in Matlab which provides a fast and accurate solution for the fluid flow. In addition different profiles of head motion can be quickly studied.

### 1. Modeling

Spectral methods are well adapted for the resolution of unstationnary problems in incompressible fluid mechanics, in a simple geometry (a toroidal duct in the present study). This numerical approach provides an accurate and fast solution for the fluid flow, and permits to study the global behavior of the system. More particularly, by integrating the volume flow rate, the cupula volume displacement can be approximated for different head motions.

#### 1.1. Theoretical equation of the movement

The developed model results from the Navier-Stokes equations applied to the endolymph, and takes into account the cupula as an elastic diaphragm. The fluid has a constant density  $\rho$  and a kinematic viscosity  $\nu$ . Several assumptions are considered:

- The horizontal canal is subjected to rotational movements around an axis  $(O\vec{z})$  perpendicular to its plane,
- The membranous wall is rigid,
- Endolymph is modeled as an incompressible Newtonian fluid, the flow is laminar,
- Inertia of the cupula is negligible with respect to the fluid inertia,
- If  $(U, V, W)$  are the velocity vector coordinates of a fluid particle in a curvilinear coordinates system, it is assumed that the components  $U$  and  $V$  are null and  $W(r, \theta, z, t) = W(r, t)$ ,
- A pressure-volume coefficient  $K$  is assumed. This coefficient, defined as  $K = \Delta P / \Delta V$ , characterized the volume displacement of the cupula  $\Delta V$  when the latter experiences a

transcupular pressure  $\Delta P$ . Different relations and values for this parameter have been suggested (Njeugna et al., 1986; Oman et al., 1987). In the present case, the value of  $13\text{GPa/m}^3$  is retained (Rabbitt et al., 2004). In addition, the coefficient  $K$  is related to a long time constant  $\tau_L$ , which governs the return of the cupula to its rest position, following removal of any forcing. The relation between these parameters is discussed later.

By applying the Navier-Stokes equations to the system and taking into account the presence of the cupula, the volume flow rate between the initial instant and the current  $t$  is given by:

$$\Delta V(t) = \int_0^t Q(t) dt = 2\pi \int_0^t \int_0^a r.W(r,t) dr dt \quad (1)$$

where  $a$  is the radius of the duct and  $Q$  the flow rate, and the governing integral-differential equation for the fluid flow is (Njeugna et al., 1986):

$$\rho \frac{\partial W(r,t)}{\partial t} = \frac{\Delta P}{L} - \frac{2\pi K}{L} \int_0^t \int_0^a r.W(r,t) dr dt + \frac{\mu}{r} \frac{\partial}{\partial r} \left( r \frac{\partial W(r,t)}{\partial r} \right) \quad (2)$$

where  $\Delta P$  is the transcupular pressure and  $\mu = \rho\nu$  the dynamic viscosity.

The initial and boundary conditions are  $W(r,0) = 0$ ,  $W(a,t) = 0$  respectively. The first condition means that the system is initially at rest. The second condition is the non-slip condition of the fluid at the duct wall. It must also be considered that  $\left. \frac{\partial W}{\partial r} \right|_{r=0} = 0$  which comes from the fact that even if the cylindrical coordinate system is not defined at  $r = 0$ , the fluid velocity remains finite at this position.

$\Delta P$  is the input of the system which is directly related to the angular acceleration of the head. Several expressions of  $\Delta P$  can be found through the literature (e.g. Oman et al., 1972).

### 3.2. Numerical modeling

The aim of the numerical modeling is to provide an accurate tool for the resolution of the fluid flow in the slender part of the semicircular canal, not only for a step of pressure as Njeugna (1986) did, but for different kind of head motions.

- **Spatial discretization**

In order to solve the integro-differential equation (2) a spectral collocation method based on Chebyshev polynomials is used (Canuto et al., 1988; Jdrzejewski, 2001). Following standard procedures the conventional differentiation formulation can be described as follows. A one-dimensional domain  $-1 \leq \xi \leq 1$  is considered. This domain of interest is discretized using  $N$  Gauss-Lobatto points defined as:

$$\xi_i = \cos\left(\frac{\pi i}{N}\right), i=0, \dots, N \quad (3)$$



An approximation of the function  $W(\xi)$  defined on  $[-1,1]$  is obtained by polynomial interpolation :

$$W(\xi) = \sum_{i=0}^N \lambda_i(\xi)W(\xi_i) \quad (4)$$

where  $\lambda_i(\xi)$  are the Lagrange interpolation polynomials. In the case of the Gauss-Lobatto points  $\xi_i$ ,  $\lambda_i(\xi)$  are defined by:

$$\lambda_i(\xi) = \left( \frac{1-\xi^2}{\xi-\xi_i} \right) (-1)^{i+1} \frac{T'_N(\xi)}{N^2 c_i} \quad (5)$$

where  $T'_N$  is the first derivative form of the Chebyshev polynomial of order  $N$ , and  $c_0 = c_N = 2$ ,  $c_i = 1$  for  $i=1$  to  $N-1$ .

- **Differentiation**

The  $\ell$  th-order derivative of the approximate solution  $W(\xi)$  defined on  $[-1,1]$  is evaluated at the collocation points using a differentiation operator. This one is obtained by differentiating the interpolation functions as follows:

$$\frac{d^\ell W}{d\xi^\ell}(\xi_i) = \sum_{k=0}^N \lambda_k^{(\ell)}(\xi_i)W(\xi_k) = \sum_{k=0}^N D_{ik}^\ell W(\xi_k) \quad (6)$$

where  $D_{ik}$  is a differentiation matrix which links the derivative of  $W$  computed at the collocation points with the values of  $W$  at the same points. The zero-order differentiation matrix is the identity matrix whereas the first-order is defined by:

$$D_{ik} = \frac{c_i (-1)^{k+1}}{c_k (\xi_i - \xi_k)} \text{ for } i \neq k$$

$$D_{ii} = -\frac{\xi_i}{2(1-\xi_i^2)} \text{ for } i=1, \dots, N-1$$

$$D_{00} = -D_{NN} = \frac{2N^2+1}{6}$$

Higher orders of derivative are simply obtained by evaluating the differentiation matrix  $D$  to the considered power.

- **Formulation of the governing equation**

For this problem, a first order temporal scheme is used. An implicit scheme is chosen for the viscosity terms in order to avoid a large numerical transient phenomenon. According to this, Eq. (2) can be written as:

$$\rho \frac{W^{n+1}(r,t)}{\Delta t} - \frac{\mu}{r} \left( \frac{\partial W^{n+1}(r,t)}{\partial r} + r \frac{\partial^2 W^{n+1}(r,t)}{\partial r^2} \right) = \frac{\Delta P}{L} - \frac{2\pi K}{L} \int_0^a r.W(r,t)drdt + \rho \frac{W^n(r,t)}{\Delta t} \quad (7)$$

If the following variable is substituted :  $r = \frac{a}{2}(\xi+1)$ , then Eq. (7) finally becomes:

$$\rho \frac{W^{n+1}(\xi, t)}{\Delta t} - \frac{4\mu}{a^2} \left( \frac{1}{(\xi+1)} \frac{\partial W^{n+1}(\xi, t)}{\partial \xi} + \frac{\partial^2 W^{n+1}(\xi, t)}{\partial \xi^2} \right) = \frac{\Delta P}{L} - \frac{\pi K a^2}{2L} \int_0^{t_n} \int_{-1}^1 (\xi+1) W(\xi, t) d\xi dt + \rho \frac{W^n(\xi, t)}{\Delta t} \quad (8)$$

or in matricial form:

$$\left( [I] - \frac{4\nu\Delta t}{a^2} \left( \left[ \frac{1}{(1+\xi_i)} \right] [D]^{(1)} + [D]^{(2)} \right) \right) [W^{n+1}(\xi_i, t)] = \frac{\Delta t}{\rho} \left( \frac{\Delta P}{L} - \frac{\pi K a^2}{2L} \int_0^{t_n} \int_{-1}^1 (\xi+1) W(\xi, t) d\xi dt + \rho \frac{[W^n(\xi_i, t)]}{\Delta t} \right) \quad (9)$$

Eq. (9) takes the form of a linear system  $[A][W^{n+1}] = [B]$ . The boundary conditions are inserted in the first and last line of the matrix [A] which defines respectively the no-slip condition at the duct wall and a slope equal to zero at the centre of the cross section of the duct. The corresponding values in [B] are null. Finally the matrix [A] must be invert in order to obtain the velocity vector at each new time step  $t^{n+1}$ .

In order to compute the integral term it should be noted that:

$$\int_{-1}^1 (\xi+1) W(\xi, t) d\xi = \sum_{j=0}^N \left( W(\xi_j, t) \int_{-1}^1 (\xi+1) \lambda_j(\xi) d\xi \right) \quad (10)$$

where  $\lambda_j(\xi)$  is entirely known. The terms  $\int_{-1}^1 (\xi+1) \lambda_j(\xi) d\xi$  can thus be evaluated once at  $t=0$ .

- **Validation of the numerical parameters**

Several simulations in response to a pressure step are computed in order to test the required numerical parameters, i.e. the number of collocation points and the size of the time-step. As it can be seen in Fig. 1a, the numerical solution rapidly converges for a small number of collocation points. Therefore it is not necessary to retain a large value for N which would increase the computation time. Furthermore the value of the velocity field at any points can be obtained by using the interpolation function Eq. (4) in order to have a smooth velocity function.

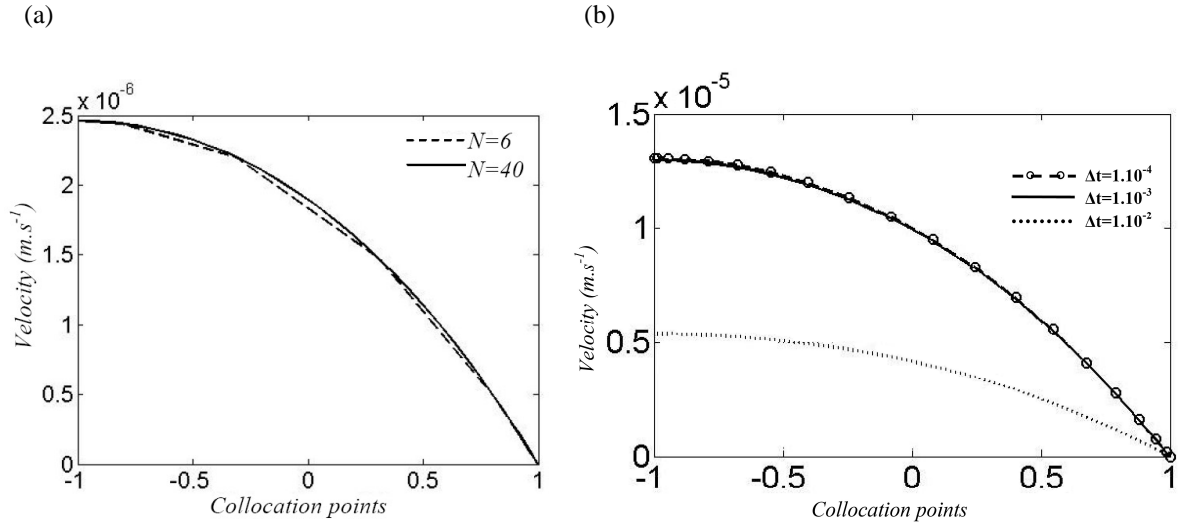


**Fig. 1.** (a) Velocity curves for different numbers of collocation points. (b) Velocity curves for different time step at  $t=0.02s$ , with  $t_0=0.02s$  and  $\Delta P=0.05Pa$ .

In order to obtain an accurate solution the size of the time-step  $\Delta t$  must be carefully chosen. If the input is a pressure step, the size of the time-step will depend upon the duration time  $t_0$  that pressure needs in order to reach its final value. Numerically the rising part of the step of pressure is defined by a fourth order polynomial such as the pressure and its first time derivative are continuous functions. Then for  $t > t_0$  the pressure keeps a constant value. For  $t_0 = 0.1s$ , a time step of  $10^{-2}$  which constitutes a good compromise between the accuracy of the results and the computation time is retained. However, if one wants to decrease the value of  $t_0$ , for instance to  $0.02s$ , then the time step should at least be lower to  $1.10^{-3}$ . Fig. 1b illustrates this latter case by plotting some velocity curves for different time-step in response to a step of pressure of  $0.05 Pa$  with  $t_0$  equal to  $0.02s$ . As it can be expected a time-step of  $0.01s$  is not sufficient for giving an accurate result because the numerical solution has not yet converged. The two other studied time-steps give almost identical results at  $t=0.02s$ .

## 2. Validation of the spectral model

In order to validate the spectral model, we use analytical solution available for the case of a step of pressure (Poncin, 1940; Obrecht, 1976).

In the 40s, the problem of non stationary laminar viscous flow in a capillary tube was studied and solved by Poncin (1940). Afterwards this problem was reformulated by Obrecht by taking into account a punctual elasticity (Obrecht, 1976). He found an exact solution to Eq. (2) in response to a step of pressure:

$$W(r,t) = 16\beta\gamma \sum_{i=1}^{\infty} \left( \frac{1}{\varphi(x_i)} \times \frac{J_0\left(\frac{r}{a}x_i\right) - J_0(x_i)}{J_0(x_i)} e^{\frac{-x_i^2}{4\alpha}t} \right) \quad (13)$$

where :

- $J_0$  is the zeroth-order Bessel function of the first kind;
- $x_i$  is the  $i^{\text{th}}$  root of the equation:  $2\gamma J_1(x) - J_0(x) \times (x^4 + \gamma)x = 0$ ;
- $\varphi(x_i) = 12\gamma x_i^2 - (x_i^4 + \gamma)^2$ ;
- $\beta = \frac{a^2 P_0}{4\nu\rho L}$ ;  $\gamma = \frac{\pi a^6 K}{\rho\nu^2 L}$  with  $P_0$  is the magnitude of the pressure step.

Fig. 2 shows the response to a step of pressure of 0.05Pa with  $t_0$  equal to 0.1s for both the analytical solution and the spectral model. The analytical and numerical results differ a lot for  $t$  below 0.1s. This is due to the transient part of the numerical model which takes into account the raise of pressure. However the curves accurately match from  $t$  close to 0.1s.

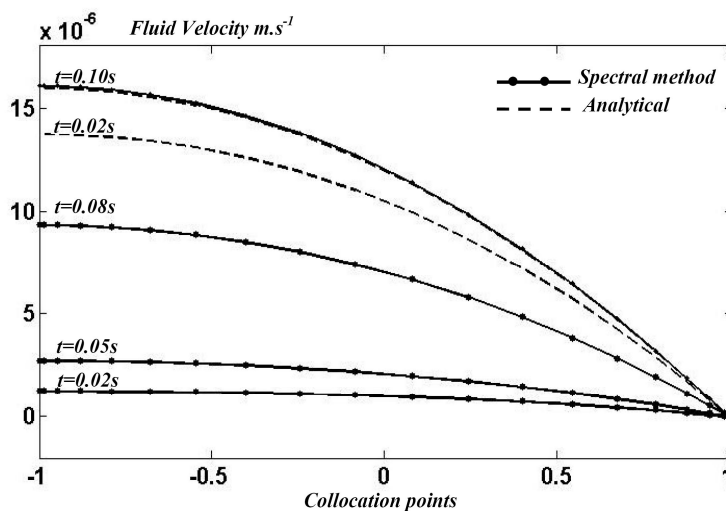


**Fig. 2.** Comparison of the velocity curves of the analytical and spectral model at different instant. Result of both models clearly differs at  $t=0.02s$  because of the transient part of the spectral model. However, both models provide identical results at 0.1s so that velocity curves are superimposed.

### 3. Study of different cases

The major advantage of the spectral numerical model is the possibility to rapidly study several angular movements of the head, which are represented by different mathematical pressure functions. Two cases are here presented, a rotation of the head at a constant angular velocity and a sinusoidal angular acceleration of the head.

- **Constant head rotation**

This first case simulates a head rotation at a constant angular velocity. Practically, the subject is strapped into a rotating chair and experiences a rotation around a vertical axis at a constant angular velocity. The rotational motion starts at  $t=0$  and stops at  $t=25s$ . This is implemented in the model by taking into account two short step of pressure (positive at  $t=0$  and negative at  $t=25s$ ) which represents the acceleration and deceleration of the head respectively. The upward and downward slope of these steps are computed by using a fourth order polynomial so as to avoid numerical problems.

An appropriate picture of the cupula displacement is the volume flow rate integral defined by Eq. (1). It can be seen that  $\Delta V$  varies exponentially according to two time constants like the behavior defined by the torsion pendulum model (Fig. 3a). Physically, that means the sensation of rotation associated with the short time constant is instantaneous. However this sensation reduces exponentially, with a time constant  $\tau_L$ , even though the angular velocity remains at a constant level. The value of this long time constant directly depends on the parameter  $K$ . The higher the cupula stiffness is, the lower the time constant governing its return to its rest position. Fig. 3b shows the normalised volume displacement of the cupula for a constant head angular velocity and for different values of  $K$ . The relation between  $K$  and  $\tau_L$  seems to be linear, which is consistent with other studies (e.g. Van Buskirk et al., 1977). In the present model, a value of  $K$  equal to  $13\text{GPa}/\text{m}^3$  yields a time constant close to 6.6s. Therefore, if one wants to consider the time constant of 4.2s - recently derived by Dai et al. (1999) - the value of  $K$  should be taken close to  $20.4\text{GPa}/\text{m}^3$ .

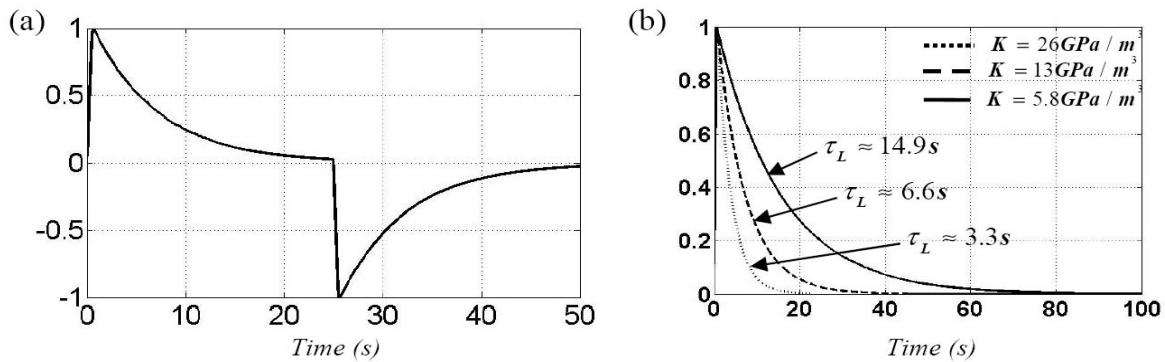


**Fig. 3.** Normalized volume displacement of the endolymph for a head angular rotation at a constant angular velocity. (a) The rotation is stopped at  $t=25\text{s}$ . (b) The rotation is maintained and the plots are for different values of  $K$ .

- **Sinusoidal angular acceleration**

Here a sinusoidal angular acceleration is considered. It is implemented in the model by a sinusoidal pressure  $\Delta P = P_0 \cos(\omega t)$ . From the analytical solution of the fluid velocity Eq. (13), an expression for the outflow in response to a sinusoidal pressure can also be derived by using the step response and the convolution product. In a steady state the outflow is given by:

$$Q(t) = \frac{4\pi a^4 P_0}{\rho L v} \sum_{i=1}^{\infty} \frac{x_i^4}{\varphi(x_i)} D_i \cos(\omega t + \phi_i) \quad (14)$$

where  $D_i = \frac{\delta^2}{\sqrt{\delta^4 + x_i^4}}$ ,  $\delta = a\sqrt{\frac{\omega}{v}}$  and  $\phi_i = \arctan\left(\frac{x_i}{\delta}\right)^2$ .

The outflow curves are shown in Fig. 4 for two different frequencies. In addition the outflow expression according to Poiseuille's law is also plotted. It can be noticed that in steady state, Eq. (14) can be reduced to its first term with the ratio  $x_1^4 / \varphi(x_1) \approx 1/32$ . Therefore, Eq. (14) can be approximated in steady state by:

$$Q \approx \frac{\pi a^4 P_0}{8\rho L v} \quad (15)$$

which is analogous to Poiseuille's law. This result only holds for frequencies superior to 0.08Hz (Fig. 4).

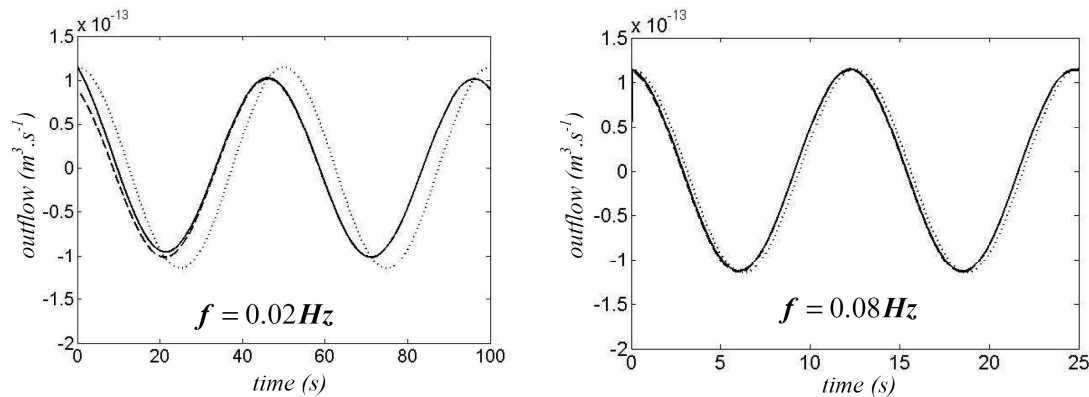


**Fig. 4.** Outflow curves for the numerical model (continuous line), analytical model (dashed line) and the Poiseuille's expression (dotted line).

It should be noticed that the required time-step  $\Delta t$  depends on the value of the pulsation  $\omega$ . According to the value of  $\omega$  the size of  $\Delta t$  must be carefully chosen in order to ensure the calculations to be independent of  $\Delta t$ . For example a frequency of 0.08Hz requires a time-step of 0.1 whereas from 0.5Hz a time step of 0.01 must be chosen (Fig. 10).

## Conclusion

The proposed numerical model simulates the flow of endolymph in a semicircular canal by considering the cupula as an elastic diaphragm. The velocity profiles, the outflow, and the volume displacement can be computed for different kinds of pressure, i.e. for different head motions. The numerical parameters have been analysed and then evaluated in order to ensure the convergence of the results. The major advantage of this numerical model is its flexibility that gives it an ability to be parametric. It has been shown that in response to a step of angular velocity the cupula behaves like the original torsion pendulum model, i.e governed by two time constants. The long time constant governing the return of the cupula to its rest position directly depends on the value of  $K$  representing its stiffness. It is shown that the higher the value of  $K$  is, the lower the long time constant is. In case of a sinusoidal angular acceleration of the head, the analytical and numerical models give identical results except during the transient part. Furthermore, it can be noticed that for frequencies higher than 0.08Hz, Poiseuille's law relating the pressure to the outflow gives similar results.

## Appendix 2: Quaternions and spatial rotation

Quaternions provide a convenient mathematics notation for representing orientations and rotations of objects in three dimensions. Compared to Euler angles they are simpler to compose and avoid the problem of gimbal lock. Compared to rotations matrices they are more efficient because the representation of a rotation as a quaternion (4 numbers) is more compact than the representation as an orthogonal matrix (9 numbers).

A quaternion is a generalized complex number consisting of four components such as:

$$q = q_0 + iq_1 + jq_2 + kq_3$$

where  $q_0, q_1, q_2$  and  $q_3$  are real numbers and  $i^2 = j^2 = k^2 = -1$ .

The four element unit quaternion vector  $(q_0, q_1, q_2, q_3)$  can be transformed into a 3 by 3 direction cosine matrix (DCM) which is defined by:

$$DCM = \begin{pmatrix} q_0^2 + q_1^2 - q_2^2 - q_3^2 & 2(q_1q_2 + q_0q_3) & 2(q_1q_3 - q_0q_2) \\ 2(q_1q_2 - q_0q_3) & q_0^2 - q_1^2 + q_2^2 - q_3^2 & 2(q_2q_3 + q_0q_1) \\ 2(q_1q_3 + q_0q_2) & 2(q_2q_3 - q_0q_1) & q_0^2 - q_1^2 - q_2^2 + q_3^2 \end{pmatrix}$$

The quaternion parameters  $(q_0, q_1, q_2, q_3)$  can be converted into the equivalent three Euler angles (roll, pitch, yaw) by comparing elements in the direction cosine matrix, as function of the Euler rotation angles, with elements in the direction cosine matrix, as function of a unit quaternion vector.

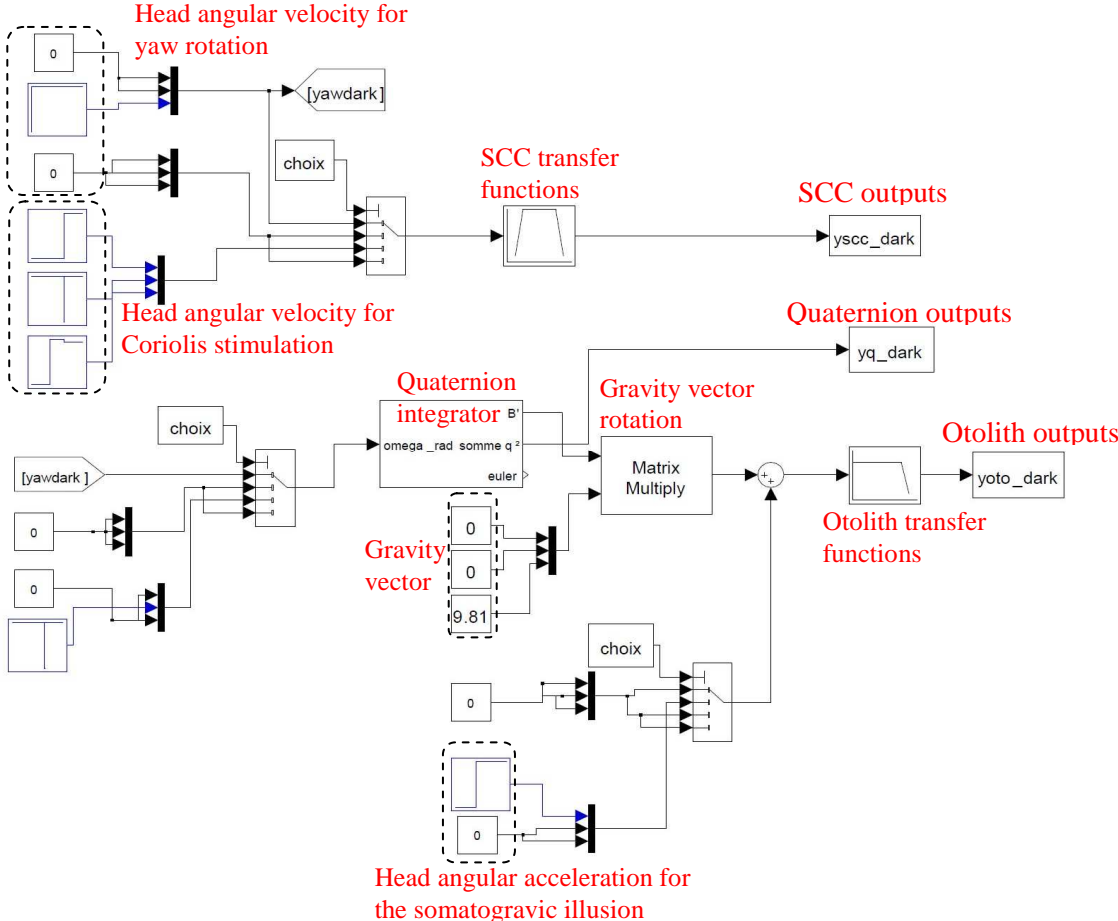
The following relationships between DCM elements and individual Euler angles can be derived:

$$\phi = a \tan \left( \frac{2(q_0q_1 + q_2q_3)}{q_0^2 - q_1^2 - q_2^2 + q_3^2} \right)$$

$$\theta = a \sin(-2(q_3q_1 - q_2q_0))$$

$$\Psi = a \tan \left( \frac{2(q_2q_1 + q_0q_3)}{q_0^2 + q_1^2 - q_2^2 - q_3^2} \right)$$

# Appendix 3: Example of Simulink model used to generate sensors output for motion paradigms in darkness





## Appendix 4: EKF and UKF models: Matlab code

- Graphical user interface

```
% %%%%%%%%%%%%%%%%%%%%%%%%%%%%%%%%%%%%%%%%%%%%%%%%%%%%%%%%%%%%%%%%%%%%%%%%%%
% Contact: Pierre Selva (pierre_bhc@hotmail.fr)
% %%%%%%%%%%%%%%%%%%%%%%%%%%%%%%%%%%%%%%%%%%%%%%%%%%%%%%%%%%%%%%%%%%%%%%%%%%

% Begin initialization code - DO NOT EDIT
function varargout = EKF_GUI(varargin)
gui_Singleton = 1;
gui_State = struct('gui_Name',       mfilename, ...
                  'gui_Singleton',  gui_Singleton, ...
                  'gui_OpeningFcn', @EKF_GUI_OpeningFcn, ...
                  'gui_OutputFcn',  @EKF_GUI_OutputFcn, ...
                  'gui_LayoutFcn',  [], ...
                  'gui_Callback',   []);
if nargin && ischar(varargin{1})
    gui_State.gui_Callback = str2func(varargin{1});
end

if nargout
    [varargout{1:nargout}] = gui_mainfcn(gui_State, varargin{:});
else
    gui_mainfcn(gui_State, varargin{:});
end
% End initialization code - DO NOT EDIT

% *****
% --- Executes just before EKF_GUI is made visible.

function EKF_GUI_OpeningFcn(hObject, eventdata, handles, varargin)
movegui('center');
%GUI initialization
set(handles.edit1,'String','10'); %bandwidth in head angular velocity
set(handles.edit2,'String','1'); %bandwidth in head linear acceleration
set(handles.edit3,'String','1'); %process noise in head angular velocity
set(handles.edit4,'String','1'); %process noise in head linear
acceleration
set(handles.edit5,'String','0.0001'); %fictitious process noise quaternion
set(handles.edit6,'String','0.0001'); %measurement noise SCC
set(handles.edit7,'String','0.0001'); %measurement noise otolith
set(handles.edit8,'String','0'); %measurement noise quaternion
set(handles.edit9,'String','0.0001'); %measurement noise vision
set(handles.ekf,'Value',1);
set(handles.ukf,'Value',0);
handles.xekf=0;
handles.choix_dark=1;
handles.xukf=[];
handles.choix=1;
handles.ukf=0;
handles.ekf=1;
handles.model=1;
handles.simulation=zeros(1,2);

handles.br=str2num(get(handles.edit1,'String'));
handles.bt=str2num(get(handles.edit2,'String'));
```

```

handles.Q_w=str2num(get(handles.edit3,'String'));
handles.Q_A=str2num(get(handles.edit4,'String'));
handles.Q_quat=str2num(get(handles.edit5,'String'));
handles.Rscc=str2num(get(handles.edit6,'String'));
handles.Roto=str2num(get(handles.edit7,'String'));
handles.Rquat=str2num(get(handles.edit8,'String'));
handles.Rvision=str2num(get(handles.edit9,'String'));
handles.Q=[handles.Q_quat*eye(4,4) zeros(4,21);
           zeros(3,4) handles.Q_w*eye(3) zeros(3,18);zeros(3,25);
           zeros(3,10) handles.Q_A*eye(3) zeros(3,12);
           zeros(12,25)];

handles.Rdark=diag([handles.Rquat,handles.Rscc,handles.Rscc,handles.Rscc,handles.Roto,handles.Roto,handles.Roto]);

handles.Rlight=diag([handles.Rscc,handles.Rscc,handles.Rscc,handles.Rvision,handles.Rvision,handles.Rvision,handles.Rvision,handles.Rvision,handles.Rvision,handles.Rvision,handles.Rvision,handles.Rvision,handles.Rvision]);

handles.output = hObject;
handles.ukfangvel_V=0;
handles.ukfangle_V=0;
handles.ukflinvel_V=0;
handles.ukflinacc_V=0;
handles.ekfangvel_V=0;
handles.ekfangle_V=0;
handles.ekflinvel_V=0;
handles.ekflinacc_V=0;

% Update handles structure
guidata(hObject, handles);

% ***** Create the output VARARGOUT function DO NOT EDIT
function varargout = EKF_GUI_OutputFcn(hObject, eventdata, handles)
varargout{1} = handles.output;

%*****
% ***** update of the parameters specified by the user*****
%*****

% bandwidth
function edit1_Callback(hObject, eventdata, handles)
handles.br=str2num(get(hObject,'String'));
guidata(hObject, handles);

function edit1_CreateFcn(hObject, eventdata, handles)
if ispc && isequal(get(hObject,'BackgroundColor'),
get(0,'defaultUicontrolBackgroundColor'))
    set(hObject,'BackgroundColor','white');
end

function edit2_Callback(hObject, eventdata, handles)
handles.bt=str2num(get(hObject,'String'));
guidata(hObject, handles);

function edit2_CreateFcn(hObject, eventdata, handles)
if ispc && isequal(get(hObject,'BackgroundColor'),
get(0,'defaultUicontrolBackgroundColor'))

```

```

        set(hObject, 'BackgroundColor', 'white');
    end

% process noise in head angular velocity
function edit3_Callback(hObject, eventdata, handles)
handles.Q_w=str2num(get(hObject, 'String'));
handles.Q(5:7,5:7)=handles.Q_w*eye(3);
guidata(hObject, handles);

function edit3_CreateFcn(hObject, eventdata, handles)
if ispc && isequal(get(hObject, 'BackgroundColor'),
get(0, 'defaultUiControlBackgroundColor'))
    set(hObject, 'BackgroundColor', 'white');
end

% process noise in head linear acceleration
function edit4_Callback(hObject, eventdata, handles)
handles.Q_A=str2num(get(hObject, 'String'));
handles.Q(11:13,11:13)=handles.Q_A*eye(3);
guidata(hObject, handles);

function edit4_CreateFcn(hObject, eventdata, handles)
if ispc && isequal(get(hObject, 'BackgroundColor'),
get(0, 'defaultUiControlBackgroundColor'))
    set(hObject, 'BackgroundColor', 'white');
end

% fictitiou process noise for the quaternion
function edit5_Callback(hObject, eventdata, handles)
handles.Q_quat=str2num(get(hObject, 'String'));
handles.Q(1:4,1:4)=handles.Q_quat*eye(4);
guidata(hObject, handles);

function edit5_CreateFcn(hObject, eventdata, handles)
if ispc && isequal(get(hObject, 'BackgroundColor'),
get(0, 'defaultUiControlBackgroundColor'))
    set(hObject, 'BackgroundColor', 'white');
end

% meaisurement noise
function edit6_Callback(hObject, eventdata, handles)
handles.Rscc=str2num(get(hObject, 'String'));
handles.R(2:4,2:4)=handles.Rscc*eye(3);
handles.Rright(1:3,1:3)=handles.Rscc*eye(3);
guidata(hObject, handles);

function edit6_CreateFcn(hObject, eventdata, handles)
if ispc && isequal(get(hObject, 'BackgroundColor'),
get(0, 'defaultUiControlBackgroundColor'))
    set(hObject, 'BackgroundColor', 'white');
end

function edit7_Callback(hObject, eventdata, handles)
handles.Roto=str2num(get(hObject, 'String'));
handles.R(5:7,5:7)=handles.Roto*eye(3);
handles.Rright(10:12,10:12)=handles.Roto*eye(3);
guidata(hObject, handles);

function edit7_CreateFcn(hObject, eventdata, handles)

```

```

if ispc && isequal(get(hObject,'BackgroundColor'),
get(0,'defaultUicontrolBackgroundColor'))
    set(hObject,'BackgroundColor','white');
end

function edit8_Callback(hObject, eventdata, handles)
handles.Rquat=str2num(get(hObject,'String'));
handles.R(1,1)=handles.Rquat;
handles.Rlight(13,13)=handles.Rquat;
guidata(hObject, handles);

function edit8_CreateFcn(hObject, eventdata, handles)
if ispc && isequal(get(hObject,'BackgroundColor'),
get(0,'defaultUicontrolBackgroundColor'))
    set(hObject,'BackgroundColor','white');
end

function edit9_Callback(hObject, eventdata, handles)
handles.Rvision=str2num(get(hObject,'String'));
handles.Rlight(4:9,4:9)=handles.Rvision*eye(6);
guidata(hObject, handles);

function edit9_CreateFcn(hObject, eventdata, handles)
if ispc && isequal(get(hObject,'BackgroundColor'),
get(0,'defaultUicontrolBackgroundColor'))
    set(hObject,'BackgroundColor','white');
end

%*****
% ***** Run of the simulation *****
%*****

function pushbutton2_Callback(hObject, eventdata, handles)

handles.simulation(1,2)=1; % means the simulation button has been pushed

if handles.model==1 % yaw rotation in darkness
% generation of the sensors output using a simulink model
    sTime=40;
    y=[];
    choix=handles.choix_dark;
    options=simset('SrcWorkspace','current');
    sim('EKF_entreedarkbis',[],options);
    y(1,:)=yq_dark(:,1)';
    y(2:4,:)=yscc_dark(:,1:3)';
    y(5:7,:)=yoto_dark(:,1:3)';
    handles.y=y;
    handles.R=handles.Rdark
    guidata(hObject, handles);

elseif handles.model==2 % forward acceleration in dark
% load output sensor measurements
load y_forw_acc_comp.mat;
% or can generate sensor measurements using a simulink model
% sTime=100;
% y=[];

```

```

% choix=handles.choix_dark;
% options=simset('SrcWorkspace','current');
% sim('EKF_entreedarkbis',[],options);
% y(1,:)=yq_dark(:,1)';
% y(2:4,:)=yscc_dark(:,1:3)';
% y(5:7,:)=yoto_dark(:,1:3)';
handles.R=handles.Rdark
handles.y=y;
guidata(hObject, handles);

elseif handles.model==3 % yaw circular vection
% load output sensor measurements
load y_yawvection_40s_cte;
handles.y=y;
handles.R=handles.Rright;
guidata(hObject, handles);

elseif handles.model==4 % forward linear vection
load y_linvection_40s_cte;
handles.y=y;
handles.R=handles.Rright;
guidata(hObject, handles);

elseif handles.model==5 % roll vection
load yrollvection_40s_cte;
handles.y=y;
handles.R=handles.Rright;
guidata(hObject, handles);

elseif handles.model==6 % coriolis
% generate sensor outpus using a simulink model
sTime=220;
y=[];
choix=handles.choix_dark;
options=simset('SrcWorkspace','current');
sim('EKF_entreedarkbis',[],options);
y(1,:)=yq_dark(:,1)';
y(2:4,:)=yscc_dark(:,1:3)';
y(5:7,:)=yoto_dark(:,1:3)';
handles.y=y;
handles.R=handles.Rdark
guidata(hObject, handles);

elseif handles.model==7 % off-vertical axis rotation
% load sensor outputs
load y_OVAR45_v2;
handles.y=y;
handles.R=handles.Rdark
guidata(hObject, handles);

elseif handles.model==8 % pseudo-coriolis
% load sensor outputs
load ypseudocoriolis_simulink_avecy;
handles.y=y;
handles.R=handles.Rright;
guidata(hObject, handles);
end

% if the EKF algorithm is selected
if handles.ekf==1

```

```

% if the selected experiment is performed in darkness
if handles.model==1 || handles.model==2 || handles.model==6 ||
handles.model==7

[handles.xekf,handles.angleekf,handles.timeekf]=EKF_dark(handles.br,handles
.bt,handles.Q,handles.Rdark,handles.y,handles.model);

if handles.model==1
    set(handles.ekfangvel, 'Value',1);
    handles.ekfangvel_V=get(handles.ekfangvel, 'Value');
    set(handles.ekfangle, 'Value',1);
    handles.ekfangle_V=get(handles.ekfangle, 'Value');
    set(handles.ekflinvel, 'Value',0);
    handles.ekflinvel_V=get(handles.ekflinvel, 'Value');
    set(handles.ekflinacc, 'Value',0);
    handles.ekflinacc_V=get(handles.ekflinacc, 'Value');

elseif handles.model==2
    set(handles.ekflinacc, 'Value',1);
    handles.ekflinacc_V=get(handles.ekflinacc, 'Value');
    set(handles.ekfangvel, 'Value',0);
    handles.ekfangvel_V=get(handles.ekfangvel, 'Value');
    set(handles.ekfangle, 'Value',1);
    handles.ekfangle_V=get(handles.ekfangle, 'Value');
    set(handles.ekflinvel, 'Value',0);
    handles.ekflinvel_V=get(handles.ekflinvel, 'Value');
end
% display of the computation time
    handles.timeekf=(round(handles.timeekf*100))/100;
    set(handles.tpsekf, 'String', [num2str(handles.timeekf), 's']);

% if the selected experiment is performed in the light

else

[handles.xekf,handles.angleekf,handles.timeekf]=EKF_light(handles.br,handle
s.bt,handles.Q,handles.Rlight,handles.y);

if handles.model==3
    set(handles.ekfangvel, 'Value',1);
    handles.ekfangvel_V=get(handles.ekfangvel, 'Value');
    set(handles.ekfangle, 'Value',1);
    handles.ekfangle_V=get(handles.ekfangle, 'Value');
    set(handles.ekflinvel, 'Value',0);
    handles.ekflinvel_V=get(handles.ekflinvel, 'Value');
    set(handles.ekflinacc, 'Value',0);
    handles.ekflinacc_V=get(handles.ekflinacc, 'Value');

elseif handles.model==4
    set(handles.ekflinacc, 'Value',1);
    handles.ekflinacc_V=get(handles.ekflinacc, 'Value');
    set(handles.ekflinvel, 'Value',1);
    handles.ekflinvel_V=get(handles.ekflinvel, 'Value');
    set(handles.ekfangvel, 'Value',0);
    handles.ekfangvel_V=get(handles.ekfangvel, 'Value');
    set(handles.ekfangle, 'Value',1);
    handles.ekfangle_V=get(handles.ekfangle, 'Value');

elseif handles.model==5
    set(handles.ekfangvel, 'Value',1);

```

```

handles.ekfangvel_V=get(handles.ekfangvel, 'Value');
set(handles.ekflinacc, 'Value', 0);
handles.ekflinacc_V=get(handles.ekflinacc, 'Value');
set(handles.ekflinvel, 'Value', 0);
handles.ekflinvel_V=get(handles.ekflinvel, 'Value');
set(handles.ekfangle, 'Value', 1);
handles.ekfangle_V=get(handles.ekfangle, 'Value');
end
% display of the computation time
handles.timeekf=(round(handles.timeekf*100))/100;
set(handles.tpsekf, 'String', [num2str(handles.timeekf), 's']);
end

% if the UKF algorithm is selected

elseif handles.ukf==1
[handles.xukf,handles.angleukf,handles.timeukf]=UKF(handles.br,handles.bt,h
andles.Q,handles.R,handles.y);

if handles.model==1 || handles.model==3
set(handles.ukfangvel, 'Value', 1);
handles.ukfangvel_V=get(handles.ukfangvel, 'Value');
set(handles.ukfangle, 'Value', 1);
handles.ukfangle_V=get(handles.ukfangle, 'Value');
set(handles.ukflinvel, 'Value', 0);
handles.ukflinvel_V=get(handles.ukflinvel, 'Value');
set(handles.ukflinacc, 'Value', 0);
handles.ukflinacc_V=get(handles.ukflinacc, 'Value');

elseif handles.model==2
set(handles.ukflinacc, 'Value', 1);
handles.ukflinacc_V=get(handles.ukflinacc, 'Value');
set(handles.ukfangvel, 'Value', 0);
handles.ukfangvel_V=get(handles.ukfangvel, 'Value');
set(handles.ukfangle, 'Value', 1);
handles.ukfangle_V=get(handles.ukfangle, 'Value');
set(handles.ukflinvel, 'Value', 0);
handles.ukflinvel_V=get(handles.ukflinvel, 'Value');

elseif handles.model==4
set(handles.ukflinacc, 'Value', 1);
handles.ukflinacc_V=get(handles.ukflinacc, 'Value');
set(handles.ukflinvel, 'Value', 1);
handles.ukflinvel_V=get(handles.ukflinvel, 'Value');
set(handles.ukfangvel, 'Value', 0);
handles.ukfangvel_V=get(handles.ukfangvel, 'Value');
set(handles.ukfangle, 'Value', 1);
handles.ukfangle_V=get(handles.ukfangle, 'Value');

elseif handles.model==5
set(handles.ukfangvel, 'Value', 1);
handles.ukfangvel_V=get(handles.ukfangvel, 'Value');
set(handles.ukflinacc, 'Value', 0);
handles.ukflinacc_V=get(handles.ukflinacc, 'Value');
set(handles.ukflinvel, 'Value', 0);
handles.ukflinvel_V=get(handles.ukflinvel, 'Value');
set(handles.ukfangle, 'Value', 1);
handles.ukfangle_V=get(handles.ukfangle, 'Value');
end
% display of the computation time
handles.timeukf=(round(handles.timeukf*100))/100;

```

```

        set(handles.tpsukf, 'String', [num2str(handles.timeukf), 's']);
    end
    guidata(hObject, handles);

%*****
% ***** selection of the simulated experiment *****
%*****

function popupmenu1_Callback(hObject, eventdata, handles)
switch get(handles.popupmenu1, 'Value')
    case 1
        handles.model=1;handles.simulation=zeros(1,2);
        handles.choix_dark=1; handles.sTime=100;
        handles.xekf=[];
        guidata(hObject,handles);
    case 2
        handles.model=2;handles.simulation=zeros(1,2);
        handles.choix_dark=2;handles.sTime=100;
        handles.xekf=[];handles.xukf=[];
        guidata(hObject,handles);
    case 3
        handles.model=3;handles.simulation=zeros(1,2);
        handles.xekf=[];handles.xukf=[];
        guidata(hObject,handles);
    case 4
        handles.model=4;handles.simulation=zeros(1,2);
        handles.xekf=[];handles.xukf=[];
        guidata(hObject,handles);
    case 5
        handles.model=5;handles.simulation=zeros(1,2);
        handles.xekf=[];handles.xukf=[];
        guidata(hObject,handles);
    case 6
        handles.model=6;handles.simulation=zeros(1,2);
        handles.choix_dark=3;handles.sTime=220;
        handles.xekf=[];handles.xukf=[];
        guidata(hObject,handles);
    case 7
        handles.model=7;handles.simulation=zeros(1,2);
        handles.xekf=[];handles.xukf=[];
        guidata(hObject,handles);
    case 8
        handles.model=8;handles.simulation=zeros(1,2);
        handles.Q(1:4,1:4)=1e-6*eye(4);
        guidata(hObject,handles);
end

function popupmenu1_CreateFcn(hObject, eventdata, handles)
if ispc && isequal(get(hObject, 'BackgroundColor'),
get(0, 'defaultUiControlBackgroundColor'))
    set(hObject, 'BackgroundColor', 'white');
end

%*****
% ***** Save the state vector to a .mat file *****
%*****

function pushbutton12_Callback(hObject, eventdata, handles)
    if handles.simulation(1,2)==1;

```



```

        if handles.ekf==1
            EKF_save(handles.xekf,handles.angleekf);
        elseif handles.ukf==1
            EKF_save(handles.xukf,handles.angleukf);
        end
    else
        errordlg({'You have to run a simulation'},'Error!');
    end

    %*****
    % ***** selection of the EKF / UKF algorithm *****
    %*****

function ekf_Callback(hObject, eventdata, handles)
handles.ekf=get(hObject,'Value');
handles.ukf=0;
guidata(hObject, handles);

function ukf_Callback(hObject, eventdata, handles)
handles.ukf=get(hObject,'Value');
handles.ekf=0;
guidata(hObject, handles);

% *****
% ***** PLOT *****
% *****

% ***** plot all the state variables *****
function pushbutton7_Callback(hObject, eventdata, handles)
    if handles.simulation(1,2)==0
        errordlg({'You have to run a simulation'},'Error!');
        return
    end

t=0:0.04:(size(handles.y,2)-1)*0.04;
if handles.ekf==1
    for i=1:25
        figure('Name',['EKF x(',num2str(i),')'],'NumberTitle','off');
        plot(t,handles.(['xekf'])(i,:));
        title(['x(',num2str(i),')'])
    end
    figure('Name',['EKF perceived roll angle'],'NumberTitle','off');
    plot(t,handles.angleekf(1,:));
    title('EKF perceived roll angle')
    figure('Name',['EKF perceived pitch angle'],'NumberTitle','off');
    plot(t,handles.angleekf(2,:));
    title('EKF perceived pitch angle')
    figure('Name',['EKF perceived yaw angle'],'NumberTitle','off');
    plot(t,handles.angleekf(3,:));
    title('EKF perceived yaw angle')

elseif handles.ukf==1
    for i=1:25
        figure('Name',['UKF x(',num2str(i),')'],'NumberTitle','off');
        plot(t,handles.(['xukf'])(i,:), 'r');
        title(['x(',num2str(i),')'])
    end
    figure('Name',['UKF perceived roll angle'],'NumberTitle','off');

```

```

    plot(t,handles.angleukf(1,:), 'r');
    title('UKF perceived roll angle')
    figure('Name', ['UKF perceived pitch angle'], 'NumberTitle', 'off');
    plot(t,handles.angleukf(2,:), 'r');
    title('UKF perceived pitch angle')
    figure('Name', ['UKF perceived yaw angle'], 'NumberTitle', 'off');
    plot(t,handles.angleukf(3,:));
    title('UKF perceived yaw angle', 'r')
end

figure('Name', 'Caption', 'Position', [30 300 300 400], 'NumberTitle', 'off')
uicontrol('Style', 'Text', 'Position', [20 350 250 22], 'String', 'EKF-UKF
states variables', 'FontSize', ...
    14, 'ForegroundColor', [0 0 0], 'BackgroundColor', [0.8 0.8
0.8], 'FontWeight', 'bold');
uicontrol('Style', 'Text', 'Position', [20 300 250 22], 'String', 'x1 to x4 :
quaternions', 'FontSize', ...
    11, 'ForegroundColor', [0 0 0], 'BackgroundColor', [0.8 0.8 0.8]);
uicontrol('Style', 'Text', 'Position', [20 260 250 22], 'String', 'x5 to x6 :
perceived angular velocity', 'FontSize', ...
    11, 'ForegroundColor', [0 0 0], 'BackgroundColor', [0.8 0.8 0.8]);
uicontrol('Style', 'Text', 'Position', [20 220 250 22], 'String', 'x7 to x10 :
perceived linear velocity', 'FontSize', ...
    11, 'ForegroundColor', [0 0 0], 'BackgroundColor', [0.8 0.8 0.8]);
uicontrol('Style', 'Text', 'Position', [20 180 250 22], 'String', 'x14 to x19 :
SCC TF', 'FontSize', ...
    11, 'ForegroundColor', [0 0 0], 'BackgroundColor', [0.8 0.8 0.8]);
uicontrol('Style', 'Text', 'Position', [20 140 250 22], 'String', 'x20 to x25 :
Otoliths TF', 'FontSize', ...
    11, 'ForegroundColor', [0 0 0], 'BackgroundColor', [0.8 0.8 0.8]);

% ***** plot Euler angles *****

function pushbutton9_Callback(hObject, eventdata, handles)
    if handles.simulation(1,2)==0
        errordlg({'You have to run a simulation'}, 'Error!');
        return
    end

t=0:0.04:(size(handles.y,2)-1)*0.04;

if handles.ekf==1
    figure('Name', ['EKF perceived roll angle'], 'NumberTitle', 'off');
    plot(t,handles.angleekf(1,:));
    title('EKF perceived roll angle')
    figure('Name', ['EKF perceived pitch angle'], 'NumberTitle', 'off');
    plot(t,handles.angleekf(2,:));
    title('EKF perceived pitch angle')
    figure('Name', ['EKF perceived yaw angle'], 'NumberTitle', 'off');
    plot(t,handles.angleekf(3,:));
    title('EKF perceived yaw angle');

elseif handles.ukf==1
    figure('Name', ['UKF perceived roll angle'], 'NumberTitle', 'off');
    plot(t,handles.angleukf(1,:), 'r');
    title('UKF perceived roll angle')
    figure('Name', ['UKF perceived pitch angle'], 'NumberTitle', 'off');
    plot(t,handles.angleukf(2,:), 'r');

```

```

        title('UKF perceived pitch angle')
        figure('Name', ['UKF perceived yaw angle'], 'NumberTitle', 'off');
        plot(t, handles.angleukf(3,:), 'r');
        title('UKF perceived yaw angle')
    end

% ***** Plot the results provided by the EKF *****
function plotekf_Callback(hObject, eventdata, handles)
    if handles.simulation(1,2)==0
        errordlg({'You have to run a simulation'}, 'Error!');
        return
    end

t=0:0.04:(size(handles.y,2)-1)*0.04;
if handles.ekfangvel_V==1
    figure1 = figure('Name', 'EKF perceived angular
velocity', 'NumberTitle', 'on', 'Position', [200 80 700 650]);
    subplot1 =
subplot(3,1,1, 'Parent', figure1, 'YGrid', 'on', 'XGrid', 'on', 'FontSize', 12);
    box('on');
    hold('all');
    title('roll', 'FontSize', 12, 'FontWeight', 'bold');
    plot(t, handles.xekf(5,:), 'LineWidth', 1);
    xlabel('Time (sec)', 'FontSize', 10);
    ylabel('rad/s', 'FontSize', 12);

    subplot2 =
subplot(3,1,2, 'Parent', figure1, 'YGrid', 'on', 'XGrid', 'on', 'FontSize', 12);
    box('on');
    hold('all');
    title('pitch', 'FontSize', 12, 'FontWeight', 'bold');
    plot(t, handles.xekf(6,:), 'LineWidth', 1);
    xlabel('Time (sec)', 'FontSize', 10);
    ylabel('rad/s', 'FontSize', 12);

    subplot3 =
subplot(3,1,3, 'Parent', figure1, 'YGrid', 'on', 'XGrid', 'on', 'FontSize', 12);
    box('on');
    hold('all');
    title('yaw', 'FontSize', 12, 'FontWeight', 'bold');
    plot(t, handles.xekf(7,:), 'LineWidth', 1);
    xlabel('Time (sec)', 'FontSize', 10);
    ylabel('rad/s', 'FontSize', 12);
end

if handles.ekflinvel_V==1
    figure2 = figure('Name', 'EKF perceived linear
velocity', 'NumberTitle', 'on', 'Position', [200 80 700 650]);
    subplot1 =
subplot(3,1,1, 'Parent', figure2, 'YGrid', 'on', 'XGrid', 'on', 'FontSize', 12);
    box('on');
    hold('all');
    title('Vx', 'FontSize', 12, 'FontWeight', 'bold');
    plot(t, handles.xekf(8,:), 'LineWidth', 1);
    xlabel('Time (sec)', 'FontSize', 10);
    ylabel('m/s', 'FontSize', 12);

    subplot2 =
subplot(3,1,2, 'Parent', figure2, 'YGrid', 'on', 'XGrid', 'on', 'FontSize', 12);
    box('on');

```

```

    hold('all');
    title('Vy', 'FontSize',12, 'FontWeight', 'bold');
    plot(t, handles.xekf(9,:), 'LineWidth',1);
    xlabel('Time (sec)', 'FontSize',10);
    ylabel('m/s', 'FontSize',12);

    subplot3 =
subplot(3,1,3, 'Parent', figure2, 'YGrid', 'on', 'XGrid', 'on', 'FontSize',12);
    box('on');
    hold('all');
    title('Vz', 'FontSize',12, 'FontWeight', 'bold');
    plot(t, handles.xekf(10,:), 'LineWidth',1);
    xlabel('Time (sec)', 'FontSize',10);
    ylabel('m/s', 'FontSize',12);
end

if handles.ekflinacc_V==1
    figure3 = figure('Name', 'EKF perceived linear
acceleration', 'NumberTitle', 'on', 'Position', [200 80 700 650]);
    subplot1 =
subplot(3,1,1, 'Parent', figure3, 'YGrid', 'on', 'XGrid', 'on', 'FontSize',12);
    box('on'); hold('all');
    title('Ax', 'FontSize',12, 'FontWeight', 'bold');
    plot(t, handles.xekf(11,:), 'LineWidth',1);
    xlabel('Time (sec)', 'FontSize',10);
    ylabel('m/s2', 'FontSize',12);

    subplot2 =
subplot(3,1,2, 'Parent', figure3, 'YGrid', 'on', 'XGrid', 'on', 'FontSize',12);
    box('on'); hold('all');
    title('Ay', 'FontSize',12, 'FontWeight', 'bold');
    plot(t, handles.xekf(12,:), 'LineWidth',1);
    xlabel('Time (sec)', 'FontSize',10);
    ylabel('m/s2', 'FontSize',12);

    subplot3 =
subplot(3,1,3, 'Parent', figure3, 'YGrid', 'on', 'XGrid', 'on', 'FontSize',12);
    box('on'); hold('all');
    title('Az', 'FontSize',12, 'FontWeight', 'bold');
    plot(t, handles.xekf(13,:), 'LineWidth',1);
    xlabel('Time (sec)', 'FontSize',10);
    ylabel('m/s2', 'FontSize',12);
end
if handles.ekfangle_V==1
    figure4 = figure('Name', 'EKF perceived
angles', 'NumberTitle', 'on', 'Position', [200 80 700 650]);
    subplot1 =
subplot(3,1,1, 'Parent', figure4, 'YGrid', 'on', 'XGrid', 'on', 'FontSize',12);
    box('on'); hold('all');
    title('Roll angle', 'FontSize',12, 'FontWeight', 'bold');
    plot(t, handles.angleekf(1,:), 'LineWidth',1);
    xlabel('Time (sec)', 'FontSize',10);
    ylabel('rad', 'FontSize',12);

    subplot2 =
subplot(3,1,2, 'Parent', figure4, 'YGrid', 'on', 'XGrid', 'on', 'FontSize',12);
    box('on'); hold('all');
    title('pitch angle', 'FontSize',12, 'FontWeight', 'bold');
    plot(t, handles.angleekf(2,:), 'LineWidth',1);
    xlabel('Time (sec)', 'FontSize',10);

```

```

ylabel('rad','FontSize',12);

subplot3 =
subplot(3,1,3,'Parent',figure4,'YGrid','on','XGrid','on','FontSize',12);
box('on');hold('all');
title('Yaw angle','FontSize',12,'FontWeight','bold');
plot(t,handles.angleekf(3,:), 'LineWidth',1);
xlabel('Time (sec)','FontSize',10);
ylabel('rad','FontSize',12);
end

% ***** Plot the results provided by the UKF *****
function plotukf_Callback(hObject, eventdata, handles)
    if handles.simulation(1,2)==0
        errordlg({'You have to run a simulation'}, 'Error!');
        return
    end

t=0:0.04:(size(handles.y,2)-1)*0.04;

if handles.ukfangvel_V==1
    figure5 = figure('Name','UKF perceived angular
velocity','NumberTitle','on','Position',[200 80 700 650]);
    subplot1 =
subplot(3,1,1,'Parent',figure5,'YGrid','on','XGrid','on','FontSize',12);
box('on');
hold('all');
title('roll','FontSize',12,'FontWeight','bold');
plot(t,handles.xukf(5,:), 'LineWidth',1);
xlabel('Time (sec)','FontSize',10);
ylabel('rad/s','FontSize',12);

    subplot2 =
subplot(3,1,2,'Parent',figure5,'YGrid','on','XGrid','on','FontSize',12);
box('on');
hold('all');
title('pitch','FontSize',12,'FontWeight','bold');
plot(t,handles.xukf(6,:), 'LineWidth',1);
xlabel('Time (sec)','FontSize',10);
ylabel('rad/s','FontSize',12);

    subplot3 =
subplot(3,1,3,'Parent',figure5,'YGrid','on','XGrid','on','FontSize',12);
box('on');
hold('all');
title('yaw','FontSize',12,'FontWeight','bold');
plot(t,handles.xukf(7,:), 'LineWidth',1);
xlabel('Time (sec)','FontSize',10);
ylabel('rad/s','FontSize',12);
end

if handles.ukflinvel_V==1
    figure6 = figure('Name','UKF perceived linear
velocity','NumberTitle','on','Position',[200 80 700 650]);
    subplot1 =
subplot(3,1,1,'Parent',figure6,'YGrid','on','XGrid','on','FontSize',12);
box('on');
hold('all');
title('Vx','FontSize',12,'FontWeight','bold');

```

```

plot(t,handles.xukf(8,:), 'LineWidth',1);
xlabel('Time (sec)', 'FontSize',10);
ylabel('m/s', 'FontSize',12);

subplot2 =
subplot(3,1,2, 'Parent',figure6, 'YGrid', 'on', 'XGrid', 'on', 'FontSize',12);
box('on');
hold('all');
title('Vy', 'FontSize',12, 'FontWeight', 'bold');
plot(t,handles.xukf(9,:), 'LineWidth',1);
xlabel('Time (sec)', 'FontSize',10);
ylabel('m/s', 'FontSize',12);

subplot3 =
subplot(3,1,3, 'Parent',figure6, 'YGrid', 'on', 'XGrid', 'on', 'FontSize',12);
box('on');
hold('all');
title('Vz', 'FontSize',12, 'FontWeight', 'bold');
plot(t,handles.xukf(10,:), 'LineWidth',1);
xlabel('Time (sec)', 'FontSize',10);
ylabel('m/s', 'FontSize',12);
end

if handles.ukflinacc_V==1
figure7 = figure('Name', 'UKF perceived linear
acceleration', 'NumberTitle', 'on', 'Position', [200 80 700 650]);
subplot1 =
subplot(3,1,1, 'Parent',figure7, 'YGrid', 'on', 'XGrid', 'on', 'FontSize',12);
box('on'); hold('all');
title('Ax', 'FontSize',12, 'FontWeight', 'bold');
plot(t,handles.xukf(11,:), 'LineWidth',1);
xlabel('Time (sec)', 'FontSize',10);
ylabel('m/s2', 'FontSize',12);

subplot2 =
subplot(3,1,2, 'Parent',figure7, 'YGrid', 'on', 'XGrid', 'on', 'FontSize',12);
box('on'); hold('all');
title('Ay', 'FontSize',12, 'FontWeight', 'bold');
plot(t,handles.xukf(12,:), 'LineWidth',1);
xlabel('Time (sec)', 'FontSize',10);
ylabel('m/s2', 'FontSize',12);

subplot3 =
subplot(3,1,3, 'Parent',figure7, 'YGrid', 'on', 'XGrid', 'on', 'FontSize',12);
box('on');hold('all');
title('Az', 'FontSize',12, 'FontWeight', 'bold');
plot(t,handles.xukf(13,:), 'LineWidth',1);
xlabel('Time (sec)', 'FontSize',10);
ylabel('m/s2', 'FontSize',12);
end
if handles.ukfangle_V==1
figure8 = figure('Name', 'UKF perceived
angles', 'NumberTitle', 'on', 'Position', [200 80 700 650]);
subplot1 =
subplot(3,1,1, 'Parent',figure8, 'YGrid', 'on', 'XGrid', 'on', 'FontSize',12);
box('on'); hold('all');
title('Roll angle', 'FontSize',12, 'FontWeight', 'bold');
plot(t,handles.angleukf(1,:), 'LineWidth',1);
xlabel('Time (sec)', 'FontSize',10);
ylabel('rad', 'FontSize',12);

```

```

        subplot2 =
subplot(3,1,2,'Parent',figure8,'YGrid','on','XGrid','on','FontSize',12);
    box('on'); hold('all');
    title('pitch angle','FontSize',12,'FontWeight','bold');
    plot(t,handles.angleukf(2,:), 'LineWidth',1);
    xlabel('Time (sec)','FontSize',10);
    ylabel('rad','FontSize',12);

        subplot3 =
subplot(3,1,3,'Parent',figure8,'YGrid','on','XGrid','on','FontSize',12);
    box('on');hold('all');
    title('Yaw angle','FontSize',12,'FontWeight','bold');
    plot(t,handles.angleukf(3,:), 'LineWidth',1);
    xlabel('Time (sec)','FontSize',10);
    ylabel('rad','FontSize',12);
end

% ***** Plot the results provided by both the EKF and UKF *****

function pushbutton15_Callback(hObject, eventdata, handles)
    if handles.simulation(1,2)==0
        errordlg({'You have to run a simulation'},'Error!');
        return
    end

t=0:0.04:(size(handles.y,2)-1)*0.04;
if handles.ukfangvel_V==1 || handles.ekfangvel_V==1
    figure10 = figure('Name','EKF-UKF perceived angular
velocity','NumberTitle','on','Position',[200 80 700 650]);
        subplot3 =
subplot(3,1,3,'Parent',figure10,'YGrid','on','XGrid','on','FontSize',12);
box('on'); hold('all');
title('yaw','FontSize',12,'FontWeight','bold');

        if handles.ekfangvel_V==1
            plot(t,handles.xekf(7,:), 'LineWidth',1);
        end
        if handles.ukfangvel_V==1
            plot(t,handles.xukf(7,:), '--r', 'LineWidth',1);
        end

legend('EKF','UKF');
xlabel('Time (sec)','FontSize',10);
ylabel('rad/s','FontSize',12);
subplot1 =
subplot(3,1,1,'Parent',figure10,'YGrid','on','XGrid','on','FontSize',12);
box('on');
hold('all');
title('roll','FontSize',12,'FontWeight','bold');
        if handles.ekfangvel_V==1
            plot(t,handles.xekf(5,:), 'LineWidth',1);
        end
        if handles.ukfangvel_V==1
            plot(t,handles.xukf(5,:), '--r', 'LineWidth',1);
        end

legend('EKF','UKF');
xlabel('Time (sec)','FontSize',10);

```

```

ylabel('rad/s', 'FontSize', 12);

subplot2 =
subplot(3,1,2, 'Parent', figure10, 'YGrid', 'on', 'XGrid', 'on', 'FontSize', 12);
box('on'); hold('all');
title('pitch', 'FontSize', 12, 'FontWeight', 'bold');

    if handles.ekfangvel_V==1
        plot(t, handles.xekf(6, :), 'LineWidth', 1);
    end
    if handles.ukfangvel_V==1
        plot(t, handles.xukf(6, :), '--r', 'LineWidth', 1);
    end

legend('EKF', 'UKF');
xlabel('Time (sec)', 'FontSize', 10);
ylabel('rad/s', 'FontSize', 12);
end

if handles.ukflinvel_V==1 || handles.ekflinvel_V==1

figure11 = figure('Name', 'EKF-UKF perceived linear
velocity', 'NumberTitle', 'on', 'Position', [200 80 700 650]);
subplot1 =
subplot(3,1,1, 'Parent', figure11, 'YGrid', 'on', 'XGrid', 'on', 'FontSize', 12);
box('on'); hold('all');
title('Vx', 'FontSize', 12, 'FontWeight', 'bold');

    if handles.ekflinvel_V==1
        plot(t, handles.xekf(8, :), 'LineWidth', 1);
    end
    if handles.ukflinvel_V==1
        plot(t, handles.xukf(8, :), '--r', 'LineWidth', 1);
    end
legend('EKF', 'UKF');
xlabel('Time (sec)', 'FontSize', 10);
ylabel('m/s', 'FontSize', 12);

subplot2 =
subplot(3,1,2, 'Parent', figure11, 'YGrid', 'on', 'XGrid', 'on', 'FontSize', 12);
box('on'); hold('all');
title('Vy', 'FontSize', 12, 'FontWeight', 'bold');

    if handles.ekflinvel_V==1
        plot(t, handles.xekf(9, :), 'LineWidth', 1);
    end
    if handles.ukflinvel_V==1
        plot(t, handles.xukf(9, :), '--r', 'LineWidth', 1);
    end
legend('EKF', 'UKF');
xlabel('Time (sec)', 'FontSize', 10);
ylabel('m/s', 'FontSize', 12);

subplot3 =
subplot(3,1,3, 'Parent', figure11, 'YGrid', 'on', 'XGrid', 'on', 'FontSize', 12);
box('on'); hold('all');
title('Vz', 'FontSize', 12, 'FontWeight', 'bold');

    if handles.ekflinvel_V==1

```



```

        plot(t,handles.xekf(11,:), 'LineWidth',1);
    end
    if handles.ukflinvel_V==1
        plot(t,handles.xukf(11,:), '--r', 'LineWidth',1);
    end
    legend('EKF', 'UKF');
    xlabel('Time (sec)', 'FontSize',10);
    ylabel('m/s', 'FontSize',12);

end

if handles.ukflinacc_V==1 || handles.ekflinacc_V==1

figure12 = figure('Name','EKF-UKF perceived linear
acceleration', 'NumberTitle', 'on', 'Position',[200 80 700 650]);
subplot1 =
subplot(3,1,1, 'Parent', figure12, 'YGrid', 'on', 'XGrid', 'on', 'FontSize',12);
box('on'); hold('all');
title('Ax', 'FontSize',12, 'FontWeight', 'bold');

    if handles.ekflinacc_V==1
        plot(t,handles.xekf(11,:), 'LineWidth',1);
    end
    if handles.ukflinacc_V==1
        plot(t,handles.xukf(11,:), '--r', 'LineWidth',1);
    end
    legend('EKF', 'UKF');
    xlabel('Time (sec)', 'FontSize',10);
    ylabel('m/s2', 'FontSize',12);

subplot2 =
subplot(3,1,2, 'Parent', figure12, 'YGrid', 'on', 'XGrid', 'on', 'FontSize',12);
box('on'); hold('all');
title('Ay', 'FontSize',12, 'FontWeight', 'bold');
    if handles.ekflinacc_V==1
        plot(t,handles.xekf(12,:), 'LineWidth',1);
    end
    if handles.ukflinacc_V==1
        plot(t,handles.xukf(12,:), '--r', 'LineWidth',1);
    end
    legend('EKF', 'UKF');
    xlabel('Time (sec)', 'FontSize',10);
    ylabel('m/s2', 'FontSize',12);

subplot3 =
subplot(3,1,3, 'Parent', figure12, 'YGrid', 'on', 'XGrid', 'on', 'FontSize',12);
box('on');hold('all');
title('Az', 'FontSize',12, 'FontWeight', 'bold');

    if handles.ekflinacc_V==1
        plot(t,handles.xekf(13,:), 'LineWidth',1);
    end
    if handles.ukflinacc_V==1
        plot(t,handles.xukf(13,:), '--r', 'LineWidth',1);
    end
    legend('EKF', 'UKF');
    xlabel('Time (sec)', 'FontSize',10);
    ylabel('m/s2', 'FontSize',12);

end

```

```

if handles.ukfangle_V==1 || handles.ekfangle_V==1

figure13 = figure('Name','EKF-UKF perceived
angles','NumberTitle','on','Position',[200 80 700 650]);
subplot1 =
subplot(3,1,1,'Parent',figure13,'YGrid','on','XGrid','on','FontSize',12);
box('on'); hold('all');
title('Roll angle','FontSize',12,'FontWeight','bold');

    if handles.ekfangle_V==1
        plot(t,handles.angleekf(1,:), 'LineWidth',1);
    end
    if handles.ukfangle_V==1
        plot(t,handles.angleukf(1,:), '--r', 'LineWidth',1);
    end
legend('EKF','UKF');
xlabel('Time (sec)','FontSize',10);
ylabel('rad','FontSize',12);

subplot2 =
subplot(3,1,2,'Parent',figure13,'YGrid','on','XGrid','on','FontSize',12);
box('on'); hold('all');
title('pitch angle','FontSize',12,'FontWeight','bold');

    if handles.ekfangle_V==1
        plot(t,handles.angleekf(2,:), 'LineWidth',1);
    end
    if handles.ukfangle_V==1
        plot(t,handles.angleukf(2,:), '--r', 'LineWidth',1);
    end
legend('EKF','UKF');
xlabel('Time (sec)','FontSize',10);
ylabel('rad','FontSize',12);

subplot3 =
subplot(3,1,3,'Parent',figure13,'YGrid','on','XGrid','on','FontSize',12);
box('on');hold('all');
title('Yaw angle','FontSize',12,'FontWeight','bold');

    if handles.ekfangle_V==1
        plot(t,handles.angleekf(3,:), 'LineWidth',1);
    end
    if handles.ukfangle_V==1
        plot(t,handles.angleukf(3,:), '--r', 'LineWidth',1);
    end
legend('EKF','UKF');
xlabel('Time (sec)','FontSize',10);
ylabel('rad','FontSize',12);

end

% ***** selection of the curves to plot *****
function ekfangvel_Callback(hObject, eventdata, handles)
handles.ekfangvel_V=get(hObject,'Value');
guidata(hObject, handles);

function ekflinvel_Callback(hObject, eventdata, handles)
handles.ekflinvel_V=get(hObject,'Value');
guidata(hObject, handles);

```

```
function ekflinacc_Callback(hObject, eventdata, handles)
handles.ekflinacc_V=get(hObject, 'Value');
guidata(hObject, handles);
```

```
function ekfangle_Callback(hObject, eventdata, handles)
handles.ekfangle_V=get(hObject, 'Value');
guidata(hObject, handles);
```

```
function ukfangvel_Callback(hObject, eventdata, handles)
handles.ukfangvel_V=get(hObject, 'Value');
guidata(hObject, handles);
```

```
function ukflinvel_Callback(hObject, eventdata, handles)
handles.ukflinvel_V=get(hObject, 'Value');
guidata(hObject, handles);
```

```
function ukflinacc_Callback(hObject, eventdata, handles)
handles.ukflinacc_V=get(hObject, 'Value');
guidata(hObject, handles);
```

```
function ukfangle_Callback(hObject, eventdata, handles)
handles.ukfangle_V=get(hObject, 'Value');
guidata(hObject, handles);
```

- Extended Kalman filter function (in darkness)

```
function [xe,angle,tps]=EKF_dark(br,bl,Q,R,y,modele)
tic

% *****
% initialisation
% *****
xe=[1 0 0 0 0 0 0 0 0 0 0 0 0 0 0 0 0 0 0 0 0 0 0 0];
P=diag([0.01*ones(1,4) 1e-2*ones(1,21)]);
h=0.01; % Runge Kutta time step integration
%%sensors transfer functions
ta_scc=80;tscc=6;
Ko=33.3;t1_oto=10;t1_oto=0.016;t2_oto=5;
[Ascc,Bscc,Cscc,Dscc]=tf2ss([ta_scc*tscc 0 0],[ta_scc*tscc ta_scc+tscc 1]);
[Aoto,Boto,Coto,Doto]=tf2ss([Ko*t1_oto Ko],[t1_oto*t2_oto t1_oto+t2_oto 1]);

% *****
% Main algorithm
% *****
wait=waitbar(0, 'Please wait');

for i=2:size(y,2)
    waitbar(i/size(y,2));
    z(:,i)=y(:,i)+sqrt(R)*randn(size(y,1),1);
    xe(:,i)=xe(:,i-1);
    % 4 order Runge Kutta integration
    for j=1:4
        s01=statespacemodel(xe(:,i),br,bl,Ascc,Aoto);
```

```

s02=jacobian(xe(:,i),br,bl,Ascc,Aoto)*P+P*jacobian(xe(:,i),br,bl,Ascc,Aoto)
'+Q;
    xe1=xe(:,i)+h*s01;
    P1=P+h*s02;
    s11=statespacemodel(xe1,br,bl,Ascc,Aoto);

s12=jacobian(xe1,br,bl,Ascc,Aoto)*P1+P1*jacobian(xe1,br,bl,Ascc,Aoto)'+Q;
    xe2=xe(:,i)+h*(s01+s11)/4;
    P2=P+h*(s02+s12)/4;
    s21=statespacemodel(xe2,br,bl,Ascc,Aoto);

s22=jacobian(xe2,br,bl,Ascc,Aoto)*P2+P2*jacobian(xe2,br,bl,Ascc,Aoto)'+Q;
    xe(:,i)=xe(:,i)+h*(s01+s11+4*s21)/6;
    P=P+h*(s02+s12+4*s22)/6;
end

% Measurement matrix
H(1,:)=[2*xe(1,i) 2*xe(2,i) 2*xe(3,i) 2*xe(4,i) zeros(1,21)];
a=[Ascc(1,2) Ascc(1,1) 0 0 0 0;0 0 Ascc(1,2) Ascc(1,1) 0 0;0 0 0 0
Ascc(1,2) Ascc(1,1)];
b=[416.25 4162.5 0 0 0 0;0 0 416.25 4162.5 0 0;0 0 0 0 416.25
4162.5];
H(2:7,1:25)=[zeros(3,4) eye(3) zeros(3,6) a zeros(3,6); zeros(3,19)
b];

% predicted measurement
z_est(1,i)=xe(1,i)^2+xe(2,i)^2+xe(3,i)^2+xe(4,i)^2;
z_est(2:7,i)=H(2:7,:)*xe(:,i);
% Kalman gain
K=P*H'*inv(H*P*H'+R);
% update of the predicted state vector
xe(:,i)=xe(:,i)+K*(z(:,i)-z_est(:,i));
% update of the covariance matrix
P=(eye(25)-K*H)*P*(eye(25)-K*H)'+K*R*K';
end

tps=toc;

% *****
% Computation of Euler angles from quaternion parameters
% *****
duration=(size(y,2)-1)*0.04;
t=0:0.04:duration;
q0=xe(1,:);
q1=xe(2,:);
q2=xe(3,:);
q3=xe(4,:);
t=t';
options=simset('SrcWorkspace','current');
sim('quat_euler',[],options);
angle=angle';
close(wait);

```

- Extended Kalman filter function (experiment in light)

```
function [xe,angle,tps]=EKF_light(br,bl,Q,R,y)
```

```

tic
% *****
% initialisation
% *****
xe=[1 0 0 0 0 0 0 0 0 0 0 0 0 0 0 0 0 0 0 0 0 0 0 0 0 0];
P=0.0001*eye(25,25);
step=0.01; % Runge Kutta time step integration
%%sensors transfer functions
ta_scc=80;tscc=6;
Ko=33.3;t1_oto=10;t1_oto=0.016;t2_oto=5;
[Ascc,Bscc,Cscc,Dscc]=tf2ss([ta_scc*tscc 0 0],[ta_scc*tscc ta_scc+tscc 1]);
[Aoto,Boto,Coto,Doto]=tf2ss([Ko*t1_oto Ko],[t1_oto*t2_oto t1_oto+t2_oto
1]);

% state propogation equations
f=@(x)[0.5*(-x(5)*x(2)-x(6)*x(3)-x(7)*x(4));
    0.5*(x(5)*x(1)+x(7)*x(3)-x(6)*x(4));
    0.5*(x(6)*x(1)-x(7)*x(2)+x(5)*x(4));
    0.5*(x(7)*x(1)+x(6)*x(2)-x(5)*x(3));
    -br*x(5);-br*x(6);-br*x(7);x(11);x(12);x(13);-bl*x(11);-bl*x(12);-
    bl*x(13);
    x(15);
    Ascc(1,2)*x(14)+Ascc(1,1)*x(15)+x(5);x(17);Ascc(1,2)*x(16)+Ascc(1,1)*
    x(17)+x(6); x(19);
    Ascc(1,2)*x(18)+Ascc(1,1)*x(19)+x(7);
    x(21);
    Aoto(1,1)*x(21)+Aoto(1,2)*x(20)+(19.62*(x(2)*x(4)-x(1)*x(3))-x(11));
    x(23); Aoto(1,1)*x(23)+Aoto(1,2)*x(22)+(19.62*(x(3)*x(4)+x(1)*x(2))-
    x(12));
    x(25); Aoto(1,1)*x(25)+Aoto(1,2)*x(24)+(9.81*(x(1)*x(1)+x(4)*x(4)-
    x(3)*x(3)-x(2)*x(2))-x(13));]; % nonlinear state equations

% measurement equations
h=@(x)
[Ascc(1,2)*x(14)+Ascc(1,1)*x(15)+x(5);Ascc(1,2)*x(16)+Ascc(1,1)*x(17)+x(6);
Ascc(1,2)*x(18)+Ascc(1,1)*x(19)+x(7);x(5);x(6);x(7);x(8);x(9);x(10);Coto(1,
2)*x(20)+Coto(1,1)*x(21);Coto(1,2)*x(22)+Coto(1,1)*x(23);
Coto(1,2)*x(24)+Coto(1,1)*x(25);x(1)*x(1)+x(2)*x(2)+x(3)*x(3)+x(4)*x(4)];

%jacobian of f
gradf=@(x) [0 -0.5*x(5) -0.5*x(6) -0.5*x(7) -0.5*x(2) -0.5*x(3) -0.5*x(4)
zeros(1,18);0.5*x(5) 0 0.5*x(7) -0.5*x(6) 0.5*x(1) -0.5*x(4) 0.5*x(3)
zeros(1,18);0.5*x(6) -0.5*x(7) 0 0.5*x(5) 0.5*x(4) 0.5*x(1) -0.5*x(2)
zeros(1,18);0.5*x(7) 0.5*x(6) -0.5*x(5) 0 -0.5*x(3) 0.5*x(2) 0.5*x(1)
zeros(1,18);zeros(3,4) -br*eye(3) zeros(3,18);zeros(3,10) eye(3)
zeros(3,12);zeros(3,10) -bl*eye(3) zeros(3,12);zeros(2,4) [0;1] zeros(2,8)
[0 1;Ascc(1,2) Ascc(1,1)] zeros(2,10);zeros(2,5) [0;1] zeros(2,9) [0
1;Ascc(1,2) Ascc(1,1)] zeros(2,8);zeros(2,6) [0;1] zeros(2,10) [0
1;Ascc(1,2) Ascc(1,1)] zeros(2,6);zeros(1,19) 0 1 0 0 0 0;-19.62*x(3)
19.62*x(4) -19.62*x(1) 19.62*x(2) zeros(1,6) -1 0 0 zeros(1,6) Aoto(1,2)
Aoto(1,1) 0 0 0 0;zeros(1,19) 0 0 0 1 0 0;19.62*x(2) 19.62*x(1) 19.62*x(4)
19.62*x(3) zeros(1,6) 0 -1 0 zeros(1,6) 0 0 Aoto(1,2) Aoto(1,1) 0
0;zeros(1,19) 0 0 0 0 0 1;19.62*x(1) -19.62*x(2) -19.62*x(3) 19.62*x(4)
zeros(1,6) 0 0 -1 zeros(1,6) 0 0 0 0 Aoto(1,2) Aoto(1,1)];];

% *****
% Main algorithm
% *****
wait=waitbar(0,'Please wait');

```

```

for i=2:size(y,2)
waitbar(i/size(y,2));
z(:,i)=y(:,i)+sqrt(R)*randn(size(y,1),1); % sensors output
xe(:,i)=xe(:,i-1);
% 4 order Runge Kutta integration
for j=1:4
s01=f(xe(:,i));
s02=gradf(xe(:,i))*P+P*gradf(xe(:,i))'+Q;
xel=xe(:,i)+step*s01;
P1=P+step*s02;
s11=f(xel);
s12=gradf(xel)*P1+P1*gradf(xel)'+Q;
xe3=xe(:,i)+step*(s01+s11)/4;
P3=P+step*(s02+s12)/4;
s21=f(xe3);
s22=gradf(xe3)*P3+P3*gradf(xe3)'+Q;
xe(:,i)=xe(:,i)+step*(s01+s11+4*s21)/6;
P=P+step*(s02+s12+4*s22)/6;
end

% jacobian of h
a=[Ascc(1,2) Ascc(1,1) 0 0 0 0;0 0 Ascc(1,2) Ascc(1,1) 0 0;0 0 0 0
Ascc(1,2) Ascc(1,1)];
b=[416.25 4162.5 0 0 0 0;0 0 416.25 4162.5 0 0;0 0 0 0 416.25
4162.5];
H(1:13,1:25)=[zeros(3,4) eye(3) zeros(3,6) a zeros(3,6);
zeros(3,4) -eye(3) zeros(3,18);
zeros(3,7) -eye(3) zeros(3,15);
zeros(3,19) b;
2*xe(1,i) 2*xe(2,i) 2*xe(3,i) 2*xe(4,i) zeros(1,21)];

% predicted measurement
z_est(1:12,i)=H(1:12,:)*xe(:,i);
z_est(13,i)=xe(1,i)^2+xe(2,i)^2+xe(3,i)^2+xe(4,i)^2;

%cross covariance
P12=P*H';
%Kalman filter gain
K=P12*inv(H*P12+R);
% update of the predicted state vector
xe(:,i)=xe(:,i)+K*(z(:,i)-z_est(:,i));
% update of the covariance matrix
P=(eye(25)-K*H)*P*(eye(25)-K*H)'+K*R*K';

end

% *****
% Computation of Euler angles from quaternion parameters
%*****
tps=toc;
duration=(size(y,2)-1)*0.04;
t=0:0.04:duration;
q0=xe(1,:);
q1=xe(2,:);
q2=xe(3,:);
q3=xe(4,:);
t=t';
options=simset('SrcWorkspace','current');
sim('quat_euler',[],options);
angle=angle';

```

```
close(wait);
```

- Unscented Kalman filter function

```
function [xe,angle,tps]=UKF(br,b1,Q,R,y)
tic
% *****
% initialisation
% *****

xe0=[1 0 0 0 0 0 0 0 0 0 0 0 0 0 0 0 0 0 0 0 0 0 0 0 0]'; % state vector
h=0.01; % Runge Kutta integration time step
P=1e-4*eye(25); % initial covariance matrix P
dt=0.04; % update time step of the estimated state vector
xe=zeros(25,751); % estimated state vector
xe(:,1)=xe0;
n=size(xe(:,1),1); % dimension of the state vector
alpha=0.5; beta=2; kappa=3-n; lambda=alpha^2*(n+kappa)-n; % parameters of
the UKF

%%sensors transfer functions
ta_scc=80;tscc=6;
Ko=33.3;t1_oto=10;t1_oto=0.016;t2_oto=5;
[Ascc,Bscc,Cscc,Dscc]=tf2ss([ta_scc*tscc 0 0],[ta_scc*tscc ta_scc+tscc 1]);
[Aoto,Boto,Coto,Doto]=tf2ss([Ko*t1_oto Ko],[t1_oto*t2_oto t1_oto+t2_oto
1]);
Ascc1=Ascc(1,1);
Ascc2=Ascc(1,2);
Aoto1=Aoto(1,1);
Aoto2=Aoto(1,2);
Coto1=Coto(1,1);
Coto2=Coto(1,2);

% *****
% noisy output generation
% *****
if size(y,1)==7
    zr=zeros(7,751);
    for i=1:size(y,2)
        zr(:,i)=y(:,i)+sqrt(R)*randn(7,1);
    end

elseif size(y,1)==13
    zr=zeros(13,751);
    for i=1:size(y,2)
        zr(:,i)=y(:,i)+sqrt(R)*randn(13,1);
    end
end

% *****
% Main algorithm
% *****

wait=waitbar(0,'Please wait');

for k=2:size(y,2)
    waitbar(k/size(y,2));
```

```

xe(:,k)=xe(:,k-1);

% if the re-normalization is considered at each time step
% xe(1,k)=xe(1,k)/sqrt(xe(1,k)^2+xe(2,k)^2+xe(3,k)^2+xe(4,k)^2);
% xe(2,k)=xe(2,k)/sqrt(xe(1,k)^2+xe(2,k)^2+xe(3,k)^2+xe(4,k)^2);
% xe(3,k)=xe(3,k)/sqrt(xe(1,k)^2+xe(2,k)^2+xe(3,k)^2+xe(4,k)^2);
% xe(4,k)=xe(4,k)/sqrt(xe(1,k)^2+xe(2,k)^2+xe(3,k)^2+xe(4,k)^2);

%unscented transformation
%%1) weights
WM = zeros(2*n+1,1);
WC = zeros(2*n+1,1);
for j=1:2*n+1
    if j==1
        wm = lambda / (n + lambda);
        wc = lambda / (n + lambda) + (1 - alpha^2 + beta);
    else
        wm = 1 / (2 * (n + lambda));
        wc = wm;
    end
    WM(j) = wm;
    WC(j) = wc;
end
c = n + lambda;

%%2)Sigma points generation

A = chol(P)';
X = [zeros(size(xe(:,k))) A -A];
X = sqrt(c)*X + repmat(xe(:,k),1,size(X,2));

%%3) Sigman points transformation (propagation)
Y = [];

% if the Runge Kutta integration is considered
% for i=1:(2*n+1)
%     for j=1:4
%         s01=xdot(X(:,i),Ascc,Aoto,br,bl);
%         xe1=X(:,i)+h*s01;
%         s11=xdot(xe1,Ascc,Aoto,br,bl);
%         xe2=X(:,i)+h*(s01+s11)/4;
%         s21=xdot(xe2,Ascc,Aoto,br,bl);
%         X(:,i)=X(:,i)+h*(s01+s11+4*s21)/6;
%     end
% end
% Y=X;

% if the Euler integration is considered
for i=1:(2*n+1)
    for j=1:4
        dot_x=zeros(size(X));
        % classic formulatoin ofr the quaternion
        dot_x(1,i)=0.5*(-X(5,i)*X(2,i)-X(6,i)*X(3,i)-X(7,i)*X(4,i));
        dot_x(2,i)=0.5*(X(5,i)*X(1,i)+X(7,i)*X(3,i)-X(6,i)*X(4,i));
        dot_x(3,i)=0.5*(X(6,i)*X(1,i)-X(7,i)*X(2,i)+X(5,i)*X(4,i));
        dot_x(4,i)=0.5*(X(7,i)*X(1,i)+X(6,i)*X(2,i)-X(5,i)*X(3,i));
        % formulation 2 for the quaternion
        % dot_x(1,i)=0.5*(-X(5,i)*X(2,i)-X(6,i)*X(3,i)-
X(7,i)*X(4,i))+0.9*X(1,i)*(1-X(1,i)^2-X(2,i)^2-X(3,i)^2-X(4,i)^2);

```



```

    % dot_x(2,i)=0.5*(X(5,i)*X(1,i)+X(7,i)*X(3,i)-
X(6,i)*X(4,i))+0.9*X(2,i)*(1-X(1,i)^2-X(2,i)^2-X(3,i)^2-X(4,i)^2);
    % dot_x(3,i)=0.5*(X(6,i)*X(1,i)-
X(7,i)*X(2,i)+X(5,i)*X(4,i))+0.9*X(3,i)*(1-X(1,i)^2-X(2,i)^2-X(3,i)^2-
X(4,i)^2);
    % dot_x(4,i)=0.5*(X(7,i)*X(1,i)+X(6,i)*X(2,i)-
X(5,i)*X(3,i))+0.9*X(4,i)*(1-X(1,i)^2-X(2,i)^2-X(3,i)^2-X(4,i)^2);
    dot_x(5,i)=-br*X(5,i);
    dot_x(6,i)=-br*X(6,i);
    dot_x(7,i)=-br*X(7,i);
    dot_x(8,i)=X(11,i);
    dot_x(9,i)=X(12,i);
    ot_x(10,i)=X(13,i);
    dot_x(11,i)=-bl*X(11,i);
    dot_x(12,i)=-bl*X(12,i);
    dot_x(13,i)=-bl*X(13,i);
    dot_x(14,i)=X(15,i);
    dot_x(15,i)=Ascc2*X(14,i)+Ascc1*X(15,i)+X(5,i);
    dot_x(16,i)=X(17,i);
    dot_x(17,i)=Ascc2*X(16,i)+Ascc1*X(17,i)+X(6,i);
    dot_x(18,i)=X(19,i);
    dot_x(19,i)=Ascc2*X(18,i)+Ascc1*X(19,i)+X(7,i);
    dot_x(20,i)=X(21,i);
    dot_x(21,i)=Aoto1*X(21,i)+Aoto2*X(20,i)+(19.62*(X(2,i)*X(4,i)-
X(1,i)*X(3,i))-X(11,i));
    dot_x(22,i)=X(23,i);

dot_x(23,i)=Aoto1*X(23,i)+Aoto2*X(22,i)+(19.62*(X(3,i)*X(4,i)+X(1,i)*X(2,i)
)-X(12,i));
    dot_x(24,i)=X(25,i);

dot_x(25,i)=Aoto1*X(25,i)+Aoto2*X(24,i)+(9.81*(X(1,i)*X(1,i)+X(4,i)*X(4,i)-
X(3,i)*X(3,i)-X(2,i)*X(2,i))-X(13,i));

% % Euler integration
X(:,i) = X(:,i) + 0.01 * dot_x(:,i);
end
end
Y = X;

mu = zeros(size(Y,1),1);
S = zeros(size(Y,1),size(Y,1));
C = zeros(size(xe,1),size(Y,1));
for i=1:size(X,2)
    mu = mu + WM(i) * Y(:,i); % predicted state mean
end
for i=1:size(X,2)
    S = S + WC(i) * (Y(:,i) - mu) * (Y(:,i) - mu)'; % covariance of the
estimated state
    C = C + WC(i) * (X(1:size(xe,1),i) - xe(:,k)) * (Y(:,i) - mu)'; %
cross-covariance Pxy
end

P=S+Q; %predicted state covariance
xe(:,k)=mu;

%% update
% recompute a new set of sigma points

```

```

%%1) weights
WM = zeros(2*n+1,1);
WC = zeros(2*n+1,1);
for j=1:2*n+1
    if j==1
        wm = lambda / (n + lambda);
        wc = lambda / (n + lambda) + (1 - alpha^2 + beta);
    else
        wm = 1 / (2 * (n + lambda));
        wc = wm;
    end
    WM(j) = wm;
    WC(j) = wc;
end
c = n + lambda;

%%2) sigma points
A = chol(P)';
X = [zeros(size(xe(:,k))) A -A];
X = sqrt(c)*X + repmat(xe(:,k),1,size(X,2));

%%3) SP propagation through the measurement equations
z = [];
if size(zr,1)==7
    for i=1:(2*n+1)
        z(1,i) = sqrt(X(1,i)^2+X(2,i)^2+X(3,i)^2+X(4,i)^2);
        z(2,i) =Ascc2*X(14,i)+Ascc1*X(15,i)+X(5,i);
        z(3,i) =Ascc2*X(16,i)+Ascc1*X(17,i)+X(6,i);
        z(4,i) =Ascc2*X(18,i)+Ascc1*X(19,i)+X(7,i);
        z(5,i) =Coto2*X(20,i)+Coto1*X(21,i);
        z(6,i) =Coto2*X(22,i)+Coto1*X(23,i);
        z(7,i) =Coto2*X(24,i)+Coto1*X(25,i);
    end
elseif size(zr,1)==13
    for i=1:(2*n+1)
        z(1,i)=Ascc2*X(14,i)+Ascc1*X(15,i)+X(5,i);
        z(2,i)=Ascc2*X(16,i)+Ascc1*X(17,i)+X(6,i);
        z(3,i)=Ascc2*X(18,i)+Ascc1*X(19,i)+X(7,i);
        z(4,i)=-X(5,i);
        z(5,i)=-X(6,i);
        z(6,i)=-X(7,i);
        z(7,i)=-X(8,i);
        z(8,i)=-X(9,i);
        z(9,i)=-X(10,i);
        z(10,i)=Coto2*X(20,i)+Coto1*X(21,i);
        z(11,i)=Coto2*X(22,i)+Coto1*X(23,i);
        z(12,i)=Coto2*X(24,i)+Coto1*X(25,i);
        z(13,i)=X(1,i)^2+X(2,i)^2+X(3,i)^2+X(4,i)^2;
    end
end

mu = zeros(size(z,1),1);
S = zeros(size(z,1),size(z,1));
C = zeros(size(xe,1),size(z,1));
for i=1:size(X,2)
    mu = mu + WM(i) * z(:,i);
end
for i=1:size(X,2)
    S = S + WC(i) * (z(:,i) - mu) * (z(:,i) - mu)'; % covariance of the
measurement Py

```

```

        C = C + WC(i) * (X(1:size(xe(:,k),1),i) - xe(:,k)) * (z(:,i) - mu)';
% cross-covariance
end

S = S + R;
K = C / S; % Kalman gain matrix
xe(:,k) = xe(:,k) + K * (zr(:,k) - mu); % update of the predicted state
P = P - K * S * K'; % update of the covariance matrix
end

tps=toc;
% *****
% Computation of Euler angles from quaternion parameters
% *****

duration=(size(y,2)-1)*0.04;
t=0:0.04:duration;
q0=xe(1,:);
q1=xe(2,:);
q2=xe(3,:);
q3=xe(4,:);
t=t';
options=simset('SrcWorkspace','current');
sim('quat_euler',[t],options);
angle=angle';
close(wait);

```

## **Modélisation du système vestibulaire et modèles non-linéaires de perception de l'orientation spatiale**

L'oreille interne est un organe fascinant du corps humain. Elle contient des organes sensoriels très précis et hypersensibles, ce qui lui permet de jouer un rôle majeur dans la perception de nos mouvements et de notre orientation spatiale.

Dans un premier temps, ce travail de thèse a porté sur la modélisation du fonctionnement des senseurs d'orientation de l'oreille interne. Un démonstrateur type « Réalité Virtuelle » a été développé sous Matlab/Simulink afin de visualiser en temps réel l'état de chaque senseur. Une modélisation plus détaillée par éléments finis et tenant compte d'interactions fluide/structure a permis d'étudier la dynamique des fluides au sein de chaque capteur ainsi que le déplacement de membranes - éléments clés permettant de coupler le déplacement du fluide avec la stimulation de cellules sensorielles.

Dans un second temps, ce travail de thèse s'est orienté vers le développement de modèles non-linéaires et tridimensionnels de perception de l'orientation spatiale. Ces modèles supposent que notre cerveau estime/calcul nos perceptions d'orientation, de vitesse, et d'accélération de façon « optimale ». Par conséquent, les modèles développés se sont appuyés sur deux techniques d'estimation non-linéaires basées sur le filtre de Kalman (« Extended Kalman filter » & « Unscented Kalman filter »). En réponse à différents profils de stimulation, ces modèles permettent de prédire diverses illusions sensorielles connues dans le monde de l'aéronautique. En tant qu'applications potentielles, ces modèles pourraient être utilisés d'une part lors d'investigation de crash d'appareil afin de détecter si le pilote a été sujet à un phénomène de désorientation spatiale, et d'autre part pour le développement d'algorithmes de contrôle des simulateurs de vols.

Mots clés : Système vestibulaire, Fluide/structure interaction, Modèles éléments-finis, Réalité virtuelle, Estimation optimale, Filtres de Kalman non-linéaire, Illusions sensorielles

### **Modeling of the vestibular system and nonlinear models for human spatial orientation perception**

The non-auditory section of the human inner ear, the vestibular system, is recognized as the prime motion sensing center. The vestibular system is comprised of two primary sensory organs and represents an inertial measuring device which allows us to sense self-motion with respect to the six degrees of freedom in space.

The scope of the work presented in this thesis concerns on one hand the modelling of the vestibular sensors, and on the other hand nonlinear models for human spatial orientation perception.

First, a virtual reality model of the vestibular sensors has been developed so as to visualize in real time the state of each sensor in response to any kind of head motion. Second, a three-dimensional model of the entire set of canals using fluid-structural finite-elements simulations has been proposed. Using a strong coupling between the fluid flow and the structural displacements and also an Arbitrary Lagrangian Eulerian (ALE) approach for the moving mesh, we analyze displacements of the cupulae and fluid velocity during head rotation.

Third, we developed a nonlinear model of human spatial orientation based on the Unscented Kalman Filter. This model successfully predicts the responses to a number of vestibular, visual and visual-vestibular motion paradigms. It turns out that the UKF yields more accurate and less oscillatory responses than Pommellet's Extended Kalman Filter model. As a prospect, this model could be used to investigate aircraft crashes so as to detect whether or not pilots have experienced a phenomenon of spatial disorientation.

Key words : Vestibular system, Fluid/Structure interaction, Finite-element models, virtual reality, Optimal state estimation, Nonlinear Kalman filtering, Sensory illusions